Time-Resolved Spectroscopy on Copper(I) Carbene Complexes

Inaugural Dissertation

for the attainment of the title of doctor
in the Faculty of Mathematics and Natural Sciences
at the Heinrich Heine University Düsseldorf

presented by

Oliver Nolden
from Tönisvorst

Düsseldorf, May 2023

from the institute of physical chemistry II
at the Heinrich Heine University Düsseldorf

Published by permission of the
Faculty of Mathematics and Natural Sciences at
Heinrich Heine University Düsseldorf

Supervisor: Prof. Dr. Peter Gilch
Co-supervisor: Prof. Dr. Christian Ganter

Date of the oral examination: 30/06/2023

Acknowledgements

First and foremost, I would like to thank my PhD supervisor, Prof. Dr. Peter Gilch. Thanks to him, I was able to develop enormously during my doctoral studies and to dive deeply into the world of physical chemistry, i.e. into the microcosm of space and – obviously – time. I would also like to thank him for the trust he placed in me and for the constructive discussions we had. I would also like to express my sincere gratitude for the organization of the DFG Research Training Group, of which I was allowed to be a part as an associated researcher.

Furthermore, I would like to thank Prof. Dr. Christian Ganter. In one aspect for taking over the second review, but above all for the constructive discussions, the well-balanced feedback and his profound knowledge of copper complexes.

Furthermore, I would like to thank Prof. Dr. Thomas J. J. Müller. On the one hand for the excellent organization of the DFG Research Training Group, on the other hand for many useful comments on my research. For example, thanks to him, after a long search, a suitable solvent for the linear copper complex could be found, which enabled a great progress in this research project.

I would also like to thank Dr. Martina Holz for taking part in the organization of the Research Training Group and for always being available for all kinds of questions.

Besides that, a special thanks goes to my research colleagues and everyone who helped me with my projects: Jennifer Kremper, who supported me with numerous experiments and good ideas in the course of her bachelor thesis as well as in the research internship and beyond; Oliver Röth, who provided active support with many experiments in the course of his master thesis; Philipp Schmeinck for the synthesis of the copper complex as well as lively exchange about the compound's recalcitrant behavior; Jasper Guhl for the numerous quantum chemical calculations and just as many physical-philosophical discussions about copper complexes and its peculiarities; my colleague and former office partner Wiebke Haselbach for many cordial and profound conversations as well as for the measurements at the nsTA device; Mahbobeh Morshedi, who always managed to give me a good feeling at work and for the measurements at the fsFl device; my former colleague and office partner Dr. Kristoffer A. Thom, who always provided me with good answers and discussions; Franziska Bergstein for being always available for all kinds of technical difficulties that occurred; all my other colleagues whom I have not mentioned by name here.

Likewise, I would like to thank my last two office colleagues Simon Zimmermann and Matthias Jantz. Without these bright guys the last year would not have been filled with so much humour, definitely.

Last but not least, I would like to thank the people who, away from the university, gave me the strength and stamina to accomplish this feat. I think especially of my parents, who have been incredibly supportive along the way. Similarly, I am immensely grateful to my sister and my partner. It is not a simple task to express enough appreciation for your positive inspiration.

Additionally, I would also like to thank the Willicher Kegelclub and consorts for the many distracting conversations and activities that have always reminded me of a life away from science and research.

In addition, I would like to thank all those who would have liked me to thank them, and all those I have actually forgotten.

Thank you!

Publications, Presentations, Posters

Publications in Peer-Reviewed Journals

- Nolden, O., Fleck, N., Lorenzo, E.R., Wasielewski, M.R., Schiemann, O., Gilch, P., Richert, S. (2021): Excitation Energy Transfer and Exchange-Mediated Quartet State Formation in Porphyrin-Trityl Systems. In: *Chemistry – A European Journal*, 27, 2683-2691. DOI: 10.1002/chem.202002805
- Mayländer, M., Nolden, O., Franz, M., Chen, S., Bancroft, L., Qiu, Y., Wasielewski, M.R., Gilch, P., Richert, S. (2022): Accessing the triplet state of perylenediimide by radical-enhanced intersystem crossing. In: *Chemical Science*, 13, 6732-6743. DOI: 10.1039/D2SC01899C
- Nolden, O., Kremper, J., Haselbach, W., Morshedi, M., Guhl, J., Schmeinck, P., Marian, C. M., Ganter, C., Gilch, P., (2022): Femtosecond Spectroscopy and Quantum Chemistry of a Linearly Coordinated Copper(I) Carbene Complex. In: *ChemPhotoChem*, 7, e202200231. DOI: 10.1002/cptc.202200231
- Morshedi, M., Nolden, O., Janke, P., Haselbach, W., Schmitt, M., Gilch, P., (2023): The Photophysics of 2-Cyanoindole Probed by Femtosecond Spectroscopy. In: *Photochem Photobiol Sci*, 22, 745–759. DOI: 10.1007/s43630-022-00348-3
- Thom, K. A.[+], Nolden, O.[+], Weingart, O., Izumi, S., Minaka, S., Takeda, Y., Gilch, P., (2022): Femtosecond Spectroscopy on a Dibenzophenazine-Cored Macrocycle Exhibiting Thermally Activated Delayed Fluorescence. In: *ChemistryOpen*, 12, e202300026. DOI: 10.1002/open.202300026.

[+] These authors contributed equally.

Conference participation

- **Poster presentation**: Nolden, O., Thom, K. A., Diekmann, J., and Gilch, P., Time-resolved Spectroscopy on Chemical and Biological Processes, ELI Beamlines, Ultrafast Spectroscopy User Workshop, Dolní Brežany, Czechia; 09/2019
- **Oral presentation**: Nolden, O., Reiffers, A., Rademacher, M., and Gilch, P., CO_2 Release in Carboxyl Substituted Phthalimides, 9th Central European Conference on Photochemistry, Bad Hofgastein, Austria; 02/2020
- **Poster presentation**: Nolden, O., Röth, O., Morshedi, M., and Gilch, P., Copper(I) Carbene Emitters Studied by Femtosecond Spectroscopy, 10th Central European Conference on Photochemistry, Bad Hofgastein, Austria; 02/2022

Abstract

Organic light-emitting diodes (OLEDs) are an emerging technology that have attracted significant attention due to their prominent use in displays and other lighting applications. The development of efficient OLEDs requires the identification and optimization of suitable emitter materials that can generate bright light in a range of colors. Copper(I) carbene complexes have been suggested as promising candidates for OLED emitters due to their unique photophysical properties. In this thesis, two copper(I) carbene complexes are investigated using a range of spectroscopic methods, first and foremost time-resolved techniques, to explore their potential as OLED emitters and to deepen the understanding of their photophysics.

The first study explores the photophysics of a linearly coordinated copper(I) carbene complex, namely, [1,3-bis(2,6-diisopropylphenyl)imidazol-2-ylidene] (2-picoline) copper(I) tetrafluoroborate (NHCCuPy, Figure **A**). Previous studies showed that the emission characteristics of the compound strongly depend on the environment. Here, these observations are picked up, and conclusive results are drawn on the compound's structure and photophysics in solution. For a systematic approach, the complex was investigated in coordinating and non-coordinating solvents.

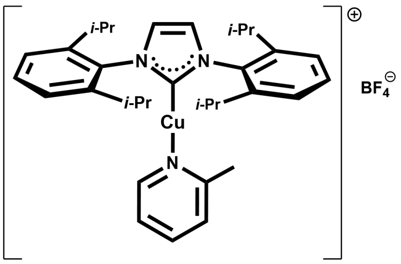

Figure A. Structure of NHCCuPy.

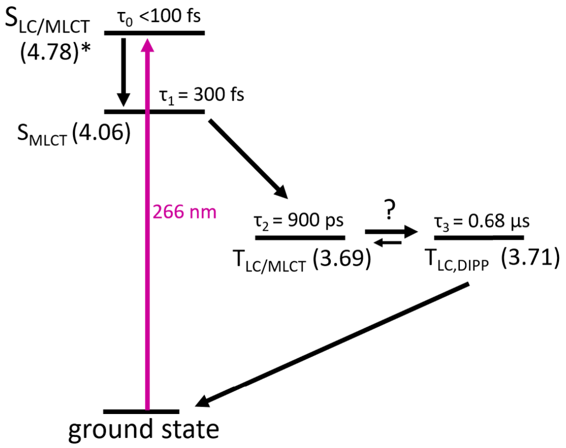

Figure B. Kinetic scheme proposed for NHCCuPy.

In coordinating solvents evidence is obtained for an equilibrium reaction between solvent and solute forming a trigonal complex with distinct absorption, emission, and excited state kinetic behavior. In contrast, in non-coordinating solvents, the results indicate that the linear species, also present in single crystals, constitutes the dominant species. Its excited state kinetics is successfully deciphered by time-resolved experiments and quantum chemical computations (see Figure **B**).

In the second study, a similar copper(I) carbene complex, in which the 2-picoline ligand is replaced by a chelating dibenzoylmethanoate ligand (1,3-bis(2,6-diisopropylphenyl)imidazol-2-ylidene](dibenzoylmethanoate) copper(I), abbreviated: NHCCuDBM, Figure **C**) is investigated. Here, it is systematically elaborated on whether or not this trigonal complex exhibits a suitable emission behavior and why.

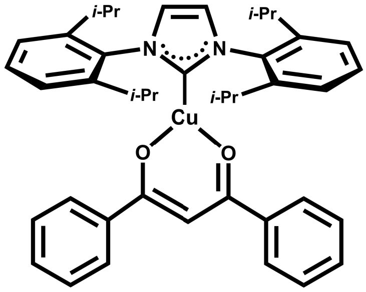

Figure C. Structure of NHCCuDBM.

First, the ligand dibenzoylmethanoate and its protonated form dibenzoylmethane are examined in detail. The latter shows a high radiative rate constant for its lowest excited singlet state. However, this state is efficiently quenched due to isomerization processes occurring in the excited state. These processes are absent in the complex and the overall excited state lifetime is extended by roughly two orders of magnitude.

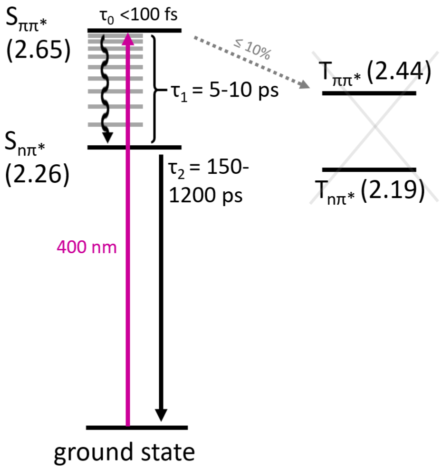

Figure D. Kinetic scheme proposed for NHC-CuDBM.

Despite this prolongation of the excited state lifetime, also the complex is virtually non-emissive. This behavior is clarified by the character and energetic order of the lowest excited states. In contrast to the free DBM, where the lowest excited state is of $\pi\pi^*$ character, in the complex the lowest excited state constitutes a state dominantly of $n\pi^*$ character with a small oscillator strength typical for these states. Taking into account spectroscopic results and quantum chemical calculations, a comprehensive picture of the compound's excited state kinetics is obtained (see Figure **D**). Significant population of a triplet state is considered unlikely. Based on these results, structural suggestions are made to enable the complexes' emission. Furthermore, a connection is drawn to the peculiar environmental dependence addressed in the first study.

Zusammenfassung

Organische Leuchtdioden (OLEDs) stellen eine vielversprechende Technologie dar, die aufgrund ihrer prominenten Verwendung in Displays und anderen Beleuchtungsanwendungen viel Aufmerksamkeit erregen. Die Entwicklung effizienter OLEDs erfordert die Identifizierung und Optimierung geeigneter Emittermaterialien. Kupfer(I)-Carben- Komplexe wurden aufgrund ihrer besonderen photophysikalischen Eigenschaften als geeignete Kandidaten für OLED-Emitter vorgeschlagen. In dieser Arbeit werden zwei solcher Komplexe unter Verwendung einer Reihe spektroskopischer Methoden untersucht. Dabei kommen insbesondere zeitaufgelöste Spektroskopiemethoden zum Einsatz.

Die erste Studie untersucht die Photophysik eines linear koordinierten Kupfer(I)-Carben-Komplexes, genauer [1,3-Bis(2,6-diisopropylphenyl)imidazol-2-yliden]-(2-picolin)-Kupfer(I)-tetrafluoroborat (NHCCuPy, s. Abbildung **A**). Vorrangegangene Studien hatten ergeben, dass die Emissionseigenschaften dieses Komplexes stark von seiner Umgebung abhängig sind. In dieser Arbeit werden diese Beobachtungen aufgegriffen sowie Rückschlüsse auf Struktur und Photophysik der Verbindung in Lösung gezogen.

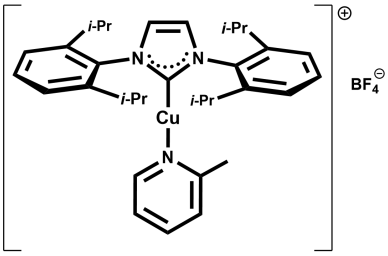

Figure A. Structure of NHCCuPy.

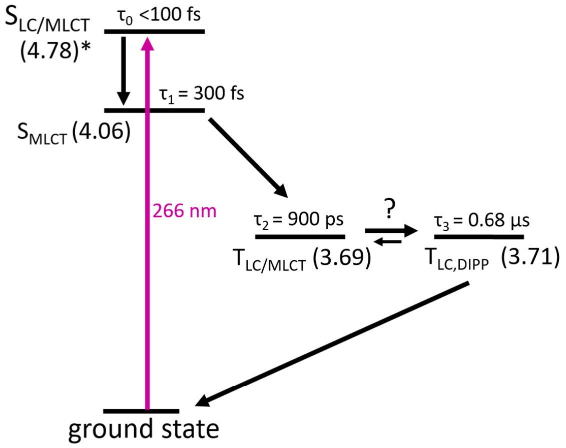

Figure B. Kinetic scheme proposed for NHCCuPy.

Zur systematischen Untersuchung wird der Komplex in koordinierenden und nicht-koordinierenden Lösungsmitteln untersucht. In koordinierenden Lösungsmitteln wird eine Gleichgewichtsreaktion zwischen Lösungsmittel und Komplex nachgewiesen. Dabei bildet sich ein neuer, trigonaler Komplex mit stark verschiedenem Absorptions- und Emissionsverhalten. Im Gegensatz dazu deuten die Ergebnisse in nicht-koordinierenden Lösungsmitteln darauf hin, dass der lineare Komplex, der auch in Einkristallen nachgewiesen ist, die dominante Struktur darstellt. Die Kinetik der angeregten Zustände wird erfolgreich mittels zeitaufgelöster Experimente und unter Zuhilfenahme quantenchemischer Berechnungen entschlüsselt (s. Abbildung **B**).

Im Rahmen der zweiten Studie wird ein ähnlicher Kupfer(I)-Carben-Komplex, bei dem der 2-Picolin-Ligand durch den Chelat-Liganden Dibenzoylmethanato ersetzt ist, untersucht ([1,3-Bis(2,6-diisopropylphenyl)imidazol-2-yliden]-(dibenzoylmethanato)-Kupfer(I); NHCCuDBM; s. Abbildung **C**). Dabei wird dieser Komplex systematisch auf sein Emissionsverhalten und die zugrunde liegenden Ursachen für dieses Verhalten untersucht.

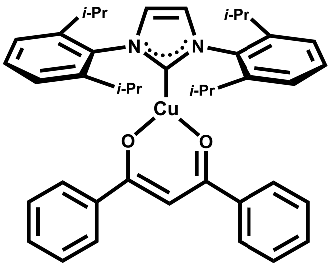

Figure C. Structure of NHC-CuDBM.

Zunächst wird der Ligand Dibenzoylmethanoat und seine protonierte Form Dibenzoylmethan im Detail spektroskopisch untersucht. Letztere weist eine hohe strahlende Ratenkonstante für den niedrigsten angeregten Singulettzustand auf. Dieser Zustand wird jedoch durch Isomerisierungsprozesse effizient gelöscht. Diese desaktivierenden Prozesse werden für den Komplex nicht beobachtet und die Lebensdauer des angeregten Zustands wird um etwa zwei Größenordnungen verlängert.

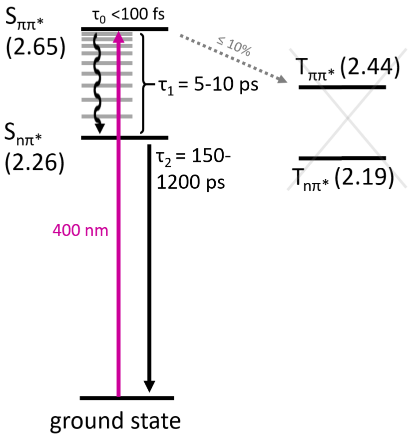

Figure D. Kinetic scheme proposed for NHC-CuDBM.

Trotz dieser Verlängerung des angeregten Zustands weist der Komplex kaum Emission auf. Dieses Verhalten lässt sich durch den Charakter und die energetische Reihenfolge der niedrigsten angeregten Zustände erklären. Im Gegensatz zum frei vorliegenden DBM, bei dem der niedrigste angeregte Zustand $\pi\pi^*$-Charakters aufweist, besitzt der niedrigste angeregte Zustand im Komplex hauptsächlich $n\pi^*$-Charakter mit einer typischerweise kleinen Oszillatorstärke.

Unter Berücksichtigung der spektroskopischen Ergebnisse sowie quantenchemischer Berechnungen wird ein umfassendes Bild der angeregten Zustände und ihrer Kinetik für den Komplex erhalten (s. Abbildung **D**). Eine signifikante Population des

Triplettzustands wird als unwahrscheinlich bewertet.

Basierend auf diesen Ergebnissen werden strukturelle Vorschläge gemacht, die die Emission des Komplexes bzw eines Derivates ermöglichen könnten. Darüber hinaus wird eine Verbindung zu der besonderen Umgebungabhängigkeit von Komplexen und ihrer Photophysik, die in der ersten Studie bereits behandelt wird, hergestellt.

List of Abbreviations

BBO	β-barium borate
CAAC	cyclic (amino)-(alkyl)carbene
CAArC	cyclic (amino)-(aryl)carbene
CE	chelated enol
CI	conical intersection
Cx	cyclohexane
CTTS	charge-transfer-to-solvent
DADS	decay associated difference spectrum
DBM	dibenzoylmethane
DFT	density functional theory
EBL	electron blocking layer
ETL	electron transport layer
ESA	excited state absorption
ESIPT	excited state intramolecular proton transfer
EtOH	ethanol
EVR	external vibrational energy redistribution
exc	excitation
FC	Franck-Condon
fs	femtosecond (10^{-15} s)
fsTA	femtosecond transient absorption
FWHM	full width at half maximum
GSB	ground state bleach
HBL	hole blocking layer
HOMO	highest occupied molecular orbital
HTL	hole transport layer
IC	internal conversion
IRF	instrument response function
ISC	intersystem crossing
IVR	intramolecular vibrational energy redistribution
LCAO	linear combination of atomic orbitals
LED	light emitting diode
LLCT	ligan-to-ligand charge-transfer
LUMO	lowest unoccupied molecular orbital

MC	metal-centered
MeCN	acetonitrile
MLCT	metal-to-ligand charge-tranfer
MO	molecular orbital
MRCI	multireference configuration interaction
NCE	non-chelated enol
Nd:YAG	neodymium-doped yttrium aluminum garnet; Nd:$Y_3Al_5O_{12}$
NHC	1,3-bis(2,6-diisopropylphenyl)imidazol-2-ylidene
NIR	near-infrared
NOPA	non-linear optical parametric amplifier
ns	nanosecond (10^{-9} s)
nsTA	nanosecond transient absorption
OLED	organic light emitting diode
OPA	optical parametric amplifier
PET	photoinduced electron transfer
ps	picosecond (10^{-12} s)
Py	2-methylpyridine (2-picoline)
RAHB	resonance-assisted hydrogen bonding
RGB	red-green-blue
rISC	reverse intersystem crossing
SE	stimulated emission
SFG	sum frequency generation
SHG	second harmonic generation
SNR	signal-to-noise ratio
SOC	spin-orbit coupling
TA	transient absorption
TADF	thermally activated delayed fluorescence
TD-DFT	time-dependent density functional theory
TFE	2,2,2-trifluoroethanol
THG	third harmonic generation
Ti:Sa	sapphire (Al_2O_3) doped with titanium ions (Ti^{3+})
TPA	two-photon absorption
TTA	triplet-triplet annihilation
UV	ultraviolet (light)
VC	vibronic coupling
VR	vibrational relaxation
Vis	visible (light)
ZPVE	zero-point vibrational energy

Contents

1. Introduction

1.1. Organic Light Emitting Diodes

Artificial lighting, or the use of light sources to artificially illuminate indoor and outdoor spaces, has a long and fascinating history dating back thousands of years. The earliest known artificial light sources were made from materials such as animal fat, beeswax, and vegetable oils, and were used in ancient civilizations such as Egypt, Greece, and Rome.[1,2] These early lighting sources were simple but effective and provided people with a way to see and work after dark. Over time, artificial lighting technology evolved, with new materials and techniques being developed to create brighter, more efficient light sources. In the early 19th century, gas lighting became popular in urban areas, with streetlamps and indoor gas lighting becoming commonplace.[3] However, gas lighting was eventually replaced by electric lighting, which was first introduced in the late 19th century.[4]

Since the introduction of incandescent light bulbs, the world of artificial lighting has evolved rapidly. The development of fluorescent tubes, halogen bulbs, and light-emitting diodes (LEDs) have all provided new levels of efficiency and brightness, while smart lighting systems have made it possible to control lighting remotely and even customize it according to individual preferences. One of the more recent advancements in artificial lighting technology is the organic light-emitting diode (OLED). Unlike traditional light sources that rely on a filament or gas to produce light, OLEDs use thin layers of organic materials that emit light when stimulated by an electrical current. OLED lighting has several advantages over traditional lighting technologies, including improved energy efficiency, longer lifespan, and the ability to create flexible, ultra-thin light sources. OLEDs are already being used in a variety of applications, including TV screens, computer monitors, and smartphone displays. The use of OLEDs as a general source for room lighting yet continues to be a goal in the development of this technology.

To further improve the efficiency and lifespan of OLEDs, one focus in research has been on developing new emitter substances as part of OLED devices. In particular, the approach of using transition metal complexes, especially copper(I) complexes, has received considerable attention due to their unique photophysical properties. These properties, within the context of an OLED application, are described in detail in the following sections. Before, the device structure and the underlying principle of operation of an OLED are briefly summarized.

1.1.1. Principle of Operation and Device Structure

OLEDs consist of several layers, each of which performs a specific function to emit light efficiently. The device structure of an OLED typically includes the following components[1]:

- Substrate: The bottom layer that provides support to the device.
- Anode: An electrode that injects holes into the organic layers.
- Hole Transport Layer (HTL): A layer of organic material that facilitates the transport of holes from the anode to the emissive layer.
- Electron Blocking Layer (EBL): A layer of organic material that prevents electrons from leaking into the adjacent layer.
- Emissive Layer: A thin layer of organic material that emits light when an electric current is applied. The emissive layer contains the emitter substance that determines the color (i.e. energy) of the emitted light.
- Hole Blocking Layer (HBL): A layer of organic material that prevents holes from leaking into the adjacent layer.
- Electron Transport Layer (ETL): A layer of organic material that facilitates the transport of electrons from the cathode to the emissive layer.
- Cathode: An electrode that injects electrons into the organic layers.

The principle of operation of an OLED involves the injection of holes[2] and electrons into the organic layers, where they recombine to produce light. An applied voltage causes electrons to propagate from the cathode to the electron transport- and hole-blocking layer, while

---

[1] Principally it is possible to have an OLED only consisting of an emissive layer sandwiched between an anode and a cathode.[5] However, due to massive research regarding the optimization of the device structures, nowadays, OLEDs contain many more layers increasing not only their complexity but also their luminescence, lifetime, power efficiency, and internal efficiency.[6]

[2] Holes (also referred to as electron holes) denote positively charged vacancies in the organic semiconductor material. They represent the absence of an electron at a position in an atomic or molecular lattice where an electron would normally reside. Therefore, it does not constitute a real particle and is referred to as a quasiparticle. In this context, holes are considered the positively charged counterpart of negatively charged electrons.[7]

holes propagate from the anode to the hole transport- and electron-blocking layer, with both eventually reaching the "shared" emissive layer.[6] On their way through the organic layers, the electrons are, according to the molecular orbital theory, located in the lowest unoccupied molecular orbitals (LUMOs) while holes are located in the highest occupied molecular orbitals (HOMOs) of the respective molecules in each layer[3] (see Figure 1.1).[8] During the process, electrons transition from the LUMO of one molecule to that of a neighboring molecule, resulting in the reduction of the latter to a radical anion. Similarly, in hole transport, neighboring molecules' HOMOs undergo a successive exchange of charges leading to a stepwise oxidation to radical cations. This movement of charge carriers is also referred to as "hopping" due to its cascading nature.[9]

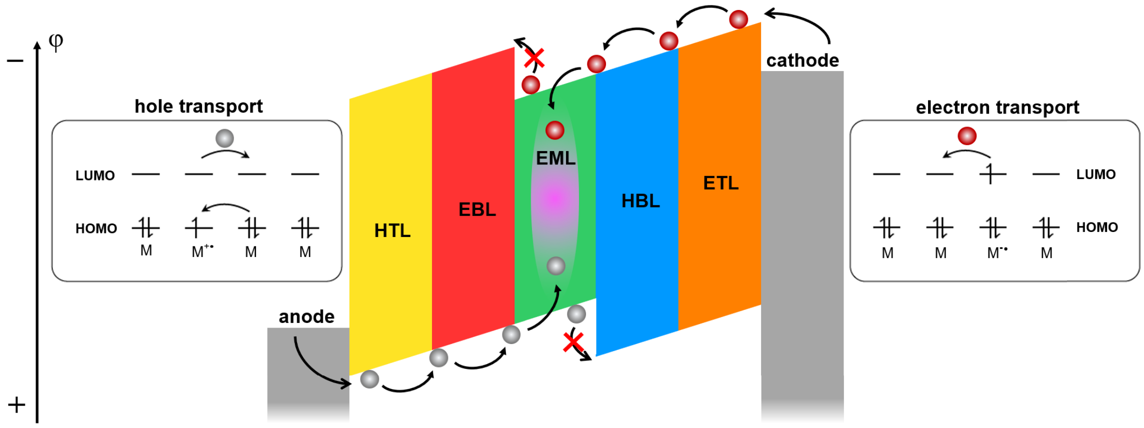

Figure 1.1.: Schematic architecture and principle of operation of an OLED. Holes (white circles) are injected at the anode, and electrons (red circles) are injected at the cathode. Electrons and holes move towards each other and transmit through different organic layers until they reach the emitting layer (green) which is doped with the emitting substance(s) (purple). Further movement of electrons and holes beyond this layer is prevented by blocking layers (red, blue). The electron transport through the LUMOs is simplified on the right side, and the hole transport through the HOMOs is shown analogously on the left side. The upper and lower edges of the depicted organic layers qualitatively mark the LUMO and HOMO levels of each layer. The vertical axis shows the electric potential and goes from a positive to a negative electric potential. Based on refs.[10,11,12].

The direction that electrons and holes take is given by the voltage gradient. On the electron injecting side the electron transport layer reduces the energy difference of the LUMOs between the cathode and the adjacent layer so that it can still be overcome by the electrons. On the

---

[3] It should be noted that referring to HOMO and LUMO and respective transitions between those molecular orbitals constitutes a simplification of the real situation.

hole-injecting side, the difference in energy of the HOMOs is reduced by the hole transport layer. Furthermore, high hole mobility and low electron mobility are desired for the HTL, and vice versa in the case of the ETL.[13,14] By introducing a carrier blocking layer (EBL and HBL) between the carrier transport and the emissive layer, the OLEDs efficiency can be increased significantly.[6] The purpose of the EBL is to prevent electrons from transitioning from the emissive layer to the HTL, while the HBL stops holes from moving past the emissive layer towards the cathode. This structure makes sure, that electrons and holes recombine in the emissive layer forming an exciton, a Coulomb-correlated bound pair of electron and hole.[15] In the context of OLEDs, the exciton can be viewed as the emitter molecule in an electronically excited state.[4] As the excited state of the emitter molecules deactivates, photons are emitted with frequencies equivalent to the respective HOMO-LUMO gap of the emitter molecule.

1.1.2. Singlet- and Triplet Harvesting

Among other things, LEDs and OLEDs differ in the type of exciton formed. In the case of LEDs, Wannier-Mott, and in the case of OLEDs, Frenkel excitons are generated. In Frenkel excitons, the electron and the hole are situated on the same molecule and their binding energy[5] is around 0.1–1 eV.[16] The Wannier-Mott excitons have a spatial extent of about 100 Å and their binding energies are much less significant (10–30 meV) compared to their organic counterparts.[16] As (potential) emitters for OLEDs are studied here, only Frenkel-type excitons, where the electron-hole pair is localized on the same molecule, are considered in the following. In the exciton one unpaired electron is located in the LUMO while the other unpaired electron (i.e. the hole) is located in the HOMO. As electrons and holes have a spin quantum number s of $\frac{1}{2}$, values of either 1 or 0 result for the total spin S according to eq. 1.1.

$$S = \mid s_1 - s_2 \mid ... \mid s_1 + s_2 \mid \tag{1.1}$$

For a total spin of $S = 0$ the multiplicity M, according to eq. 1.2, equals 1. Therefore, such a state is referred to as a singlet state, and the number of possible states (i.e. degenerate

---

[4] Here, a differentiation between Frenkel excitons as part of OLEDs, and Wannier-Mott excitons as part of inorganic LEDs, is important. More on that in section 1.1.2.

[5] In this context, the binding energy refers to the amount of energy needed to separate the exciton into a free electron and hole.

states; see eq. 1.2) amounts to 1, respectively.[17]

$$M = 2 \cdot S + 1 = \#states \tag{1.2}$$

In the case of a total spin of $S = 1$, the multiplicity M equals 3. This state is referred to as a triplet state, which possesses a three-fold degeneracy, accordingly. This is a consequence of the different possibilities to have two (quantum mechanical) spins aligned with the respective magnetic quantum numbers M_S of -1, 0, and 1 (see Figure 1.2).[17]

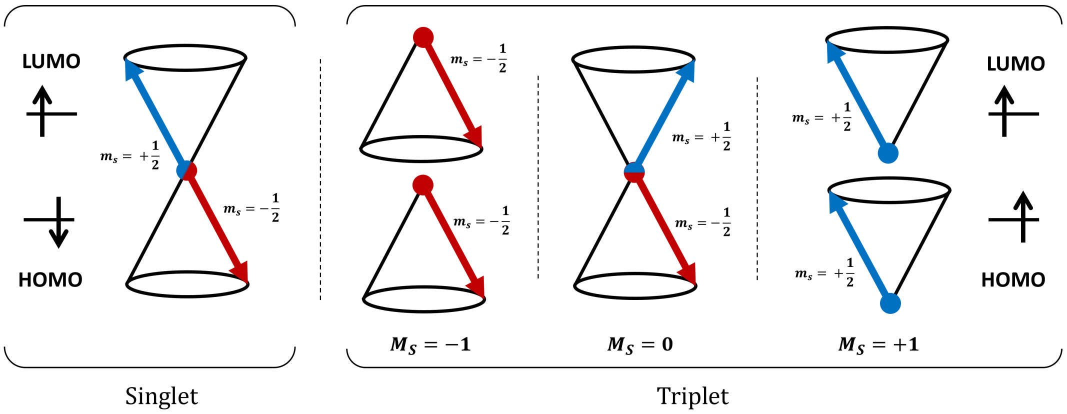

Figure 1.2.: Multiplicities of a two electron system. For a total spin of $S = 0$ (left) a singlet state is present. For a total spin of $S = 1$ a triplet state is present with three possible values for the magnetic quantum number M_S (-1, 0, and $+1$).

Since the injected holes and electrons (i.e. the unpaired electrons in HOMO and LUMO) are not correlated, they recombine in a stochastic manner. Due to the different amounts of possible orientations (i.e. singlet: 1; triplet: 3), 25% of the generated excitons are of singlet, and 75% are of triplet character as a "simple" statistical effect.[18] The harvesting of both singlet and triplet excitons for the emission of light, therefore, represents a major challenge. The terms singlet- and triplet harvesting refer to this challenge and ways to utilize all the generated excitons for the light emission process, respectively. Principally, this can be achieved by transferring all the excitation energy either into the singlet manifold (triplet harvesting) or into the triplet manifold (singlet harvesting).[19,20] In the literature, this terminology is not consistent and it is sometimes referred to the other way around.[21,22] Here, the former is used. In practice, singlet harvesting is achieved for emitters showing fast intersystem crossing (ISC), usually from the lowest singlet state to the lowest triplet state outcompeting other deactivating mechanisms of the singlet state (mainly fluorescence or internal conversion). By that, up to 100% of excitons formed end up in a phosphorescent triplet state. These emitters are referred to as phosphorescent emitters, accordingly.

Regarding triplet harvesting, mainly two approaches exist. Conversion of the 75% triplet excitons into singlet excitons is achieved by reverse intersystem crossing (rISC) either from the lowest triplet state to the lowest singlet state, which is referred to as thermally activated delayed fluorescence (TADF)[23] or from an upper excited triplet state to a lower lying singlet state, which is referred to as HIGHrISC[24] or hot exciton[25]. Singlet- and triplet harvesting and the respective types of emitters are schematically summarized in Figure 1.3. A more detailed description of the TADF process is given in the following section 1.2, which introduces copper(I) complexes within the context of an OLED application.

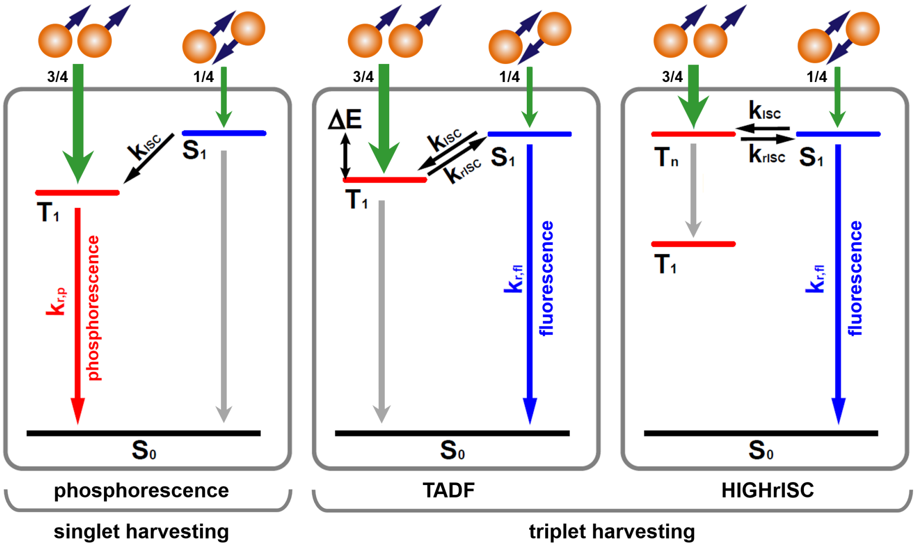

Figure 1.3.: Scheme on singlet and triplet harvesting and the principle of operation of the different OLED emitter types. Phosphorescence emitters show fast ISC rate constants quickly converting the singlet excitons into triplet ones (singlet harvesting), which deactivate via phosphorescence (red arrow). TADF emitters possess a small $S_1 - T_1$ energy gap ΔE, allowing (amid other requirements) the conversion of the triplet excitons into singlet ones (triplet harvesting), which deactivates via fluorescence (blue arrow), due to fast rISC. Similarly, HIGHrISC emitters make use of fast rISC. Here, a long-lived upper triplet states mediates the conversion of the triplet excitons into singlet ones. Gray arrows mark undesired deactivating pathways. Figure adapted from ref.[26].

1.2. Copper(I) Complexes for OLED Application

Since the first solid-state electroluminescent device based on a transition metal complex as the emitting substance was introduced in 1996,[27] remarkable progress has been made in the last two decades. Phosphorescent organo-transition metal compounds have become a focus of intense research, particularly due to their feasibility as efficient OLED emitters. Here, especially the platinum group has attracted a lot of attention. To this date, two of the most frequently applied central metal ions in phosphorescent OLED emitters are Pt(II) and Ir(III).[28,29,30]

A famous example and perhaps the most studied compound of this material class is tris(2-phenylpyridine)iridium(III), commonly referred to as Ir(ppy)3.[12,30] This complex is widely used due to its high efficiency and stability. It has a relatively short-lived ($\approx 1.6\ \mu$s) green emission with a peak wavelength of around 520 nm and a narrow emission spectrum, which makes it suitable for use in RGB (red-green-blue) displays as a green emitter.[31] Complexes based on Pt(II) and Ir(III) ions usually exhibit high phosphorescence quantum yields. Although this transition (i.e. excited triplet → singlet ground state) is formally forbidden, it becomes sufficiently allowed due to spin-orbit coupling (SOC) mediated by the heavy metal. Similarly, the intersystem crossing from the energetically higher singlet to the phosphorescent triplet state is increased due to SOC. This enables these complexes – applied in OLED devices – to exploit both singlet and triplet excitons for emission (see section 1.1.2, singlet harvesting).[28]

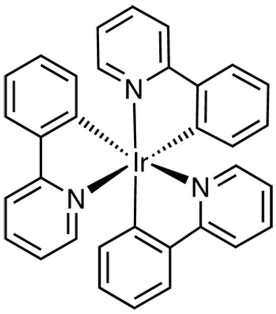

Figure 1.4.: Structure of Ir(ppy)$_3$.

However, despite the potential benefits, the use of these rare-earth complexes poses certain drawbacks due to their scarcity and high costs,[32,33] uncertain toxicities,[34] and issues regarding undesired dd^* transitions due to their non-radiative nature (see below).[35]

Consequently, alternative emitter materials are needed, such as compounds utilizing first-row transition metals, which are more readily available.[36] One candidate that attracted much of interest is the Cu(I) ion. Besides wide-spread availability and existing recycling cycles, with a closed shell d^{10} configuration, complexes based on Cu(I) additionally have the advantage that undesired metal centered dd^* transitions are absent. As these dd^* states are usually non-emissive, they significantly contribute to non-radiative deactivation and even trigger decomposition. This is particularly true for blue-emitting compounds where the emissive and the dd^* states can be in close energetic proximity.[35] However, due to relatively small spin-orbit coupling constants for copper complexes compared to those based on heavier elements, phosphorescent decay times are expected to be long. This in turn would, besides a lowered brightness, result in unwanted saturation effects such as triplet-triplet annihilation or other efficiency roll-off effects.[36,37] Despite this, many Cu(I) complexes proofed to be highly efficient emitters.[38] This can be explained by the fact that many of these emitters are actually not phosphorescent emitters – although initially assumed[39] – but fluorescent emitters, more precise, thermally activated delayed fluorescence emitters.

For such Cu(I) complexes a pronounced metal-to-ligand charge transfer (MLCT) character was found for the lowest excited singlet (S_1) and triplet states (T_1). The respective transitions involved induce noticeable spatial separation between the relevant orbitals (i.e. the HOMO and LUMO), leading to small exchange integrals and as a result narrow energy gaps between the S_1 and the T_1 states, often less than 100 meV.[36] For some Cu(I) complexes, intersystem crossing processes occur within around 10 ps[36] or even a few hundred fs,[40] resulting in fast thermal equilibration between the lowest singlet and triplet states. The ratio of the population of these states is determined by a Boltzmann distribution. Thus, for high enough temperatures (i.e. room temperature) and a sufficient oscillator strength for the S_1 to ground state S_0 transition, the decay of the excited singlet state dominates the emission decay time. Under these circumstances, the triplet state is predominantly depleted by thermally activated delayed fluorescence.[36] A detailed description of the electronic structure, typically present in emitting Cu(I) complexes, is given in section 2.4.

Over the past decade, Cu(I) complexes have been the subject of increasing interest due to these unique properties making them highly desirable for producing efficient OLED devices that emit light in a range of colors at relatively low cost. Figure 1.5 showcases some promising Cu(I) complexes[41,42,43,44] for OLEDs reported in recent years, providing insight into their photophysical properties, including emission wavelength, lifetime, and quantum yields.

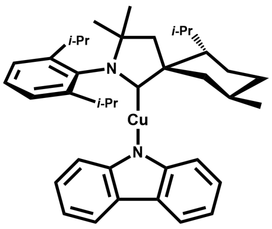

a

CAAC-CuCz

$\boldsymbol{\lambda_{max}^{em}}$ **= 474 nm**

$\boldsymbol{\phi_{PL}}$ **= 1.0**

$\boldsymbol{\tau}$ **= 2.8 μs**

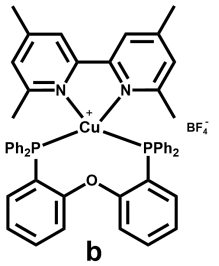

b

[Cu(POP)(4,4‘,6,6‘-bpy)]$^+$ BF_4^-

$\boldsymbol{\lambda_{max}^{em}}$ **= 555 nm**

$\boldsymbol{\phi_{PL}}$ **= 0.74**

$\boldsymbol{\tau}$ **= 11 μs**

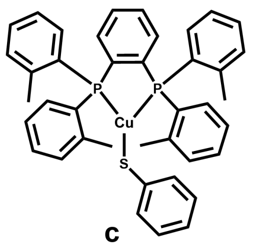

c

Cu(LMe)(SPh)

$\boldsymbol{\lambda_{max}^{em}}$ **= 592 nm**

$\boldsymbol{\phi_{PL}}$ **= 0.24**

$\boldsymbol{\tau}$ **= 1.4 μs**

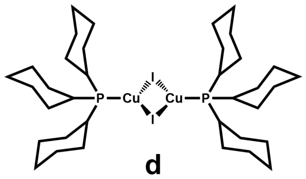

d

[CuI(PCy$_3$)]$_2$

$\boldsymbol{\lambda_{max}^{em}}$ **= 448 nm**

$\boldsymbol{\phi_{PL}}$ **= 0.43**

$\boldsymbol{\tau}$ **= 3.8 μs**

Figure 1.5.: Four examples of copper(I) complexes with potential application in OLEDs. a) two-coordinate complex CAAC-CuCz[43] (CAAC = Cyclic(alkyl)(amino)carbene, Cz = Carbazole); b) four-coordinate complex [Cu(POP)(4,4‘,6,6‘-bpy)]$^+$ BF_4^- [41] (POP = bis(2-(diphenylphosphanyl)phenyl)ether, bpy = 2,2’-bipyridine); c) three-coordinate complex Cu(LMe)(SPh)[42] (LMe = 1,2-bis[bis(2-methylphenyl)phosphino]-benzene, SPh = thiophenolate); d) dinuclear copper(I) cluster [CuI(PCy$_3$)]$_2$[44] (Cy = cyclohexyl). With λ_{max}^{em} the wavelength of the emission maximum, Φ_{PL} the quantum yield of emission, and τ the emission lifetime. Values were obtained at room temperature.

1.2.1. N-Heterocyclic Carbenes

Carbene synthesis attempts have been ongoing since 1835.[45,46] However, it was not until 1988 that Bertrand and his colleagues successfully isolated the first free carbene.[47] Shortly after, in 1991, Arduengo and his team presented the first carbene that was stabilized by incorporation in a nitrogen heterocycle, leading to the development of the well-known class of N-heterocyclic carbenes (NHC).[48] Although initially viewed as just a laboratory curiosity,[49] NHCs have become important ligands for transition metals, with numerous applications in academic research, one of which is the potential application as an OLED emitter, and even large-scale industrial processes, primarily in the field of catalysis.[46]

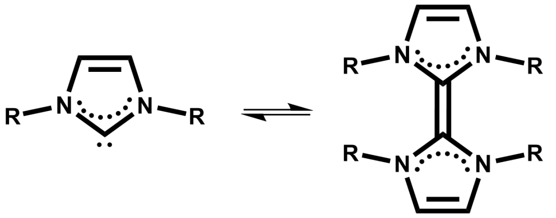

Figure 1.6.: Structure of the imidazol-2-ylidene group and the Wanzlick equilibrium.

Carbenes are characterized by their neutral nature and the presence of a divalent carbon atom with a six-electron valence shell. The presence of an incomplete electron octet and coordinative unsaturation makes free carbenes inherently unstable compounds.[46] To prevent dimerization of the carbenes, which leads to the Wanzlick equilibrium[50] (see Figure 1.6), the substituents adjacent to the carbene carbon are typically bulky groups, such as isopropylphenyl (iPr) or adamantyl groups.[46] Amid their application in OLEDs, as ligands of transition metal complexes, these bulky substituents further prevent large structural distortions in the excited state and consequential non-radiative deactivation.[51]

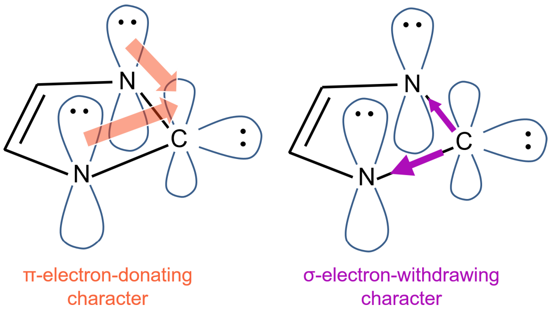

Figure 1.7.: Scheme on the electronic structure of the ground state of imidazol-2-ylidenes with the σ-electron withdrawing and π-electron donating character of the nitrogen atoms.

NHCs have an electronic singlet ground-state configuration, which is stabilized by the nitrogen atoms – inductively, through the σ-electron withdrawing effect lowering the energy of the occupied σ-orbital and mesomerically, through the π-electron donating effect shifting electron density into the empty π-orbital of the carbon atom (see Figure 1.7).[46] The most commonly used derivative of the NHC class is imidazol-2-ylidene (see Figure 1.6).[49]

Over the course of this thesis, two copper(I) carbene complexes – NHCCuPy and NHCCuDBM (Figure 1.8) – were investigated with respect to their photophysical properties. A detailed description and introduction of each is given in the respective results section 5.1 (NHCCuPy) and section 5.2 (NHCCuDBM).

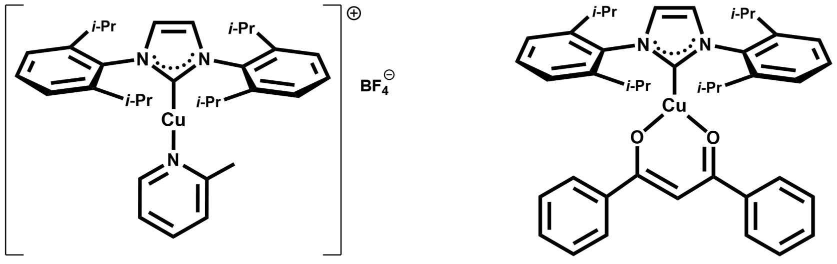

NHCCuPy **NHCCuDBM**

Figure 1.8.: Molecular structures of the two copper(I) NHC complexes that were investigated over the course of this thesis. Here, the complex bearing a 2-methylpyridine (2-picoline) ligand is referred to as NHCCuPy, and the complex bearing the dibenzoylmethanoate ligand is referred to as NHCCuDBM.

1.3. Structure and Overview of the Thesis

As outlined in the previous sections, copper(I) complexes with their unique properties might serve as a sustainable alternative for existing OLED emitters. This thesis aims to investigate the photophysical properties of copper(I) carbene complexes to help assess their potential as OLED emitters. To determine the suitability of a substance as an OLED emitter, various properties must be evaluated. These properties include the behavior of the substance after photoexcitation encompassing its emission behavior. A qualitative understanding of these properties is essential and includes aspects such as the occurrence of different processes after excitation, for example (reverse) intersystem crossing, i.e. the population of singlet or triplet states, furthermore the fluorescence or phosphorescence behavior, as well as the stability under electronic excitation and the general environmental dependence of these properties.

Additionally, a quantitative discussion is necessary, which involves factors such as the emission parameters of the substance i.e. quantum yields and radiative lifetimes, the amount of excitation energy lost via non-radiative deactivation, or the excited state deactivation time.

This thesis investigates two copper(I) complexes with respect to their photophysical properties, utilizing various spectroscopic methods, including stationary UV/Vis absorption spectroscopy, stationary fluorescence spectroscopy, femtosecond and nanosecond time-resolved transient absorption spectroscopy as well as femtosecond time-resolved fluorescence spectroscopy.

The thesis is structured into several chapters, beginning with a chapter on the fundamentals of the relevant properties and their interrelationships (chapter 2), followed by a chapter summarising the spectroscopic methods used in the investigation (chapter 3). The experimental details and instrumental parameters are described in a separate chapter (chapter 4). The central chapter of the thesis focuses on the photophysical characterization of the two copper carbene complexes, with each investigation presented and discussed individually (chapter 5). The last chapter (chapter 6) provides a concise summary of the accomplishments and challenges encountered, followed by a forward-looking perspective.

2. Fundamentals of Photophysics

The term photophysics refers to the physical processes of molecules and atoms occurring upon their interaction with light. This includes the absorption, and emission of light, as well as the population and the depletion of excited states.

One important conceptual tool used in photophysics is the Jablonski diagram, which is a graphical representation of the electronic states and transitions that occur when a molecule absorbs light (see Figure 2.1). The concept of the Jablonski diagram was initially proposed by Aleksander Jablonski in 1933.[52,53]

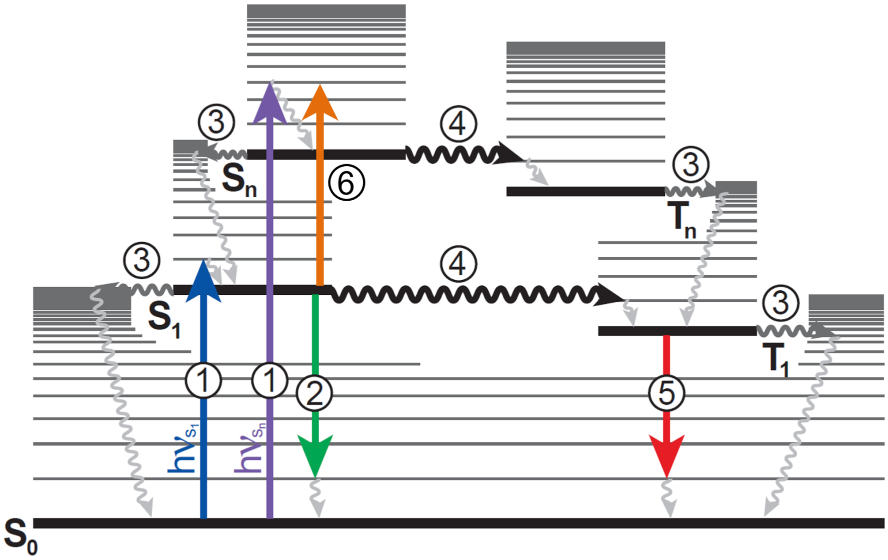

Figure 2.1.: Jablonski diagram illustrating the most important photophysical processes. Thick horizontal lines represent the vibrational ground states of the electronic states ($S_0, S_1, ..., S_n$ and $T_1, ..., T_n$), thin and greyish horizontal lines correspond to excited vibrational levels. Vertical arrows upwards symbolize absorption processes (① excitation from the electronic ground state into upper excited states (purple), into the lowest excited state (blue), and ⑥ transient absorption from an excited state into upper ones (orange)). Vertical arrows downwards symbolize radiative transitions (② fluorescence in green, and ⑥ phosphorescence in red). Wavy horizontal arrows correspond to non-radiative transitions between electronic states (③ internal conversion, and ④ intersystem crossing). Angled, light grey arrows represent vibrational relaxation within an electronic state. Adapted from ref.[54].

The diagram consists of a series of thick horizontal lines representing the different electronic energy states and thin horizontal lines representing the vibrational states within an electronic state of a molecule. The lowest line represents the ground state, which is the state in which the molecule exists under normal conditions. For the vast majority of molecules, this ground state constitutes a singlet state (S_0). Although, especially amongst transition metal complexes, other multiplicities are rather common due to the presence of unpaired electrons in the metal d-orbitals. For instance, chromium (Cr) complexes are known to exhibit a variety of ground state configurations, including high-spin states with unpaired electrons in multiple d-orbitals. One example is the chromium(II) complex [Cr(acac)$_2$], where acac represents acetylacetonate ligands, which has a ground state with a total spin of $S = 2$, and thus a quintet ground state according to eq. 1.2.[55]

When the molecule absorbs light, it is promoted to a higher energy state usually of the same spin multiplicity ($S_1, ..., S_n$). The excited state is represented by a higher horizontal line in the diagram. Usually, an electronic excitation is accompanied by a vibrational excitation within the respective electronic state, which is referred to as a vibronic transition.[17]

From the excited state, the molecule can undergo various deactivating processes to return to the ground state. These processes are represented by vertical arrows indicating a loss of energy as well as horizontal arrows for isoenergetic processes. From the vibrationally and electronically excited state, an energy loss[1] can occur through vibrational relaxation (VR). Additionally, isoenergetic transitions to other electronic states take place. If such a transition occurs between states of the same multiplicity, it is referred to as internal conversion (IC), while a change in multiplicity (e.g., $S_1 \rightarrow T_1$) constitutes an intersystem crossing (ISC) process. The recovery of the ground state can additionally occur through the emission of fluorescence, in case of a $S_n \rightarrow S_0$ transition or phosphorescence for a $T_n \rightarrow S_0$ transition. In most cases, the emission occurs from the lowest excited state. This common behavior is described by the rule of Kasha (see section 2.2).[57] Furthermore, not only the ground state

Table 2.1.: Typical time scales[2] of some photophysical processes.[56]

process	time scale
absorption	$\approx$ 1 as [3]
VR & IVR	100 fs – 1 ps
IC	1 ps – 1 μs
ISC	1 ps – 1 s
fluorescence	1 ns – 10 ns
phosphorescence	1 μs – 1 ms

---

[1] The term "energy loss" refers to the system of the molecule transferring its energy to surrounding molecules, e.g. solvent molecules.

[3] These typical time scales are particularly applicable to organic molecules. Principally they also apply to transition metal complexes, although, for reasons especially stated in this chapter, such as increased spin-orbit coupling constants and a higher density of states, the lower limit value of these time scales is expected to be shorter for transition metal complexes.

[3] In principle, it is difficult to define the time scale of absorption. One definition is the time it takes for a photon to "pass" a molecule. For a molecule with a diameter of 10 Å, this time amounts to $\approx$ 1 as.

but also excited states are capable of absorbing photons, leading to what is known as transient absorption (TA). Additionally, transient absorption can originate from absorbing photoproducts. An overview of the typical time scales on which these processes occur is given in Table 2.1.

In the following sections, the processes that are relevant to this work are examined in greater detail. These include the absorption and emission of photons, which are initially outlined in a generalized manner. Subsequently, relevant tools for quantifying these processes are presented (section 2.1). As the substances being studied are copper(I) complexes, a more detailed description of their electronic structure and transitions is further provided (section 2.4). Non-radiative deactivation processes, such as intersystem crossing and the associated phenomenon of the spin-orbit coupling, which are highly relevant in the context of potential emitter molecules and transition metal complexes, are discussed (section 2.2 and 2.2.1).

2.1. Absorption and Emission

The phenomenon of absorption occurs when a photon (i.e. electromagnetic wave) of a specific frequency ν (or wavelength λ) interacts with the electrons of an atom or molecule in such a way, that the electrons absorb the energy of the photon and transition to a discrete state of higher energy. The photon is annihilated in the process. The Bohr frequency condition relates the energy difference ΔE between an initial state m and a final state n of an atom or molecule to the frequency ν (or wavelength λ) of the absorbed photon. The condition was first proposed by Niels Bohr to explain the discrete spectra of atoms.[58] The Bohr frequency condition is given by equation 2.1:

$$E_n - E_m = \Delta E = h \cdot \nu = h \cdot \frac{c_0}{\lambda} \tag{2.1}$$

where h is Planck's constant, ν is the frequency, λ the wavelength of the absorbed photon, and c_0 the speed of light in vacuum.

When a molecule absorbs a photon, there is an almost immediate redistribution of electron density. However, the response of the atomic nuclei to this redistribution is slower and the nuclei do not change their relative position at first. This is due to the significantly larger mass of the atomic nuclei, which are more than $\approx$ 2000 times more massive than an electron. This difference in the time scale of electron and nuclear motion is the basis of the Born-Oppenheimer approximation.[53,59]

For the molecule to undergo a transition to a different vibrational level during an electronic transition, the new vibrational level must be compatible with the nuclear position and momentum of the molecule in the originating vibrational and electronic state. In the classical model of vibrations, prior to the excitation the equilibrium coordinates are adopted and the momentum is zero. Therefore, this compatibility is given at the turning points of the vibrational motion, where the momentum of the oscillating system matches the value of zero. Thus, the excitation occurs vertically (nuclear position does not change) between the potential energy surfaces (momentum equals zero) of the two electronic states. A more quantitative description of the probability of an electronic transition in a molecule taking into account these vibrational levels is given by the Franck-Condon factors (FC).[60,61,62] These are given by the square of the overlap integral S of the involved vibrational wave functions χ_i and χ_f according to equation 2.2.

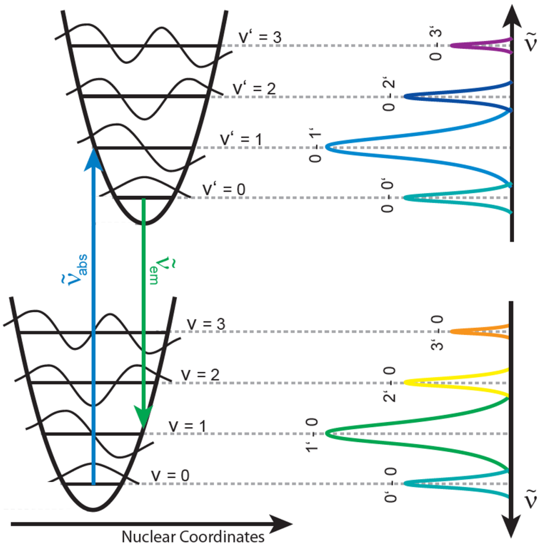

Figure 2.2.: Illustration of the Franck-Condon principle. The potential curves of the two states involved are harmonically approximated. Adapted from ref.[54].

$$FC_{i,f} = \langle \chi_i | \chi_f \rangle \tag{2.2}$$

A small overlap of the wave functions results in a small value for the Franck-Condon factor and thus a low probability for the corresponding transition. The shape of an absorption band can thus be described by considering the Franck-Condon factors for different transitions (see Figure 2.2).

From an experimental point of view, the absorption of light by a molecule or an atom can be quantified through the application of the Lambert-Beer law.[63,64] This law states that the absorption, experimentally defined as the negative decadic logarithm of the ratio of the incident light intensity to the transmitted light intensity through a sample (eq. 2.3), is linked to the concentration c and optical path length d of a sample according to eq. 2.4.

$$A(\lambda) = -\log \frac{I(\lambda)}{I_0(\lambda)} \tag{2.3}$$

$$A(\lambda) = \varepsilon(\lambda) \cdot c \cdot d \tag{2.4}$$

The factor of proportionality $\varepsilon(\lambda)$ between the absorption A, the concentration of the sample c, and the optical path length d is the absorption coefficient. Accordingly, the absorption coefficient is a measure of the decrease in intensity of electromagnetic radiation as it passes through a given sample. Usually, $\varepsilon(\lambda)$ is expressed in units of $\mathrm{M}^{-1}\mathrm{cm}^{-1}$.

The absorption coefficient in turn is related to the oscillator strength, which characterizes the strength of a certain electronic transition, through the following equation 2.5:[62]

$$f = \frac{4 \cdot m_e \cdot \epsilon_0 \cdot c_0}{e_0^2 \cdot N_A} \cdot \int \varepsilon(\nu) \mathrm{d}\nu \tag{2.5}$$

with the electron mass m_e, the vacuum permittivity ϵ_0, the elementary charge e_0, and Avogadro's constant N_A. The integral in the expression $\int \varepsilon(\nu)\mathrm{d}\nu$ corresponds to a sum over all (relevant) FC factors. The calculation of f via $\int \varepsilon(\nu)\mathrm{d}\nu$ is valid for a transition(band) that is spectrally isolated (i.e. does not overlap energetically with other transitions). The oscillator strength compares the real absorption behavior, based on the laws of quantum mechanics, with the expectations of classical physics.[17] According to classical physics, absorption is described as the vibration of electrons in response to the oscillating electric field of light. The oscillator strength can also be expressed from a quantum mechanical point of view (eq. 2.6), in which it is related to the quantum mechanically accessible transition dipole moment μ_{mn} for an initial state m and a final state n:[62]

$$f = \frac{4 \cdot \pi \cdot m_e \cdot \nu_{mn}}{3 \cdot \hbar \cdot e_0^2} \cdot |\mu_{mn}|^2 \tag{2.6}$$

with m_e the electron mass, e_0 the elementary charge, and the reduced Planck's constant $\hbar$.

As absorption describes a transition from a state m to a state n of higher energy and the simultaneous annihilation of a photon, the phenomenon of emission covers the opposite process, whereby a distinction must be made between spontaneous and stimulated emission.

In the process of stimulated emission, the atom or molecule in its excited state n returns to its ground state m by releasing a photon of energy equal ΔE. Stimulated emission and absorption from the same pair of states share the same transition probability.[53] However, stimulated emission requires the presence of a resonant photon within the lifetime of the excited state. Typically, this requirement is given for time-resolved spectroscopic techniques where the sample is irradiated by (multiple) intense laser pulses (see section 3.2.1). In contrast, spontaneous emission can occur in the absence of an external electromagnetic field. In this case, zero-point fluctuations of the electromagnetic field "stimulate" the emission.[53]

One way of quantifying the emitting capability of a molecule with respect to spontaneous emission is given by the radiative rate constant k_{rad}. The radiative rate constant for a molecule can be estimated by a relation derived by Strickler and Berg 1962,[65] and further adapted by Birks and Dyson 1963,[66] which is given by eq. 2.7.[53]

$$k_{rad}^{SB} = \frac{8\pi \ln(10) \cdot c_0}{N_A} \cdot \frac{n_{em}^3}{n_{abs}} \cdot \frac{g_n}{g_m} \cdot \frac{\int I(\tilde{\nu})\,\mathrm{d}\tilde{\nu}}{\int \tilde{\nu}^{-3} \cdot I(\tilde{\nu})\,\mathrm{d}\tilde{\nu}} \int \frac{\varepsilon(\tilde{\nu})}{\tilde{\nu}}\,\mathrm{d}\tilde{\nu} \tag{2.7}$$

In the equation, c_0 is the speed of light in vacuum, N_A is Avogadro's constant, n_{abs} and n_{em} are the mean refractive indices for the absorption and emission frequencies, respectively, g_m and g_n are the degeneracies of the lower and upper states, respectively, $I(\tilde{\nu})$ is the wavenumber dependent fluorescence signal, and $\varepsilon(\tilde{\nu})$ is the wavenumber dependent absorption coefficient. From the equation, it follows that there is a relation between the transition probability of spontaneous emission and absorption. Strong absorption transitions, thus, exhibit high radiative rate constants k_r. The Strickler-Berg relation is only valid if the included spectral bands result from the same transition, for instance, $S_0 \rightarrow S_1$ and $S_1 \rightarrow S_0$.

Another quantification of the emission capabilities of a substance is the quantum yield of emission. By definition, it is given by the relation of the number of emitted N_{em} to the number of absorbed photons N_{abs}. Furthermore, it can be expressed by the radiative rate constant k_{rad} in relation to all rate constants that represent the excited state's deactivation, such as the rate constant of internal conversion k_{IC} or intersystem crossing k_{ISC} (see eq. 2.8).

$$\Phi_{Fl} = \frac{N_{em}}{N_{abs}} = \frac{k_{rad}}{k_{rad} + k_{IC} + k_{ISC} + ...} \tag{2.8}$$

As the lifetime of an excited state is the reciprocal of the sum of all its deactivating rate constants (eq. 2.9), the fluorescence quantum yield Φ_{Fl} can also be obtained by multiplying the excited state lifetime with the radiative rate constant (eq. 2.10).[53]

$$\tau_{Fl} = \frac{1}{k_{rad} + k_{IC} + k_{ISC} + ...} \tag{2.9}$$

$$\Phi_{Fl} = k_{rad} \cdot \tau_{Fl} \tag{2.10}$$

Accordingly, with the aid of the above-stated estimation for the radiative rate constant and a known quantum yield of emission[4] the lifetime of the emitting state can be obtained. As a consequence, purely based on steady-state spectroscopic data, it is possible to obtain crucial kinetic (i.e. time-resolved) information.

2.2. Non-Radiative Deactivation Processes

In the search for new OLED emitters, the knowledge of individual photophysical processes is essential. In addition to the desired radiative deactivation (see section 2.1), it is also highly relevant to consider the non-radiative processes that occur after the electronic excitation of the molecule. With the right knowledge about these phenomena, their causes, and their effects, these processes can be addressed and prevented upon suitable adjustments, for instance with regard to the molecular structure. Here, the most relevant processes within the scope of transition metal complexes, especially Cu(I) complexes are highlighted. The process of intersystem crossing as a highly pertinent process for such compounds is separately addressed including the enabling mechanism of spin-orbit coupling (SOC) (see section 2.2.1).

Non-radiative processes refer to the transitions between different electronic states of molecules, wherein there is no absorption or emission of photons. These transitions occur initially in an isoenergetic manner, implying that the energy of the molecule remains constant. However, this energy is converted into vibrational energy of a lower electronic state, which, thus, results in the dissipation of energy as heat. Typical time scales for this process also known as vibrational relaxation are given in Table 2.1. The rate constant for non-radiative processes typically increases exponentially as the energy gap between the electronic states decreases.

---

[4] Information on the experimental determination of the fluorescence quantum yield Φ_{Fl} are given in section 3.1.2.

This phenomenon is known as the energy-gap law. Kasha's rule is based on the energy-gap law,[67] and it states that emission occurs from the lowest electronically excited state of the respective multiplicity.[53,57] As the excitation energy increases, the density of electronic states also increases, and their energetic separation decreases, respectively. If an upper excited state is occupied, all transitions to energetically lower lying states (e.g. $S_2 \rightarrow S_1$, $T_2 \rightarrow T_1$ or $T_2 \rightarrow S_1$) are usually fast compared to the transition between the first excited and the ground state ($S_1 \rightarrow S_0$ or $T_1 \rightarrow S_0$) due to the large energy gap between these states. Especially organic molecules but also some transition metal complexes have been experimentally verified to comply with this rule.[68,69,70] Although, in the case of the latter, it is important to note that with many different excited states of different character often in close energetic proximity to each other, transitions between these states are not always efficient. As a result, many metal complexes defy Kasha's rule.[71]

Fermi's golden rule is one of the most significant approaches used for calculating the rate constants k_{nr} associated with non-radiative (as well as radiative) transitions. The calculation of the non-radiative rate constant is done through the application of time-dependent perturbation theory. Unlike radiative transitions, which are affected by periodic perturbations caused by alternating electromagnetic fields, non-radiative processes are influenced by constant and weak perturbations. The wavefunctions of two states involved in the transition are eigenfunctions of the molecular Hamiltonian in absence of this perturbation. In presence of this perturbation, they are no longer eigenfunctions and thus may evolve in time. The description of the non-radiative process between two states $m \rightarrow n$ using Fermi's golden rule is given by equation 2.11.[62]

$$k_{nr} = \frac{2\pi}{\hbar}\left|H_{m,n}\right|^2 \langle \rho_n \cdot FC \rangle_T \tag{2.11}$$

In the equation, ρ_n represents the density of final states. The product $\rho_n \cdot FC$ stands for the Franck-Condon weighted density of states (FCWD). For the situation $T > 0$ more than one initial state is occupied making a thermal average $\langle\rangle_T$ necessary. $H_{m,n}$ describes the matrix element of the perturbation, which in turn is given by the wave functions of the initial Ψ_m and final states Ψ_n, and a perturbation operator $\hat{H}_P$ according to eq. 2.12.[62]

$$H_{m,n} = \left\langle \Psi_m \middle| \hat{H}_P \middle| \Psi_n \right\rangle \tag{2.12}$$

As the wavefunctions are no longer eigenfunctions of the Hamiltonian in presence of the perturbation this matrix element can be non-zero.

Internal conversion refers to the non-radiative transition between two electronic states of the same multiplicity (e.g. $S_1 \rightarrow S_0$ or $T_2 \rightarrow T_1$). For IC to occur, there must be interactions between the motion of the nuclei and the electrons. These interactions, known as vibronic couplings, cause the momenta of the atomic nuclei to influence the electronic wave functions, distorting the electron density distribution (breakdown of the Born–Oppenheimer approximation).[72]

Regarding the relaxation of vibrational excitation, two main pathways can be considered.[73] One pathway is the intramolecular vibrational energy redistribution (IVR). In this process, energy initially concentrated in a high vibrational level is redistributed to multiple vibrational levels of lower energy. This is the case, for instance, when the energy of an initially populated high-frequency stretching vibration is transferred to several lower-energy vibrational modes such as bending vibrations. Such a redistribution cannot be explained by the harmonic approximation. Only the consideration of anharmonicities occurring in real systems can explain IVR processes.[74,75] As IVR constitutes a purely intramolecular process it occurs also in the gas phase.[56] However, this does not mean that the process is fully unaffected by the environment. For instance, upon solvent-solute interactions, vibrational energies can be shifted and thereby change the resonance conditions for the transfer of vibrational energy. Especially for transition metal complexes, IVR has been assigned a crucial dissipating agent.[76,77]. This can be illustrated by the number of normal modes of vibration ($\#modes$) for a non-linear molecule, which is given by eq. 2.13.

$$\#modes = 3N - 6 \tag{2.13}$$

In the equation, N denotes the number of atoms of the molecule. Whereas small three-atomic molecules, such as H_2O possess only three normal modes, the number becomes large for large polyatomic molecules. For instance, the transition metal complexes studied in this thesis NHCCuPy and NHCCuDBM have 234 and 276 normal modes, respectively.

Another pathway for the dissipation of the vibrational energy is the transfer to surrounding molecules. This intermolecular process occurs when molecules "collide" (i.e. the spatial distance becomes sufficiently small enough) with surrounding molecules, such as matrix or solvent molecules, so that an energy transfer occurs to these neighboring molecules.[78]

Both processes have an influence on the absorption and fluorescence spectra. Usually, immediately after photoexcitation, the molecule is in a high-energy vibrational state of a corresponding electronic state. From this high-energy vibrational state the energetic distance to the next higher electronic state is smaller compared to the vibrational ground state. As the vibrational relaxation proceeds, lower vibrational states are populated and the energetic distance to the next higher electronic state increases. As a consequence the signal of the transition into the higher electronic state shifts to higher energy. This time-dependent transformation of the (transient) absorption or emission band due to vibrational relaxation can be observed and investigated using time-resolved spectroscopy.[79] Upon photoexcitation of a molecule in solution, these processes usually proceed within $10^{-14} - 10^{-12}$ s, much faster than the typical lifetimes of other deactivating processes (see Table 2.1). Hence, vibrational relaxation usually takes place prior to these processes.[80] More information on the overall form and dynamics of absorption and emission spectra in solution is given in section 2.3.

2.2.1. Intersystem Crossing and Spin-Orbit Coupling

Whereas internal conversion describes the isoenergetic transition between two states of the same multiplicity, ISC covers the isoenergetic transition between two states of different multiplicity, e.g. $S_1 \rightarrow T_1$. Furthermore, the vibronic coupling relevant to IC plays only a subordinate role for the ISC. Here, spin-orbit coupling has a decisive role, which allows the formally – due to the conservation of angular momentum – forbidden transition to take place.

Spin-orbit coupling is based on the interaction between the electron's spin angular momentum $\hat{s}$ and its orbital angular momentum $\hat{l}$ around the atomic nucleus. This interaction is caused by a coupling of the magnetic moments. Consequently, to compensate for the necessary change of the spin quantum number over the course of an ISC transition (i.e. between states with different multiplicity), there is a corresponding change in the magnetic quantum number of the orbital angular momentum. A change in the quantum number of the orbital angular momentum results in a change of the nature of the orbitals involved in the transition. Specifically, the quantum number of the orbital angular momentum describes the spatial orientation of the orbitals and contributes to the formation of different types of orbitals, including σ-, π-, n-, or d-orbitals.

Mostafa El-Sayed derived certain rules, now referred to as the El-Sayed rules, that are used to predict the rate constants of ISC in various molecular systems in a qualitative manner.[81,82] According to El-Sayed's rules, the ISC is faster if the electronic state changes its nature with respect to the orbital character during the transition. For instance, this is the case for an $^1\pi\pi^* \rightarrow {}^3n\pi^*$ transition. On the other hand, ISC is slower if the electronic state's orbital character remains unchanged during the transition (e.g. $^1\pi\pi^* \rightarrow {}^3\pi\pi^*$).

These rules, well-established in organic systems, can principally be adapted to transition metal complexes. However, with a stark contribution of the metal d-orbitals and the overall diverse orbital contributions to the electronic transitions, further adaptions to this rule are made.[83] While ISC is slower – similar to organic compounds – if the interacting states result from the same molecular orbitals, it becomes fast for singlet and triplet states originating from different d-orbital contributions. For instance, for a singlet $d\pi^*$ state and a triplet $d'\pi^*$, both of pronounced MLCT character and with $d \neq d'$ (while $\Delta m_l \pm 1$), ISC is expected to be fast.[67]

Generally, the SOC constants for the d electrons in (heavy) transition metal elements are significantly larger than those of other main group elements. Accordingly, the higher the MLCT nature involved in the singlet and triplet excited states, the stronger the SOC and the faster the ISC transition.

Table 2.2.: Spin-orbit coupling constants (SOCC) for some transition metal atoms (in cm^{-1}).[84,85]

atom	group, period	$\mid SOCC \mid$ / cm^{-1}
Cr	6, 4	135
Fe	8, 4	255
Co	9, 4	390
Cu	11, 4	810
Zr	4, 5	270
Mo	6, 5	450
Ru	8, 5	745
Ag	11, 5	2150
W	6, 6	2100
Os	8, 6	2300
Au	11, 6	4900

Table 2.2 lists the SOCCs of some transition metals. As indicated, a large spin-orbit coupling is particularly present for the heavier elements. This relationship, known as the heavy atom effect, can be illustrated by the following equation 2.14 for the Hamiltonian for spin-orbit coupling $\hat{H}_{SO}$ for a hydrogenic atom[5].[62]

---

[5] As stated in the text, this equation 2.14 is only valid for hydrogenic atoms, i.e. for the interaction of one electron with a nucleus of charge Z, without considering any electron-electron interaction. Applying this to objects other than hydrogen, helium$^+$, lithium^{2+} etc. constitutes a very crude approximation.

$$\hat{H}_{SO} = \frac{Z^4 e^2}{8\pi\epsilon_0 m_e^2 c_0^2} \cdot \vec{l} \cdot \vec{s} \tag{2.14}$$

With Z the nuclear charge number, e the elementary charge, ϵ_0 the vacuum permittivity, m_e the electron mass, and c_0 the speed of light in vacuum. According to the equation, the spin–orbit coupling scales with the fourth power of the nuclear charge number (Z^4), which implies that the SOC interactions are considerably larger for atoms further down in the periodic Table.[83] However, considering non-hydrogenic systems with more than one electron, this effect can significantly decrease due to the screening of the nuclear charge by the presence of the other electrons.[83]

As this example shows it is important to note that these rules only constitute rules of thumb and deviations from these are common as many factors must be considered simultaneously making in-depth theoretical quantum chemical studies inevitable. For instance, one study demonstrated for several similarly coordinated and isoelectronic d^{10} complexes based on Cu(I), Ag(I), and Au(I) ions that in contrast to expectations based on the heavy metal effect, the Cu(I) complexes exhibit the highest SOC strength[6].[86] Upon conducting a more thorough theoretical analysis, it was discovered that the respective S_1 states of these complexes have very distinct characteristics. Specifically, the S_1 state of the Cu(I) complex is of mixed MLCT/$d\pi^*$ nature, with MLCT character accounting for approximately 20-45%, while the S_1 state of the Au(I) complex can be identified as a nearly pure $\pi\pi^*$ transition.[83,86]

2.3. Solvent Effects

According to the Franck-Condon principle (see section 2.1), transitions into different vibrational states within the same electronic transition occur with different probabilities. Therefore, these transitions of varying intensity, also known as vibrational progressions, ought to be visible in the absorption or emission spectra. Specifically, this is the case for spectra recorded in the gas phase. However, for spectra recorded in solution, the vibrational progressions may be faint and difficult to discern, depending on the nature of the solvent. The appearance of vibrational progressions in solution depends on the strength of the intermolecular interactions between

---

[6] On average, these Cu(I) complexes exhibit both a higher quantum yield of emission (Cu(I): 0.250, Ag(I): 0.015, Au(I): 0.056) and a shorter phosphorescence time constant (Cu(I): 29 μs, Ag(I): 148 μs, Au(I): 73 μs).[86]

the solute and solvent molecules. In non-polar solvents, weak van der Waals interactions lead to the partial observation of vibrational progressions. In contrast, polar or protic solvents with strong dipole-dipole and hydrogen-bonding interactions cause significant broadening of the absorption and emission energies, making it difficult to observe vibrational progressions.[87]

Besides that and with respect to transition metal complexes, it should be noted, that the nature of the electron transition also influences the possibility of vibrational progressions to appear. For example, it is typical for an MLCT band to be rather broad and structure-less. One reason for this is the large change in dipole moment for a CT transition. Another reason is that for the respective electronic transition, which originates from different spatially separated orbitals from different vibronic contributors, the energy of the vibrational states involved is spread more continuously.[88,89]

In addition to the shape of the absorption or emission band, a solvent environment can further have an impact on the position of the bands, i.e. on the energy of the transition. Shifts in transition energies can be observed if compared to the vacuum, or in between solvents of different polarity and proticity. These effects dominantly result from the interaction between the molecule's electric dipole moment and the dipole moments of the solvent molecules stabilizing the respective electronic state by the amount of the solvation energy (see Figure 2.3). If the molecule's electronic distribution (i.e. dipole moment) changes upon excitation, different solvation energies for the ground- and the excited states occur, causing a relative lowering of these states in comparison to vacuum. This in turn leads to decreased or increased energy differences for the transition between these states. If the dipole moment of the ground state $\mid \mu_G \mid$ is greater than the dipole moment of the ex-

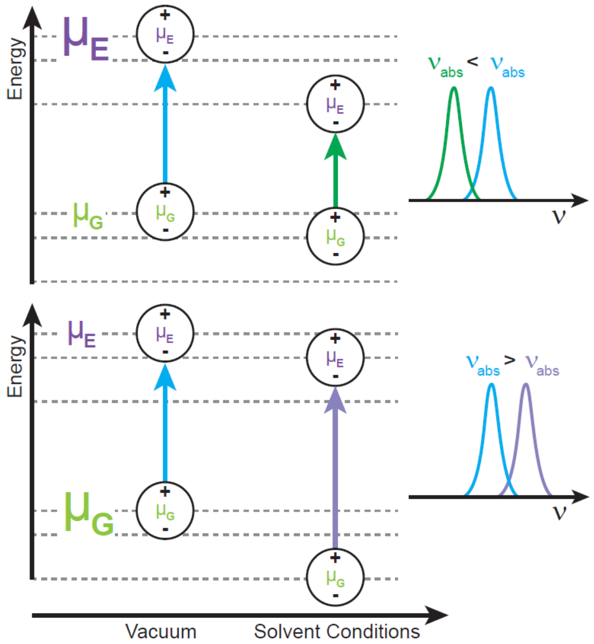

Figure 2.3.: Schematic representation of different solvatochromic shifts caused by different dipole moments of ground- μ_G and excited state μ_G. Figure adapted from ref.[54].

cited state $\mid \mu_E \mid$, the ground state is more stabilized by the dipole moment of the surrounding molecules than the excited state is, which results in a blue- or hypsochromic shift of the absorption band. This is referred to as negative solvatochromism. Conversely, if $\mid \mu_G \mid < \mid \mu_E \mid$, the excited state is more stabilized, resulting in a red- or bathochromic shift of the absorption band, which is referred to as positive solvatochromism.[87]

These effects are in particular relevant for many transition metal complexes since an electronic transition is usually accompanied by a large redistribution of electron density (i.e. change in dipole moment), for instance upon a ligand-to-ligand or metal-to-ligand charge transfer transition.[90,91]

As stated above, also the proticity of the solvent molecules influences the energy of an electronic transition. Protic solvents can form hydrogen bonds, which contribute significantly to solvation energy, i.e. to the stabilization of the respective state. For molecules with heteroatoms, the electron density is partially localized on the heteroatom's n-orbital, promoting the formation of H-bonds. The resulting stabilization of the n-orbital leads to a negative solvatochromism (i.e. increased energy) of $n\pi^*$ transitions[7] with increasing proticity of the solvent.[87]

Apart from a change in a transition band's maximum relative to the vacuum, or between solvent molecules of different polarity, solvation can also affect the shift between absorption and emission bands relative to each other that is known as Stokes shift (see Figure 2.4). In thermal equilibrium, surrounding solvent molecules are in the energetically most favorable orientation around the solute molecule. Upon electronic excitation of the molecule, which occurs vertically in accordance with the

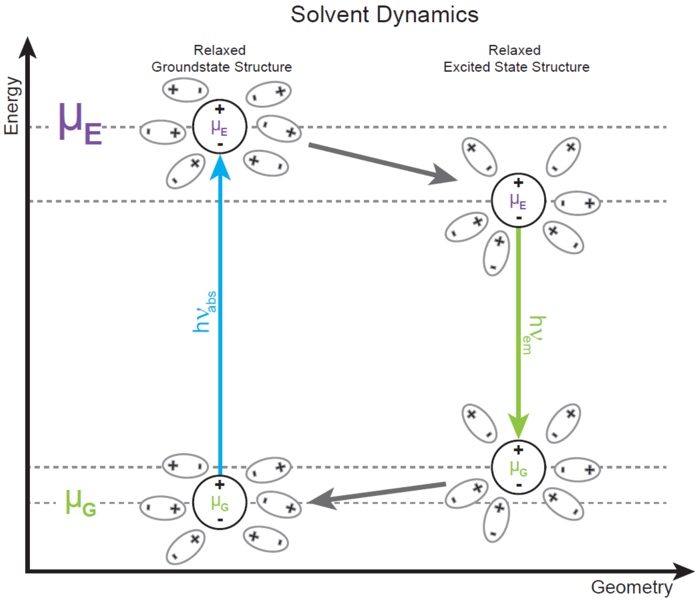

Figure 2.4.: Schematic illustration of solvation effects on the Stokes shift for the situation $\mu_E > \mu_G$ in a polar solvent. Figure adapted from ref.[54].

---

[7] Or a similar transition involving electron density that originates from the n-orbital, e.g. $n\sigma^*$ or nd^* transitions.

Franck-Condon principle, the electron density distribution within the molecule changes, and consequently, the surrounding molecules (initially) adopt an unfavorable orientation. Subsequently, the solvent molecules reorganize, which leads to a (time-dependent) stabilization of the electronically excited state, a process known as dielectric relaxation. Depending on the size of the solvent molecules, this process usually takes between 100 femtoseconds and several picoseconds.[92,93]

As the emission also occurs vertically, initially an energetically unfavorable orientation of the solvent molecules upon returning to the ground state results. Subsequently, within the typical time span for dielectric relaxation, the solvent molecules reorganize.

Moreover, solvent molecules can directly "participate" in the electronic excitation of the solute molecule. For instance, charge-transfer-to-solvent (CTTS) transitions occur for several halide anions and some alkalides such as Na^-, K^-, and Rb^- as intense absorption bands in the deep UV (≈ 270 nm). These bands arise from the interaction between the ions and the solvent.[94] However, the presence of CTTS states is not exclusive to atomic ions but is also present in molecules and metal complexes. A well-known example is the aqueous ferrous cyanide $[Fe(CN)_6]^{4+}$ that exhibits CTTS states within the range of 260-295 nm,[95] making them readily accessible for time-resolved spectroscopic studies.[96]

Also, chemical reactions can occur between the solvent and the solute. In the case of metal complexes, usually, this means the substitution of ligands or the additional coordination of solvent molecules to the metal center. The donor number (DN), according to Viktor Gutmann, serves as a measure for the coordination affinity of a solvent molecule towards a metal ion. It is defined as the negative enthalpy for the 1:1 adduct formation between a solvent molecule as the Lewis base and the standard Lewis acid antimony pentachloride ($SbCl_5$). In other words, it represents the ability of a solvent to donate electrons to a metal ion and form a coordination complex. Solvents with higher donor numbers have a greater ability to donate

Table 2.3.: Donor number values for typical solvents (in kcal/mol).[97,98]

solvent	DN / $\frac{\mathrm{kcal}}{\mathrm{mol}}$
toluene	0.1
acetonitrile	14.1
acetone	17.0
methanol	19.0
tetrahydrofuran	20.0
dimethyl sulfoxide	29.8
ethanol	31.5
pyridine	33.1

electrons and form coordination complexes with metal ions. Solvents with low donor numbers, on the other hand, have a weaker coordination affinity towards metal ions and are less likely to form coordination complexes.[98,99]. For some typical solvents, the donor numbers are listed in Table 2.3.

2.4. Electronic Structure of Cu(I) Complexes

This section discusses the electronic structure and the resulting photophysical properties of transition metal complexes, specifically Cu(I) compounds, and how these properties are determined by their frontier orbitals. The four main transition types are explained namely ligand-centered, metal-centered, metal-to-ligand, and ligand-to-metal charge transfer transitions. Furthermore, the influence of these transitions on the overall emission properties of Cu(I) compounds is described.

The photophysical properties of transition metal complexes, including Cu(I) compounds, are largely determined by their frontier orbitals, which are, according to the molecular orbital theory, the highest occupied and lowest unoccupied molecular orbitals. These molecular orbitals give rise to the lowest excited electronic states. To some extent, the frontier orbitals can be described by the occupied d and unoccupied d^*-orbitals of the central metal and the occupied π and unoccupied π^*-orbitals of the ligands, also referred to as chromophoric ligands. For non-chromophoric ligands, also known as ancillary ligands, the π-orbitals are of low energy and the π^*-orbitals of high energy, and thus have no effect on the lowest electronic states. However, their presence can have a significant impact on the overall electronic structure, for instance through the coordination geometry or electron-inducing or withdrawing effects.[100,101] According to this (simplified) view, four different electronic transitions can occur, which are described in the following and summarized in Figure 2.5.[71,102,103]

Ligand-centered (LC) transitions involve the excitation of an electron from a π to a π^*-orbital, with both orbitals usually located on the same ligand. In heteroleptic complexes (i.e. with various ligands), excitation can occur between different ligands, resulting in a ligand-to-ligand charge transfer (LLCT) transition.

If an electron is excited from a d-orbital of the central metal atom to another unoccupied metal orbital, it results in a metal-centered (MC) transition. The most typical MC transition is the dd^* transition if the unoccupied orbital is of d^* character. In the context of OLED application, dd^* transitions are considered detrimental as they usually deactivate non-radiatively. This can be attributed to a low oscillator strength of the transition due to its parity-forbidden nature.[104] In typical OLED emitters, based on iridium or platinum, the d^*-orbitals are generally at very high energies due to a large ligand field splitting. Consequently, dd^* states are not among the low-energy states in these cases.[105] However, if they are energetically close enough to the lowest excited states, which can be the case, especially for blue emitting compounds, so that they can be thermally populated at room temperature, they can have a significant influence on the compounds emitting properties.[101] In contrast to that, the emission behavior of Cu(I) based complexes is not affected by dd^* states. This is due to the fact that the d-shell of the Cu(I) ion has a d^{10} configuration, which implies it is fully occupied and has no empty accessible d^*-orbitals, and therefore no dd^* states are present. Due to this characteristic, Cu(I) compounds have the potential to be ideal candidates for developing stable blue emitters with high emission quantum yields.[102]

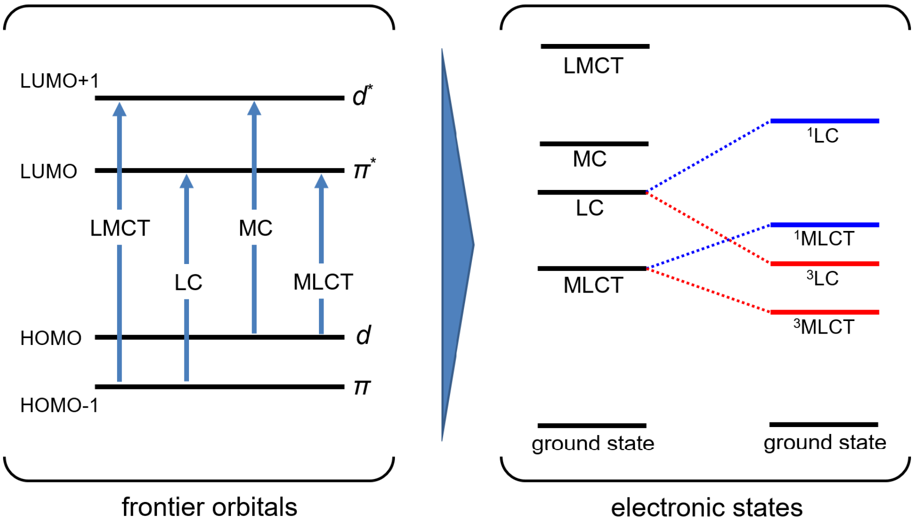

Figure 2.5.: Schematic representation of the frontier orbitals (d/d^*-orbitals for the metal and π/π^* for the ligand) and how the lowest excited states and the respective character of each (MLCT, LC, MC, LMCT) are made up of transitions involving these frontier orbitals. Due to exchange interactions, which depend on the state's character, the states are further split into singlet and triplet ones. Based on refs.[71,101].

Metal-to-ligand charge transfer (MLCT) transitions refer to the transfer of charge (i.e. electron density) from the central metal to one of the ligands, usually an unoccupied π^*-orbital, upon excitation. This type of transition is a key factor that determines the emission behavior of many complexes that are relevant for OLEDs. Due to the high contribution of hole density from the metal center in the emitting states, strong spin-orbit coupling can be induced, leading to fast intersystem crossing processes. Although the spin-orbit coupling constant of copper is rather small compared to metals like iridium or platinum, the charge transfer character of the lowest excited states of many copper(I) complexes showed to be much more pronounced.[102] This allows many Cu(I) complexes to show thermally activated delayed fluorescence (see section 1.2).[36,37]

The opposite process of an MLCT transition with respect to the source and sink of electron density is described by a ligand-to-metal charge transfer (LMCT) transition. For these transitions to show relevance (i.e. constitute low energy) ligands with free electron pairs of high orbital energy (e.g., sulfur- or selenium-containing ligands) or a central metal ion in a high oxidation state with energetically low-lying d^*-orbitals (e.g., Mn(VII) or Pt(IV)) are required.[101] This requirement is usually not fulfilled for Cu(I) complexes, which makes the LMCT state rather unimportant regarding the photophysics of such compounds.

In the following, the importance of the MLCT character of the lowest excited states for Cu(I) complexes with respect to the property of TADF is more closely described.[102] Due to exchange interactions of the electrons, the above-described states are energetically split into states with different spin configurations (see Figure 2.5). For a singlet ground state, these are usually singlet and triplet excited states.[8] As discussed in section 1.3, the exploitation of both excited states for the OLED emission constitutes an important task. For an energy gap between these singlet and triplet states which is in the order of the thermal energy $k_B \cdot T$, the excited state population of the triplet state can be transferred into the fluorescent singlet state. For a situation where the lowest excited singlet and triplet states are of MLCT character, i.e. the HOMO is predominantly located on the metal center (approximately a d-orbital), and the LUMO on the ligand's π^*-orbital , the energy gap between these two states ($\Delta E(S_1 - T_1)$) is roughly twice the exchange integral K, which is given by equation 2.15.[62,106] This equation is not only valid for this specific excitation as stated above but – replacing the given indices – for all kinds of excitations.

$$\Delta E(S_1 - T_1) \approx 2 \cdot K_{d\pi^*} = 2 \cdot \left\langle \Psi_d(r_1)\Psi_{\pi^*}(r_2) \middle| \frac{e_0^2}{4\pi\epsilon_0 r_{12}} \middle| \Psi_d(r_2)\Psi_{\pi^*}(r_1) \right\rangle \tag{2.15}$$

---

[8] However, depending on the number of electrons, states with higher multiplicities are in principle possible.

In the equation, $K_{d\pi^*}$ represents the exchange integral, r_1 and r_2 are the electron coordinates, r_{12} the spacial separation of the electrons, Ψ_d and Ψ_{π^*} the wave functions of the respective d and π^* frontier orbitals (i.e. HOMO and LUMO), ϵ_0 the vacuum permittivity and e_0 the elementary charge. The equation highlights that the exact magnitude of the exchange integral, and thus of the $S_1 - T_1$ splitting, is determined by the spatial separation of the frontier orbitals involved. This spatial separation increases as the charge-transfer character of the electronic state increases, leading to the reduction of the exchange integral and consequently of $\Delta E(S_1 - T_1)$. As depicted in Figure 2.5, an MLCT state, with the d and π^*-orbitals located at different parts of the complex, thus, exhibits a rather small singlet-triplet splitting, since the unpaired electrons are spatially farther apart and therefore interact to a lesser extent. In a corresponding LC state, where the π and π^* are for instance located on the same ligand, only a small spatial separation of the electron wave functions is present leading to a rather large exchange integral and as a result to a large singlet-triplet splitting.

However, it is important to note, that the representation of the electronic states discussed above and illustrated in Figure 2.5 only draws a simplified picture. In reality, the molecular orbitals in transition metal complexes are not of pure ligand-π or metal-d character and thus do not constitute pure LC or MLCT states. Furthermore, the strong spin-orbit coupling induced by the central metal ion (see section 2.2.1) leads to a mixture of states of different multiplicity.[101]

3. Background on the Applied Methods

In this section, the methods that were applied to obtain the presented results are listed and explained. Furthermore, their principles of operation and the setups, as used for the experiments presented in this thesis, are described. For specific experimental details with regard to the measurements and results, see chapter 4.

3.1. Steady State Spectroscopy

3.1.1. UV/Vis Absorption Spectroscopy

UV/Vis absorption spectroscopy is an analytical technique used to investigate the electronic resonances of molecules by measuring the amount of light that is absorbed by the sample.[53] In general, any UV/Vis spectrophotometer consists of (1) a light source (e.g. light bulb), (2) the sample(-holder), (3) a dispersing element (e.g. grating or prism) to separate the different wavelengths, and (4) a detector- (e.g. photomultiplier or diode array) and a data processing system (e.g. plotter oscilloscope and/or a computer). Typically, spectral information is obtained either by the selection (scanning) of small wavelength intervals that are detected individually (double beam UV/Vis spectrophotometer, see below) or by the simultaneous detection of a large wavelength interval (diode array spectrophotometer).[107] As the double beam UV/Vis spectrophotometer was used for the results presented in this thesis, the basic principle of operation and typical setup of such will be explained in the following.

The ratio of the spectral intensity of the light, which is transmitted through the sample $I(\lambda)$, and the incident light $I_0(\lambda)$ provides the transmittance $T(\lambda)$. The extinction $E(\lambda)$ is obtained by the decadic logarithm of the transmittance (see eq. 3.1 and 3.2). Besides information on the absorption of the sample, the extinction further includes information on scattering, diffraction, and reflection of the sample. As the latter typically constitute only minor contributions (due to precautions made with regard to sample purity and dilution) that usually are corrected for automatically using a reference (see below), the extinction equals approximately the absorption $A(\lambda)$.[108]

$$T(\lambda) = \frac{I(\lambda)}{I_0(\lambda)} \tag{3.1}$$

$$A(\lambda) \approx E(\lambda) = -\log\left(T(\lambda)\right) \tag{3.2}$$

Besides the expression of eq. 3.2, $A(\lambda)$ can also be expressed by means of the Beer-Lambert law (see eq. 2.4 in section 2.1). Here, a linear correlation of $A(\lambda)$ with the concentration of the sample c and the optical path length d is given introducing the absorption coefficient $\epsilon(\lambda)$ as a factor of proportionality. From the absorption coefficient, in turn, further parameters, such as the oscillator strength of a transition, can be derived (see section 2.1).[108]

The typical optical setup is illustrated using the example of a double beam UV/Vis spectrophotometer as applied here (see Figure 3.1).

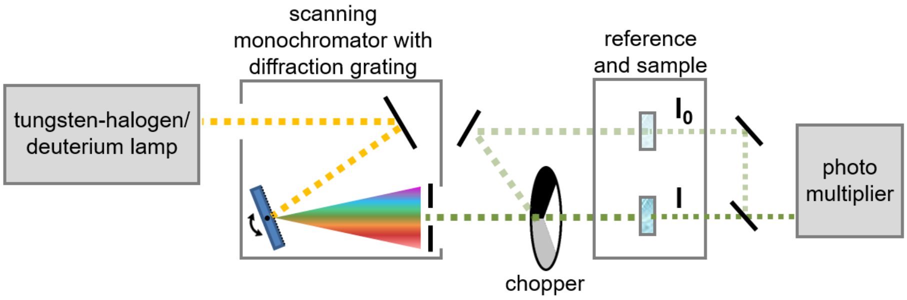

Figure 3.1.: Scheme of the optical setup of a double beam spectrophotometer as it was used throughout the measurements presented in this thesis. The spectrally broad light from the light source is marked as a yellow line. The scanning monochromator[1] selects one wavelength to pass (green line). A three-segment optical chopper (reflection, open, close) sends the beam further to the reference, lets the beam pass to the sample or blocks the beam. Transmitted reference and sample beam (I_0 and I, respectively) are detected by a photomultiplier.

The light source typically constitutes a tungsten-halogen lamp covering a spectral range from the near UV to the NIR (≈ 300 - 2500 nm) and a deuterium arc lamp explicitly for the UV down to wavelengths of ≈ 160 nm. The scanning monochromator spatially separates the wavelengths of the spectrally broad light source. A small wavelength interval is selected by a slit of specific width. Depending on the size of the slit, a larger or smaller interval is selected allowing for a higher/lower intensity of the beam at the expense of a lower/higher spectral resolution. As the dispersing element (typically a diffraction grating) rotates, several

---

[1] It is noted that the way the grating and its operation are schematically represented here and throughout may be misleading. However, for the sake of simplicity and clear visibility of the spectrally fanned light, a more complex representation is omitted.

wavelength intervals are scanned over time so that the intensity can be expressed as a function of the wavelength. Each selected wavelength interval passes through an optical chopper that either reflects or transmits the beam. The reflected beam is directed to the reference (usually the pure solvent) and constitutes the signal $I_0(\lambda)$ after transmission of the reference. Its intensity is "counted" as a transmittance of $T(\lambda) = 1$. The other beam passes through the sample constituting the signal $I(\lambda)$. Both sample and reference beam are detected by a photomultiplier in synchronism with the optical chopper. Additionally, the optical chopper may also allow for a dark signal to be recorded blocking both the reference and sample beam. By so, the measured intensities $I_0(\lambda)$ and $I(\lambda)$ can be corrected by subtracting the dark signal I_{dark}.

3.1.2. Fluorescence Spectroscopy

Based on the name of this method, one is inclined to assume that only fluorescence can be detected. However, in principle, fluorometer devices are able to detect all sorts of emission phenomena without differentiating their origins. Nevertheless, certain spectrometers are specifically suitable for detecting phenomena such as phosphorescence, which usually constitutes low quantum yields at room temperature. Such devices allow, for instance, for simultaneous cooling of the sample and a time-delayed detection after excitation in order to avoid interfering with fluorescence signals. In the following, it is referred to the basic design and the principle of operation of a fluorometer as such was used over the course of this thesis.

Fluorometers usually consist of (1) a spectrally broad light source, (2) two monochromators, (3) the sample(holder), and (4) a detection and data processing unit (see Figure 3.2). One monochromator is located before the sample selecting the excitation wavelength, and the other one is located behind the sample selecting the detection wavelength. The entrance of the second monochromator is usually positioned rectangular to the excitation beam. This arrangement ensures that as little as possible of the excitation light is detected as well. In the case of a diode array detector that is capable of detecting a range of dispersed wavelengths at once, the second monochromator is replaced by a polychromator. The Kerr setup, described in section 3.2.3, which is also capable of recording steady-state emission spectra, possesses a diode array detector as well as a linear excitation-detection geometry.

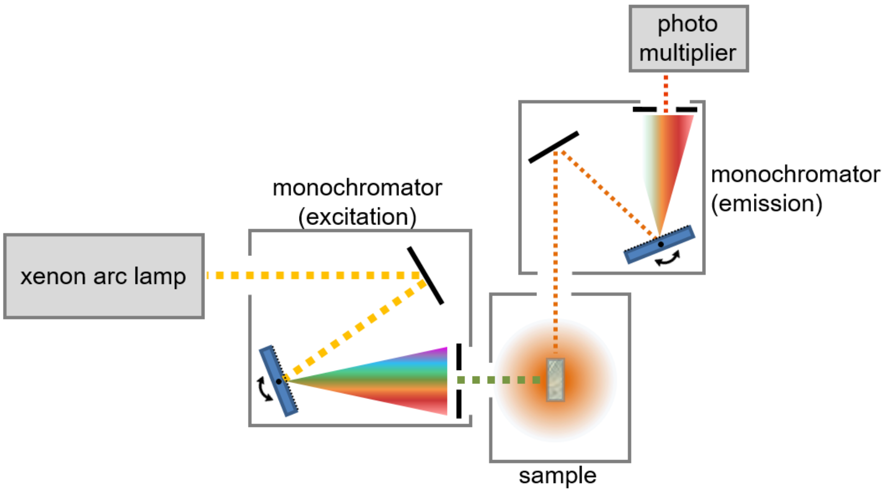

Figure 3.2.: Scheme of the optical setup of a fluorometer as it was used throughout the measurements presented in this thesis. The spectrally broad light from the light source is marked as a yellow line. The (scanning) monochromator selects one wavelength (green line) to excite the sample. The emission (orange line) is detected at a right angle after it passed a second (scanning) monochromator selecting a specific wavelength.

Most fluorometers allow for both emission spectra and excitation spectra to be recorded. For the recording of an emission spectrum, the excitation wavelength is fixed while the detection wavelength is scanned over a range of wavelengths yielding the respective emission spectrum. For an excitation spectrum only a specific wavelength is selected for detection while the excitation wavelengths are scanned over a range of wavelengths resulting in the excitation spectrum. In the case of a sample that shows fluorescence and obeys Kasha's rule (see section 2.1), the excitation spectrum ought to resemble the absorption spectrum.

In contrast to absorption spectroscopy where the output quantity A constitutes a relative one depending on the ratio I/I_0, which can be further quantified using Beer's law (see section 2.1 and section 3.1.1), emission spectra are usually recorded in absolute units such as counts. As this quantity depends on many experimental factors such as the intensity and wavelength of the excitation beam, a quantification of the sample's emission is not straightforward. A universally valid quantification of a molecule's emission property is given by the emission quantum yield, which is defined by the ratio of emitted to absorbed photons (see section 2.1).[87] This quantity can be accessed experimentally using an integrating sphere (also known as Ulbricht sphere).[109] It constitutes an optical device that features a hollow spherical cavity coated with a diffuse white reflective material. The key characteristic of this device is its ability to scatter or diffuse light uniformly. This further enables the device to directly measure the number of absorbed and emitted photons, which is why it is often referred to as an absolute method for the determination of the emission quantum yield.[110] Another commonly used approach, known as the relative method for quantum yield measurements, involves comparing the emission of the sample to that of a reference standard with a known quantum yield.[87] For the calculation, the ratio of the integrals of the emission bands $\int I(\lambda)\,\mathrm{d}\lambda$ – both recorded under identical experimental conditions – is formed and multiplied with the known quantum yield $\Phi_{Fl,ref}$.

$$\Phi_{Fl} = \Phi_{Fl,ref} \frac{\int I(\lambda)\,\mathrm{d}\lambda}{\int I(\lambda)_{ref}\,\mathrm{d}\lambda} \frac{A(\lambda_{exc})_{ref}}{A(\lambda_{exc})} \frac{n(\lambda_{em})^2}{n(\lambda_{em})^2_{ref}} \tag{3.3}$$

The absorption at the excitation wavelength $A(\lambda_{exc})$ of both the sample and reference as well as the refractive index of the solvent at the emission wavelength $n(\lambda_{em})$ further enter the computation. Comparing emission bands in very different spectral regions can lead to errors in the measurement of fluorescence quantum yields. Also, high values of absorption for sample or reference can lead to distorted results due to inner filter effects. For this reason, it is advised to keep the absorption of the sample and reference smaller than 0.05.

These inner filter effects are categorized into the primary (also known as type I) and the secondary (also known as type II) inner filter effect. The primary inner filter effect takes into account that the intensity of the excitation light is reduced at the area of detection, which is - for a rectangular detection geometry - approximately the center of the cuvette.[111] The secondary inner filter effect considers the reabsorption of emitted photons due to an overlap of the absorption and emission spectrum of the sample.[112] The significance of each process is determined by the absorption of the sample at the excitation and emission wavelengths. Consequently, the fluorescence intensities are proportional to the concentration of the sample only within a restricted range of absorption values.

3.2. Time-Resolved Spectroscopy

3.2.1. UV/Vis Absorption Spectroscopy with Femtosecond Resolution

The UV/Vis absorption spectroscopy setup with femtosecond time resolution (fsTA) as it was employed in the course of this thesis has been described before.[54,113,114,115] This technique is based on the pump-probe principle. Two separate laser beams (i.e. the pump- and the probe beam) originating from the same femtosecond pulsed laser source are needed (see Figure 3.3). The purpose of the "monochromatic" pump beam[2] is to photoexcite the sample, the spectrally broad probe beam probes the sample at a specific time after the photoexcitation.

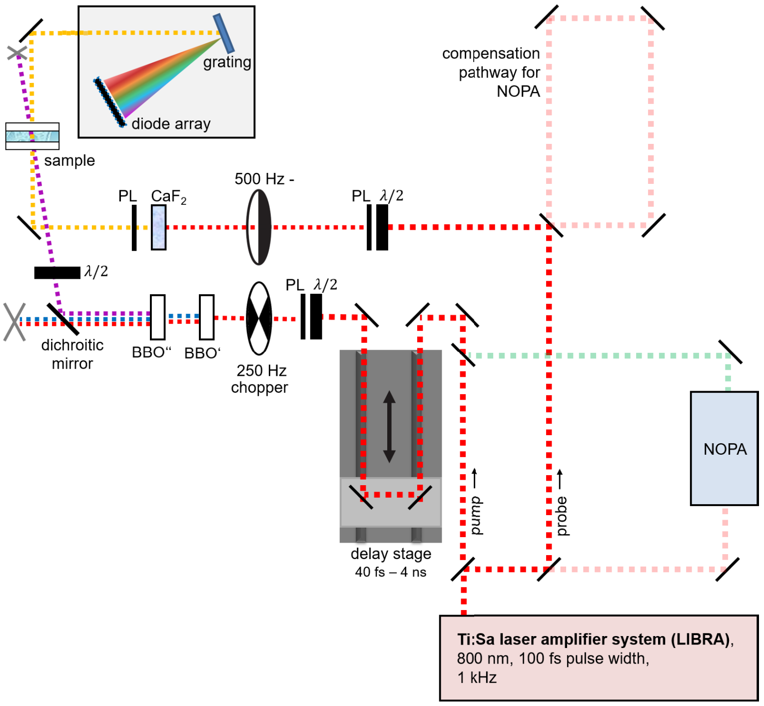

Figure 3.3.: Scheme of the optical setup for the fsTA as it was used throughout the measurements presented in this thesis. The fundamental of the Ti:Sa laser amplifier system (800 nm) is marked as a red dotted line, the frequency-doubled (after BBO', 400 nm) and frequency triplet (after BBO", 266 nm) are marked as blue and violet, respectively. The whitelight (after CaF_2 plate) is indicated by a yellow line. Polarizers are marked as PL, $\lambda/2$ plates as $\lambda/2$. Simultaneous usage of a polarizer and a $\lambda/2$ plate make up an attenuation unit. Lenses and apertures are not included in the scheme.

A delay stage that is placed in the path of the pump beam extends the pathway the light travels before reaching the sample. Because of the finite speed of light, a spatial distance corresponds to a time interval. In that way the delay stage accounts for the specific time delay between pump and probe pulses, covering time delays of ≈ 40 fs to a maximum of ≈ 4 ns. The excitation wavelength of the pump beam is set via frequency doubling and, if needed, subsequent sum frequency generation. For a Ti:Sa femtosecond laser source with a fundamen-

---

[2] In contrast to a continuous wave laser that usually emits light with a very narrow spectrum, a pulsed laser exhibits a broader spectrum. According to the Fourier transform, the temporal and spectral properties of a pulse are interconnected. Thus, the shorter a pulse is, the larger its frequency bandwidth. This relationship is characterized by the transform limit, which is the minimal product of temporal width and spectral width and amounts to 0.441.[116] Accordingly, the bandwidth (FWHM) of a 100 fs Gaussian pulse with a central wavelength of 800 nm is 11 nm.

tal of 800 nm (as it was used in the course of this thesis), this corresponds to wavelengths of 400 and 266 nm, respectively. The processes of frequency doubling and sum frequency generation are achieved by the usage of suitable nonlinear optical crystals such as β-barium borate (BBO) crystals (see section 4.3.1 for more details on the exact components). Other excitation wavelengths (between ≈ 470 and ≈ 700 nm) are obtained via non-collinear optical parametric amplification (NOPA). Since for the experiments presented here, only excitation wavelengths of 400 and 266 nm were used, it is referred to refs.[54,113,117] for a detailed description of the NOPA process. The output wavelengths of the NOPA can again be frequency doubled for respective wavelengths between ≈ 235 and ≈ 350 nm. The spectrally broad probe pulse is obtained via a process referred to as whitelight generation (supercontinuum generation): if a femtosecond laser beam is focused onto certain transparent media such as a $\mathrm{CaF_2}$ crystal, a collection of nonlinear processes act together in order to cause spectral broadening.[118] Subsequently, the spectrally broad probe beam transmits the sample, which is constantly refreshed using, for instance, a flow cell cuvette, before it is dispersed by a grating and detected by a photodiode array.

The wavelength and time-dependent transient absorption signal $\Delta A(\lambda, t_D)$ is obtained by the negative decadic logarithm of the ratio of the detected intensity of the probe beam with ($I(\lambda, t_D)_{pump/probe}$) and without ($I(\lambda)_{probe}$) pump (i.e. photoexcitation of the sample) as expressed in eq. 3.4.

$$\Delta A(\lambda, t_D) = -\log\left(\frac{I(\lambda, t_D)_{pump/probe}}{I(\lambda)_{probe}}\right) \tag{3.4}$$

To achieve the separate detection of $I(\lambda, t_D)_{pump/probe}$ and $I(\lambda)_{probe}$, a chopper with half of the femtosecond laser repetition rate (i.e. 1 kHz/2 = 500 Hz) is placed in the pump beam[3]. In this chopper arrangement (also referred to as two-cycle mode) the background signal of the detector is not automatically incorporated and needs to be measured and corrected separately. Also, it is not accounted for undesired signals originating from pump beam scattering as part of the signal $I(\lambda, t_D)_{pump/probe}$. To correct for these signals the four-cycle mode is applied. For this, a second chopper is needed operating at a quarter of the femtosecond laser repetition rate (i.e. 1 kHz/4 = 250 Hz). In this way, four consecutive laser pulses (i.e. combinations of

---

[3] Alternatively, $I(\lambda, t_D)_{pump/probe}$ and $I(\lambda)_{probe}$ can be detected simultaneously and without using any choppers. For such a detection scheme, the probe beam is separated after the whitelight generation using a beam splitter and detected by an additional reference detector.[119,120]

chopper modes) account for one transient absorption signal (see Figure 3.4).

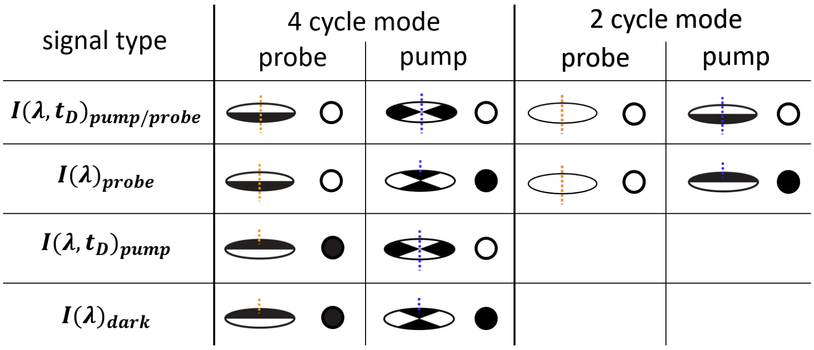

Figure 3.4.: Obtained signals depending on the chopper position for the four-cycle- and the two-cycle mode.

In the four-cycle mode, the corrected transient absorption signal is calculated based on eq. 3.5.

$$\Delta A(\lambda, t_D) = -\log\left(\frac{I(\lambda, t_D)_{pump/probe} - I(\lambda, t_D)_{pump}}{I(\lambda)_{probe} - I(\lambda)_{dark}}\right) \tag{3.5}$$

According to eq. 3.4 and 3.5, the obtained transient absorption signal is positive when the nominator (i.e. the corrected probe signal with photoexcitation) is smaller than the denominator (i.e. the corrected probe signal without photoexcitation). In this case and for a certain detection wavelength, the photo-excited sample absorbs more light than the non-excited sample. These positive signals can either originate from excited state absorption (ESA; Figure 3.5 orange) or from ground state absorption of photoproducts. Negative transient absorption signals, obtained when the nominator is larger than the denominator, result from two distinct phenomena. The detected probe signal with photoexcitation is larger than the one without photoexcitation either when the excited sample shows less absorption for a specific wavelength than the unexcited sample does, which is referred to as ground state bleaching (GSB, Figure 3.5 blue), or the excited sample is contributing to an increase of the probe intensity by stimulated emission (SE, Figure 3.5 green, and section 2.1). These processes can occur simultaneously and the overall (i.e. observed) transient absorption signal always constitutes the sum of their contributions. The three possible signal types of ESA, GSB, and SE and their occurrence in transient absorption spectroscopy are summarized schematically in Figure 3.5.

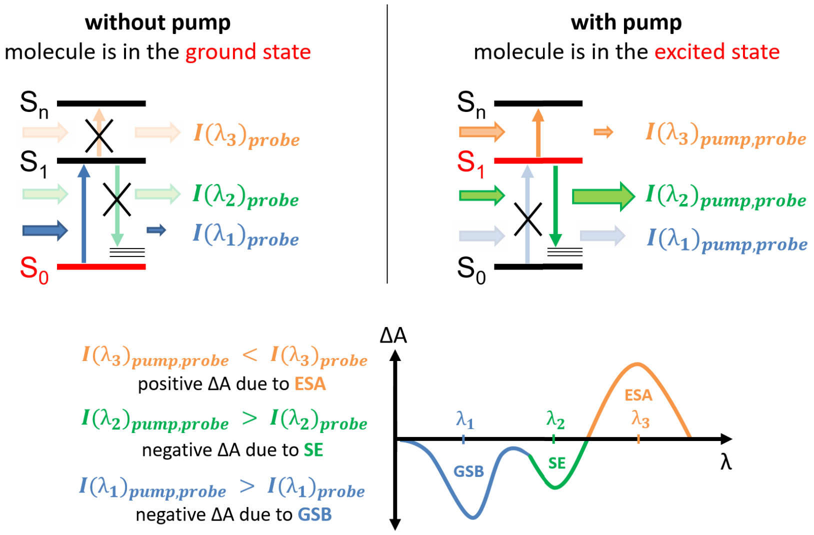

Figure 3.5.: Scheme on the formation and manifestation of excited state absorption (ESA), ground state bleach (GSB) and stimulated emission (SE) as part of fsTA spectroscopy. As an example, three wavelengths λ_1, λ_2, and λ_3 of the probe beam were depicted to emphasize, based on the increase or decrease of $I(\lambda_1, \lambda_2, \lambda_3)_{probe}$ with (top right) and without (top left) preceding photoexcitation (pump), the formation of $\Delta A(\lambda, t_D)$.

Apart from the expression of $\Delta A(\lambda, t_D)$ given in eq. 3.4 and 3.5, $\Delta A(\lambda, t_D)$ can further be expressed via a modified Beer's law according to eq. 3.6.

$$\Delta A(\lambda, t_D) = \Delta\varepsilon(\lambda) \cdot c^*(t_D) \cdot d \tag{3.6}$$

In this equation, $\Delta\varepsilon(\lambda)$ is the difference absorption coefficient of the ground state and the excited state of the sample, $c^*(t_D)$ the time-dependent concentration of molecules in the excited state, and d the effective optical path length. This equation is only valid if one transient species is present at a time.

3.2.2. UV/Vis Absorption Spectroscopy with Nanosecond Resolution

With femtosecond transient absorption spectroscopy the time range ≈ 10 fs to ≈ 10 ns can be covered[4]. Nanosecond transient absorption spectroscopy (nsTA) covers processes from ≈ 20 ns to some milliseconds. In contrast to the fsTA, here the required time resolution is long enough to allow for an electronically triggered detection system instead of a pump-probe scheme based on an optical delay. This further allows for a complete and continuous scan

---

[4] For delay times beyond ≈ 10 ns the optical path length becomes too long.

of the time regime (20 ns - ms) with one rather long probe pulse ($\approx$ ms) upon a single nanosecond excitation pulse. In principle also continuous wave light would be possible for probing. However, this would imply a smaller number of photons per time resulting in higher noise. The transmitted probe light, which increases or decreases over time, is detected with a photomultiplier. This method is known as laser flash photolysis. The time resolution of the experiment is typically either given by the sampling rate of the oscilloscope, which samples the signal of the photomultiplier, or by the response time of the photomultiplier itself. The excitation beam originates from a nanosecond Nd:YAG (neodymium-doped yttrium aluminum; Nd:$Y_3Al_5O_{12}$) pulsed laser system with a fundamental of 1064 nm. Via non-linear optics the fourth harmonic (266 nm) is generated for the photoexcitation of the sample. As the nsTA method requires a rather long (and spectrally broad) probe pulse, a separate light source for the probe beam is applied. A xenon flash lamp that delivers stable high-intensity whitelight pulses over hundreds of microseconds serves this purpose.

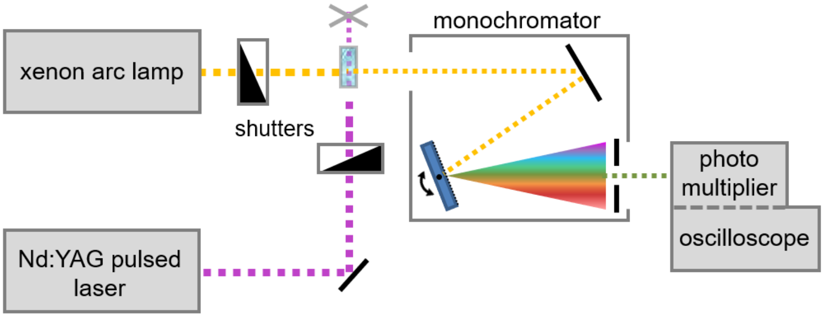

Figure 3.6.: Scheme of the nsTA setup as it was used throughout the measurements presented in this thesis. The spectrally broad light from the pulsed xenon arc lamp is marked as a yellow line. The (scanning) monochromator selects one wavelength at a time, which is eventually detected by a photomultiplier.

For the calculation of the transient absorption signal $\Delta A(\lambda, t_D)$, it is referred to section 3.2.1 as well as eq. 3.4 and eq. 3.5 as the same principle is applied here. In contrast to the fsTA setup, in the nsTA, choppers are replaced by mechanical shutters that are synchronized electronically with the excitation and probe pulses.

3.2.3. Femtosecond Fluorescence Spectroscopy via the Kerr Effect

A comprehensive description of the methods principle and the respective setup was given before in refs.[121,122,123].

Time-resolved fluorescence spectroscopy with femtosecond resolution as applied here is based on the optical Kerr effect. The Kerr effect in general describes a non-linear optical phenomenon where the optical properties of a material (Kerr medium) change in response to an applied electric field.[124] Here, the electrical field originates from an intense, short (≈ 100 fs) laser pulse, also referred to as the gate pulse. The optical properties of the material change in such a way that its refractive index depends on the polarization and propagation direction of light, a property also referred to as birefringence.[124] Based on the optical Kerr effect an optical gate can be realized. After excitation with a pulsed laser, the fluorescence of the sample passes a first polarizer (see Figure 3.7, PL1), and the Kerr medium. A second polarizer on the way to the detector has its transmission axis at 90° with respect to the first one. Thus, in absence of an electric field (no gate pulse), the fluorescence will not be detected. In the presence of an electrical field (i.e. gate pulse), the Kerr medium temporarily becomes birefringent (approximately for the duration of the gate pulse) changing the polarization of the fluorescent light. This time section of the fluorescent light can now pass the second polarizer and is detected. As both the laser pulses for excitation of the sample as well as the gate pulses are synchronized and the gate pulse being precisely delayed upon passing a controllable delay stage, time-resolved spectra with femtosecond resolution of the samples fluorescence can be recorded as a set of spectra for different delay stage settings.

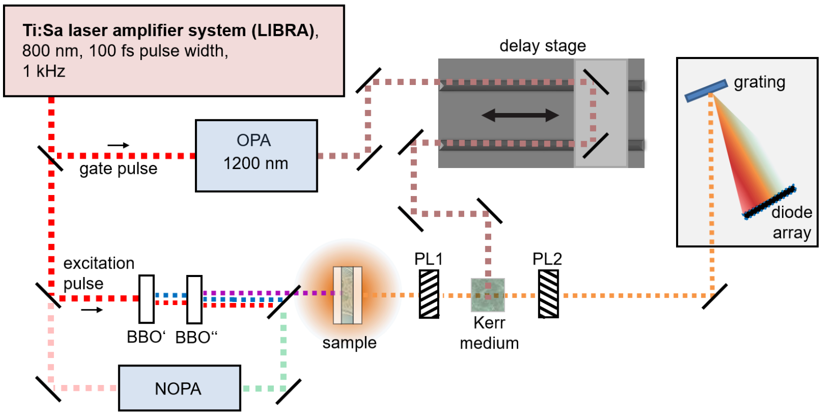

Figure 3.7.: Scheme of the Kerr setup as it was used throughout the measurements presented in this thesis.

The setup with its basic components is schematically given in Figure 3.7. For experimental details, including experimental parameters for the here presented measurements, see section 4.3.3.

3.3. Data Processing

Interpreting a large amount of three-dimensional data - that is the strength of the signal, the wavelength, and the delay time - generated by time-resolved spectroscopy, is not straightforward. One mathematical tool that is applied is the global fit analysis.[125] The term $global$ refers to the simultaneous analysis of a large number of (or all) detection wavelengths (i.e. time traces) which allows for a greater amount of data to be considered for one fitting procedure and therefore leads to increased accuracy for the determination of the time constants τ_i. In the global analysis employed here the following trial function was used (eq. 3.7).

$$\Delta A_{obs}(\lambda, t) = IRF \otimes \sum_i \Delta A_i(\lambda) \cdot e^{-(t/\tau_i)} \tag{3.7}$$

In the expression, $\Delta A_{obs}(\lambda, t)$ is the observed difference absorption for a given delay time t and a given detection wavelength λ, IRF is the instrumental response function of the device (see below), $\otimes$ symbolises the convolution with the trial function, $\Delta A_i(\lambda)$ represents the wavelength-dependent amplitudes of the decay exponentials with time constant τ_i. In a global approach the time constant τ_i applies to all wavelengths.

Clearly, this expression is based on the assumption that the data can be described by a sum of exponential terms. Such a form results as a solution for any kinetic scheme provided that all elementary processes are of first or pseudo-first order.[125] Although this is not always the case (see below), with experimental precaution and prior knowledge with regard to (ultra) fast processes, the application of global fitting is appropriate in many cases.[125] For instance, deviations might be present for early delay times and time resolutions of $\lesssim 100$ fs due to the formation of coherent wave packets.[126] These create an oscillating signal that cannot be fit exponentially. Also, processes that cause a spectral shift such as vibrational cooling or dielectric relaxation (see section 2.3) defy proper exponential fitting along the time axis.[127] Furthermore, some fast chemical reactions such as excited-state proton transfer (ESPT) possess such involved kinetics that proper fitting is intricate[128]. Diffusion-controlled reactions including triplet-triplet annihilation (TTA) are of second-order kinetic and therefore not covered by exponential means. As such processes commonly take place on a nano- to microsecond timescale, they are relevant for the UV/Vis absorption spectroscopy with nanosecond resolution (section 3.2.2).

The IRF describes the temporal response of the instrument for an infinitely small short signal. The width of the IRF (e.g. its FWHM) is taken as a measure of time resolution. For pump-probe experiments and optimized conditions, the IRF equals the crosscorrelation function, which in turn can be determined by measuring instantaneous signals observed for very early delay times, such as two-photon absorption (TPA) or stimulated Raman scattering (SRS).[129]

Amplitude spectra or decay-associated difference spectra (DADS) refer to the plots that display all the amplitudes $\Delta A_i(\lambda)$ of a single exponential term i versus the corresponding wavelengths (λ). The sum of all DADS equals the signal at time zero corrected for the finite time resolution. DADS are useful in providing information on whether the signal increases or decreases over time for a specific time constant at a particular wavelength. In line with the nature of the decaying exponential function, positive amplitudes indicate signal decreases while negative ones indicate signal increases. Therefore, it is important to note that DADS do not reflect the spectra of individual species present in the sample but rather, depict the overall change in signal associated with a specific exponential term.

Regarding the experiments presented in this thesis, the global fit analysis was applied using the IDL-based software $Z20$ developed by the research group of Prof. Dr. W. Zinth (LMU München). Here, both a Levenberg-Marquardt algorithm[130] for the approximation of the time constants τ_i and a linear regression for the amplitudes $\Delta A_i(\lambda)$ are applied in an alternating manner. The number of exponential terms necessary are usually determined by visual examination of the data prior to the fitting. One exponential term with a fixed time constant of 10^8 fs for the fsTA and 10^8 μs for the nsTA is added to account for any "leftover" signals that extend the observable time window.

4. Experimental Section

In chapter 3 the principle of operation of the applied methods as well as their setups, as they were used for the experiments presented in this thesis, have been described. In this chapter, specific experimental details necessary for reproducing the experiments are given.

Part of the steady-state characterization of the complex NHCCuPy (see section 5.1) was conducted by Jennifer Kremper in the course of her bachelor's thesis, part of the respective steady-state characterization of complex NHCCuDBM (see section 5.1) was conducted by Oliver Röth in the course of his master's thesis, both were made under my supervision. Chemicals that were used are provided together with their degree of purity and the respective supplier. NHCCuPy was synthesized by Philipp Schmeinck according to the route given in section 4.5.1. The participation of others than the author of this thesis regarding the conduction of the experiments is further detailed in the respective sections in chapter 5.

4.1. Steady State UV/Vis Absorption Spectroscopy

Steady-state UV/Vis absorption measurements were conducted using the two-beam spectrophotometers Lambda 19 and Lambda 1050+ from PerkinElmer. The dissolved samples and the respective solvents were measured in standard 1-cm fused silica cuvettes (QX) from Hellma Analytics. For measurements involving high concentrations of the sample, standard 1-mm-path-length fused silica cuvettes (QX) were used.

4.2. Steady State Emission Spectroscopy

Since two distinct spectroscopic methods were used for the steady state emission measurements, in the following each is separately explained with respect to experimental details. In both methods, the solvent correction was done manually by the subtraction of a separate solvent measurement.

4.2.1. Fluorescence Spectroscopy using FluoroMax-4

For the steady state measurements in a rectangular excitation-detection geometry, the FluoroMax-4 manufactured by Horiba was used. The bandpass of the rectangularly aligned monochromators – one for the excitation beam and one for the emission beam – was set to a spectroscopic resolution of 5 nm if not mentioned otherwise. The initially recorded emission signal ($S1$) is corrected for the wavelength-dependent spectral sensitivity of the detection system. Furthermore, this corrected emission signal ($S1c$) is divided by the intensity of the excitation beam ($R1c$), which is separately detected by a reference detector and equally corrected for its spectral sensitivity ($S1c/R1c$).

The luminescence quantum yields presented in this thesis were determined using thymidine in water ($\Phi_{lum} = 1.32 \cdot 10^{-4}$[131]), tris(bipyridine)ruthenium(II) chloride in water ($\Phi_{lum,air} = 0.028$[132], section 5.1), coumarin102 in ethanol ($\Phi_{lum} = 0.76$[133]), and N-methylphthalimid in acetonitrile ($\Phi_{lum} = 8 \cdot 10^{-4}$[123], section 5.2) as references. If not mentioned otherwise, the absorption of the samples was set to $\leq$ 0.05 to avoid inner filter effects. For the determination of the FQY of DBM and NHCCuDBM, the samples' absorption had values of $\approx$ 0.2. Therefore, the integrated fluorescence signal was corrected for primary inner filter effects using a calibration curve. The curve was acquired by measuring different solutions with different absorptions ($\approx$ 0.05 - $\approx$ 2) and subsequent plotting of the integrated emission signal $S(A)$ versus the absorption A. The behavior was fitted with a trial function (eq. 4.1) adapted from ref.[134]:

$$S(A) = f \cdot \left(10^{-\frac{A}{d} \cdot (x_m - \frac{\Delta x}{2})} - 10^{-\frac{A}{d} \cdot (x_m + \frac{\Delta x}{2})}\right) \tag{4.1}$$

In the equation, A is the absorption, d is the optical path length of the cuvette (1 cm), x_m is the center of the detection area, and Δx is the width of the detection area. The fit yields 0.66 cm (NHCCuDBM), 0.61 cm (DBM) for x_m, and 0.015 cm for both NHCCuDBM and DBM for Δx. Fluorescence data were corrected by dividing them by the right-hand side of equation 4.1.

4.2.2. Fluorescence Emission Using the Kerr-Setup

For the steady-state emission measurements in a linear excitation-detection geometry, the Kerr setup was employed[1]. The excitation was tuned to 266 nm. The sensitivity of the instrument was determined and corrected for using an OSRAM 64250 HLX halogen lamp serving as a black body radiator with an operating temperature of 3350 K. The sample was constantly flown through a custom-made flow cell (1-mm-path-length fused silica, Hellma Analytics) using a REGLO Analog MS-2/8 peristaltic pump manufactured by ISMATEC.

4.3. Time-Resolved Spectroscopy

The experimental details involving the time-resolved UV/Vis absorption spectroscopy experiments with femto- and nanosecond time resolutions as well as the fluorescence spectroscopy experiments with femtosecond time resolution are described in the following.

4.3.1. UV/Vis Absorption Spectroscopy with Femtosecond Resolution

For more details on the optical setup of UV/Vis absorption spectroscopy with femtosecond resolution (fsTA) and background of the method see section 3.2.1 as well as refs.[54,113,123,135,136].

The following paragraph of experimental details with respect to the measurements of NHC-CuPy is reprinted from the respective publication[40] written by the author of this thesis. The measurements of the complex NHCCuDBM were performed in the same manner. A 1 kHz Ti:Sa laser amplifier system (Coherent Libra) served as pulse source. The output wavelength is 800 nm and the pulse duration is 100 fs. To yield 266 and 400 nm pump pulses, the 800 nm laser output was frequency doubled and tripled using β-barium borate crystals, respectively. The pump pulse energy at the sample was adjusted to ≈ 1 μJ and the beam had a focal diameter of 160 μm (full width at half maximum (FWHM)) at the sample. The absorption change was probed with a white light continuum generated in CaF_2 with a diameter of 100 μm on the sample. The relative polarization of the pump and probe beam was set to the magic angle. The time resolution was ≈ 180 fs. The spectra were recorded at 139 time delay settings between –1 to 1 ps on a linear and from 1 ps to 3.4 ns on a logarithmic time scale. For every delay setting, 2000 spectra were recorded and the data were averaged over 4

---

[1] For a more detailed description of the optical setup that was used, see sections 3.2.3 and 4.3.3 as well as ref.[54].

succeeding delay scans. The instrumental shift of time zero with wavelength was determined via the optical Kerr effect and corrected for. To remove signal contributions of the solvent and to account for time-zero femtosecond artifacts, a separate measurement of the solvent was subtracted with proper scaling depending on the absorption of the sample solution.[137] The sample was constantly flown through a custom-made flow cell (1-mm-path-length fused silica, Hellma Analytics) using a REGLO Analog MS-2/8 peristaltic pump manufactured by ISMATEC. The sample absorption at the excitation wavelength was set to ≈ 0.7 per mm.

4.3.2. UV/Vis Absorption Spectroscopy with Nanosecond Resolution

Time-resolved UV/Vis absorption data with nanosecond time resolution (nsTA) for the investigation of NHCCuPy was acquired with a laser flash photolysis spectrometer LP980 from Edinburgh Instruments. The experimental details stated here are reprinted from the respective publication[40] written by the author of this thesis.

The instrument operates in a rectangular excitation-detection geometry. For the photoexcitation, the fourth harmonic (266 nm) of ND:YAG laser (Spitlight 600, InnoLas) with a repetition rate of 5 Hz and a pulse duration of 12 ns (FWHM) was utilized. The respective beam diameter amounted to ≈ 8 mm with and average energy per pulse of 2 mJ. A pulsed xenon lamp (Osram XBO 150 W/CR OFR) was used as a probe beam. After the transmission of the sample and subsequent dispersion by a grating monochromator, the probe light is detected by a photomultiplier (Hamamatsu, PMT-900). The solution was pumped through a fused silica flow cell (Hellma Analytics) with a path length of 5 mm in pump and 10 mm in probe direction using a REGLO Analog MS-2/8 peristaltic pump manufactured by ISMATEC. The sample absorption at the excitation wavelength was set to 1.6 per cm. The solutions of the samples were deoxygenized by purging them with nitrogen (Air Liquide, 5.0). For this, the sample solution, which is pumped from the sample flask into the cuvette during the measurement, was purged at least 45 minutes before the measurement as well as during the measurement. Before the gas is fed through the sample and to reduce the effect of evaporation, the nitrogen gas passes through two gas wash bottles filled with the respective solvent.

4.3.3. UV/Vis Fluorescence Spectroscopy with Femtosecond Resolution using the Kerr Setup

The Kerr setup was employed for the UV/Vis fluorescence spectroscopy with femtosecond resolution. For a more detailed description of the optical setup that was used, see sections 3.2.3 as well as refs.[54,121]. For the excitation, the same laser source as for the fsTA was used. Using two BBOs (type I, 29°, 1 mm, and type II, 55.5°, 0.5 mm) the excitation was tuned to 266 nm. The energy per pulse is set to $\approx 1\ \mu$J, for the gate pulse 12 μJ. The diameter of the excitation beam at the sample amounted to 80 μm (FWHM). The time resolution of the instrument was 270 fs. For all samples, an integration time of 2 s was applied. The sensitivity of the instrument was determined and corrected for using an OSRAM 64250 HLX halogen lamp serving as a black body radiator with an operating temperature of 3350 K. The sample was constantly flown through a custom-made flow cell (1-mm-path-length fused silica, Hellma Analytics) using a REGLO Analog MS-2/8 peristaltic pump manufactured by ISMATEC.

4.4. Quantum Chemical Calculations

The methodological details of the quantum chemical calculations with respect to the investigation of NHCCuPy are partially reprinted from the respective publication by the same author as this thesis.[40] For the calculations of NHCCuDBM and the ligand DBM, the same methodological details apply. The calculations were conducted by Jasper Guhl (Institute of Theoretical Chemistry and Computer Chemistry, Prof. C. M. Marian).

The optimized geometries were obtained from Kohn-Sham density functional theory (DFT) for the ground state, from time dependent-DFT (TD-DFT) for the singlet excited states, and from the Tamm-Dancoff approximation (TDA-TDDFT) for triplet excited states. A PBE0 functional, the GD3 dispersion correction, and a def2-SV(P) basis set for all atoms as implemented in Gaussian were used.[138,139,140,141] The copper core was treated with a cc-pVDZ-PP basis set in conjunction with the Stuttgart-Köln MCDHF RSC ecp, and the oxygen was treated with a def2-TZVPD basis in the calculations of the free ligand.[142,143] Solvent effects were accounted for with the standard IEF-PCM.[144] Its point charges were exported from Gaussian to Turbomole, to be used for the DFT/MRCI calculations.[145,146] The DFT/MRCI calculations used the optimized geometry, including the point charges, and employed the R2018 Hamiltonian,[147] the same basis, but the BH-LYP functional.[147,148,149] For the calculation of ISC rate constants in the Condon approximation, the spin-orbit coupling (SOC) matrix elements were calculated via SPOCK, and the vibrational overlap via VIBES, utilizing internal coordinates and a temperature of 300 K.[150,151] Based on the computed oscillator strengths f_i, absorption coefficient spectra $\epsilon_i(\tilde{\nu})$ were obtained. Herein, the relation between the spectral integral covering an electronic transition band and f_i according to eq. 4.2[108] was employed.

$$f_i = \frac{4 \cdot \epsilon_0 \cdot m_e \cdot c_0^2}{e_0^2} \cdot \frac{\ln 10}{N_A} \int_0^\infty \epsilon_i(\tilde{\nu})\, d\tilde{\nu} \tag{4.2}$$

In the equation, ϵ_0 is the vacuum electric permittivity, m_e the electron mass, c_0 the speed of light in vacuum, e_0 the elementary charge, and N_A the Avogadro constant. The band $\epsilon_i(\tilde{\nu})$ was modelled with a Gaussian. Its width (FWHM) was chosen to match approximately the experimental one.

4.5. Chemicals

Here, all chemicals that were used in the course of this thesis are listed including the degree of purity and the providing company. The synthesis route of NHCCuPy, which was performed by Philipp Schmeinck (Institute of Organometallic Chemistry, Prof. C. Ganter) is given in the following subsection 4.5.1.

Table 4.1.: List of chemicals used in the course of this thesis, including their degree of purity and the supplier.

chemical	acronym	degree of purity	supplier
acetonitrile	MeCN	HPLC gradient grade	ChemSolute
cyclohexane	Cx	$\geq$ 99.9%	ROTH
dichloromethane	DCM	HPLC gradient grade	Fisher Chemical
ethanol	EtOH	$\geq$ 99.8%	Sigma Aldrich
2-propanol	-	99.9%	Sigma Aldrich
2,2,2-trifluoroethanol	TFE	$>$ 99%	Apollo Scientific
Nitrogen	-	99.999%	Air Liquide
2-picoline	-	$\geq$ 98.5%	Sigma Aldrich
tetrabutylammonium tetrafluoroborate	-	99.0%	Sigma Aldrich
tris(bipyridine)ruthenium(II) chloride	-	99.95%	Sigma Aldrich
dibenzoylmethane	DBM	99.0%	BLDpharm
1,3-bis(2,6-diisopropylphenyl)imidazol-2-ylidene] (dibenzoylmethanoate) copper(I)	NHCCuDBM	98%	TCI Chemicals
methylphthalimid	-	98.0%	Aldrich Chemistry
sodium hydroxide	NaOH	99.0%	AppliChem
coumarin102	-	$\geq$ 97.0%	Radiant Dyes
water	H_2O	HPLC gradient grade	Fisher Chemical

4.5.1. Synthesis Route of NHCCuPy

NHCCuPy was synthesized according to a protocol published previously and fully characterized.[152] The purity of NHCCuPy was confirmed by ^{1}H-NMR, ^{13}C{^{1}H}-NMR, elemental analysis and ESI mass spectrometry (see appendix, Figure A.1).[40,152]

In the following, the synthesis route for NHCCuPy starting from 2,6-diisopropylaniline is given. The synthesis was performed by Philipp Schmeinck (Institute of Organometallic Chemistry, Prof. C. Ganter).

As a first step, an excess of 2,6-diisopropylaniline is combined with acetic acid and reacted with glyoxal dissolved in methanol (see Figure 4.1). After a slightly exothermic reaction, the product – N,N'-bis(2,6-diisopropylphenyl)ethanediimine – crystallizes. The suspension is stirred at room temperature for 10 h before it is filtered and washed with methanol several times.

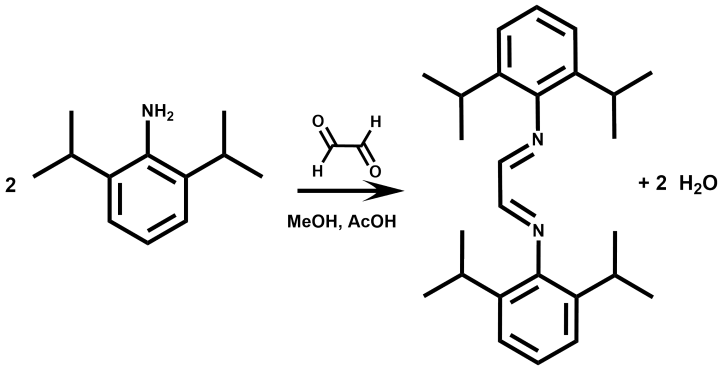

Figure 4.1.: Reaction of 2,6-diisopropylaniline with glyoxal to form N,N'-bis(2,6-diisopropylphenyl)ethanediimine. Based on ref.[153].

The previously prepared ethanediimine is combined with paraformaldehyde (see Figure 4.2). To ensure that no reagents stick to the wall, the flask wall is washed with ethyl acetate, and the solids are suspended therein. Subsequently, chloromethylsilane is added and the suspension is stirred at 70°C. Afterwards, the mixture is cooled in an ice bath and the precipitated product – 1,3-Bis-(2,6-diisopropylphenyl)imidazoliumchlorid – is filtered and washed.

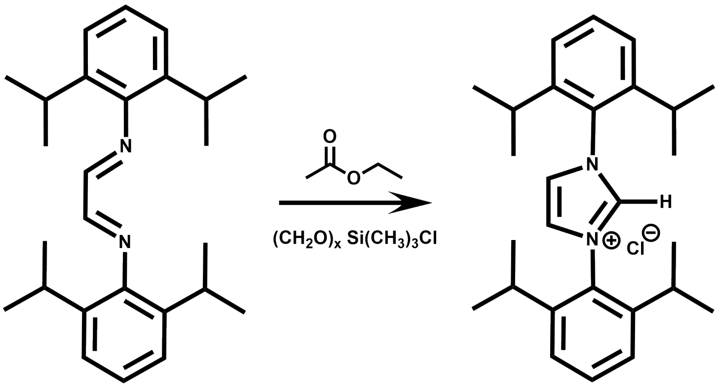

Figure 4.2.: Reaction of N,N'-bis(2,6-diisopropylphenyl)ethanediimine with paraformaldehyde to form 1,3-bis-(2,6-diisopropylphenyl)imidazoliumchlorid. Based on ref.[153].

Together with copper(I) chloride and potassium tert-butoxide the previously synthesized imidazolium salt is dissolved in tetrahydrofuran and stirred at room temperature. The solvent is then removed, taken up in dichloromethane, and filtered over celite and precipitated with hexane. The remaining product is chloro[1,3-bis(2,6-diisopropylphenyl)imidazol-2-ylidene]copper(I) (see Figure 4.3).

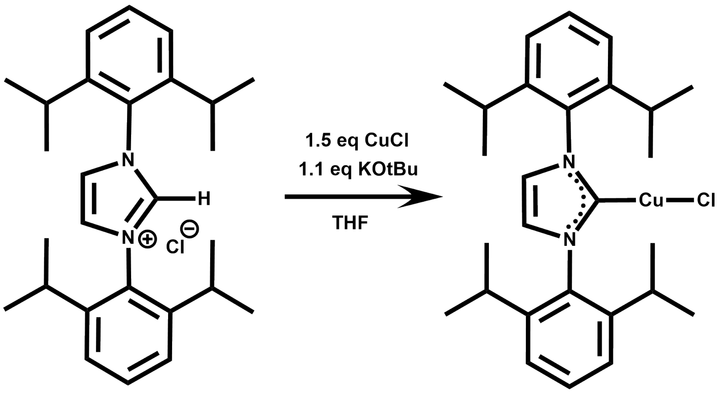

Figure 4.3.: Reaction of 1,3-bis-(2,6-diisopropylphenyl)imidazoliumchlorid with copper(I) chloride to form chloro[1,3-bis(2,6-diisopropylphenyl)imidazol-2-ylidene]copper(I). Based on ref.[153].

The product obtained in the previous step is combined with silver tetrafluoroborate and 2-picoline (2-methylpyridine) in tetrahydrofuran. As a result the silver chloride precipitates and by the addition of hexane, the desired copper carbene [1,3-bis(2,6-diisopropylphenyl)imidazol-2-ylidene]-(2-picoline)copper(I) is obtained in a yield $> 90\%$.[40,152]

5. Results

In this chapter, the results that were obtained in the course of this thesis are presented. The chapter consists of two sections (section 5.1 and section 5.2) each dealing with the photophysical investigation of a copper(I) carbene complex. As the motivations for the study of the complexes differ to some extent, in each section a separate introduction and discussion part are given.

Besides minor changes, such as layout and abbreviations for the compounds, section 5.1 is a reprint from the publication [40], by the same author as the author of this thesis.

5.1. [1,3-bis(2,6-diisopropylphenyl)imidazol-2-ylidene]-(2-picoline)copper(I) tetrafluoroborate

This section is about the photophysical characterization of [1,3-bis(2,6-diisopropylphenyl)-imidazol-2-ylidene]-(2-picoline)copper(I). For reasons of simplicity, it is referred to as NHCCuPy in the following. The motivation and background, including previous reports on the complex, are given in subsection 5.1.1. It is followed by the steady-state UV/Vis absorption and emission as well as time-resolved UV/Vis absorption characterization of the complex.

Parts of the steady-state UV/Vis absorption and emission measurements were conducted by Jennifer Kremper in the course of her bachelor thesis under the supervision of the author of this thesis. Emission measurements obtained using the fluorescence Kerr gate instrument were conducted by Mahbobeh Morshedi. Nanosecond transient absorption measurements were conducted by Wiebke Haselbach. Quantum chemical calculations were conducted by Jasper Guhl (Institute of Theoretical Chemistry and Computer Chemistry, Prof. C. M. Marian). NHC-CuPy was synthesized and characterized[1] by Philipp Schmeinck (Institute of Organometallic Chemistry, Prof. C. Ganter). The majority of figures and paragraphs of text in this section are reprinted from an open-access publication (by the authors mentioned above including the author of this thesis) covering this exact topic. [40]

---

[1] The respective characterization is found in the appendix A.1 as well as in ref. [40].

5.1.1. Introduction

Initially, the complex NHCCuPy, which bears an N-heterocyclic carbene (NHC) ligand (1,3-bis(2,6-diisopropylphenyl)imidazol-2-ylidene) as a σ-donor and 2-picoline (2-methylpyridine) as a π-acceptor ligand (see Figure 5.1), was designed as a potential TADF emitter. Studies by Liske et al. and Föller et al. demonstrated that no such behavior is observed.[152,154] Instead, the complex shows a drastic dependence on its surroundings with regard to the emission properties. As a powder and embedded in poly(methyl methacrylate) (PMMA) matrix, it exhibits emission quantum yields of up to 0.87. In single crystals and solutions of the compound, the yields are orders of magnitudes smaller. Quantum chemical computations attribute this to the presence (luminescence) or absence (no luminescence) of the coordinating counterion BF_4^-. In the complex with coordinated BF_4^-, the lowest excited state is an emissive state with a metal-to-ligand charge-transfer (MLCT) character. In absence of BF_4^-, a dark locally excited triplet state is the lowest one.[154] Heretofore, the excited state kinetics of the complex have only been traced in solid state. Here, this is augmented by time-resolved spectroscopy in solution covering a time range of 100 fs to 10 μs.

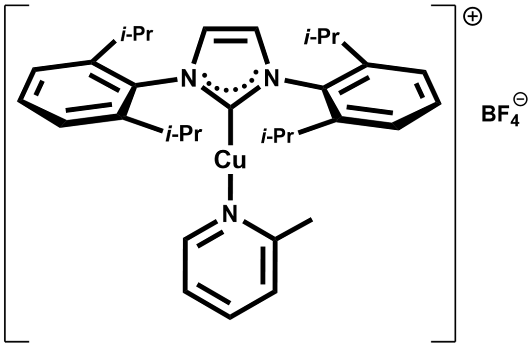

Figure 5.1.: Structure of NHCCuPy; Figure from ref.[40].

As the complex NHCCuPy has the tendency to bind additional ligands and to connect with earlier experiments,[152] it was intended to study the complex in the non-coordinating solvent dichloromethane (DCM). Yet, in femtosecond experiments on the complex dissolved in DCM and on neat DCM, the formation of a white precipitate was observed. During screening for suitable solvents, pronounced changes in the absorption spectrum of NHCCuPy in weakly coordinating solvents like acetonitrile (MeCN) and 2-propanol were observed. In the course of steady state and time-resolved UV/Vis experiments, further indications for the interaction of

NHCCuPy with MeCN and 2-propanol were observed. Based on these experimental observations, two structures that might form in the presence of coordinating solvents are suggested and their spectral properties are computed quantum chemically. No study has yet discussed the coordinating interaction of linearly coordinated copper(I) complexes with solvent molecules in depth. Therefore, the findings of this study constitute an important step towards elucidating the structural interactions of linearly coordinated complexes with a solvent environment. However, due to experimental and quantum chemical ambiguities, it is refrained from giving a distinct answer to which species is present. In 2,2,2-trifluoroethanol (TFE) the absorption signatures of NHCCuPy resemble the ones in DCM. Therefore, for the characterization of the complex in non-coordinating surroundings, TFE was used. Furthermore, emission spectroscopy was applied giving indications for coordinating interactions of the counterion BF_4^- with the copper center in non-coordinating solvents.

5.1.2. Spectroscopic Characterization in Coordinating- and Non-Coordinating Solvents

5.1.2.1. On the Vibrational Progression Observed in UV/Vis Absorption Spectra

NHCCuPy dissolved in DCM, TFE, MeCN, and 2-propanol features an absorption band lowest in energy with a maximum around 260 nm (see Figure 5.2 and A.2 in the appendix). The band is strongly affected by the solvent. In DCM, the highest peak absorption coefficient (≈ 18000 $M^{-1}cm^{-1}$) is recorded and the band is structureless. The spectrum of NHCCuPy in TFE resembles the one in DCM. For MeCN and 2-propanol as solvents, the absorption is blue-shifted compared to DCM. Furthermore, peak absorption coefficients are smaller and a vibrational progression becomes discernable. This progression is very similar to the one of the free 2-picoline ligand (see Figure 5.2).

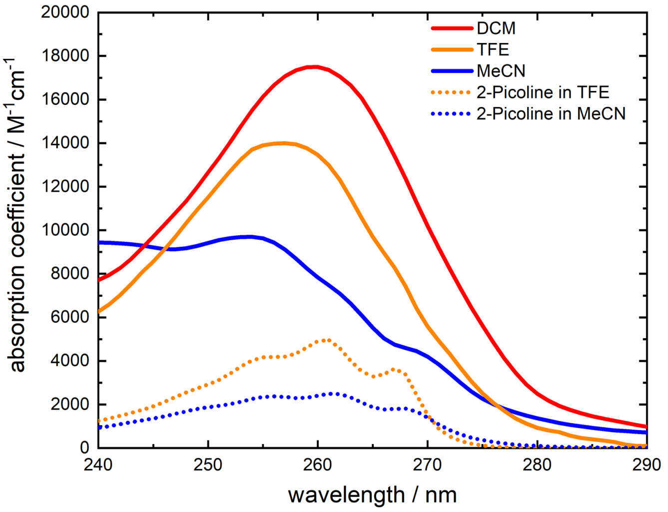

Figure 5.2.: Absorption spectra (absorption coefficients as a function of wavelength) of NHCCuPy in DCM (red), TFE (orange), and MeCN (blue). The respective spectra of 2-picoline in TFE and MeCN (orange and blue dotted respectively) are shown for comparison. Figure adapted from ref.[40].

These differences might originate from a "simple" solvatochromic effect or from a chemical reaction with the solvent (e.g. coordination). A titration experiment favors the latter interpretation (see Figure 5.3a). For very low MeCN concentrations, the spectrum of NHCCuPy in DCM is recorded. Upon MeCN addition the absorption decreases between 255 nm and 280 nm and increases beyond that region. Clear isosbestic points are seen at 255 nm and 280 nm. Singular value decomposition shows that only two singular values are necessary to describe the behavior. This and the isosbestic points suggest an equilibrium of two species.

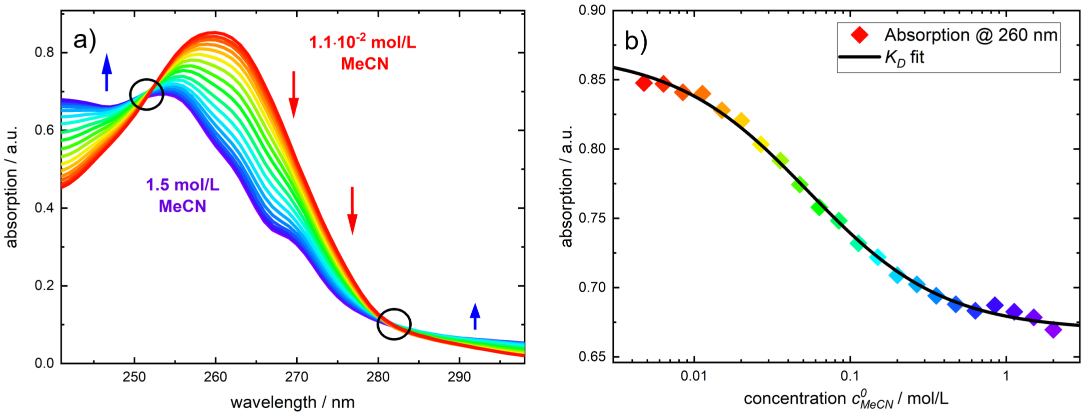

Figure 5.3.: Titration experiment on NHCCuPy a) Impact of the addition of MeCN to absorption spectra of NHCCuPy dissolved in DCM. The initial concentration c_1^0 of NHCCuPy amounted to $5 \cdot 10^{-5}$ M and remains constant throughout the experiment. Initial MeCN concentrations c^0_{MeCN} ranged from $0.8 \cdot 10^{-2}$ M (red) to 2 M (blue). Circles mark isosbestic points. b) Dependence of the absorption at 260 nm on the initial concentration of MeCN c^0_{MeCN} (values from Figure 5.3a). The diamonds mark experimental values, the line a fit as described in the text based on eq 5.1 - 5.4. Figure adapted from ref.[40].

To quantify the chemical equilibrium, a fit of the concentration dependence based on eq. 5.1 - 5.4 was performed. In this treatment, the addition of one equivalent of MeCN is assumed.

$$K_D = \frac{c_{NHCCuPy} \cdot c_{MeCN}}{c_{NHCCuPy-MeCN}} \tag{5.1}$$

$$c_{NHCCuPy} + c_{NHCCuPy-MeCN} = c^0_{NHCCuPy} \tag{5.2}$$

$$c_{MeCN} + c_{NHCCuPy-MeCN} = c^0_{MeCN} \tag{5.3}$$

$$A = (\epsilon_{NHCCuPy-MeCN} \cdot c_{NHCCuPy-MeCN} + \epsilon_{NHCCuPy} \cdot c_{NHCCuPy}) \cdot d \tag{5.4}$$

In these equations, K_D is the dissociation constant of NHCCuPy coordinated by MeCN (NHCCuPy-MeCN). $c_{NHCCuPy}$, c_{MeCN}, and $c_{NHCCuPy-MeCN}$ are the equilibrium concentrations of NHCCuPy, MeCN, and the MeCN coordinated complex NHCCuPy-MeCN, respectively. $c^0_{NHCCuPy}$ and c^0_{MeCN} are the initial concentrations of NHCCuPy and MeCN (prior to equilibration). The absorption A depends on the concentrations $c_{NHCCuPy}$ and $c_{NHCCuPy-MeCN}$ and the respective absorption coefficients $\epsilon_{NHCCuPy}$ and $\epsilon_{NHCCuPy-MeCN}$ as well as the path length $d = 1$ cm. A fit based on these equations provides a good description of the experimental behavior at 260 nm (see Figure 5.3b). During this fit only two parameters were varied, namely the dissociation constant K_D and the absorption coefficient of NHCCuPy-MeCN. According to this fit, the dissociation constant K_D equals 0.05 ± 0.006 M and $\epsilon_{NHCCuPy-MeCN}$ equals 13415 ± 33 M^{-1}cm^{-1}. This absorption coefficient determined by fitting is larger than the one obtained experimentally for NHCCuPy in pure MeCN. This is rationalized by the different solvents. In the case of the titration experiment the solvent is DCM, in the other case it is MeCN. An analysis based on the assumption that NHCCuPy binds two equivalents of MeCN and releases one equivalent of 2-picoline was also performed (see Figure 5.4 and Figure 5.5 and eq. 5.5 - 5.8).

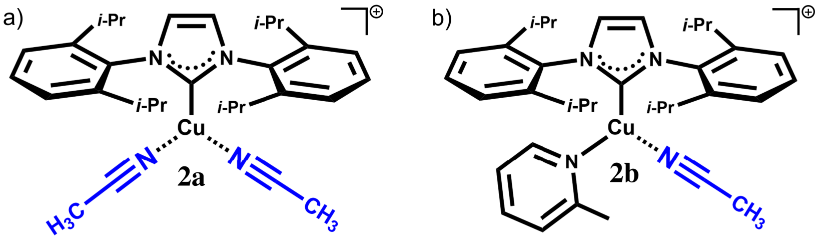

Figure 5.4.: Proposed structures of NHCCuPy in MeCN with a) two MeCN molecules replacing one 2-picoline (**2a**) b) one MeCN coordinating to NHCCuPy forming the trigonal complex **2b**. Figure from ref.[40].

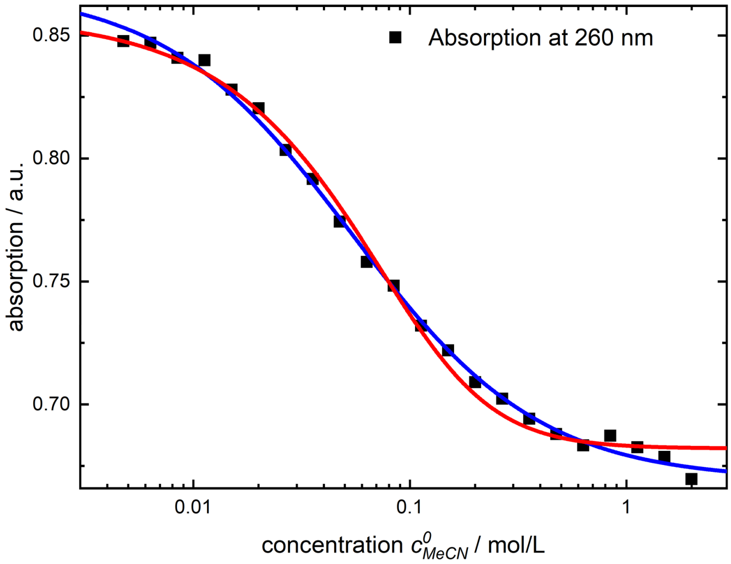

Figure 5.5.: Dependence of the absorption at 260 nm on the initial concentration of MeCN c^0_{MeCN} (values from Figure 5.3 a)). The squares mark experimental values, the red line a fit as based on eq. , the blue line a fit as based on eq. 5.1 - 5.4 (section 5.1). For concentrations c^0_{MeCN} between 0.01 and 0.1 mol/L and beyond 1 mol/L the fit (red, eq. 5.5 - 5.8) overestimates experimental values, for c^0_{MeCN} between 0.1 and 1 mol/L experimental values are underestimated. Figure from SI of ref[40].

$$K_D = \frac{c_{NHCCuPy} \cdot c^2_{MeCN}}{c_{NHCCuPy-2MeCN} \cdot c_{2-picoline}} \tag{5.5}$$

$$c_{NHCCuPy} + c_{NHCCuPy-2MeCN} = c^0_{NHCCuPy} \tag{5.6}$$

$$c_{MeCN} \approx c^0_{MeCN} \tag{5.7}$$

$$\begin{aligned} A = (&\epsilon_{NHCCuPy-2MeCN} \cdot c_{NHCCuPy-2MeCN} + \\ &\epsilon_{NHCCuPy} \cdot c_{NHCCuPy} + \epsilon_{2-picoline} \cdot c_{2-picoline}) \cdot d \end{aligned} \tag{5.8}$$

The fit that is applied in Figure 5.5 is based on eq. 5.5 - 5.8. In these equations, K_D is the dissociation constant of NHCCuPy coordinated by two molecules of MeCN (NHCCuPy-2MeCN). $c_{NHCCuPy}$, c_{MeCN}, $c_{NHCCuPy-2MeCN}$, and $c_{2-picoline}$ are the equilibrium concentrations of compound NHCCuPy, MeCN, and the complex NHCCuPy-2MeCN. $c^0_{NHCCuPy}$ and c^0_{MeCN} are the initial concentrations of NHCCuPy and MeCN (prior to equilibration). The absorption A depends on the concentrations $c_{NHCCuPy}$, $c_{NHCCuPy-2MeCN}$, and $c_{2-picoline}$ and the respective absorption coefficients $\epsilon_{NHCCuPy}$, $\epsilon_{NHCCuPy-2MeCN}$, and $\epsilon_{2-picoline}$ as well as the path length $d = 1$ cm. During this fit three parameters were varied, namely the dissociation constant K_D, the absorption coefficient of NHCCuPy-2MeCN $\epsilon_{NHCCuPy-MeCN}$, and the absorption coefficient for 2-picoline in DCM $\epsilon_{2-picoline}$. According to this fit the dissociation constant K_D equals 148 M, the absorption coefficient for 2-picoline in DCM $\epsilon_{2-picoline}$ 1201 M^{-1}cm^{-1}, and the absorption coefficient of for the hypothetical complex with two MeCN molecules $\epsilon_{NHCCuPy-2MeCN}$ 12784 M^{-1}cm^{-1}.

The respective diagram (Figure 5.5) reveals systematic deviations between experimental results and the fit. Thus, the addition of one equivalent is favored. Similar observations were made for a titration experiment using 2-propanol as a solvent for NHCCuPy. The titration experiment and respective fitting (based on one equivalent of 2-propanol) yield a K_D value of ≈ 2 M (see appendix, Figure A.2). This indicates a less favored reaction of NHCCuPy with 2-propanol compared to MeCN.

The titration experiments show that NHCCuPy and MeCN react to form a novel complex. Experiments with NHCCuPy and 2-picoline have revealed the tendency of NHCCuPy to transform into a trigonal complex with two ligands in addition to the NHC ligand.[152] In the present context, two MeCN molecules might coordinate (Figure 5.4, structure **2a**) and replace the 2-picoline ligand. Alternatively, one MeCN molecule might additionally coordinate to the Cu atom in complex NHCCuPy, leading to the trigonal planar species **2a** (see Figure 5.4). In order to better understand which species are present, it was attempted to synthesize and investigate the bis-acetonitrile complex **2a** by performing the synthetic procedure for NHCCuPy without adding 2-picoline and replacing the solvent THF with MeCN. However, all attempts to obtain **2a** in analytically pure form failed due to its instability. In solution, it undergoes a rapid conversion to the bis(NHC) copper(I) tetrafluoroborate and presumably one equivalent of tetrakis(MeCN)-copper(I) tetrafluoroborate as depicted in Figure 5.6. The former one can be detected by ^{1}H-NMR-spectroscopy and ESI mass spectrometry (see Figure A.3 in the appendix). However, this finding indicates that **2a** cannot be present in significant concentrations in the solution of NHCCuPy in MeCN, since its conversion products are not observed in those solutions. Based on this argument together with the results from the titration experiment (see Figure 5.3), it is assumed that compound **2b** is the only other species present in the solution of NHCCuPy in MeCN under the given conditions.

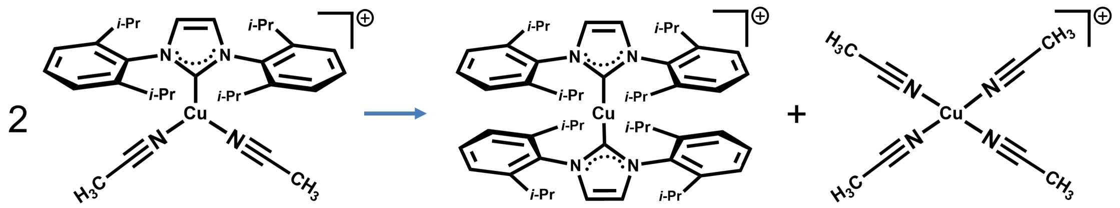

Figure 5.6.: Reaction scheme on the instability of **2a** forming bis(NHC) copper(I) tetrafluoroborate and tetrakis(MeCN)-copper(I) tetrafluoroborate.

5.1.2.2. Solvent Dependent Emission

Also, the emission spectra of NHCCuPy are solvent dependent (see Figure 5.7). In MeCN it exhibits a maximum of emission around 350 nm while in the non-coordinating solvents, the emission curves show a maximum of around 500 nm in line with previous measurements of NHCCuPy in PMMA films.[152] Contrary to the measurement in PMMA in which the luminescence quantum yield is 0.87,[152] NHCCuPy in MeCN solutions features an apparent quantum yield of approximately 10^{-5}. It is worth mentioning that the emission maximum of NHCCuPy in MeCN is similar to that of 2-picoline in MeCN (328 nm and 324 nm respectively; see Figure A.4 in the appendix). For identical absorption at the excitation wavelength, the emission signal of NHCCuPy dissolved in MeCN amounts to ≈ 0.03 of the 2-picoline signal. Assuming that in MeCN one equivalent of 2-picoline would be released if **2a** was formed (see above) and accounting for inner filter effects one would expect a reduction by 0.3. Thus, also emission spectroscopy disfavors the presence of compound **2a**.

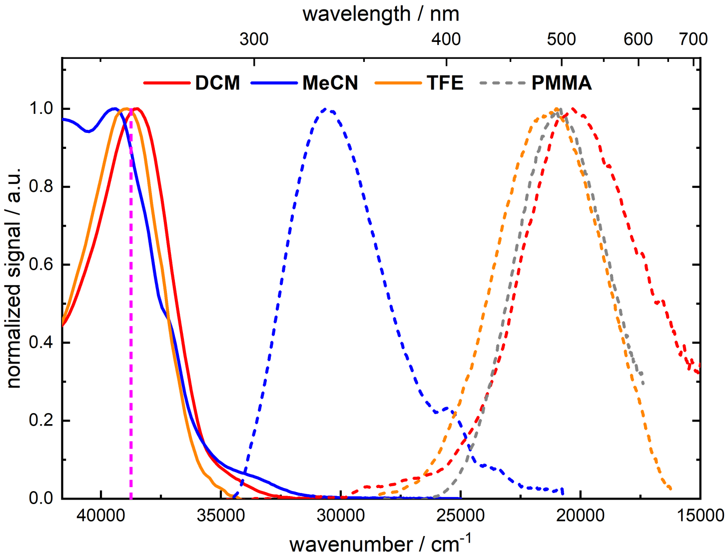

Figure 5.7.: Emission spectroscopy on NHCCuPy in different solvents and PMMA. Normalized absorption spectra (solid lines) and emission spectra (dashed lines) are shown for NHCCuPy in DCM (smoothed, red), TFE (smoothed, orange), MeCN (smoothed; blue), and PMMA (grey). For the recording of the emission spectra, the excitation wavelength was set to 260 nm as marked as a magenta vertical line in the absorption spectra. Due to the low overall signal level and the diminishing spectral sensitivity between 600 and 700 nm, the shape of the emission spectra, there might deviate from the "true" form. Figure from ref. [40].

Earlier studies on NHCCuPy as a powder had suggested that the emission of NHCCuPy is mostly due to a species in which the counterion BF_4^- interacts with NHCCuPy. To check whether this is also responsible for the emission in solution, spectra as a function of the BF_4^- concentration were recorded (see Figure 5.8).

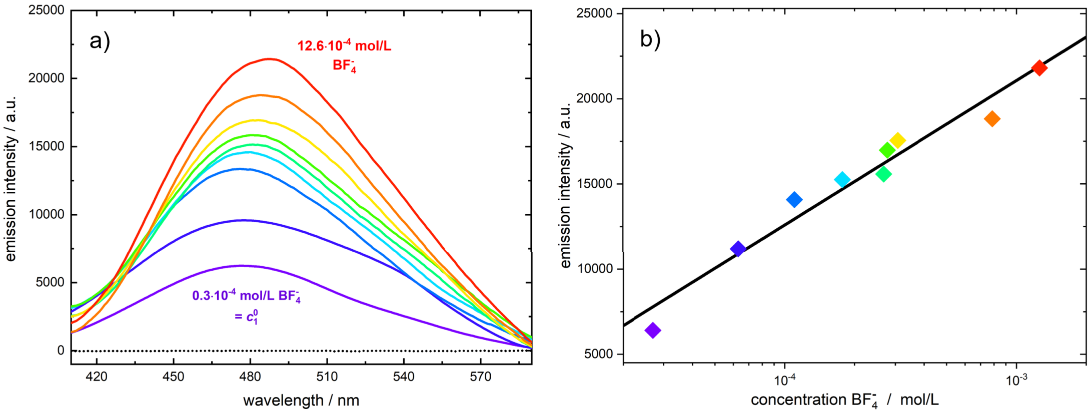

Figure 5.8.: Impact of the addition of BF$_4^-$ salt to the emission spectra of NHCCuPy dissolved in DCM. a) Emission spectra of NHCCuPy in DCM solution with an increasing amount of counterion BF$_4^-$ ranging from $0.3 \cdot 10^{-4}$ M (purple; equals the initial concentration of NHCCuPy) to $12.6 \cdot 10^{-4}$ M (red). Tetrabutylammonium tetrafluoroborate was used as BF$_4^-$ salt. Attempts to record an emission spectrum of a tetrabutylammonium tetrafluoroborate DCM solution under identical conditions resulted in a signal of essentially zero as depicted by the black dotted line. b) Plot of the emission intensity dependence on the concentration of BF$_4^-$ ions (values from Figure 5.8 a)). Figure from ref.[40].

It is clearly visible that the emission increases with the addition of the counterion BF$_4^-$. This suggests that as in solid state and polymer matrices the interaction of NHCCuPy with BF$_4^-$ increases the luminescence.[152] Furthermore, comparing the apparent quantum yield of luminescence of NHCCuPy in DCM ($\Phi_{lum} \approx 10^{-5}$) with NHCCuPy in PMMA ($\Phi_{lum} \approx 0.87$[152]) it can be derived that only a small amount of NHCCuPy is present as luminescent BF$_4^-$ coordinated complex (see Figure 5.9). The increase of the emission signal with BF$_4^-$ concentration does not saturate in the accessible range. Therefore, no dissociation constant K_D and emission quantum yield for the NHCCuPy–BF$_4^-$ complex can be derived.

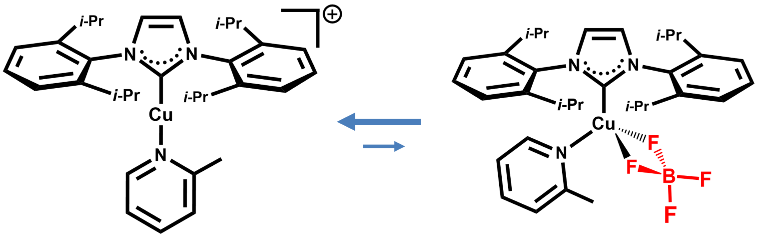

Figure 5.9.: Equilibrium between BF$_4^-$-coordinated and uncoordinated species of NHCCuPy in non-coordinating solvents. The equilibrium is expected to be predominantly on the linear species (left). Figure from ref.[40].

5.1.2.3. Time-Resolved Spectroscopy in Non-Coordinating and Coordinating Solvents

Time-resolved UV/Vis absorption spectroscopy was conducted using femtosecond (100 fs – 3 ns) as well as nanosecond (100 ns – 10 μs) transient absorption techniques. The combined results from both techniques for NHCCuPy in TFE are shown as contour plots in Figure 5.10. Due to the aforementioned difficulties with DCM and 266 nm laser pulses, here, results are only shown for TFE as a solvent. However, one successful scan on NHCCuPy dissolved in DCM reveals very similar spectro-temporal signatures as NHCCuPy dissolved in TFE (see appendix, Figure A.5). This further underlines DCM and TFE are both non-coordinating.

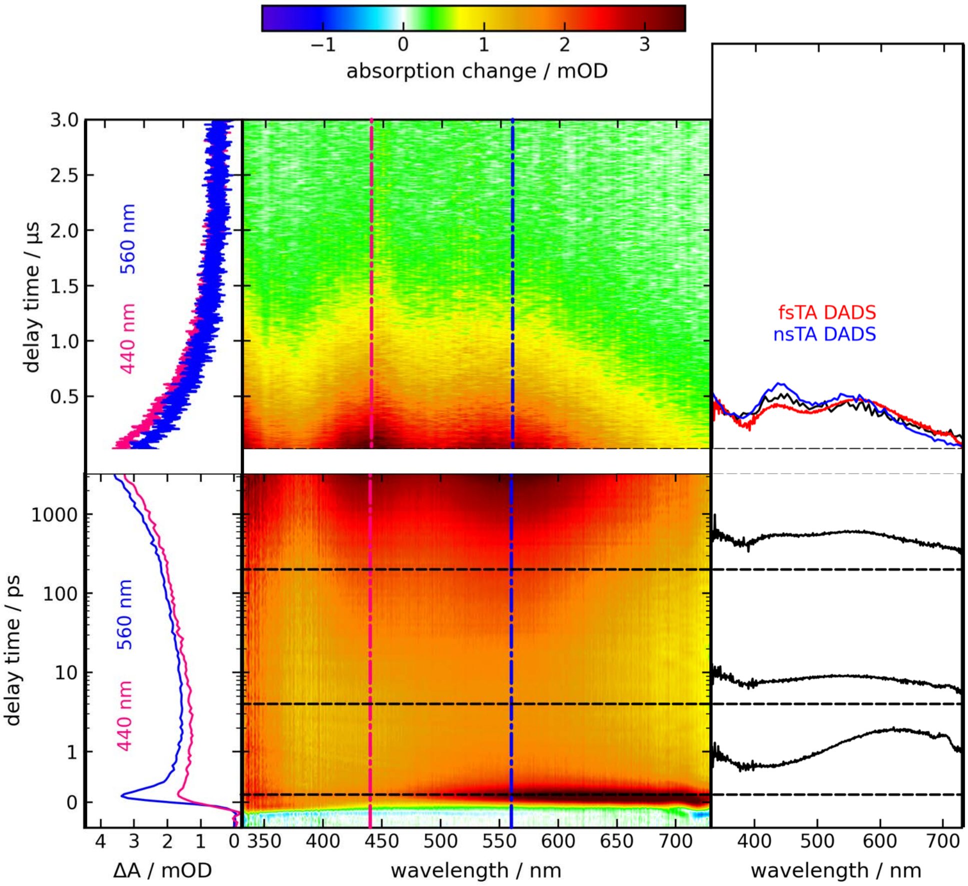

Figure 5.10.: Time-resolved spectroscopy signals acquired for NHCCuPy in TFE. The excitation was tuned to 266 nm. In the contour representation (central), the difference absorption signal is color-coded. Vertical lines mark spectral positions for the time traces plotted on the left while horizontal lines mark certain delay times for the difference spectra plotted on the right. The last decay-associated difference spectrum (DADS) from the fsTA experiment is compared to the DADS obtained from the nsTA experiment. Figure from ref.[40].

Negative signal contributions originating from stimulated emission (SE) or ground state bleach (GSB) are not observed and throughout the whole time frame and for all wavelengths, positive signals of excited state absorption (ESA) are detected. Directly after photoexcitation, a strong ESA signal covering the complete detection range shows maxima at ≈ 350 and 620 nm. Within less than one picosecond this signature gives way to one which is essentially flat with a shallow maximum at ≈ 550 nm. On a time scale of ≈ 1 ns, the fsTA signal is seen to rise. In the course of this rise a difference spectrum with peaks at ≈ 350, 450, and 550 nm forms. This distinctive pattern also appears in the nsTA experiment. This experiment reveals a microsecond lifetime for the carrier of this signature. "Late" femtosecond and "early" nanosecond spectra overlay favorably. This indicates that no kinetic component is missed due to the gap in the temporal coverage between 4 – 100 ns.

A global fit analysis was performed on the data to evaluate the kinetics of NHCCuPy. The data are fitted satisfactorily using three time constants, with $\tau_1 = 0.3$ ps, $\tau_2 = 900$ ps, $\tau_3 = 0.68$ μs. The resulting decay-associated difference spectra (DADS$_{1-3}$) are shown in Figure 5.11. Additionally, the DADS for an 'infinite' delay time, accounting for the remaining signature in the fsTA experiment at a delay time of ≈ 4 ns, is compared with the DADS resulting from the decay observed in the nsTA experiment. The similarity of these spectra confirms the above statement that no process is missed due to the temporal gap.

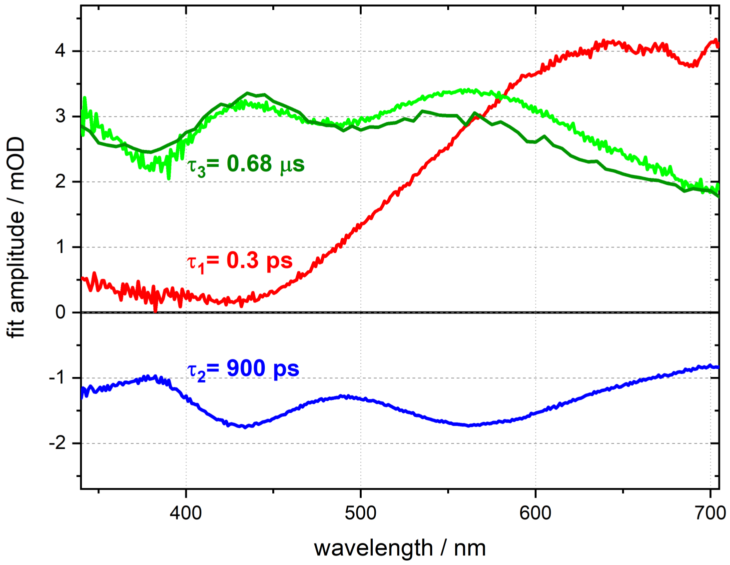

Figure 5.11.: Decay-associated difference spectra obtained from the fsTA and nsTA experiments of NHCCuPy in TFE. The bright green line shows the DADS for an infinite delay time from fsTA experiment, dark green shows the DADS for the time constant from the nsTA experiment of $\tau_3 = 0.68$ μs. Figure from ref.[40].

The respective DADS$_1$ shows a weak positive amplitude around 350 nm and a minimum around 450 nm followed by a rise for longer wavelengths peaking at 650 nm. Those positive amplitudes reveal a decay of the ESA signal, indicating that a transient species with strong absorption at 650 nm deactivates into a state that shows less absorption. As the transient spectra between 1 and 100 ps are almost without any features, contributions from a rising signal are absent. The DADS$_2$ is negative throughout the complete spectral range. It, thus, describes a spectrally broad signal rise. Minima at ≈ 350, 430, and 560 nm coincide with the maxima in the DADS$_3$. Thus, the buildup of a species is described. The DADS$_3$ describes the decay of this species presumably to the ground state. Comparable kinetics are observed for NHCCuPy in DCM. The respective results of the global fit analysis and respective DADS$_{1-3}$ are shown in Figure A.6 in the appendix.

Femtosecond and nanosecond time-resolved experiments were also performed on NHCCuPy dissolved in MeCN (see Figure 5.12). As for the time-resolved experiments of NHCCuPy in TFE or DCM no negative signal contributions are observed. However, the spectro-temporal behavior of NHCCuPy in MeCN is very distinct from the one of NHCCuPy in TFE or DCM. Right after excitation, two broad ESA bands are observed. One peaks around 330 nm, the other one at ≈ 650 nm. In contrast to the feature at 330 nm, which shows a slower decay of around 10 ps, the broad band at ≈ 650 nm decays within picoseconds. Another ESA band peaking at 440 nm appears around 100 ps. This band decays together with the band at 330 nm into a slightly less pronounced ESA feature. The decay of this signature is then observed in the nsTA experiment. Again, "late" femtosecond and "early" nanosecond spectra overlay favorably indicating that no kinetic component is missed due to the gap in the temporal coverage between 4 – 100 ns.

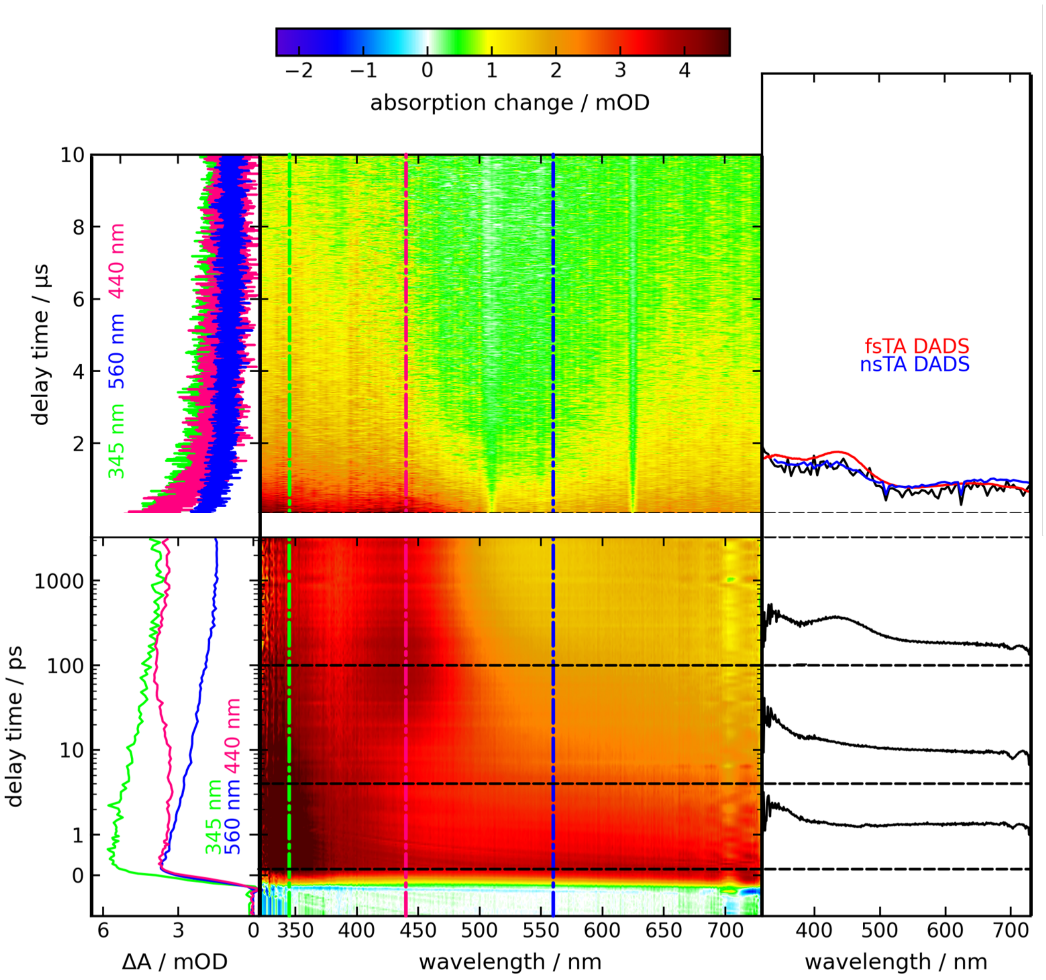

Figure 5.12.: Time-resolved spectroscopy signals acquired for NHCCuPy in MeCN. The excitation was tuned to 266 nm. In the contour representation (central), the difference absorption signal is color-coded. Vertical lines mark spectral positions for the time traces plotted on the left while horizontal lines mark certain delay times for the difference spectra plotted on the right. The last decay-associated difference spectrum (DADS) from the fsTA experiment is compared to the only DADS received from the nsTA experiment. Figure from ref. [40].

In a global analysis, data could be fitted satisfactorily using four time constants with $\tau_1 = 2.6$ ps, $\tau_2 = 40$ ps, $\tau_3 = 235$ ps, and $\tau_4 = 2.5$ μs. Respective DADS$_{1-4}$ are shown in Figure

5.13. The first DADS$_1$ only bears positive amplitudes indicating that a positive transient absorption signal is decreasing with the respective time constant of 2.6 ps. For the band peaking at ≈ 700 nm, the transient absorption signal decrease is more pronounced than for the one at 330 nm. This indicates that the subsequent species, which forms with τ_1 and decays with $\tau_2 = 40$ ps, shows higher transient absorption in the region below 500 nm and less above 500 nm as it is seen for the respective spectrum around 5-10 ps. The DADS$_2$ shows a distinct minimum at 450 nm. This minimum mirrors a maximum in the DADS$_3$ and thus indicates a rise due to the formation of another species. DADS$_3$ shows a maximum at 450 nm and a signal close to zero at ≈ 650 nm. Although the transient spectra look quite similar for 100 ps and 3 ns, this indicates that except for the region at around 600 nm there is a change in absorption between the third and fourth temporal feature mostly at ≈ 450 nm. The last DADS$_4$ eventually shows maxima at 350, 440, and 650 nm. Further, it bears the highest amplitudes on the complete detection range compared to DADS$_{1-3}$. The DADS$_4$ describes the decay of the last transient species being present presumably to the ground state.

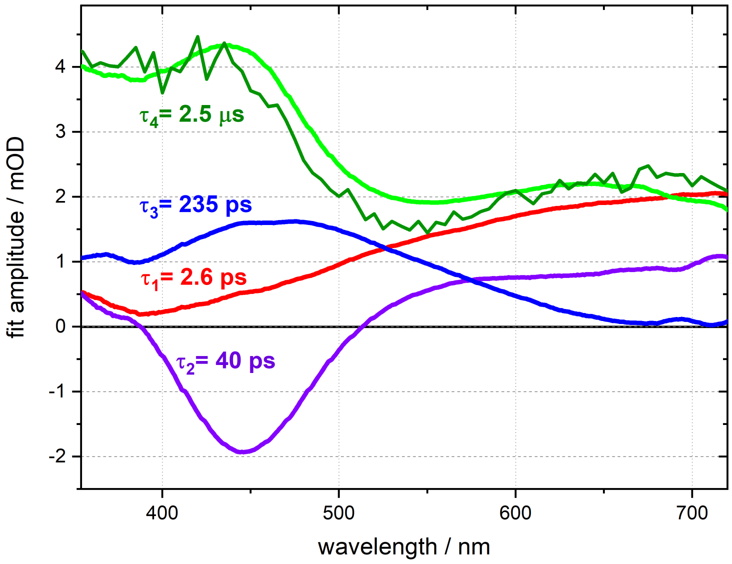

Figure 5.13.: Decay-associated difference spectra obtained from fsTA and nsTA experiment of NHCCuPy in MeCN. The bright green line shows the DADS for an infinite delay time from fsTA experiment, dark green shows the DADS for the sole decay time constant of the nsTA experiment of $\tau_4 = 2.5\ \mu$s. Figure from ref.[40].

5.1.2.4. Quantum Chemical Calculations

The spectroscopic experiments have indicated clearly that NHCCuPy reacts with coordinating solvents like MeCN. The product of this coordination was suggested to adopt structures **2a** or **2b**. In the following, quantum chemically computed absorption coefficient spectra of these species are compared with the experimental ones. Further, the absorption coefficient spectrum obtained by subtracting the one of 2-picoline from the one of NHCCuPy in MeCN ($\epsilon_{NHCCuPy-MeCN}(\lambda)-\epsilon_{2-picoline}(\lambda)$) is shown as a hypothetical experimental spectrum for **2a** assuming the quantitative formation of **2a** for NHCCuPy in MeCN (see Figure 5.14). Computed geometrical parameters are summarized in the appendix (see Table A.1 to A.14).

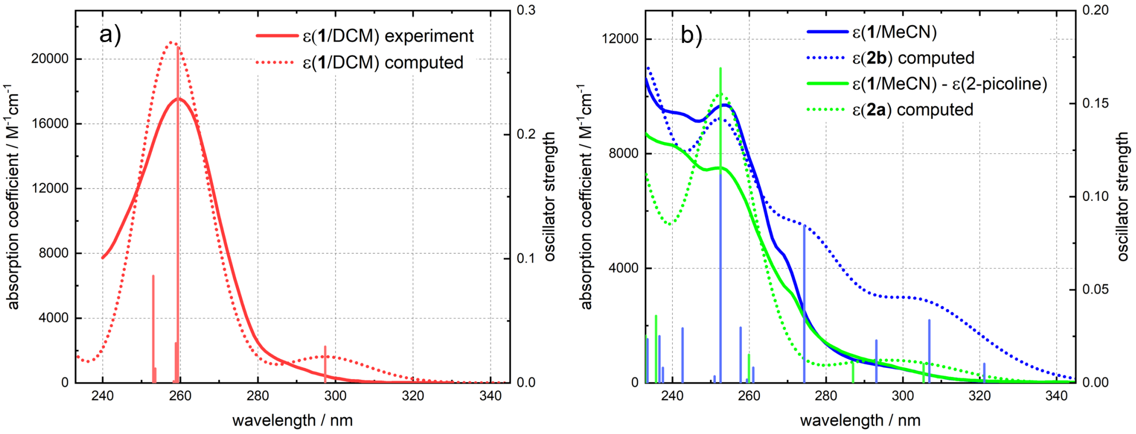

Figure 5.14.: Comparison of calculated UV/Vis absorption coefficient spectra (dashed lines, left y-axis), including the oscillator strengths of each transition (vertical lines, right y-axis) of NHCCuPy, **2a** and **2b** with experimental spectra (solid lines) of a) NHCCuPy in DCM (red), b) NHCCuPy in MeCN (blue) and a hypothetical spectrum of **2a** that is obtained by subtracting the absorption coefficient spectrum of NHCCuPy in MeCN by the one of 2-picoline ($\epsilon_{NHCCuPy-MeCN}(\lambda)-\epsilon_{2-picoline}(\lambda)$). Figure from ref.[40].

From the three species considered, compound NHCCuPy in DCM shows the highest agreement with the experimental spectrum with regard to their spectral shape and signal strength. In DCM (Figure 5.14a), it is expected that NHCCuPy is present in a linear geometry with little interaction between complex and solvent. The weak band with a maximum of around 300 nm in the computed spectrum arises from the S_1 absorption at the S_0 equilibrium geometry. Earlier work revealed, however, that the spectral position of this transition experiences a blue shift and its oscillator strength diminishes when the torsional angle between the two ligands is increased.[154] Sampling of the torsional conformations is therefore expected to bring the red edge of the computed spectrum into better agreement with the experimental spectrum, which features a shoulder in the long wavelength regime. Similar considerations apply to the low-energy bands of the trigonal complexes **2a** and **2b** in acetonitrile as solvent. As can be seen in Figure 5.14b, the experimentally observed absorption maximum at 254 nm is well reproduced by the calculations for both, **2a** and **2b**. However, more or less pronounced discrepancies between experimental and calculated spectra are observed for the spectral regions at higher or lower wavelengths than 254 nm for both structures. Thus, an unequivocal decision of which of the two species **2a** or **2b** is present cannot be made on this basis.

Furthermore, the change in total energy of **2b** in DCM relative to the linear complex NHC-CuPy in DCM and a distant MeCN molecule was calculated. In DCM, a slightly positive energy value of 1.0 kJ/mol was found, which signals a thermally neutral addition within chemical accuracy. This is in line with the weak binding affinity, i.e. large K_D value. The coordinative bonding of MeCN to the copper center leads to a marked weakening of the Cu-N(2-picoline) bond in the electronic ground state. This is reflected in an elongation of this bond from 190 pm to 202 pm. In MeCN solution, the addition of MeCN is also slightly endothermic with a calculated energy of 1.9 kJ/mol.

The stability of **2b** with respect to the ejection of the MeCN ligand was also investigated (see Figure 5.15). The lowest excited states of **2b**, the S_{MLCT}/T_{MLCT} are 48.0/50.7 kJ/mol more favorable than their counterparts for NHCCuPy. The energy gain is, however, not reflected in a stronger Cu-N(nitrile) bond. Electron density is transferred into an antibonding Cu-MeCN orbital (see Figure 5.15 and A.7), and the bond is slightly elongated by 2 pm (from 197 to 199 pm). In contrast, the Cu-N(2-picoline) bond length shrinks from 202 pm in the electronic ground state of **2b** to 189/187 pm in the S_{MLCT}/T_{MLCT} states where the copper coordination adopts a nearly T-shaped structure. The corresponding bond lengths of NHCCuPy amount to 185/184 pm in the S_{MLCT}/T_{MLCT} states. With regard to a potential substitution of the 2-picoline ligand by MeCN (formation of structure **2a**), the computations suggest that this is unlikely in the excited state. The Cu-N(2-picoline) bond is strengthened upon excitation.

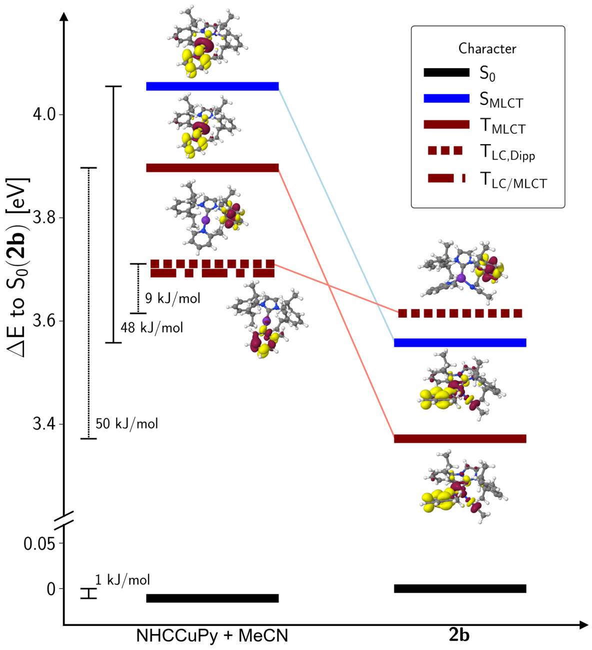

Figure 5.15.: Total adiabatic energies of lowest excited states for complex NHCCuPy and **2b** in DCM relative to the ground state of **2b**. To compare with **2b**, the ground state energy of one MeCN molecule in DCM was added to the energy of complex NHCCuPy. The respective electron difference densities are shown next to each bar. Separately, an enlarged version of the densities is provided in the appendix (Figure A.7). Figure adapted from ref.[40].

Previous examinations had shown that the excited states of NHCCuPy decay from the S_{MLCT} state through a $T_{LC/MLCT}$ intermediate into a local triplet excitation on a diisopropylphenyl (Dipp) moiety.[154] In the present study, the GD3 dispersion correction and a continuum solvation were added, in total increasing the excitation energies. The $T_{LC,Dipp}$ state is affected most by dispersion interactions, lying now almost isoenergetic to the $T_{LC/MLCT}$ state. Yet, solvent coordination affects it to a lesser extent. The $T_{LC,Dipp}$ state is lowered by 9.3 kJ/mol upon MeCN addition, not enough to constitute the adiabatically lowest excited state of the threefold coordinated complex **2b**. The intermediate $T_{LC/MLCT}$ state that is responsible for the efficient ISC from the S_{MLCT} state to the triplet manifold in NHCCuPy, gains MLCT character in **2b** and thus mixes with the T_{MLCT} state. This mixture explains why no minimum structure could be found for the T_2 state of **2b** despite substantial effort. The considerable impact of MeCN addition on the relative energies and geometrical structures of the excited states further corroborates the experimental observations that the steady state and the transient spectra change markedly.

5.1.3. Discussion: Quantum Chemical Assignment and Proposed Photokinetics

Steady-state spectroscopy of NHCCuPy in solution has indicated that NHCCuPy may react with solvent molecules. In non-coordinating solvents like TFE or DCM NHCCuPy, which is linear in its crystal structure,[152] is most likely present in a linear geometry as well. In coordinating solvents like MeCN, experiments show clear indications of a chemical reaction (e.g. coordination) between solvent and complex. Based on joint spectroscopic and quantum chemical data, suggestions on the structure of the complex are given. Furthermore, time-resolved UV/Vis spectroscopy was applied on NHCCuPy in TFE, DCM, and MeCN. In the case of non-coordinating solvents, findings are compared to quantum chemical computations reported here, extending previous reports on NHCCuPy.[154,155] As a result, a consistent picture of the photokinetics of NHCCuPy upon excitation to its longest wavelength absorption maximum is obtained. In both cases (i.e. in coordinating and non-coordinating solvents), NHCCuPy shows involved photokinetics.

From steady-state measurements, clear indications are found for an equilibrium chemical reaction for NHCCuPy in MeCN leading to the potential products **2a** or **2b**. Based upon experimental evidence (vide supra), **2b** is considered to be the species formed in this equilibrium. On the other hand, quantum chemical calculations are not conclusive as to which species is formed.

Considering the electron pair donicity (i.e. Gutmann's donor number (DN)) of 2-picoline and MeCN as a measure for their coordinating affinity[99] with MeCN bearing a value of 14.1 kcal/mol[99] and 3-picoline, 4-picoline as well as pyridine showing values of 39.0, 34.0 and 33.1 kcal/mol respectively,[99,156] one would expect 2-picoline to show a stronger affinity to the copper center than MeCN does. This again favors compound **2b** over **2a**. Quantum chemical calculations revealed that in the ground state, the coordination of MeCN on NHCCuPy is neither favored nor disfavored energetically. This is in line with the large experimental K_D value. In the excited state, the addition is clearly favorable, ruling out the ligand release in the excited state. Due to these ambiguities, a definitive structure cannot be assigned to NHCCuPy dissolved in MeCN.

Steady-state experiments of NHCCuPy in TFE or DCM show that emission occurs at similar wavelengths as in solid or PMMA environments. In those environments a coordinating interaction of the counterion BF_4^- is proposed that gives rise to a high quantum yield of emission ($\Phi_{lum} \approx 0.87$ in PMMA).[152] However, the apparent quantum yield of emission that was determined for NHCCuPy in DCM is in the order of 10^{-5}. Therefore, it is assumed that NHCCuPy in DCM or TFE is mostly present as a linear complex (see Figure 5.9) that shows virtually no emission in solution. The non-coordinating behavior of TFE is considered reasonable due to its low electron pair donicity, expressible with a negligible value of DN.[98] Based on that, it is further concluded that the signatures received from transient absorption measurements in TFE and DCM represent dominantly the linear species of NHCCuPy.

Assuming a consecutive model, a kinetic scheme (see Figure 5.17) is suggested taking into account three observable transient states. Species-associated difference spectra[157] based on this model are depicted in Figure 5.16.

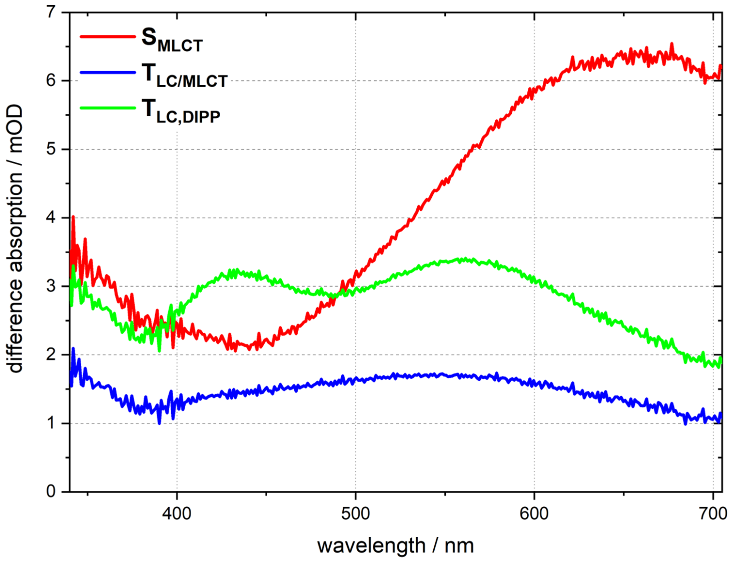

Figure 5.16.: Species-associated difference spectra (SADS) obtained from fsTA experiment of NHCCuPy in TFE. Figure from SI of ref.[40].

As expected for a consecutive model with largely differing time constants, the SADS are essentially identical to difference spectra at specific delay times. The first SADS (i.e. for the S_{MLCT} state) is identical with the spectra at time zero. The second SADS (i.e. for the $T_{LC/MLCT}$ state) is identical with the spectra around a delay time of 10-100 ps, while the third SADS (i.e. for the $T_{LC,Dipp}$ state) is identical with the spectra from 4 ns onwards. Due to the absence of GSB in the transient data, yields for the population of each excited state could not be determined. Thus, the SADS were constructed assuming yields of 100% for each transition.

Assignments of states and processes rely on quantum chemical computations on NHCCuPy. In contrast to previous reports,[154,155] the R2018 Hamiltonian, specially designed for metal complexes, a solvent continuum, and dispersion corrections were used. The latter has a large impact on the molecular geometry, shortening the H$_{Me}$—C$_{Ar,ipr}$ bond lengths from 339 and 362 pm to 313 and 315 pm, respectively. After photoexcitation into the absorption maximum, which is dominantly made up of the $S_2 \leftarrow S_0$ transition, internal conversion (IC) into the S_1 minimum is assumed to be fast and to occur within the time resolution of the instrument (≈ 100 fs). According to DFT/MRCI calculations, the S_1 state is a singlet state with $d_\sigma \rightarrow \pi_{Py}$ MLCT character where Cu d_σ electron density is transferred to the 2-picoline ligand. With regard to the adiabatic energy, four triplet states lie below the S_1 state. Based on this energetic ordering, states are referred to as T_1-T_4 in the following. The T_1 state (3.69 eV) shows both ligand-centered (LC, mainly on the 2-picoline ligand) and MLCT character ($T_{LC/MLCT}$) and constitutes the corresponding triplet state to the S_2 state. States T_2 and T_3 (3.71 eV) originate from excitations localized on the Dipp moieties of the NHC ligand ($T_{LC,Dipp}$) while the T_4 state (3.90 eV) has the same excited state character as the S_1 state (T_{MLCT}). Computed ISC rate constants for the transitions $S_1 \rightarrow T_{1,2,3,4}$ will now be compared with experimental findings. The highest ISC rate constant is observed for the transition to the $T_{LC/MLCT}$ state with a value of $k_{ISC,LC/MLCT} = 5.3 \cdot 10^{11}$ s^{-1}. This rate constant follows from a large spin-orbit coupling between the S_{MLCT} and the $T_{LC/MLCT}$ states. In both excitations, copper d-orbitals are involved. These orbitals differ in magnetic quantum number which is responsible for the large spin-orbit coupling. The second highest ISC rate constant is calculated for the transition to the two states $T_{LC,Dipp}$ with $k_{ISC,LC,Dipp} = 2.1 \cdot 10^8$ s^{-1}, followed by ISC into T_{MLCT} with $k_{ISC,MLCT} = 3.2 \cdot 10^7$ s^{-1}. The computed radiative rate constant k_{rad} of the S_1 state amounts to only $8.4 \cdot 10^6$ s^{-1}. As all ISC rate constants are orders of magnitudes higher, a very small fluorescence quantum yield is expected. This matches the experimental observation. Based on the above ISC rate constants, the $T_{LC/MLCT}$ state owns the highest probability to be populated following S_{MLCT} excitation. The inverse of $k_{ISC,LC/MLCT}$ is 2 ps, which is somewhat larger than the observed time constant τ_1 of 300 fs. According to the computations, the $T_{LC/MLCT}$ state is the lowest triplet state in terms of adiabatic energy. Yet, these computations predict the $T_{LC,Dipp}$ state to be isoenergetic with this state within

20 meV. So it cannot be excluded that the $T_{LC,Dipp}$ state is in fact the one lowest in energy. Time-resolved spectroscopy strongly favors this. After the τ_1 process, assigned to the ISC transition into $T_{LC/MLCT}$, two processes with time constants $\tau_2 = 900$ ps and $\tau_3 = 0.68$ μs are observed. If the τ_1 process populated the lowest triplet state, only one further process ought to occur. Thus, the τ_2 process is assigned to a transition between the $T_{LC/MLCT}$ state and the $T_{LC,Dipp}$ state. According to the experiment, the latter one ought to be the one lowest in energy. This lifetime of $\tau_2 = 900$ ps seems long if one takes the near degeneracy of the two states into consideration. However, these states differ strongly in character and thereby also in equilibrium geometries. This ought to result in a large reorganization energy λ and thus a substantial barrier (of $\approx \lambda/4$) for the IC transition between the two states.[158] The equilibration of the two states cannot be excluded.

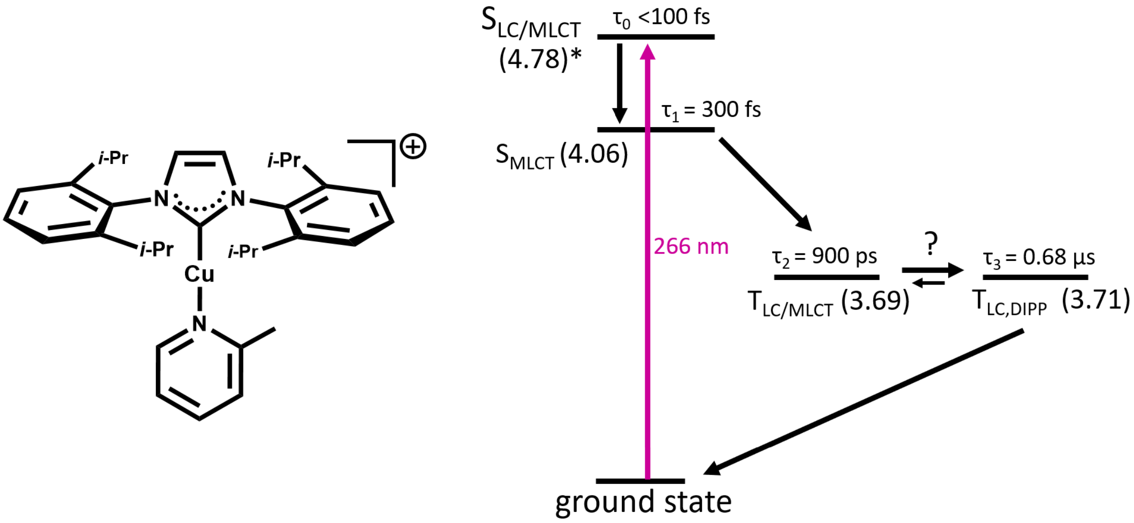

Figure 5.17.: Kinetic scheme of NHCCuPy in TFE. The time constants were received from the fs- and nsTA experiments. The electronic state assignment was done on the basis of quantum chemical calculations on the linear complex. The values in brackets show the adiabatic energies of the respective states in eV relative to the S_0 minimum. The value marked with a star shows the vertical energy of the $S_{LC/MLCT}$ state. Figure from ref.[40].

In any case, a long-lived upper triplet state, as observed here, bears the potential for luminescent application. For instance, HIGHrISC fluorophores for OLEDs make use of such long-lived upper triplet states.[24] In the HIGHrISC approach – also known as hot exciton[25] – an upper triplet state that lies energetically close to the S_1 state is used for efficient triplet harvesting via reverse intersystem crossing (rISC). The lowest populated triplet state, $T_{LC,Dipp}$

exhibits a lifetime of 0.68 μs, which is a typical value for such complexes.[159] With a calculated phosphorescence rate constant of 0.36 s^{-1} emission from $T_{LC,Dipp}$ state is outcompeted by non-radiative deactivation processes. This underlines the hypothesis that the emission that is observed originates not directly from NHCCuPy but from a coordinated counterion derivative as it is proposed in ref.[152].

5.2. [1,3-bis(2,6-diisopropylphenyl)imidazol-2-ylidene]-(dibenzoylmethanoate)copper(I)

The background to the complex 1,3-bis(2,6-diisopropylphenyl)imidazol-2-ylidene] (dibenzoylmethanoate) copper(I) (in the following referred to as NHCCuDBM) is covered in the first subsection of this section (subsection 5.2.1), subsections 5.2.2 and 5.2.3 present the experimental results towards the elucidation of the photophysics of NHCCuDBM that were obtained in the course of this thesis. First, a spectroscopic characterization of dibenzoylmethane (DBM) and its respective anion is given, including steady-state absorption and emission as well as time-resolved spectroscopy. These are followed by the spectroscopic characterization of the NHCCuDBM complex. The combined results are compared with quantum chemical calculations yielding a consistent picture of the compound's photophysics. Focus is laid on the properties of the complex dissolved in cyclohexane as a non-polar aprotic solvent, acetonitrile as a polar aprotic solvent, and ethanol as a polar protic solvent. Although the focus lies on the photophysics of the compound in the three aforementioned solvents, additionally, experimental findings are given regarding the behavior in 2,2,2-trifluoroethanol. Whereas this solvent constitutes the only suitable solvent for the spectroscopic investigation of the linear copper(I) carbene complex NHCCuPy presented in section 5.1, here, the complex is effectively decomposed by TFE as a solvent.

Parts of the steady-state UV/Vis absorption and emission measurements were conducted by Oliver Röth in the course of his master's thesis under the supervision of the author of this thesis. Time-resolved emission measurements obtained using the fluorescence Kerr gate instrument were conducted by Mahbobeh Morshedi. Quantum chemical calculations were conducted by Jasper Guhl (Institute of Theoretical Chemistry and Computer Chemistry, Prof. C. M. Marian).

5.2.1. Introduction

β-Diketones and derivatives, such as DBM, show a great variety of applications. For instance, due to their strong tendency to undergo keto-enol tautomerization and by so quickly dissipating excitation energy in a reversible manner, β-diketones are applied as UV filters (e.g. as components in sunscreens) or as model systems of keto-enol tautomerization as a number of photochemical studies revealed the processes of keto-enol tautomerization in detail[160,161,162,163,164,165,166,167,168,169,170]. It has been shown that for room temperature and in solution the chelated enol form is mostly present due to an intramolecular H-bond forming an O-C-C-C-O-H ring stabilized by resonance-assisted hydrogen bonding (RAHB).[171] Due to a $\pi\pi^*$ transition, this chelated enol (CE) form of DBM shows a strong absorption band in the near UV. As fast non-radiative deactivation processes occur in the excited state presumably involving a fast excited state intramolecular proton transfer (ESIPT), the generation of the non-chelated enol (NCE) form followed by rotamerization and recovery to the chelated enol form in the dark, DBM is essentially non-fluorescent. An overview of the isomerization processes that are presumably involved upon photoexcitation is shown in Figure 5.18.

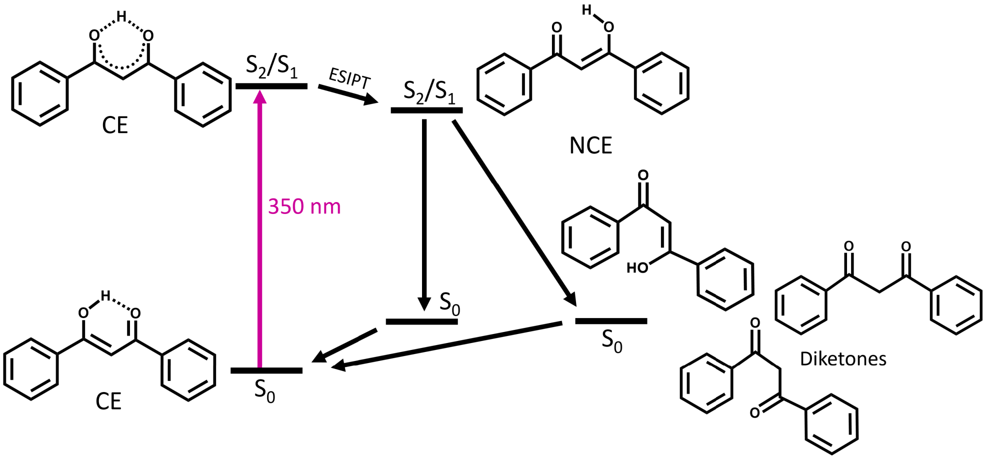

Figure 5.18.: Scheme of the photoreactivity of DBM. Upon irradiation DBM in its CE form presumably undergoes a fast ESIPT into the NCE form followed by deactivation into the ground state, either of the NCE form or of rotamerization derivatives or the keto form. This product mix reacts slowly back into the NCE ground state of DBM (approx. μs - to ms).

As of today, the literature lacks consensus on whether the strong $\pi\pi^*$ state constitutes the lowest excited state or in fact a weak $n\pi^*$ transition non-observable in the absorption spectrum. For other symmetric β-diketones, such as malonaldehyde or acetylacetone, the $n\pi^*$ state constitutes the lowest excited state, which some authors assume to apply for DBM as well.[161,170] In a recent spectroscopic study by Verma et al. the authors state that due to extended conjugation by the presence of the electron-rich benzene rings, the energy gap between the $n\pi^*$ and $\pi\pi^*$ state might be reduced and the $\pi\pi^*$ state becomes the one lower in energy.[169]

Besides applications involving the fast deactivation processes, the high binding affinity of β-diketones to transition metals leads to an easily accessible group of compounds with a diverse field of applications in areas such as NMR spectroscopy (as shift reagents),[172] laser technology,[173] electroluminescence,[174] or chemical catalysis.[175,176,177,178,179]

Here, the photophysics of a copper(I) carbene DBM complex (NHCCuDBM; see Figure 5.19) is investigated employing steady-state UV/Vis absorption and emission as well as time-resolved spectroscopy.

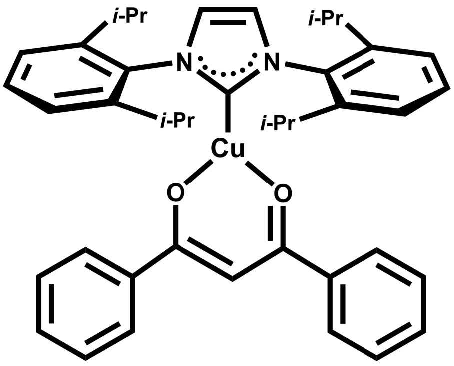

Figure 5.19.: Structure of NHCCuDBM.

The study is motivated by the potentially highly emitting character of its ligand DBM, which is, however, efficiently quenched by the isomerization processes as stated above. Upon coordination onto a metal center, these quenching processes are expected to be prohibited and thus the overall emission of DBM might be increased. Due to coordination, the photophysics of DBM can be drastically altered due to metal-ligand or ligand-ligand interaction. A recent transient spectroscopy study by Stanimirov et al. showed that the complexes europium(III)(DBM)$_3$ and aluminium(III)(DBM)$_3$ dissolved in MeCN possess both similarities and differences concerning the transient spectra and the photokinetics compared to free DBM.[180] Both complexes feature stimulated emission and excited state absorption similar to free DBM, that decays with time constants of ≈ 0.4 ps for the Eu(III) complex and ≈ 1.8 ps for the Al(III) complex compared to the respective one of DBM of ≈ 0.2 ps. Since for the Eu(III) and Al(III) complexes, isomerization of the DBM ligand ought to be prohibited due to its coordination, the excited state population presumably deactivates in other ways such as energy transfer to the metal ion in case of the Eu(III) complex.[180] However, this is not expected for Al(III), where an energy transfer from ligand to metal has not been reported yet. Hence, according to Stanimirov et al. the Al(III) complex might still share some relaxation pathways typical of the DBM ligand[2].[180]

---

[2] The exact nature of these deactivating pathway(s) in Al(DBM)$_3$ remains unclear as of yet.

In contrast, coordinating DBM to a copper(I) moiety with its closed d-shell configuration the metal might have less impact on the photophysics of the DBM ligand and metal-centered transitions are absent as deactivating channels. For similar NHC-Cu-X compounds with X = pyridine and 2-picoline, the lowest excited state constitutes a locally excited triplet state (localized on the Dipp moieties) with adiabatic energy of ≈ 3.4 eV (≈ 365 nm) and ≈ 3.7 eV (≈ 335 nm; see section 5.1), respectively.[40,154] Comparing these energy values with the lowest wavelength absorption band of DBM that peaks at ≈ 340 nm and extends to ≈ 380 nm, an excitation with lower energy than the local excitations of the DBM into which excitation energy could deactivate, seems unlikely.

Two other studies, in which the photophysics of copper(I) carbene DBM complexes bearing a cyclic (amino)-(alkyl)carbene (CAAC)[181] (Figure 5.20a) and a cyclic (amino)-(aryl)carbene (CAArC)[182] (Figure 5.20b) instead of an NHC ligand were investigated, neither contradicts nor confirms the overall idea.

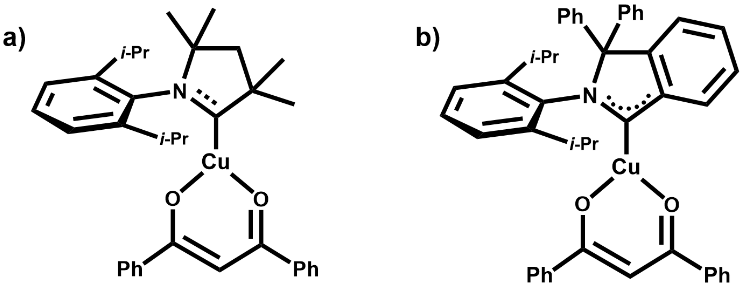

Figure 5.20.: Structures of a) CAACCuDBM and b) CAArCCuDBM.

For these complexes, a quenching mechanism due to the isomerization of the DBM ligand seems absent. The lowest absorption band, which is similar to the one of free DBM ($\lambda_{max} \approx 350$ nm), indicates that a DBM ligand centered $\pi\pi^*$ transition is present for these complexes, which is confirmed by quantum chemical calculations.[181] However, for both complexes new absorptions bands at wavelengths around 450 nm are observed, that according to the calculations arise from a $n_{DBM} \rightarrow \pi^*_{CAAC}$ CT transition in the case of the CAAC complex and mixed MLCT$_{Cu \rightarrow DBM}$/LLCT$_{DBM \rightarrow CAArC}$ transition as well as a MLCT$_{d_\sigma \rightarrow \pi^*_{CAArC}}$ transition in the case of the CAArC complex. Furthermore, both complexes show a single emission band around 750 nm with low quantum yields (< 0.01) for the solid state. According to quantum chemical calculations on the CAAC complex, this band arises from a phosphorescent triplet state of Cu/$n_{DBM} \rightarrow \pi^*_{CAAC}$ MLCT character.[181] According to the authors, the large bathochromic shift is rationalized with structural changes in the triplet excited state at which the ground state is significantly destabilized. For the CAArC complex, a solid state emission lifetime of 50 ns is given.[182] As no singlet emission is observed, for these complexes a fast intersystem crossing from the primarily excited singlet to the triplet states seems likely.

5.2.2. On the Photophysics of Dibenzoylmethane and the Respective Anion

To understand the photophysical properties of the complex, it proved useful to first have a thorough look at the respective properties of its ligand. To this end, UV/Vis absorption and emission spectra were recorded for DBM as well as the deprotonated anionic form dibenzoylmethanoate (DBM^-). Furthermore, femtosecond UV/Vis absorption and emission methods are applied for a deeper look into the molecule's photokinetics. As mentioned in subsection 5.2.1, parts of DBMs photophysics were studied before, including the lowest excited states as well as its involved deactivating mechanisms. However, to further extend these studies and for the sake of a consistent picture regarding the behavior of the complex (covered later on in section 5.2.3), some experiments including transient absorption were performed again. These results are supported by quantum chemical computations (subsection 5.2.4).

5.2.2.1. Steady-State Absorption and Emission Spectroscopy

The longest wavelength absorption band of DBM covers a range from ≈ 300 to 380 nm with little differences between each solvent (see Figure 5.21). It peaks at ≈ 340 nm. The absorption coefficient for this band varies between ≈ 22.000 $M^{-1}cm^{-1}$ for ethanol and ≈ 26.000 $M^{-1}cm^{-1}$ for cyclohexane and acetonitrile. Higher absorption coefficients for cyclohexane and acetonitrile compared to ethanol are also found for the absorption bands at higher energies. The rather high absorption coefficient for the longest wavelength band indicates an allowed transition such as a $\pi\pi^*$ transition as it is proposed in the literature.[169] This band further shows a shoulder around 360 nm presumably originating from vibrational progression.

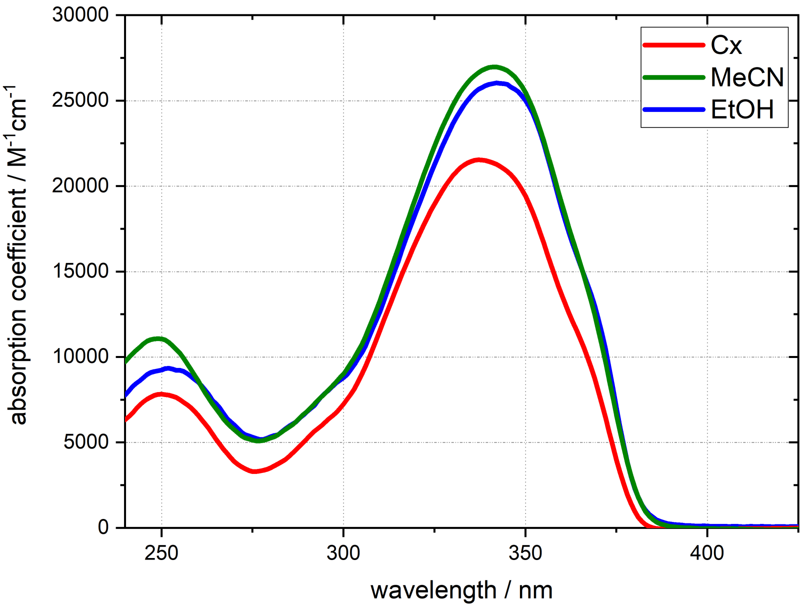

Figure 5.21.: Absorption spectra (absorption coefficients as a function of wavelength) of DBM in Cx (red), MeCN (green), and EtOH (blue).

The emission spectra of DBM show maxima at ≈ 400 nm, with cyclohexane having the highest energy emission, followed by acetonitrile and ethanol (see Figure 5.22). This indicates a slightly increased dipole moment in the exited state that is stabilized by a polar environment. The Stokes shift amounts to ≈ 4500 cm^{-1}, which can be considered as rather large for organic molecules.[183] The 0-0 energy, as an approximate value of the adiabatic energy of the lowest excited state, determined in MeCN by the crossing of the corrected absorption and emission spectra amounts to 3.32 eV.

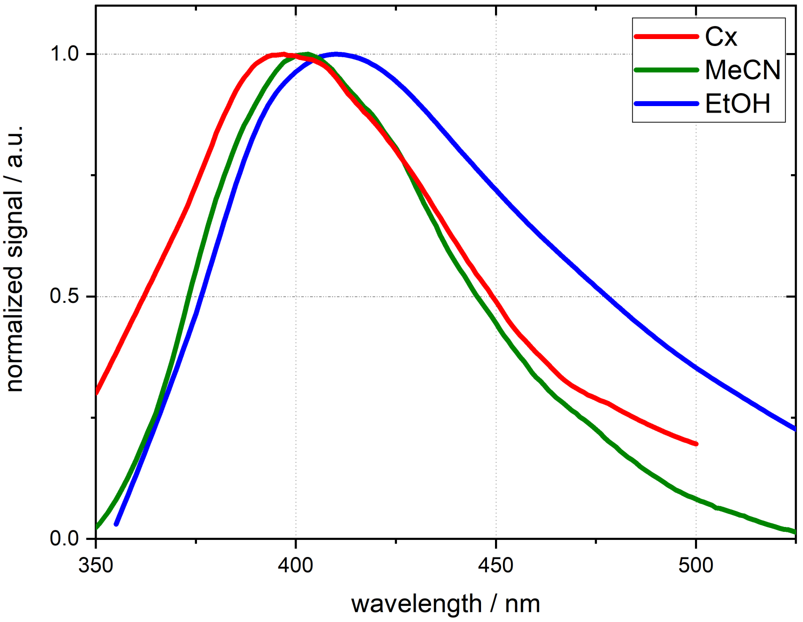

Figure 5.22.: Emission spectroscopy on DBM in solvents Cx (red, smoothed), MeCN (green, smoothed), and EtOH (blue, smoothed). For the recording of the emission spectra the excitation wavelength was set to 330 nm.

Fluorescence quantum yields are low with values of $\approx 10^{-5}$ for all solvents ($\approx 4 \cdot 10^{-5}$ for Cx and MeCN, $\approx 6 \cdot 10^{-5}$ for EtOH). A Strickler-Berg analysis yields radiative rate constants of $3.6 \cdot 10^{8}$ s^{-1} (Cx), $3.5 \cdot 10^{8}$ s^{-1} (MeCN), and $2.9 \cdot 10^{8}$ s^{-1} (EtOH). This, together with the fluorescence quantum yield gives an excited state lifetime of ≈ 110 fs for Cx and MeCN and ≈ 200 fs for EtOH. The relatively high radiative rate constants are no surprise considering the high absorption coefficient of the longest wavelength absorption maximum. The overall low fluorescence quantum yields arise from the emitting excited state being that short-lived.

For the spectroscopic investigation of the respective anion DBM^{-}, two different bases were used to achieve deprotonation. These are ammonia and sodium hydroxide, both diluted in water. Upon addition of the basic NH_3 solution to a DBM/ethanol solution, the longest wavelength absorption maximum shifts to 350 nm (see Figure 5.23a).

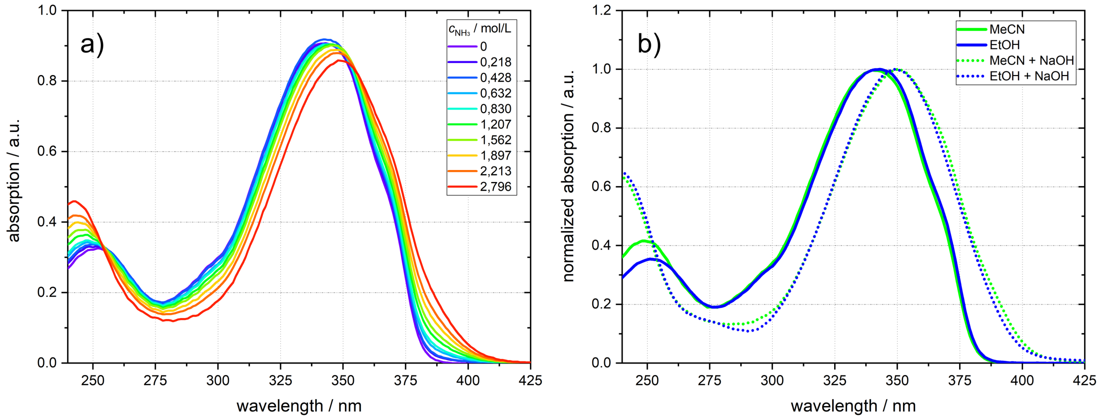

Figure 5.23.: Absorption spectroscopy on DBM and DBM$^-$. a) Dependence of the absorption spectra of DBM in ethanol from the concentration of NH_3/water solution. b) normalized absorption spectra of DBM in MeCN (solid green line) and EtOH (solid blue line) and their respective basic solutions (dashed lines) obtained by the addition of concentrated NaOH water solution.

The absorption, which is corrected for concentration changes due to the addition of NH_3 solution, decreases in the region between 250 and 350 nm (including the absorption maximum). For wavelengths beyond this region, especially 380 nm and higher wavelengths, the absorption increases. This is in line with previous reports on both the DBM and the DBM$^-$.[164] Both methods (i.e. addition of NH_3 or NaOH) result in similar spectra. Also, no significant differences are present comparing DBM$^-$ in ethanol and acetonitrile (see Figure 5.23b). Due to solubility issues, the anion could not be obtained in cyclohexane.

Comparing the emission spectra of DBM with the ones of DBM$^-$ only minor differences are observed (see Figure 5.24). The fluorescence quantum yield is decreased, from $\approx 8 \cdot 10^{-5}$ (EtOH/H_2O) to $\approx 3 \cdot 10^{-5}$ (EtOH/H_2O/NaOH). According to Strickler-Berg, the fluorescence lifetime decreases from 260 fs (EtOH/H_2O) to 160 fs (EtOH/H_2O/NaOH), with radiative rate constants of $3.0 \cdot 10^8$ s^{-1} and $2.1 \cdot 10^8$ s^{-1}, respectively. These values obtained via Strickler-Berg are in almost perfect agreement with time-resolved spectroscopy data by Stanimirov et al. where time constants of 240 fs and 150 fs were measured for the stimulated emission decay for DBM and DBM$^-$, respectively.[180] In their study, the authors obtained the anion in an ethanol solution with a pH of 11. Besides the slightly decreased time constant no significant differences were observed between DBM and DBM$^-$.

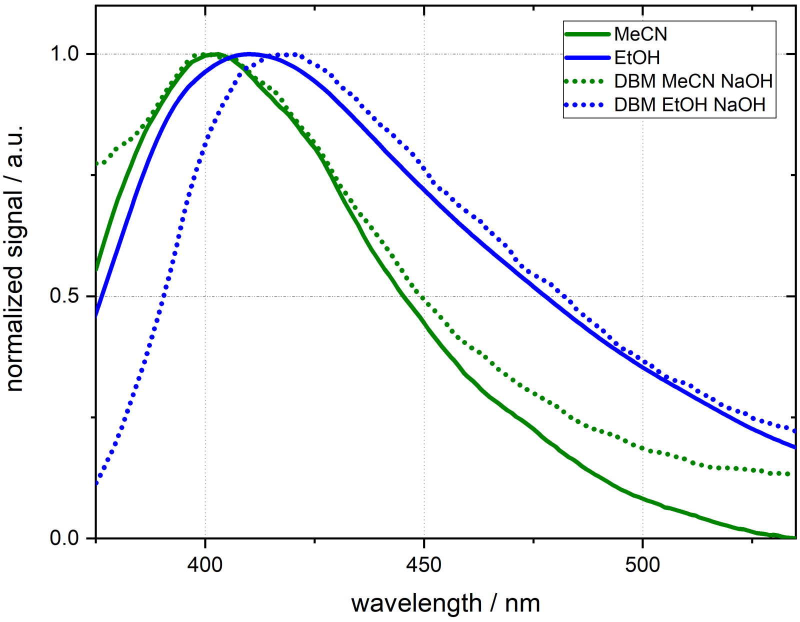

Figure 5.24.: Emission spectroscopy on DBM$^-$. Normalized emission spectra of DBM$^-$ in MeCN (solid green line) and EtOH (solid blue line) and their respective basic solutions (dashed lines) obtained by the addition of concentrated NaOH water solution. For the recording of the emission spectra the excitation wavelength was set to 340 nm.

5.2.2.2. Time-Resolved Absorption and Emission Spectroscopy

Femtosecond UV/Vis absorption spectroscopy on DBM in ethanol excited at 266 nm reveals the following characteristics. Around time zero, a distinct signature is seen with a pronounced positive transient absorption band between 380 and 420 nm and a broader band from 550 to 700 nm and beyond (see Figure 5.25). From 420 to 550 nm there is a negative signal.

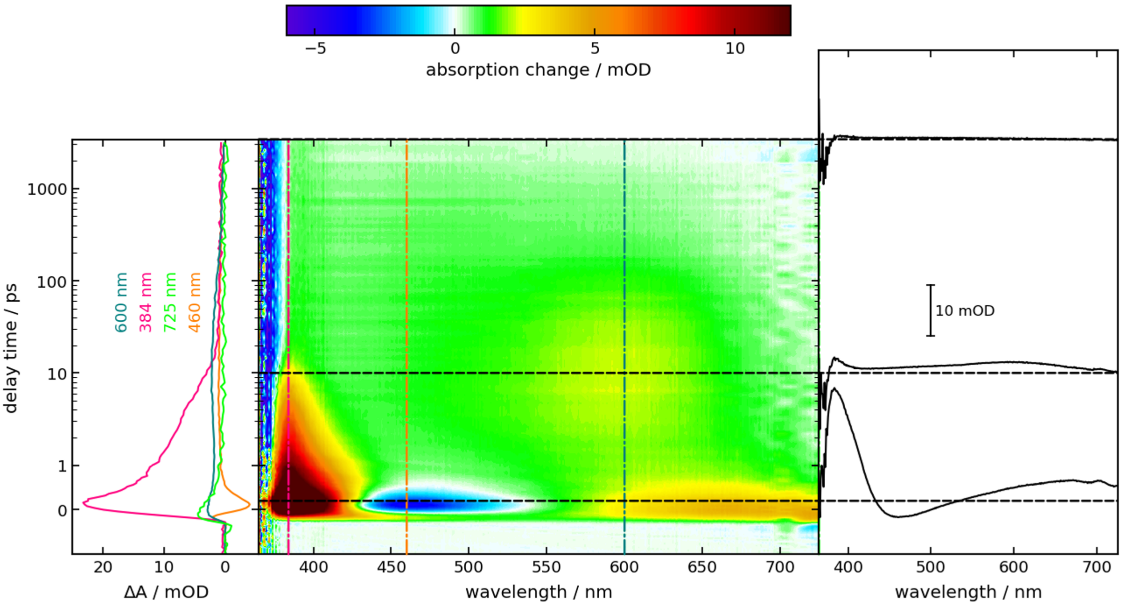

Figure 5.25.: Femtosecond time-resolved spectroscopy data acquired for DBM in EtOH. The excitation was tuned to 400 nm. In the contour representation (central), the difference absorption signal is color-coded. Vertical lines mark spectral positions for the time traces plotted on the left while horizontal lines mark certain delay times for the difference spectra plotted on the right.

As DBM bears no ground state absorption but emission there (see Figures 5.21 and 5.22), the negative signal in this region is attributed to stimulated emission. This negative emission band and the broader positive absorption band (550 – 700 nm) decay within a few hundred femtoseconds to give rise to a slightly positive band. The pronounced positive band around 400 nm decays within a few picoseconds, presumably due to vibrational cooling. The decay of this band is accompanied by the rise of a positive band at 600 nm peaking at a delay time of 10 ps. Stanimirov et al. attribute this to the population of a triplet state[3].[180] Furthermore, with the decay of the pronounced band around 400 nm, another negative signal at wavelengths smaller than 380 nm becomes discernible. This negative signal is attributed to ground state bleaching. According to previous reports[169,170,180], DBM undergoes fast photo isomerization reactions. These photoproducts, present in their electronic ground state, are likely responsible for the ground state bleach that extends with no obvious decay beyond the observable time window of ≈ 4 ns. Apart from the ground state bleach at 380 nm and below, all transient absorption signals vanish to zero within the time window.

---

[3] It should be noted that for this to be true the triplet state must be very short-lived. A rapid deactivation of the triplet state could potentially be attributed to another isomerization process originating from the triplet state.

The time-resolved absorption data of the respective anion share some similarities with DBM but also bear some distinct features (see Figure 5.26). The transient absorption signature around time zero resembles the one from protonated DBM. However, for DBM$^-$, there is no negative signal observed. Instead, around the same region (450 - 550 nm) a plateau within the positive excited state absorption band is seen. Again, this is attributed to stimulated emission as it fits the emission spectra. In contrast to the time-resolved spectra of protonated DBM, the absorption signal of DBM$^-$ increases subsequently to the short-lived feature attributed to stimulated emission. This might indicate that more than one species is present with overlapping signal contributions. One reason for that might be the partial coordination of DBM$^-$ and Na$^+$ as complexes of both have been reported before.[184] An incomplete deprotonation of DBM seems rather unlikely as the experiment was conducted with a pH >11 and DBM having a pK_a of 9.56.[185] The positive absorption bands from 450 nm and below and from 550 nm and above behave similarly to the corresponding ones in DBM, although the one for higher wavelength decays more slowly within ps. The weak feature from transient absorption data of DBM, attributed to an excited triplet state, is not observed here. As for protonated DBM, a negative signal below 400 nm becomes observable as the positive band at 400 decays.

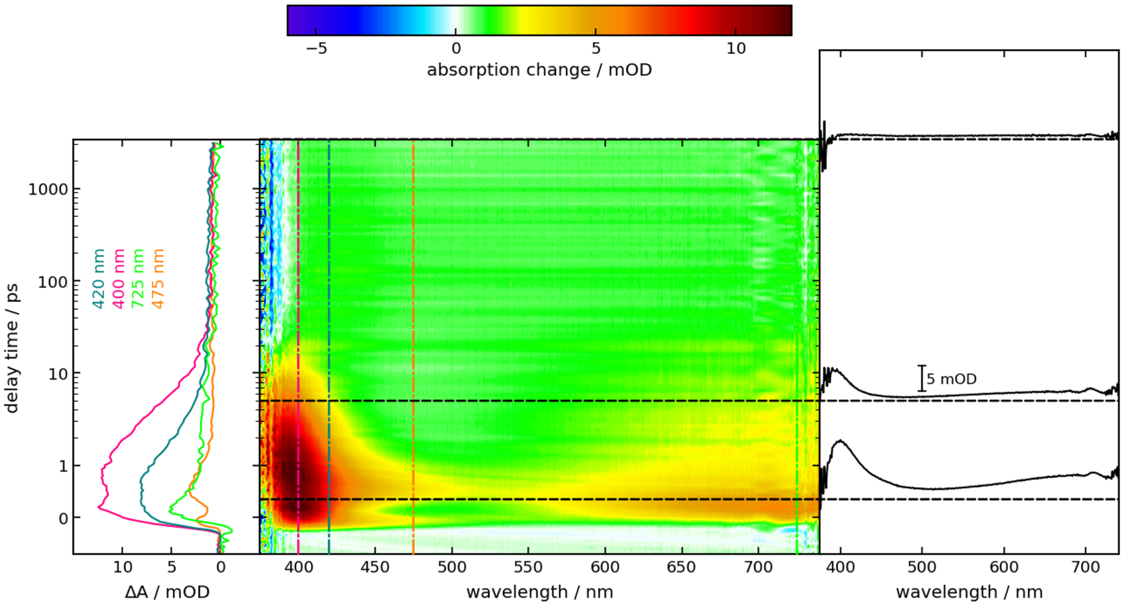

Figure 5.26.: Femtosecond time-resolved spectroscopy data acquired for DBM in EtOH/H_2O/NaOH solution. The excitation was tuned to 400 nm. In the contour representation (central), the difference absorption signal is color-coded. Vertical lines mark spectral positions for the time traces plotted on the left while horizontal lines mark certain delay times for the difference spectra plotted on the right.

Utilizing a global analysis, both data sets could be fit satisfactorily with three time constants. The respective decay-associated difference spectra (DADS) are described hereafter. Starting with the data for DBM dissolved in ethanol (w/o the addition of base), the first DADS$_1$ with a corresponding time constant τ_1 of 300 fs shows negative amplitudes between 420 and 550 nm (see Figure 5.27 top). Beyond this region, the amplitudes are positive. The negative part indicates the decay of the stimulated emission, while the positive ones correspond to the decay of excited state absorption. This time constant is well in line with the one obtained by Strickler-Berg analysis. In the literature, a time constant of 240 fs is found for this first deactivating process.[180] The second time constant τ_2 equals 1.7 ps. The corresponding DADS$_2$ shows high amplitudes for wavelengths < 450 nm. As both DADS$_1$ and DADS$_2$ have strong amplitudes around the 400 nm band, they parametrize a bi-exponential decay. For longer wavelengths (> 600 nm) slightly positive amplitudes are present. From 450 to 600 nm the amplitudes are negative. This indicates the rise of another positive transient absorption feature, the decay of which is depicted in the DADS$_3$ with $\tau_3 =$ 175 ps. The DADS$_3$ mainly features a broad positive band from 450 to 700 nm, which corresponds to the depopulation of an excited triplet state according to ref.[180], where a time constant of 201 ps was found for this process. The DADS$_{offset}$, which only bears amplitudes < 1 mOD, indicates that the greatest part of the excited state population has eventually decayed into a ground state, either of DBM or of an isomeric derivative. These small "leftover" amplitudes can either be explained by a fraction of triplet formed with lifetimes exceeding the observable time window or with solvated electrons, which are typically observed in aqueous solutions upon intense laser irradiation and possess lifetimes of a few nanoseconds and even longer in alkaline solutions.[186,187]

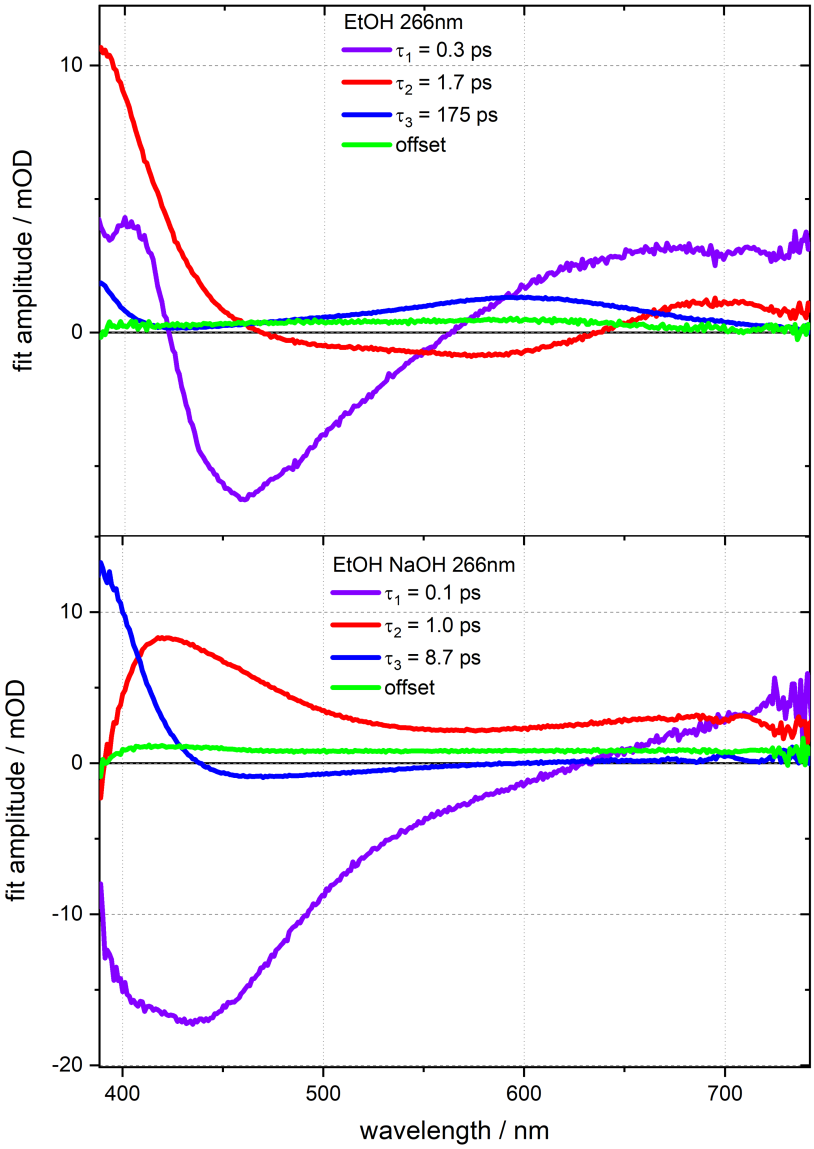

Figure 5.27.: Decay-associated difference spectra obtained from the fsTA experiments of DBM in EtOH and DBM in EtOH/H_2O/NaOH solution.

As for the transient spectra, the respective DADS of the anion DBM^- feature some similarities (see 5.27 bottom). The first time constant τ_1 is shortened to 100 fs. Also in the literature, a shortening of the first time constant to 150 fs is observed.[180] The $DADS_1$ shows substantial negative amplitudes between 400 and 600 nm with slight positive values beyond. This indicates a rather strong rise in transient absorption signal in the region 400 to 600 nm. This is accompanied by the decay of stimulated emission, which adds to the effect of the rising

ESA signal. The DADS$_2$ for the second time constant $\tau_2 = 1.0$ ps bears only positive amplitudes with a peak at 420 nm and a broad band from 550 to 700 nm indicating the decay of positive ESA signal throughout the spectral window. The last time constant τ_3 equals 8.7 ps. The respective DADS$_3$ is somewhat similar to the second DADS of DBM and shows a distinct positive band for wavelengths < 420 nm. As for DBM, this is attributed to the decay of ESA signal originating from vibrational cooling. Between 440 and 550 nm there are slightly negative values indicating a rise of transient absorption. This might be caused by a small population of an excited triplet state in analogy to the findings in DBM. The DADS$_{offset}$ shows amplitudes of ≈ 1 mOD throughout the spectral window. Again, this might be due to the population of a triplet state, the decay of which exceeds the observed time window. These results of DBM and DBM$^-$ are surprising since Stanimirov et al. did not find significant differences in the transient spectra of those two species, except a shortened lifetime τ_1 (from 240 fs for DBM to 150 fs for DBM$^-$).[180]

Transient absorption spectroscopy data are supported experimentally by the method of time-resolved fluorescence spectroscopy. The sample, DBM dissolved in an ethanol solution, was excited at 266 nm (i.e. into an upper singlet state). Here, a distinct band resembling both spontaneous (steady state) and stimulated emission is observed, peaking around 400 nm (see Figure 5.28). Within half a picosecond almost all emission signal has vanished. For a closer inspection, a global fit analysis was conducted. The data could be fit satisfactorily using only one time constant (and a fixed one for infinite delay times, see above), indicating a single exponential decay of the emission signal. The respective time-constant amounts to 300 fs. This further underlines that the lowest excited singlet state responsible for the detected emission is depopulated with a time constant of ≈ 300 fs, in line with the transient absorption experiments as well as the Strickler-Berg analysis.

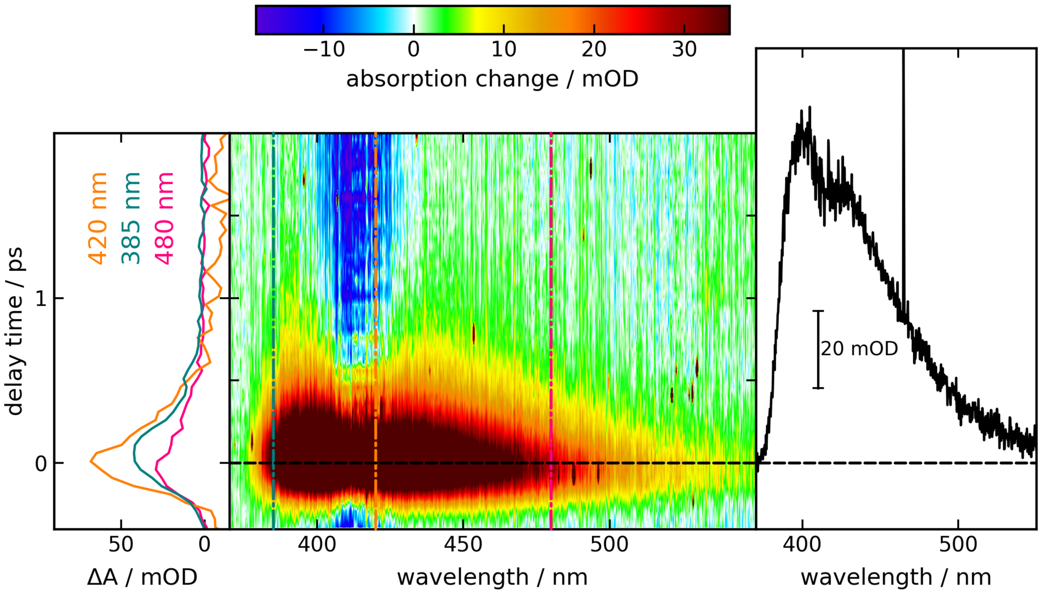

Figure 5.28.: Femtosecond transient fluorescence on DBM in EtOH, plotted as a function of detection wavelength and delay time. The sample was excited at 266 nm. In the central contour representation, reddish coloring represents large fluorescence signals. Time traces for 480, 420, and 385 nm are shown on the left. A selected spectrum is depicted on the right. Its vertical position corresponds to the respective delay time.

5.2.3. Coordinating Dibenzoylmethane onto a Copper(I) Carbene Moiety

After a thorough look at the ligand DBM and the respective anion, this section covers the spectroscopic investigation of the complex. The experiments were conducted in solutions of cyclohexane, acetonitrile, and ethanol. In the course of the femtosecond transient absorption experiments in ethanol, some abnormalities compared to the other solvents, supposedly due to the proticity of EtOH, were observed. This could be clarified using 2,2,2-trifluoroethanol as a solvent applied in additional experiments, which are presented here as well.

5.2.3.1. Steady-State Absorption and Emission Spectroscopy

The absorption spectra of the complex show their longest wavelength maximum at 345, 350, and 365 nm for ethanol, acetonitrile, and cyclohexane, respectively (see Figure 5.29).

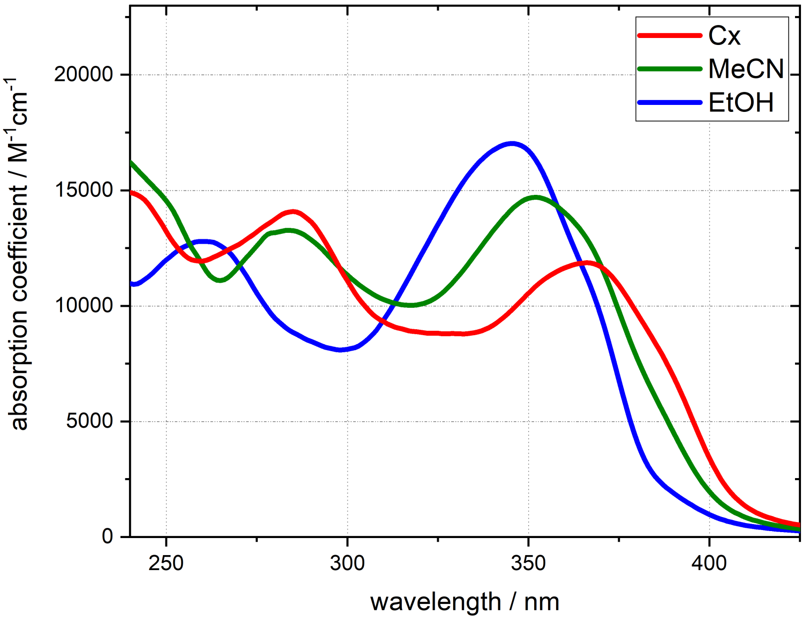

Figure 5.29.: Absorption spectra (absorption coefficients as a function of wavelength) of NHCCuDBM in Cx (red), MeCN (green), and EtOH (blue).

Regarding its shape and the rough position, this maximum looks similar to the one of DBM. In contrast to DBM though, the position of the maximum depends more on the environment (i.e. on the polarity and proticity of the solvent) and it shifts with an increasing polarity (and proticity) of the solvent to higher wavelengths marking negative solvatochromism. This can partially be explained by a decrease of the dipole moment in the excited state compared to the ground state[188] and further allows the assumption, that the electronic transition bears contributions from the copper carbene unit. A direct comparison of the spectra as in Figure 5.30 underlines the dominating character of DBM regarding the absorption maximum. Although, concerning the decreased absorption coefficient, which is almost halved, again, an electronic influence of the copper carbene upon coordination of DBM seems obvious. Furthermore, the comparison emphasizes that – as expected – the anion DBM^- serves as a better model for the comparison with the complex than the neutral molecule does.

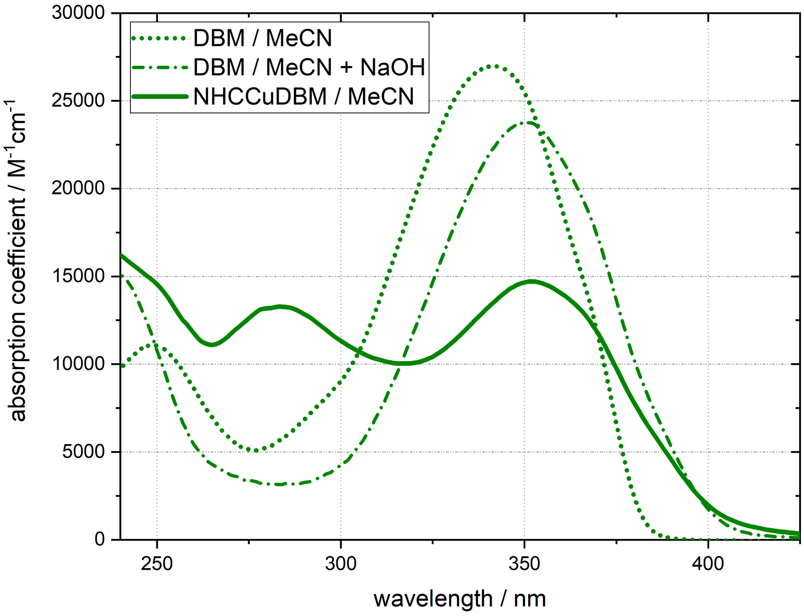

Figure 5.30.: Comparison of the absorption spectra (absorption coefficients as a function of wavelength) of NHCCuDBM, DBM, and DBM$^-$ in MeCN.

With 2,2,2-trifluoroethanol as a solvent, the absorption spectrum of the complex resembles the one of DBM (see the blue-purple line in Figure 5.31). This gives a clear indication of the DBM ligand being released in that solvent. First indications were obtained from time-resolved spectra in ethanol (see below, subsection 5.2.3.2 Figure 5.34). The ejection of the DBM ligand correlates with the proticity of the solution as the addition of hydrochloric acid to a MeCN solution of the complex resulted in the same behavior as TFE. To further elucidate this reaction, a titration experiment was conducted in which the impact of adding TFE on the absorption spectrum of NHCCuDBM in MeCN was investigated. (see Figure 5.31).

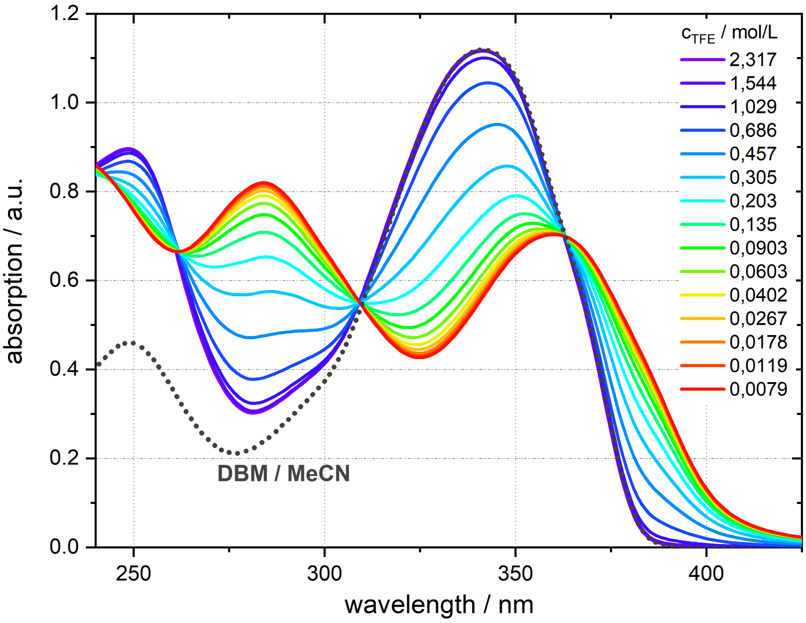

Figure 5.31.: Impact of the addition of TFE to absorption spectra of NHCCuDBM dissolved in MeCN. The initial concentration c_1^0 of NHCCuDBM amounted to $\approx 5 \cdot 10^{-5}$ M and remains constant throughout the experiment.

Upon the first additions of TFE (i.e. for low concentrations), the spectrum of the complex in MeCN is seen (red and yellow to green lines). For higher concentrations (blue lines), the spectrum eventually converges to the spectrum of DBM (for $\lambda > 300$ nm). For wavelengths smaller than 300 nm the absorption is higher than the one of DBM. This is due to the presence of the copper carbene residue presumably coordinated by a negatively charged 2,2,2-trifluoroethoxide. An absorption spectrum, which is typical for these copper carbene derivatives is obtained by the subtraction of a pure DBM/MeCN spectrum (see dotted line Figure 5.31) from the NHCCuDBM/TFE spectrum. The spectrum is shown in Figure 5.32 in comparison with the copper carbene complex NHCCuPy from section 5.1, where a detailed analysis of the UV/Vis absorption spectrum can be found (see also refs.[40,152,154]). A similar complex as the one proposed in TFE bearing the same carbene ligand and an ethoxide ligand in a linear geometry has been reported before.[189,190]

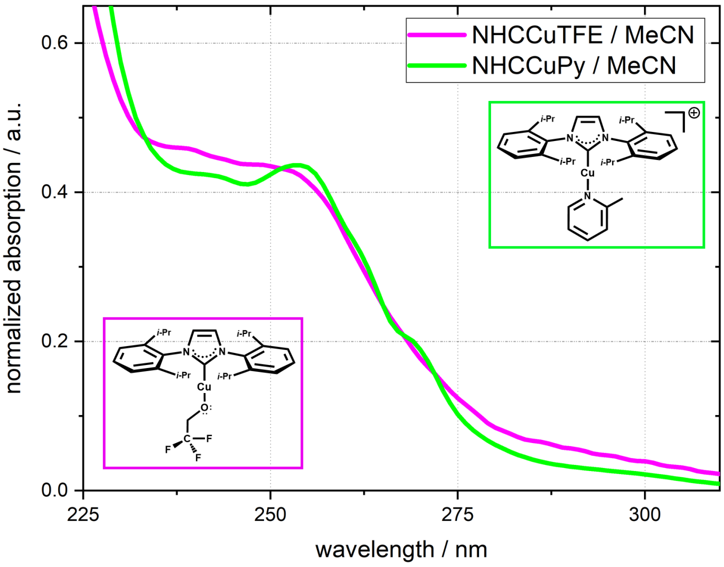

Figure 5.32.: Comparison of the absorption spectra of NHCCuPy and the complex presumably obtained for NHCCuDBM dissolved in TFE.

The emission spectra of the complex show maxima at 400 nm (EtOH, MeCN) and 425 nm (Cx). Regarding the maximums position and overall form, the emission resembles the one of DBM and DBM^- quite well (see Figure 5.33). Although, similarly to the absorption spectra, a bathochromic shift is observed going from the polar solvents EtOH and MeCN to the apolar solvent Cx (i.e. negative solvatochromism). Again, this indicates a decrease in dipole moment from the ground to the excited state.[188]

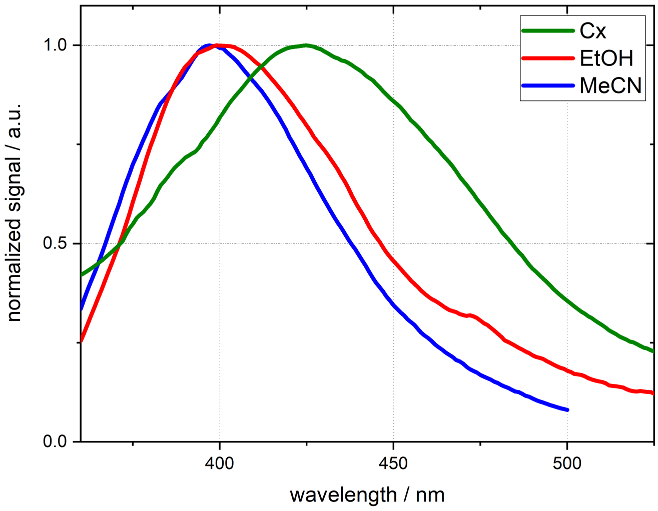

Figure 5.33.: Emission spectroscopy on the complex NHCCuDBM in solvents Cx (red, smoothed), MeCN (green, smoothed), and EtOH (blue, smoothed). For the recording of the emission spectra the excitation wavelength was set to 340 nm.

The fluorescence quantum yields are of the order of 10^{-5} as well. Although such low FQYs are prone to errors due to difficulties in the recording of the spectra, it can be said that the FQYs of the complex are systematically lower than the ones of DBM ($\approx 6 \cdot 10^{-6}$ (Cx), $\approx 1 \cdot 10^{-5}$ (MeCN), $\approx 5 \cdot 10^{-5}$ (EtOH)) with EtOH being the closest to the ones of pure DBM. A Strickler-Berg analysis revealed the radiative rate constants: $1.4 \cdot 10^8$ s^{-1} (Cx), $2.1 \cdot 10^8$ s^{-1} (MeCN), and $2.3 \cdot 10^8$ s^{-1} (EtOH). According to the above-stated FQYs, fluorescence lifetimes are expected to be as follows: ≈ 40 fs (Cx), ≈ 50 fs (MeCN), and ≈ 200 fs (EtOH). The 0-0 energy determined in MeCN solution lies at 3.22 eV, giving an indication that the lowest excited state of the complex lies energetically ≈ 0.1 eV lower than the lowest one of DBM.

5.2.3.2. Time-Resolved Absorption Spectroscopy

The time-resolved data of the complex, obtained by the pump-probe femtosecond transient absorption technique, show little impact of the different solvents on the signature of the transient spectra. However, with respect to the excited state lifetimes, effects of the solvents are evident. For the measurements that are shown the excitation wavelength is 266 nm (see Figure 5.34). Similar results were obtained by measurements with an excitation wavelength of 400 nm for Cx, MeCN, and zeonex[4] as a matrix environment (see appendix Figure A.9).

---

[4] Attempts to embed NHCCuDBM in PMMA matrix resulted in uneven distributions of the complex in the solid sample. For zeonex this behavior was not present.

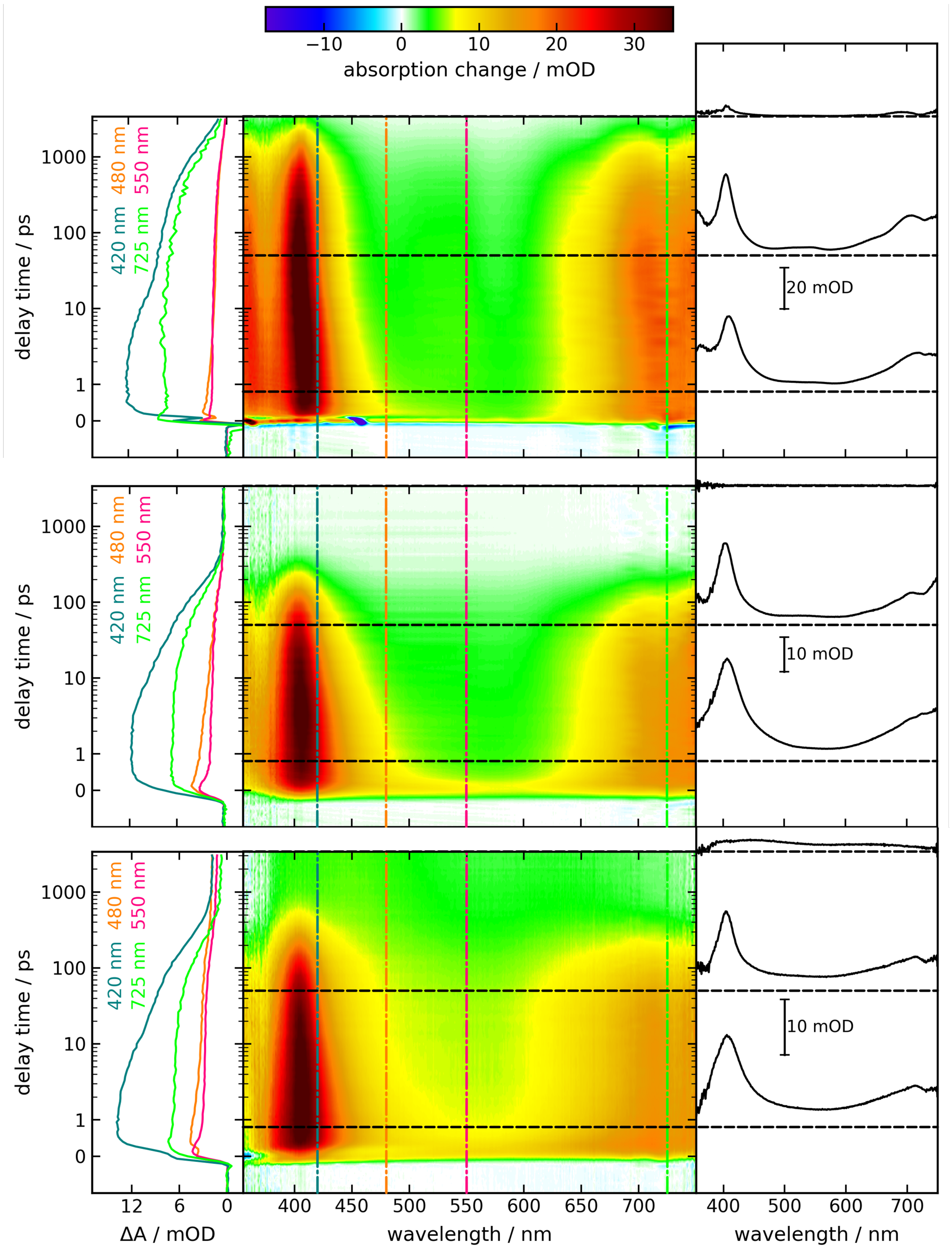

Figure 5.34.: Femtosecond time-resolved spectroscopy on NHCCuDBM in Cx (top), MeCN (middle), and EtOH solution (bottom). The excitation was tuned to 266 nm. In the contour representation (central), the difference absorption signal is color-coded. Vertical lines mark spectral positions for the time traces plotted on the left while horizontal lines mark certain delay times for the difference spectra plotted on the right.

Negative signals originating from SE or GSB are not observed. Throughout the whole time frame and for all wavelengths positive signals of ESA are detected. Around time zero and for all solvents a distinct spectral signature with a transient absorption band at ≈ 400 nm and a broader one peaking at around 700 nm is observed. This distinct spectral signature undergoes a slight change observable in a spectral shift of the 400 nm absorption band for delay times of $\approx 5 - 10$ ps for all solvents. This behavior is clearly indicated by the time trace for 420 nm (Figure 5.34, blue line). The data differ mainly (between each solvent) with regard to the observable lifetime of the excited states. In cyclohexane, the lifetime seems to be the longest. Within the accessible time window of up to ≈ 4 ns, the ESA decay is not completed. In ethanol and acetonitrile, a similar ESA feature decays within ≈ 500 ps. In the case of acetonitrile, beyond ≈ 500 ps the transient absorption is essentially zero, indicating a full ground state recovery. The measurement in EtOH shows a more distinct behavior beyond ≈ 500 ps. This is presumably due to the proticity of the solvent. These observations in EtOH led to further experiments with TFE as a solvent scrutinizing this interaction (see Figure 5.36). The dominant transient absorption spectrum, which is shared for all solvents, resembles the transient spectrum around time zero of the anion DBM$^-$ quite well indicating similar transitions being involved.

A global fit analysis yielded three relevant time constants, including a fixed one for infinite delay times that accounts for any signal, which persists beyond the observable time window. The shift of the 400 nm transient absorption band occurs with time constants of $\tau_1 = 9.7$ (Cx), 7.2 (EtOH), and 5.6 ps (MeCN). The decay of the dominating transient absorption feature occurs with time constants of $\tau_2 = 1240$ ps for cyclohexane, 200 ps for ethanol, and 141 ps for acetonitrile.

These experimentally observed excited state lifetimes for the complex are in clear contradiction to the values obtained by Strickler-Berg analysis. This might indicate that the emitting state (observed in steady-state fluorescence spectroscopy) is not the lowest excited state. Thus, the emitting state might depopulate fast, within the time resolution of the femtosecond instrument (≈ 100 fs).

The respective DADS$_{1-3}$ obtained by the global analysis are described in the following. For all solvents, DADS$_1$ shows a sharp negative band at 400 nm followed by a positive one expanding from ≈ 420 to ≈ 500 nm (see Figure 5.35). This feature, which is reminiscent of the first derivative of the respective transient spectrum[5], indicates a shift of the dominant transient absorption band at 400 nm. This in turn might indicate vibrational cooling,[191] which occurs with the time constant τ_1. DADS$_2$ shows a distinct peak at the position of the negative one from DADS$_1$ (400 nm), which expands to 450 nm, where DADS$_1$ shows positive values. A small peak is observed at 530 nm and a broad one around 700 nm. All amplitudes are positive indicating the decay of the positive ESA signal. The DADS$_3$, indicating all "leftover" signals after 4 ns (offset), differs the most between each solvent. For MeCN the amplitudes are essentially zero, which indicates that all excited state population has recovered to the ground state within the observed time window. For Cx the DADS$_3$ is qualitatively similar to DADS$_2$, although much smaller in amplitude. This might be due to the "leftover" signal exceeding the detected time window that was not fully accounted for by the global analysis and the respective time constant τ_2. However, based on this data it can not be excluded that additionally another state with a similar transient absorption spectrum is partially populated. For this reason, another fsTA measurement with delay times of 15 and 18 ns was conducted (see appendix, Figure A.11). There, the transient absorption signal is essentially zero for all wavelengths rendering the population of another state unlikely. The DADS$_3$ for EtOH is neither zero nor does it resemble the DADS$_2$. It shows a rather featureless positive broad band. This indicates that with the second time constant of $\tau_2 \approx 200$ ps another excited state is being populated with an absorption spectrum similar to DADS$_3$, presumably a triplet state.

---

[5] A comparison confirming the similarity between the DADS$_1$ and the first derivative is given in the appendix, Figure A.10.

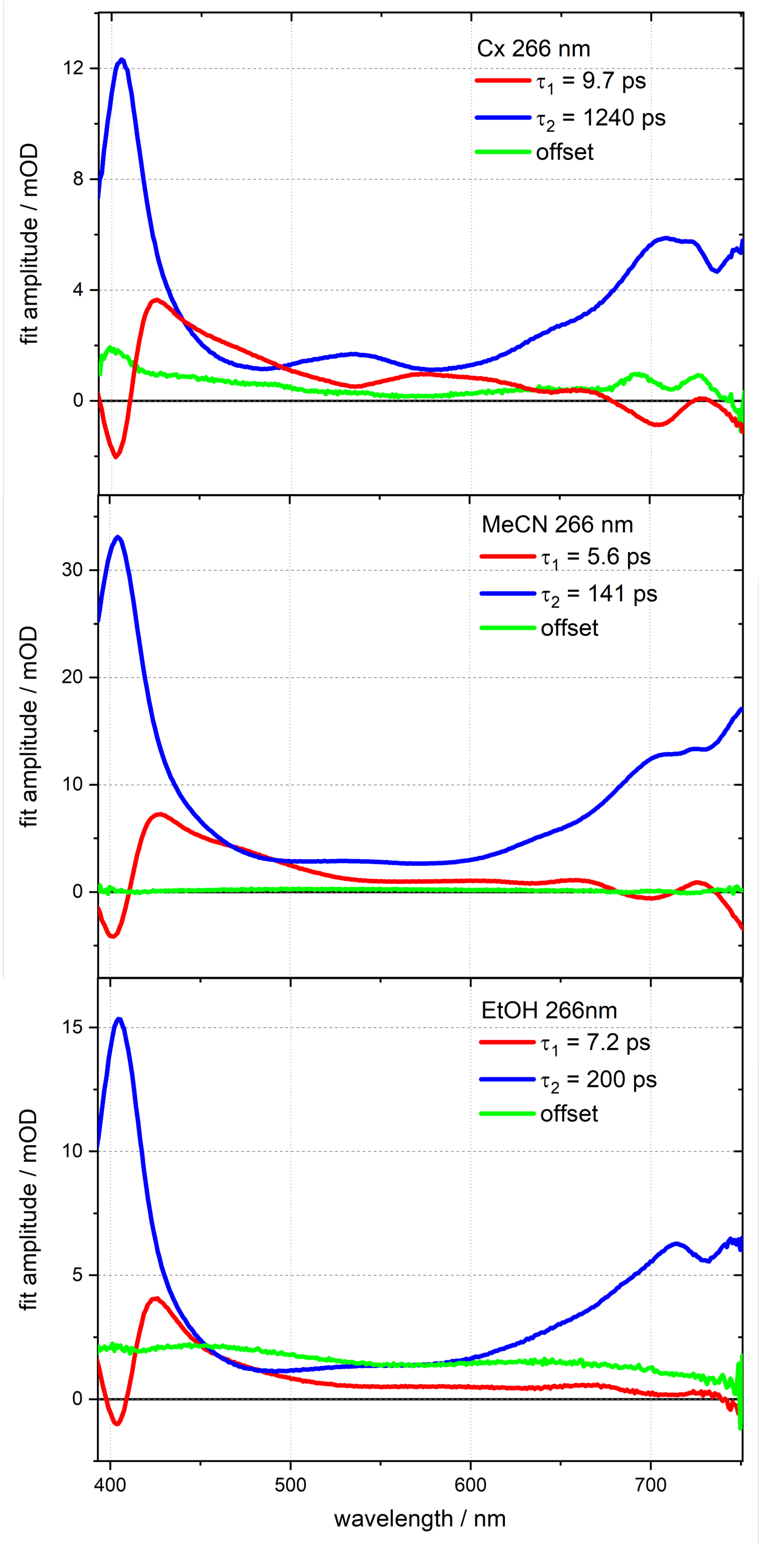

Figure 5.35.: Decay-associated difference spectra obtained from the fsTA experiments of NHCCuDBM in Cx, MeCN, and EtOH, for an excitation wavelength of 266 nm

The behavior of EtOH differing from the one in Cx and MeCN can be explained by the results of TFE as a solvent. In TFE, which bears a more acidic hydroxide group than EtOH does,[192] clear signatures are observed that resemble the ones from pure DBM especially around time zero to ≈ 10ps (see Figure 5.36). For late delay times, the signature resembles the one for the complex in EtOH. This further stresses that the complex dissolved in EtOH undergoes a partial dissociation to form DBM and a copper carbene derivative presumably coordinated by ethoxide, which is also in line with the steady-state experiments. This further indicates that in EtOH (and TFE), presumably two ground state species are present. In TFE as a solvent, the complex dissociates quantitatively.

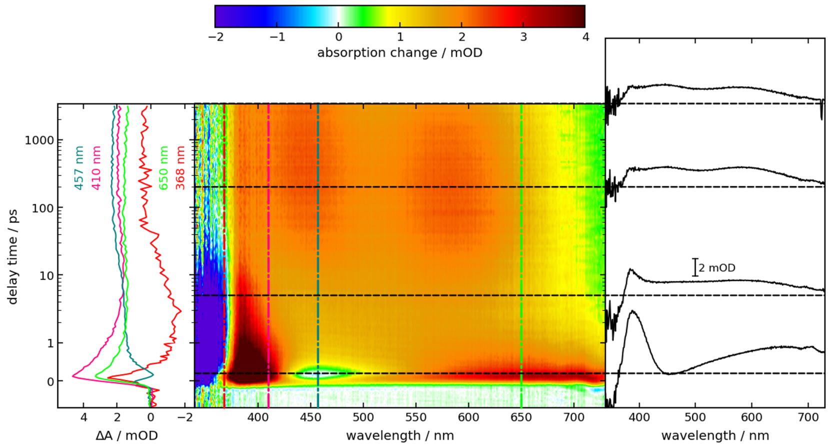

Figure 5.36.: Femtosecond time-resolved spectroscopy data acquired for NHCCuDBM in TFE. The excitation was tuned to 266 nm. In the contour representation (central), the difference absorption signal is color-coded. Vertical lines mark spectral positions for the time traces plotted on the left while horizontal lines mark certain delay times for the difference spectra plotted on the right.

5.2.4. Quantum Chemical Calculations

To further elucidate the photophysics of the ligand and the complex, quantum chemical calculations were performed. Details on the applied methods are given in the experimental section 4.4 including a description of how the calculated absorption spectra were obtained based on oscillator strengths. The computations were performed by Jasper Guhl (Institute of Theoretical Chemistry and Computer Chemistry, Prof. C. M. Marian).

The computed ground state absorption spectrum of DBM in MeCN fits the experimental one quite well with only minor discrepancies between each. The computed absorption coefficient is slightly higher for $\lambda > 370$ nm and around the peak from 320 to 350 nm (see Figure 5.37a).

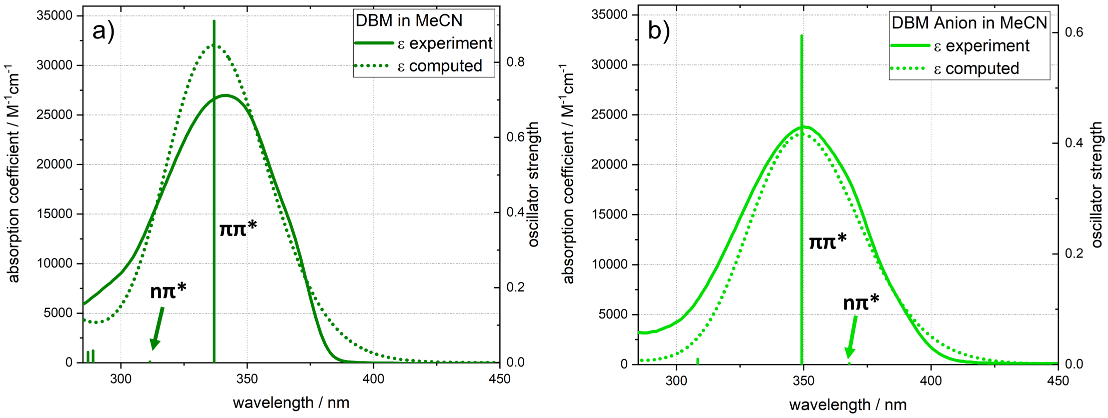

Figure 5.37.: Comparison of calculated UV/Vis absorption coefficient spectra (dashed line, left y-axis), including the oscillator strengths of each transition (vertical lines, right y-axis) of a) DBM and b) DBM$^-$ with experimental spectra (solid line).

For $\lambda < 320$ nm the computed absorption lies below the experimental one. According to the calculations, the longest wavelength absorption peak is made up of a $^1\pi\pi^*$ transition, in line with the rather large absorption coefficient of that band. Vertically, this $^1\pi\pi^*$ state constitutes the lowest excited singlet state. In the absorption spectrum, the second lowest excited state is an $^1n\pi^*$ state with a – for such transitions typical – oscillator strength of almost zero.[17] In the literature, the energetic order of the $^1\pi\pi^*$ and $^1n\pi^*$ states is not clearly given. As for other symmetric β-diketones, such as malonaldehyde or acetylacetone, the $^1n\pi^*$ state constitutes the lowest excited state, which is assumed to apply for DBM as well.[161,170] Another study suggests the possibility that due to extended conjugation by the presence of the electron-rich benzene rings, the energy gap between the "S$_2$" ($^1\pi\pi^*$) and "S$_1$" ($^1n\pi^*$) state is reduced and the $^1\pi\pi^*$ state becomes the one lower in energy.[169]

In the case of the anion DBM$^-$ the computed and the experimental spectra match quite well (see Figure 5.37b). In contrast to DBM, the lowest excited state of the anion is no longer the $\pi\pi^*$ but the $n\pi^*$ state with respect to vertical excitation energy. Presumably, due to the negative charge, the n-orbital is destabilized decreasing the energy of the $n\pi^*$ transition. In line with the experiment, the absorption coefficient is slightly decreased compared to DBM.

The difference densities of the singlet $^1\pi\pi^*$ and $^1n\pi^*$ transitions of DBM and DBM$^-$ are depicted in Figure 5.38. Based on these difference densities – a loss of electron density is marked in red, a gain in electron density is marked in yellow – the $\pi\pi^*$ and $n\pi^*$ characters of the states become clear. It should be pointed out that the difference densities must not be confused with molecular orbitals. For DBM as well as DBM$^-$ a shift of electron density originating from orbitals of mainly π character – perpendicular to the molecular plane – is seen in the case of the $\pi\pi^*$ transition. For the $n\pi^*$ state electron density originating from mainly π character orbitals is shown marking a gain in electron density (yellow), while a loss of electron density (red) can be clearly seen located on rather n character orbitals – parallel to the molecular plane – of the oxygen atoms.

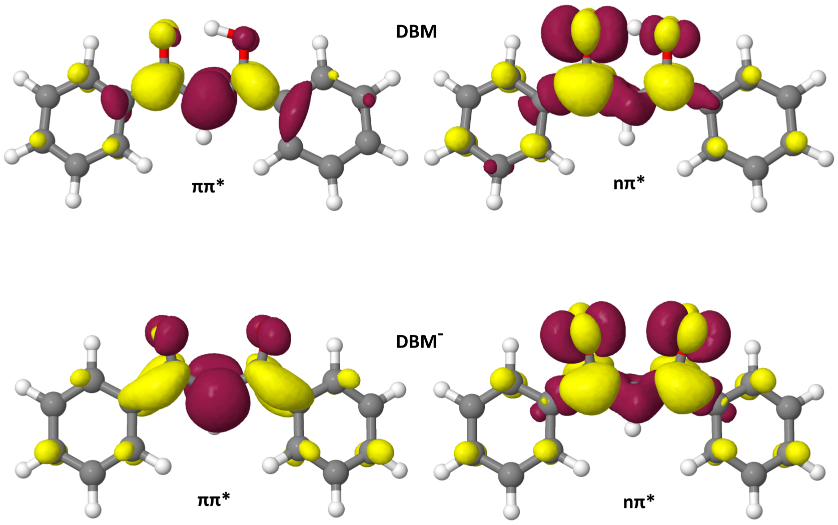

Figure 5.38.: Difference electron densities for the singlet $\pi\pi^*$ and $n\pi^*$ transitions of DBM (top) and DBM$^-$ (bottom). A loss of electron density compared to the ground state is marked in red, and a gain in electron density is marked in yellow.

To further elucidate the anions deactivating pathway its adiabatic energies as well as the

ISC rate constants were calculated. These values are summarized in Figure 5.39.

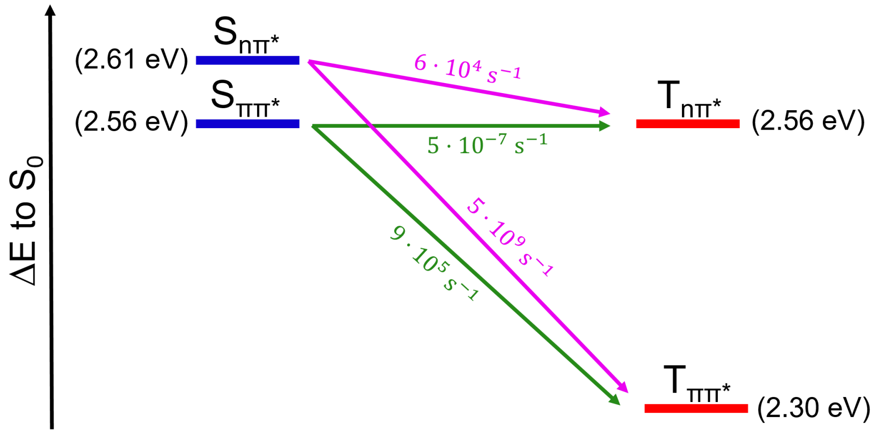

Figure 5.39.: Overview of the calculated intersystem crossing rate constants from the singlet $\pi\pi^*$ and $n\pi^*$ states to the respective triplet states of DBM$^-$. The values given in brackets are the adiabatic energies of the excited states relative to the ground state in eV.

In contrast to the vertical excitation energies given in the absorption spectra where the $^1n\pi^*$ clearly constitutes the lowest singlet state, in terms of the adiabatic energy the $^1\pi\pi^*$ state is the one lowest in energy in close proximity to the $^1n\pi^*$, which lies only 0.05 eV above it. The highest ISC rate constant is calculated for the $^1n\pi^* \rightarrow {}^3\pi\pi^*$ transition with $k_{ISC} \approx$ 5 $\cdot 10^9$ s^{-1} (reciprocal: 200 ps), followed by the $^1\pi\pi^* \rightarrow {}^3\pi\pi^*$ transition with $k_{ISC} \approx 9 \cdot 10^5$ s^{-1} (reciprocal: 1.11 μs). For the $^1n\pi^* \rightarrow {}^3n\pi^*$ transition a rate constant of $k_{ISC} \approx 6 \cdot 10^4$ s^{-1} (reciprocal: 16.7 μs) and for the $^1\pi\pi^* \rightarrow {}^3n\pi^*$ transition a value of $k_{ISC} \approx 5 \cdot 10^{-7}$ s^{-1} (reciprocal: $2 \cdot 10^6$ s) are calculated. Such a low value for the El-Sayed allowed $^1\pi\pi^* \rightarrow {}^3n\pi^*$ transition is remarkable. This low value is related to a minuscule vibronic overlap of both states[6]. The calculated geometries of the triplet and singlet $\pi\pi^*$ and $n\pi^*$ states (see appendix, Figure A.8) reveal a strong distortion of the $^1\pi\pi^*$ state from the planar geometry present in the $^1n\pi^*$ state. The $^3\pi\pi^*$ shows a less distorted geometry compared to the $^1\pi\pi^*$ allowing for a higher ISC rate constant for this transition.

For the complex, only minor differences between the experimental absorption spectrum (in Cx) and the computed one (in vacuum) are present (see Figure 5.40).

---

[6] Precisely, this value amounts to $4.4 \cdot 10^{-9}$ cm^{2}s^{-1} (it arises from the right-hand side of eq. 2.11 excluding the matrix element $|H_{m,n}|^2$, with the "energy" expressed in units of cm^{-1}). In comparison, for the $^1n\pi^* \rightarrow {}^3\pi\pi^*$ transition it is $2.8 \cdot 10^6$ cm^{2}s^{-1}, for $^1\pi\pi^* \rightarrow {}^3\pi\pi^*$ it is $5.3 \cdot 10^6$ cm^{2}s^{-1}, and for $^1n\pi^* \rightarrow {}^3n\pi^*$ it is $2.8 \cdot 10^7$ cm^{2}s^{-1}.

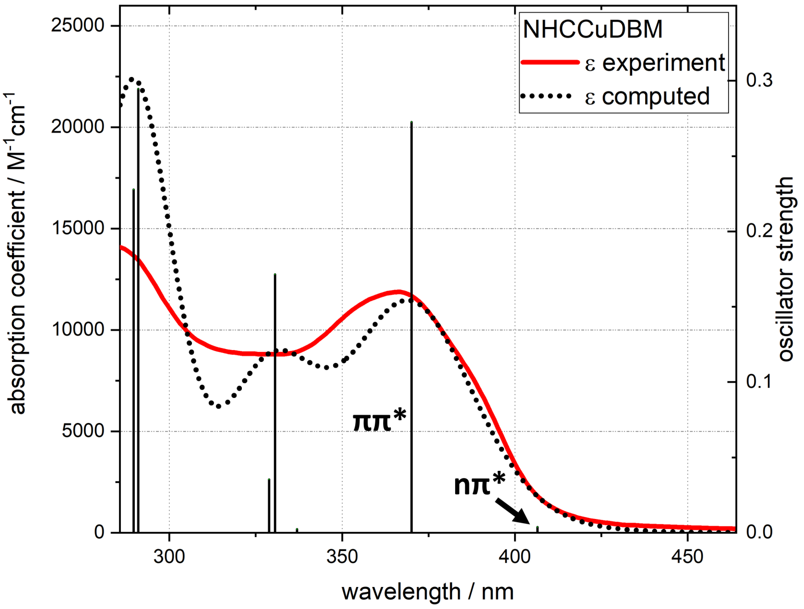

Figure 5.40.: Comparison of calculated UV/Vis absorption coefficient spectra (dashed line, left y-axis), including the oscillator strengths of each transition (vertical lines, right y-axis) of NHCCuDBM in vacuum with experimental spectra recorded in Cx (solid line).

Around 350 and 315 nm the computed spectrum shows less absorption than the experimental one. The absorption for wavelengths < 300 nm is overestimated. Overall, both spectra match quite well, especially for longer wavelengths ($\lambda > 370$ nm). Here, similar to the situation of the anion, the lowest excited state is of $n\pi^*$ character and it bears only little oscillator strength. The lowest wavelength absorption peak at 330 nm is mainly made up of a $\pi\pi^*$ transition, which is the second lowest excited state according to computation. Although, for simplicity, these two lowest states are here referred to as $\pi\pi^*$ and $n\pi^*$ states, the difference densities (see Figure 5.41) reveal that besides π- and n-orbital contributions, the transitions bear some MLCT and LLCT character as well. This is in accordance with the similar copper(I) DBM carbene complex where the carbene ligand constitutes a CAAC. There, lowest excited states with similar $\pi\pi^*$ and $n\pi^*$ and mixed MLCT orbital contributions were found.[181]

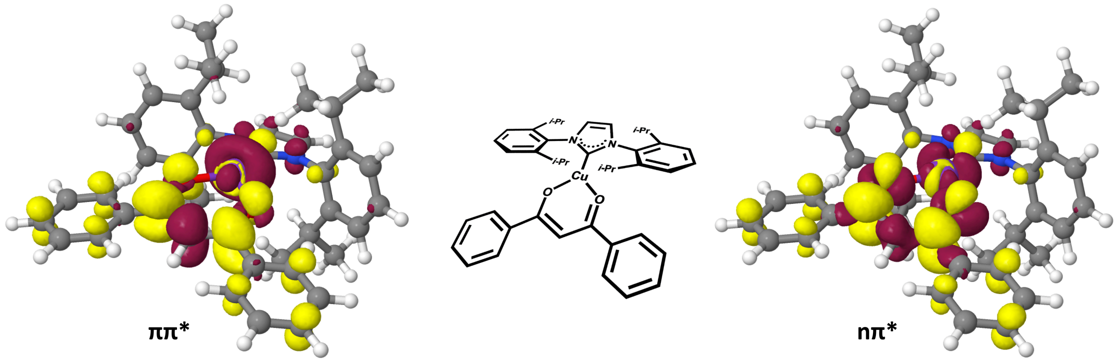

Figure 5.41.: Difference electron densities for the singlet $\pi\pi^*$ and $n\pi^*$ transitions of NHCCuDBM. A loss of electron density compared to the ground state is marked in red, and a gain in electron density is marked in yellow. For the sake of clarity, the skeletal structural formula of NHCCuDBM is given as well.

Furthermore, the equilibrium geometries of the first and second excited states were computed (see Figure 5.42). Both states show a strongly differing geometry. The equilibrium geometry of the S_2 ($\pi\pi^*$) state shows a distortion of the NHC-Cu-DBM plane in which the DBM plane is slightly tilted (by 25°) relative to the NHC-Cu plane, while both oxygen atoms (of the DBM) remain in the NHC-Cu plane (point group C_S). The angles between the C–Cu–$O_{1/2}$ moiety (see Figure 5.42) are similar with both 124°. Similarly, the respective bond lengths amount both to 1.89 Å. The C–Cu bond length amounts to 1.91 Å. In the case of the S_1 ($n\pi^*$) state, the DBM ligand is tilted (by 18°) along two different axes distinct from the one of the S_2 state (point group C_1). The C–Cu–$O_{1/2}$ angles amount to 153° and 107°, respectively. The respective bond lengths are 1.82 and 1.88 Å, respectively. The C–Cu bond length amounts to 1.94 Å.

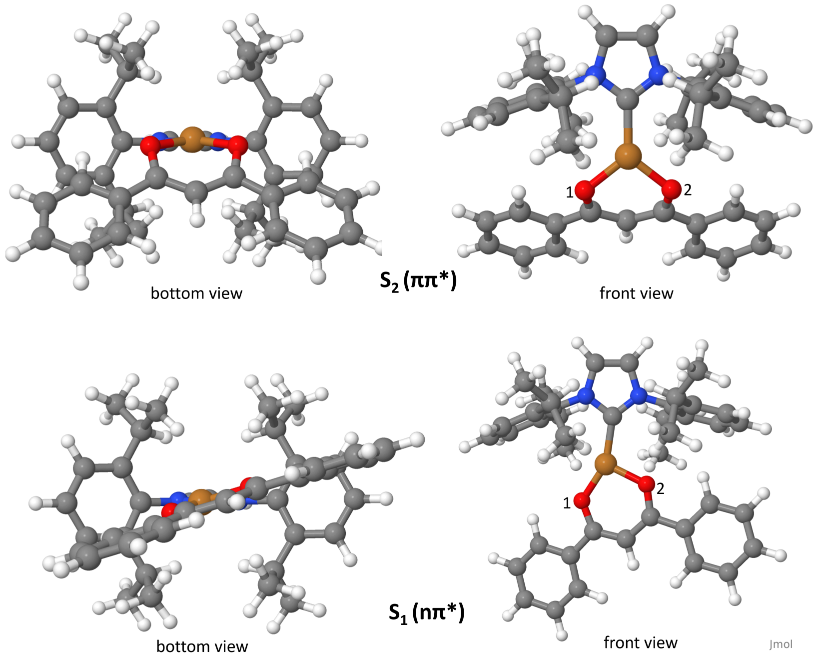

Figure 5.42.: Equilibrium geometries of NHCCuDBM in the singlet $\pi\pi^*$- (top) and the singlet $n\pi^*$ state (bottom), viewed from two different angles: "bottom" perspective (left; along the DBM-Cu-NHC axis), "front" perspective (right; perpendicular to the DBM plane).

To further study the photokinetics of the complex and to understand which state is populated upon photoexcitation (i.e. observed in the transient absorption experiment), the absorption spectra of the lowest excited singlet as well as triplet states (i.e. ${}^1\pi\pi^*$, ${}^1n\pi^*$, ${}^3\pi\pi^*$, and ${}^3n\pi^*$) were calculated quantum chemically. A comparison of these spectra with the experimental transient absorption spectrum is depicted in Figure 5.43.

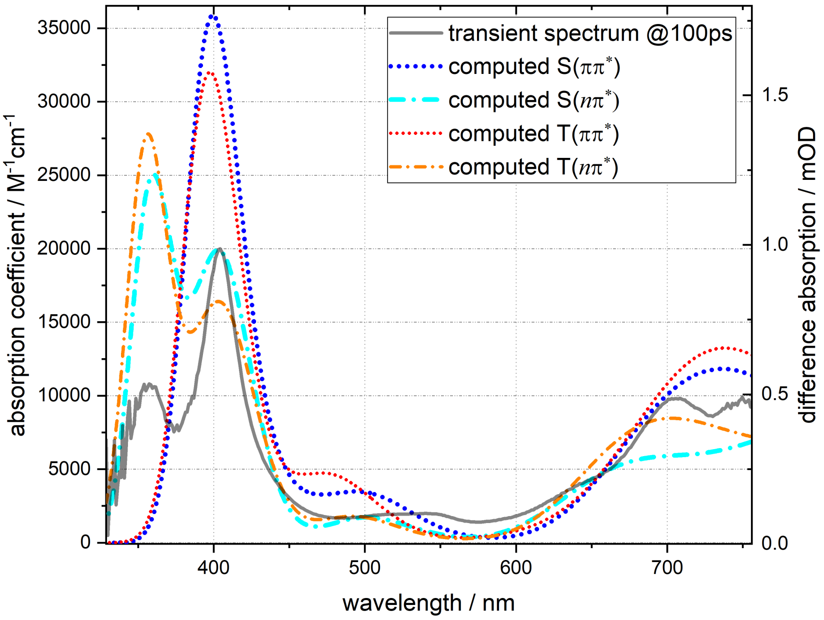

Figure 5.43.: Comparison of calculated UV/Vis absorption coefficient spectra (dashed lines, left y-axis) of the singlet (blueish) and triplet (reddish) $n\pi^*$ and $\pi\pi^*$ states of NHCCuDBM in THF, with the experimental transient absorption spectrum for a delay time of 100 ps recorded in Cx (grey solid line, right y-axis).

As seen in the comparison, all spectra are in good agreement with the experimental spectrum. For smaller wavelengths (< 400 nm) the experimentally observed absorption is weaker than the calculated one in the case of the singlet and triplet $n\pi^*$ states. This can be rationalized by ground state bleaching which contributes as a negative signal and thus lowers the observed excited state absorption signal there. In the case of the singlet and triplet $\pi\pi^*$ states, transitions with wavelengths $\lesssim 400$ nm were not calculated, due to a high density of states ($>$ 70 states in the depicted region), thus, reaching the computational limit. Based on these data, a clear differentiation between the states is not possible. However, a transition from a singlet or triplet $\pi\pi^*$ to a singlet or triplet $n\pi^*$ state (IC or ISC) would be indicated by a loss of transient absorption signal according to these calculations. Such a decrease is not seen in the transient absorption data (see section 5.2.3.2).

To evaluate the possibility of ISC occurring from the singlet $\pi\pi^*$ and $n\pi^*$ states into the respective triplet states, the ISC rate constants were calculated as well. The rate constants together with the adiabatic energies of the respective states are summarized in Figure 5.44.

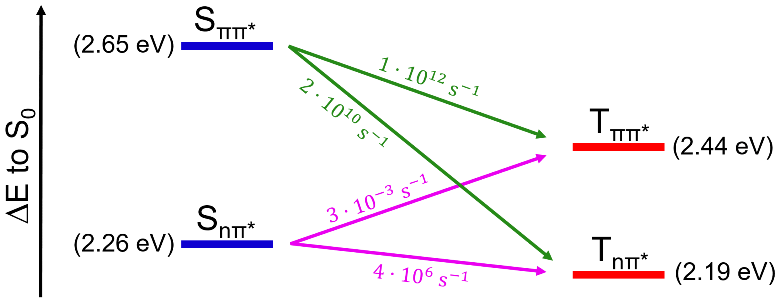

Figure 5.44.: Overview of the calculated intersystem crossing rate constants from the singlet $\pi\pi^*$ and $n\pi^*$ states to the respective triplet states of NHCCuDBM. The values given in brackets are the adiabatic energies of the excited states relative to the ground state in eV.

In contrast to the calculations of the anion, for the complex the $^1n\pi^*$ state clearly constitutes the lowest excited singlet state in terms of both adiabatic as well as vertical energies. The highest ISC rate constant is calculated for the $^1\pi\pi^* \rightarrow {}^3\pi\pi^*$ transition with $k_{ISC} \approx 1 \cdot 10^{12}$ s^{-1} (reciprocal: 1 ps), followed by the $^1\pi\pi^* \rightarrow {}^3n\pi^*$ transition with $k_{ISC} \approx 2 \cdot 10^{10}$ s^{-1} (reciprocal: 50 ps). For the $^1n\pi^* \rightarrow {}^3n\pi^*$ transition a rate constant of $k_{ISC} \approx 4 \cdot 10^6$ s^{-1} (reciprocal: 250 ns) and for the $^1n\pi^* \rightarrow {}^3\pi\pi^*$ transition a value of $k_{ISC} \approx 3 \cdot 10^{-3}$ s^{-1} (reciprocal: 333 s) are calculated. The highest ISC rate constant for an apparent El-Sayed forbidden transition can be rationalized with the MLCT character that the $\pi\pi^*$ transition holds and with the energetic proximity of the $^3\pi\pi^*$ to the $^1\pi\pi^*$ state compared to the $^3n\pi^*$ state. The lowest value for the $^1n\pi^* \rightarrow {}^3\pi\pi^*$ mainly originates from the energetic separation, i.e. the energetic higher lying $^3\pi\pi^*$ state, with ≈ 0.2 eV. An in-depth discussion of these values taking into account the experimental data is given in section 5.2.5.

5.2.5. Discussion

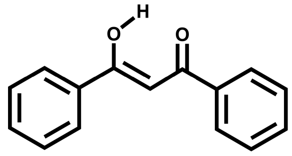

Figure 5.45.: Structure of DBM.

Regarding the spectroscopic analysis of DBM some properties and experiments have been reported before. These are the steady-state absorption as well as time-resolved absorption experiments including the time constants for the deactivating processes upon photoexcitation.[169,170,180] These properties could be confirmed, although the focus was not laid on scrutinizing the involved isomerization kinetics of DBM. Furthermore, with the fluorescence quantum yields and the Strickler-Berg analysis not being reported before (to the best of the authors' knowledge), the photophysical understanding of DBM is deepened. This includes the energetic order of the $^1n\pi^*$ and $^1\pi\pi^*$ states, regarding which, no clear indication is given in the literature.[161,169,170] Taking into account the results of the Strickler-Berg analysis (i.e. radiative rate constants), the FQYs and the subsequently obtained time constants $\tau_{1,SB}$ that match the time constant $\tau_1 = 300$ fs from both time-resolved spectroscopic techniques (transient absorption and emission) very well, indications are given for the $^1\pi\pi^*$ state constituting the emitting state. Presumably, the $^1\pi\pi^*$ also constitutes the lowest excited state, which is then quenched by the isomerization processes (see section 5.2.1). This energetic order of the lowest excited states is strongly supported by quantum chemical calculations. However, only based on the spectroscopic experiments it can not be fully excluded that the emitting and primarily excited $^1\pi\pi^*$ state deactivates with τ_1 into the $^1n\pi^*$ state, which would in this scenario constitute the lowest excited state.

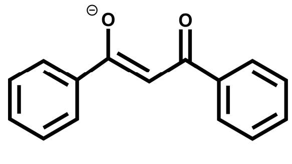

Figure 5.46.: Structure of DBM$^-$.

As the deprotonated form of DBM constitutes the ligand in the respective complex NHCCuDBM, the anion DBM$^-$ was investigated as well. Here, the steady-state absorption behavior was reproduced in comparison to a previous study.[164] Additionally, the FQYs are reported showing that the emission is overall lowered compared to DBM. This is further underlined by a Strickler-Berg analysis yielding a smaller radiative rate constant $k_{r,SB}$ and a subsequently calculated time constant for the emitting state $\tau_{1,SB}$ taking into account the FQY. In line with a previous report on the anion employing time-resolved absorption spectroscopy, the first time constant τ_1 is lowered as well. Besides that, the authors of that study did not find significant differences.[180] However, in contrast to that report, here, a behavior different from the one of DBM is found. Although the results here indicate that there might be a superposition of two ground state species, an excited state lifetime of roughly 10 ps could be found for the deprotonated form. According to quantum chemical calculations, the energetic order of the lowest excited singlet states ($^1n\pi^*$ and $^1\pi\pi^*$) is not unambiguous. Whereas in terms of vertical excitation energy, the lowest excited state is clearly the $^1n\pi^*$ state ($\Delta E = 0.18$ eV), in terms of adiabatic energies the lowest one is the $^1\pi\pi^*$ state with only 0.05 eV apart from the $^1n\pi^*$ state. Though, the overall smaller FQYs of DBM$^-$, despite an extended lifetime, compared to DBM, might indicate that the initially excited $^1\pi\pi^*$ state quickly deactivates into the $^1n\pi^*$ state. The (qualitatively similar) emission observed in the steady-state experiments for the anion would originate from the briefly populated $^1\pi\pi^*$ state. Presumably, it is then the $^1n\pi^*$ state that is quenched within roughly 10 ps upon isomerization mainly into the ground state. This is indicated by the signal of GSB rising simultaneously with the ESA decay, similarly as it is the case for the protonated DBM in the transient absorption spectra. Considering the calculated ISC rate constants, a significant population of a triplet state seems unlikely. The $^1n\pi^* \rightarrow {}^3\pi\pi^*$ transition with $k_{ISC} \approx 5 \cdot 10^9$ s^{-1} (reciprocal: 200 ps) shows the highest of the four relevant ISC rate constants. However, as the major part of the excited state population deactivates with roughly 10 ps it might be possible that a small fraction of molecules undergoes ISC into the $^3\pi\pi^*$ state. With the calculated ISC rate constant and the observed lifetime of 10 ps roughly 5% of excited state population is expected to be in a triplet state when the $^1n\pi^*$ state has decayed. This is well in line with the small featureless ESA signal (≈ 1 mOD), which persists after the decay of the dominant ESA signal and extends beyond the measured time window of the fsTA instrument.

Considering the complex NHCCuDBM, it could be shown that its ligand DBM$^-$ defines the photophysical behavior of the complex to a large extent. This is indicated by the longest wavelength steady-state absorption band, the qualitatively and quantitatively similar emitting behavior (i.e. the shape and position of the fluorescence spectra, and the FQY, respectively) as well as by the transient absorption spectra, that are similar for the anion and the complex. These findings are corroborated by quantum chemical calculations revealing that only minor orbital contributions from the metal and the

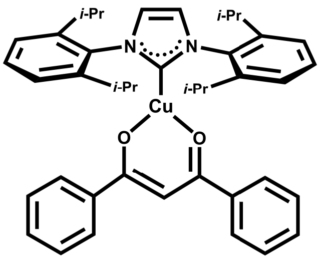

Figure 5.47.: Structure of NHCCuDBM.

carbene are involved in otherwise similar transitions between anion and complex with regard to the $^1\pi\pi^*$ and the $^1n\pi^*$ states. Presumably, for both the anion and the complex, the observed steady-state emission originates from the short-lived S_2 ($\pi\pi^*$) state, which is underlined by a Strickler-Berg analysis and a subsequently calculated fluorescence lifetime (using the FQY) of ≈ 100 fs.

As, in time-resolved data, the first observed kinetic process occurs with the time constant $\tau_1 \approx 5 - 10$ ps and the FQY is in the order of 10^{-5} – 10^{-6} (i.e. very small), the $^1\pi\pi^*$ state is very likely depopulated within the time resolution of the instrument (≈ 100 fs). Based on a comparison of the calculated excited state absorption spectra with the experimental transient absorption spectrum, it is not clear to which of the three energetically accessible states ($^1n\pi^*$, $^3\pi\pi^*$, and $^3n\pi^*$) the emitting $^1\pi\pi^*$ state decays to as these states share similar spectra[7] (see Figure 5.43). Though, based on the signal height (i.e. calculated absorption coefficient of the excited states), which shows a distinct difference between the $\pi\pi^*$ and the $n\pi^*$ states, it is considered unlikely that the state, which is populated subsequently to the $^1\pi\pi^*$ undergoes a transition into a state with different orbital character (i.e. $\pi\pi^* \rightarrow n\pi^*$ or vice versa) since no such change in transient absorption signal is observed in the experiment. Taking the calculated intersystem crossing rate constants into account, only the $^1\pi\pi^* \rightarrow {}^3\pi\pi^*$ transition with $k_{ISC} = 1 \cdot 10^{12}$ s^{-1} (reciprocal: 1 ps) might be fast enough to occur within the time resolution of the instrument (≈ 100 fs) However, this makes a subsequent $^3\pi\pi^* \rightarrow {}^3n\pi^*$ transition necessary, as the $^3n\pi^*$ state constitutes the one with the lowest adiabatic energy, and such a $\pi\pi^* \rightarrow n\pi^*$ transition, again, ought to be observable in the experiment (which is not the case, see above)[8]. The $^1\pi\pi^* \rightarrow {}^3n\pi^*$ transition with $k_{ISC} = 2 \cdot 10^{10}$ s^{-1} (reciprocal: 50 ps) seems unlikely as well. Consequently, a fast (< 100 fs) $^1\pi\pi^* \rightarrow {}^1n\pi^*$ IC transition in accordance with Kasha's rule is considered the most likely one being responsible for the rapid depopulation of the $^1\pi\pi^*$ state.

Given the $^1n\pi^*$ state constitutes the first excited state that is observed in the experiment, the time constant of $\tau_1 \approx 5 - 10$ ps can presumably either

---

[7] Only in the near-infrared (NIR) region, around 1350 nm, a transient absorption band is seen in the calculations for the $^3\pi\pi^*$ state (see appendix Figure A.12). To confirm or exclude the $^3\pi\pi^*$ based on this band, the wavelength range of the fsTA instrument needs to be extended to higher wavelengths, which is, as of today, an ongoing project.

[8] Although not representing the main deactivation pathway, for the time resolution of ≈ 100 fs and the ISC rate constant of $1 \cdot 10^{12}$ s^{-1} (reciprocal: 1 ps) it is expected that up to 10% of excited state population deactivates into the $^3\pi\pi^*$ state.

(**I**) be related to an electronic transition, which cannot be ruled out completely as the excited state spectra of the relevant states look qualitatively similar. However, due to an energetic separation of $\approx +200$ meV and the argument on the signal heights (see above) and an ISC rate constant of $k_{ISC} = 3 \cdot 10^{-3}$ s^{-1} (reciprocal: 333 s), a population of the $^3\pi\pi^*$ is highly improbable. Although the $^3n\pi^*$ is energetically in reach (-70 meV) and the signal heights are not expected to change for this transition according to the computations, the ISC rate constant is with $k_{ISC} = 4 \cdot 10^6$ s^{-1} (reciprocal: 250 ns) still far too small to be considered responsible for τ_1.

Or (**II**), the time constant τ_1 is not related to an electronic transition but to vibrational cooling. This is considered the more likely case (for reasons stated above and) due to the – for such processes typical – spectral shift of the transient absorption band that occurs with τ_1. This is supported by a comparison of the respective DADS$_1$ resembling the first derivative[191] of the transient spectrum (see appendix Figure A.10). Accordingly, the vast majority of excited molecules would eventually deactivate from the $^1n\pi^*$ state to the ground state with τ_2.

The most likely situation, covered by (**II**) is summarized in a kinetic scheme shown in Figure 5.48. Additionally, the dotted grey arrow indicates the possibility of some ($\leq 10\%$) excited state population to quickly deactivate from the $^1\pi\pi^*$ state into the $^3\pi\pi^*$. This excited state population deactivates into the ground state with time constants $\leq \tau_2$ as no transient absorption signal is observed thereafter.

These results on the complex NHCCuDBM further raise the question of why the complexes Eu(DBM)$_3$ and Al(DBM)$_3$ mentioned in the introduction (subsection 5.2.1) show a photophysical behavior similar to DBM rather than the anionic form. A notable feature is the ob-

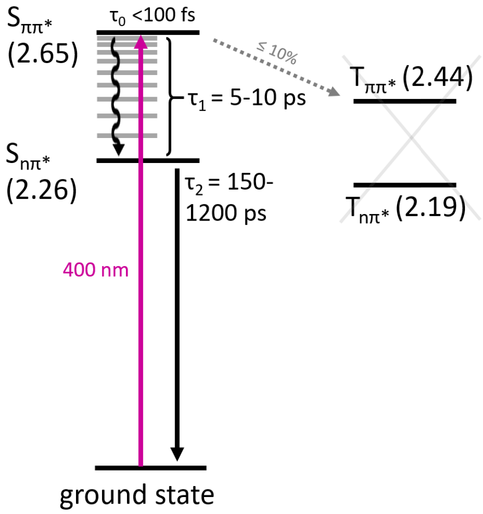

Figure 5.48.: Kinetic scheme of NHCCuPy in solution (Cx, MeCN, EtOH). The time constants were obtained from the fsTA experiments. The electronic state assignment was done on the basis of quantum chemical calculations. The values in brackets show the adiabatic energies of the respective states in eV relative to the S_0 minimum.

served stimulated emission - resembling the one of free DBM - that lasts 0.4 ps and 1.8 ps for Eu(DBM)$_3$ and Al(DBM)$_3$, respectively. This indicates that for these complexes the lowest excited state "still" constitutes the $^1\pi\pi^*$ state. One explanation might be that for the M(DBM)$_3$ complexes DBM is not fully chelated (i.e. only one oxygen is coordinated at a time) or loses its chelating character in the excited state and by so also allowing for rotamerization to occur. This would further explain the overall short lifetimes that are observed.[180] Additional quantum chemical calculations might resolve this discrepancy.

Considering the results of the trigonal CAArC[182] and CAAC[181] complexes important similarities are evident, especially in the case of the CAAC complex and its lowest excited states. There, similar $\pi\pi^*$ and $n\pi^*$ mixed MLCT states were found for the lowest excited states.[181] However, in contrast to NHCCuDBM, the CAAC complex shows emission peaking at $\approx$ 750 nm, which is rationalized with an emitting triplet state at the geometry for which the singlet ground state is strongly destabilized. As no other emission peak is observed in that study,[181] the singlet $\pi\pi^*$ does not seem to contribute to the emission for the CAAC complex, either due to a faster IC into the non-emissive singlet $n\pi^*$ state or a fast ISC into the triplet manifold[9].

Another aspect the experiments show is that from a qualitative point of view, the photophysics of the complex NHCCuDBM are very similar in the solvents Cx, MeCN, and EtOH. Even embedded in a matrix environment the complex shows a similar behavior as being dissolved. Only in EtOH minor differences are evident that could be clarified using TFE as a solvent. Depending on the proticity of the solvent, the complex is decomposed. Presumably, the DBM ligand is ejected and protonated and the respective anionic solvent is coordinated to the copper ion in an equilibrium reaction as demonstrated in a titration experiment using TFE. With respect to the excited state lifetime, the complex NHCCuDBM shows decreased time constants with an increased polarity of the solvent. This might be rationalized with a smaller $S_0 - S_1$ energy gap due to a more stabilized S_1 or more destabilized ground state by polar solvents.

Based on the findings of this study the general idea of coordinating DBM to a d^{10} metal complex to suppress any conformational changes (and by so fluorescence quenching) and extending the overall excited state lifetime could principally be proven.

---

[9] An important difference should be noted, that is, that the emission from the CAAC was measured in the solid state, whereas the here reported emission of NHCCuDBM is recorded in solution.

However, it is further shown, that due to a stabilization of the $^1n\pi^*$ state the energetic order of the lowest excited states is changed and the $^1\pi\pi^*$ constitutes the S_2 state in the complex introducing another quenching process for the emission. Presumably due to this, the overall emission is even smaller compared to DBM. Also, due to the presence of the copper metal, ISC rate constants are increased compared to the free ligand, allowing for fast ISC to occur, which could not be ruled out completely as a deactivating mechanism.

The aspect of the energetic order of the $^1\pi\pi^*$ and $^1n\pi^*$ states could be addressed in further studies. For instance, by the introduction of functional groups with a +I or +M effect on those positions of DBM where the π-orbital shows significant electron densities, a destabilization of the π-orbital can be achieved. This leads to a decrease of the excitation energy of the $\pi\pi^*$ state (if the π^*-orbital is not equally influenced, i.e. the π^*-orbital shows no significant electron density on the position of substitution). As can be seen by the π-orbital of the anion (see Figure 5.49 top) suitable +M or +I substituents in the α-position of the β-diketone unit might serve this purpose. An extension of the π-system of DBM can further be considered. For instance, by replacing DBM with a substituted derivative of bis(2-naphthoyl)methane (see Figure 5.49 bottom), the $\pi\pi^*$ state could constitute the lowest excited state while at the same time, the emission ought to be red-shifted placing the emission closer to the - due to a lack of sustainable alternatives, often desired - deep blue region (≈ 470 nm).[193] Furthermore, it might be worth considering other d^{10} metals, for instance Zinc(II). With the double positive charge located on the metal, it might stabilize the n-orbital and thus increase the energy of the $n\pi^*$ transition.

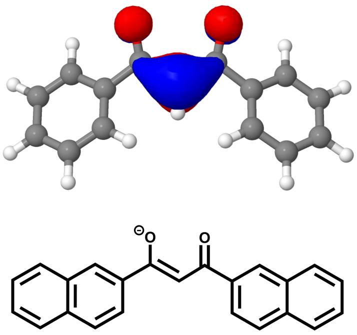

Figure 5.49.: π molecular orbital of DBM$^-$ (top). A significant electron density can be located in the α-position of the β-diketone unit, thus, making it a favorable position for +I/+M substituents. Structure of bis(2-naphthoyl)methane (bottom).

6. Résumé

In this thesis, two copper(I) carbene complexes were investigated for their photophysics. Besides fundamental photophysical properties, such as the emission behavior, for both complexes, an excited state kinetic scheme could be established as a central result. In the case of the complex NHCCuPy, upon photoexcitation, a fast intersystem crossing process of 300 fs followed by the population of a long-lived upper triplet state have been observed. This long-lived upper triplet state might render derivatives of the complex suitable for HIGHrISC applications. Contrary to that, in the case of the complex NHCCuDBM significant population of a triplet state upon photoexcitation is considered unlikely. Fast internal conversion populates the lowest excited singlet state that deactivates in $\lesssim 1$ ns into the ground state. Furthermore, it was shown that the photophysics is strongly determined by the ligand DBM. Unlike for the free ligand, emission quenching due to isomerization is not present in the complex. However, the emitting state in the complex no longer represents the lowest excited state introducing a new quenching mechanism for the emission.

Furthermore, for both complexes, a notable solvent-dependent behavior could be demonstrated and characterized. These results highlight that a solvent environment can fundamentally change the complex and its photophysics accordingly. It further emphasizes that especially with regard to the application as OLED emitters the investigation in different environments (e.g. in different solvents, embedded in a matrix, or as a single crystal) is of great importance and care should be taken to distinguish in which form the complex is actually present.

For future studies and with respect to the application as OLED emitters, it could be useful to study these complexes in sensitization experiments where the triplet state is selectively populated. This would allow further conclusions to be drawn about the triplet states and potential reverse intersystem crossing processes, with special regard to the HIGHrISC application of the complex NHCCuPy and derivatives. Based on the quantum chemically computed transient absorption spectra of NHCCuDBM in the UV/Vis region, a clear assignment of the lowest excited states observed in the experiment is rendered difficult due to their strong similarities. However, in the NIR region pronounced differences in the computed spectra are present. Therefore, it is suggested to conduct the time-resolved measurement of NHCCuDBM covering the NIR region.

Besides that, structural proposals are made for this complex, which could be implemented and investigated in future studies. These suggestions are mainly aimed at the energetic order of the lowest singlet states and could thus prevent quenching of the emission.

In summary, this thesis presents a comprehensive investigation of the photophysics of two copper(I) carbene complexes. The results demonstrate the importance of considering the solvent environment and ligand structure when studying the photophysical properties of such complexes. These findings contribute to the fundamental understanding of the properties of copper(I) carbene complexes and provide useful insights for their potential application in OLEDs.

A. Appendix

Appendix on the study of NHCCuPy

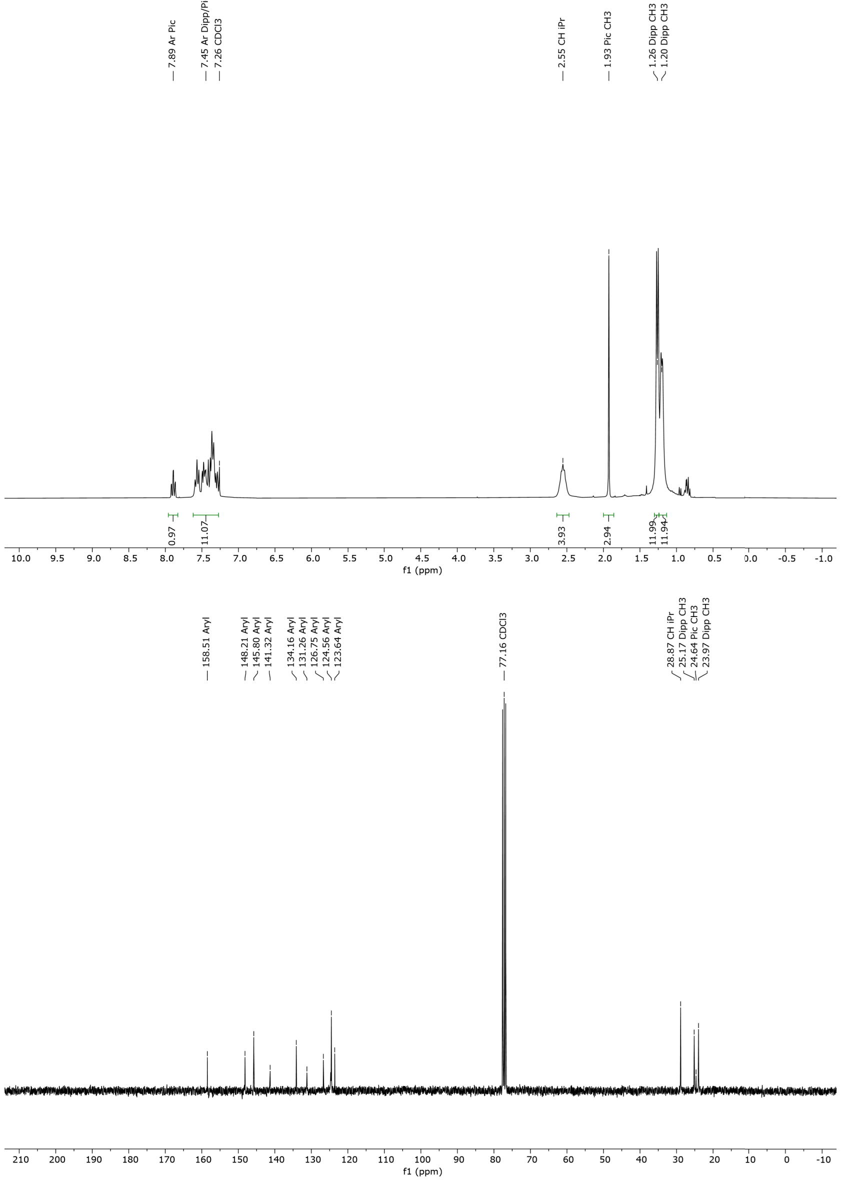

Figure A.1.: The purity of NHCCuPy was verified by ^{1}H-NMR (top), ^{13}C{^{1}H}-NMR (bottom), ESI mass spectrometry and elemental analysis. The analytical data obtained agrees well with the literature[152]. ^{1}H-NMR (300 MHz, $CDCl_3$): δ = 7.89 (ddd, J_{HH} = 7.8/1.6 Hz, 1H, Pic), 7.62-7.27 (m, 11H, Aryl Pic/Dipp), 2.55 (sept, 4H, iPr CH), 1.93 (s, 3H, Pic-CH_3), 1.26 (d, 12H, $^{3}J_{HH}$ = 6.7 Hz, Dipp CH_3), 1.22 (d, 12H, $^{3}J_{HH}$ = 6.8 Hz, Dipp CH_3), ^{13}C{^{1}H}-NMR (75 MHz, $CDCl_3$): δ 158.5 (s, aryl C), 148.2 (s, aryl C), 145.8 (s, aryl C), 141.3 (s, aryl C), 134.2 (s, aryl C), 131.3 (s, aryl C), 126.8 (s, aryl C), 124.6 (s, aryl C), 123.6 (s, aryl C), 28.9 (s, iPr CH), 25.2 (s, Dipp CH_3), 24.6 (s, Pic-CH_3), 24.0 (s, Dipp CH_3). MALDI-TOF: m/z 544.2 ([M]$^{+}$, 31%), Elem anal. Calcd. for $C_{33}H_{44}BCuF_4N_3$ (632.08): C, 62.71; H, 6.86; N, 6.65. Found: C, 62.45; H, 6.71; N, 6.53. Figure from SI of ref[40].

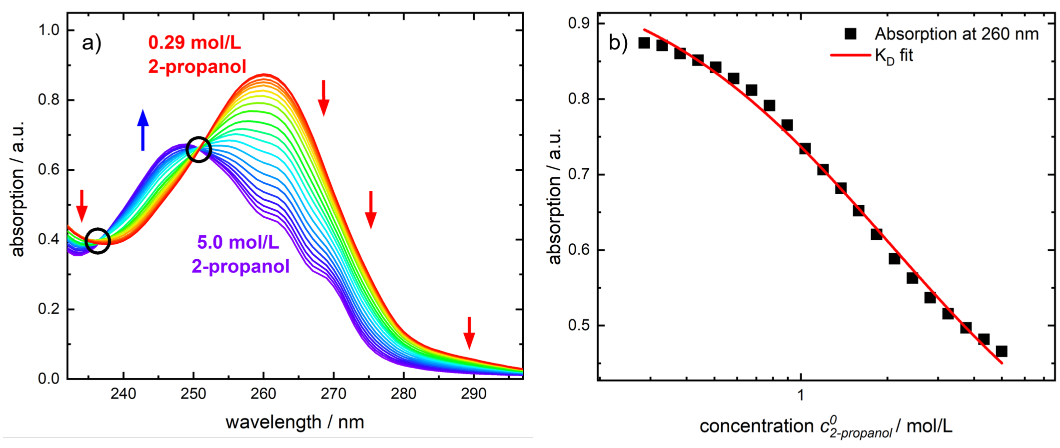

Figure A.2.: UV/Vis absorption behavior of NHCCuPy in 2-propanol. a) Impact of the addition of 2-propanol to absorption spectra of NHCCuPy dissolved in DCM. The initial concentration $c^0_{NHCCuPy}$ of NHCCuPy amounted to $5 \cdot 10^{-5}$ M and remains constant throughout the experiment. Initial 2-propanol concentrations $c^0_{2-propanol}$ ranged from 0.29 M (red) to 5 M (blue). Circles mark isosbestic points. b) Dependence of the absorption at 260 nm on the initial concentration of 2-propanol $c^0_{2-propanol}$ (values from Figure A.2 a)). The squares mark experimental values, the line a fit as described in the main part based on eq. 5.1 - 5.4. During this fit two parameters were varied, namely the dissociation constant K_D and the absorption coefficient of NHCCuPy-2-propanol in DCM $\epsilon_{NHCCuPy-2-propanol}$. According to this fit the dissociation constant K_D equals 2 M and the absorption coefficient NHCCuPy-2-propanol $\epsilon_{NHCCuPy-2-propanol}$ 4140 $M^{-1}cm^{-1}$. Figure from SI of ref[40].

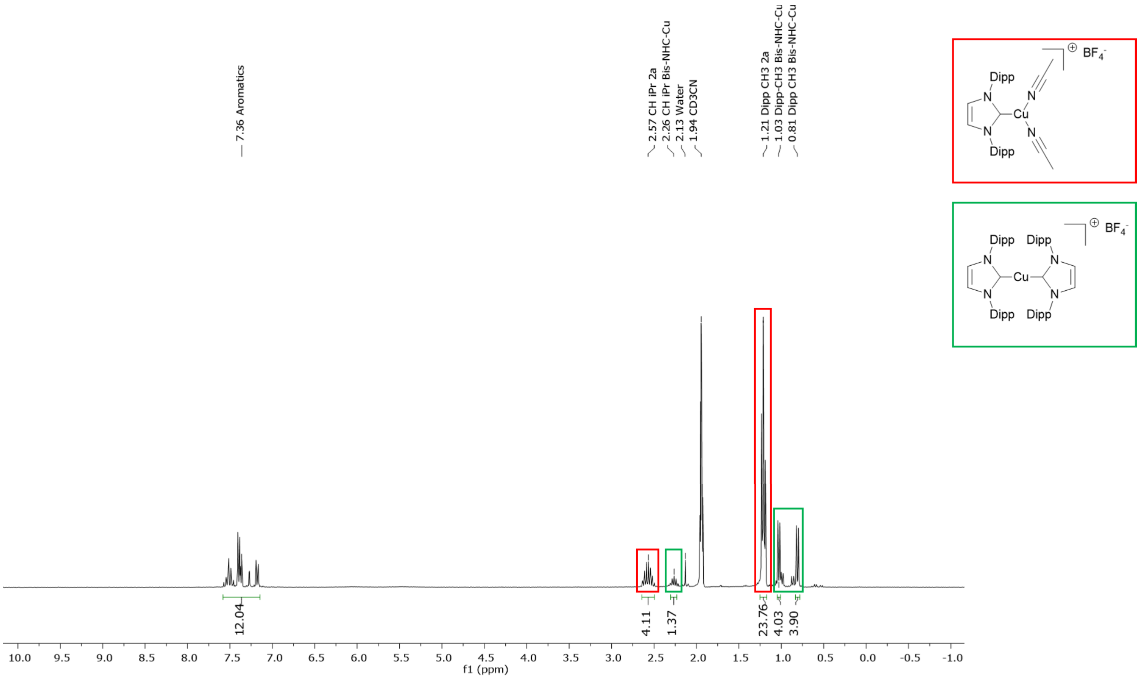

Figure A.3.: Proton NMR spectrum of the reaction mixture of the attempted synthesis of **2a** in MeCN-d^3. For this spectrum, the synthesis was performed directly in MeCN-d^3 in order to measure it with as little time loss as possible, which is why the signal for the complexated MeCN lies within the residual proton signal of the NMR solvent, to which this spectrum is also referenced. It shows two species, one being the expected **2a**, the other being the bis(NHC)-copper(I) tetrafluoroborate. Their presence is also indicated by mass spectrometry, although **2a** is not detected itself, only the mono(MeCN)-copper(I) complex. (MS (ESI(+), MeCN): m/z = 839 [IPr-Cu-IPr]$^+$, 492 [IPr-Cu-MeCN]$^+$, 388 [IPr]$^+$. Figure from SI of ref[40].

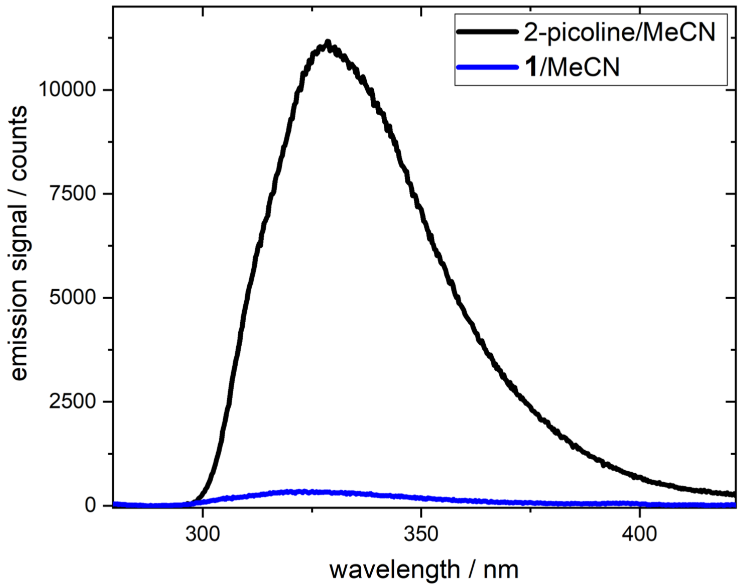

Figure A.4.: Comparison of the emission of similarly concentrated MeCN solutions of NHCCuPy (blue) and 2-picoline (black). The data were recorded using the Kerr setup described in chapter 4. Figure from SI of ref[40].

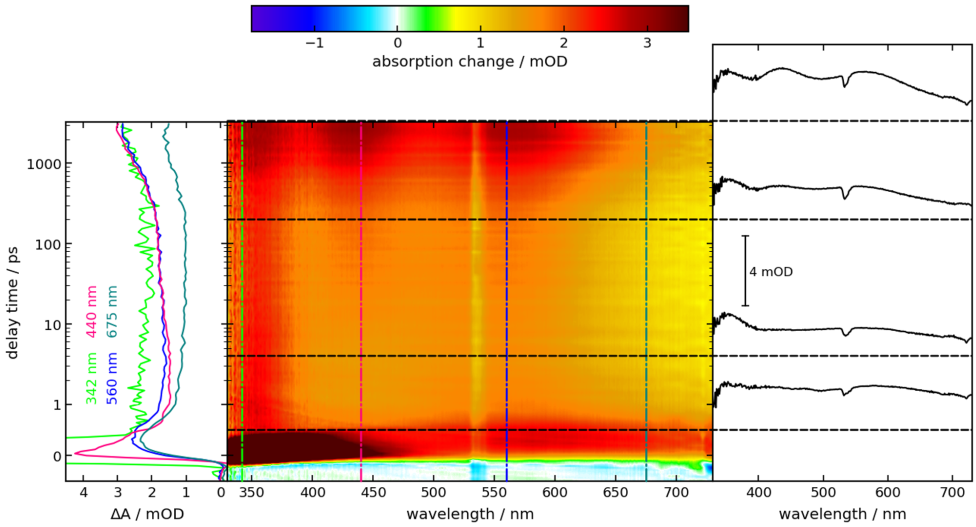

Figure A.5.: Time-resolved spectroscopy data acquired for NHCCuPy in DCM from fsTA experiment. The excitation was tuned to 266 nm. In the contour representation (central) the difference absorption signal is color-coded. Vertical lines mark spectral positions for the time traces plotted on the left while horizontal lines mark certain delay times for the difference spectra plotted on the right. Figure from SI of ref[40].

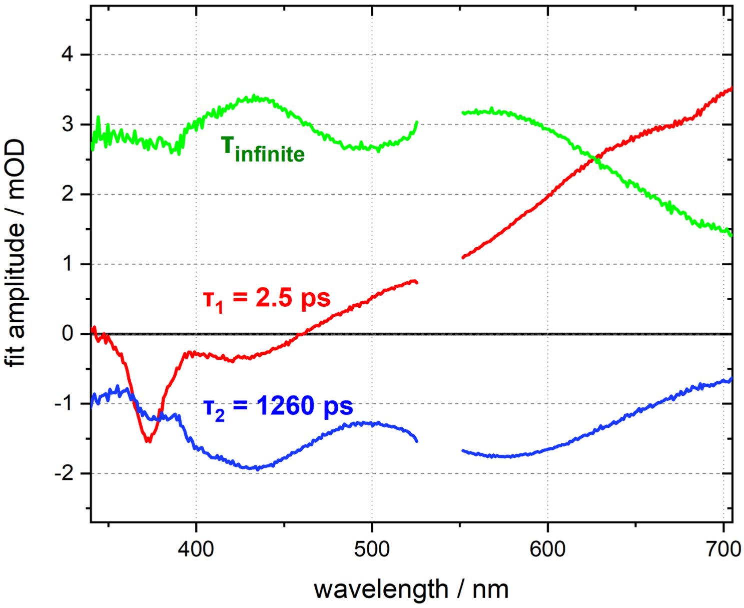

Figure A.6.: Decay-associated difference spectra obtained from fsTA experiment of NHCCuPy in DCM. Due to strong solvent contributions around time zero that could not be fully corrected for, the first time constant of 2.5 ps and the respective DADS are less reliable. Figure from SI of ref[40].

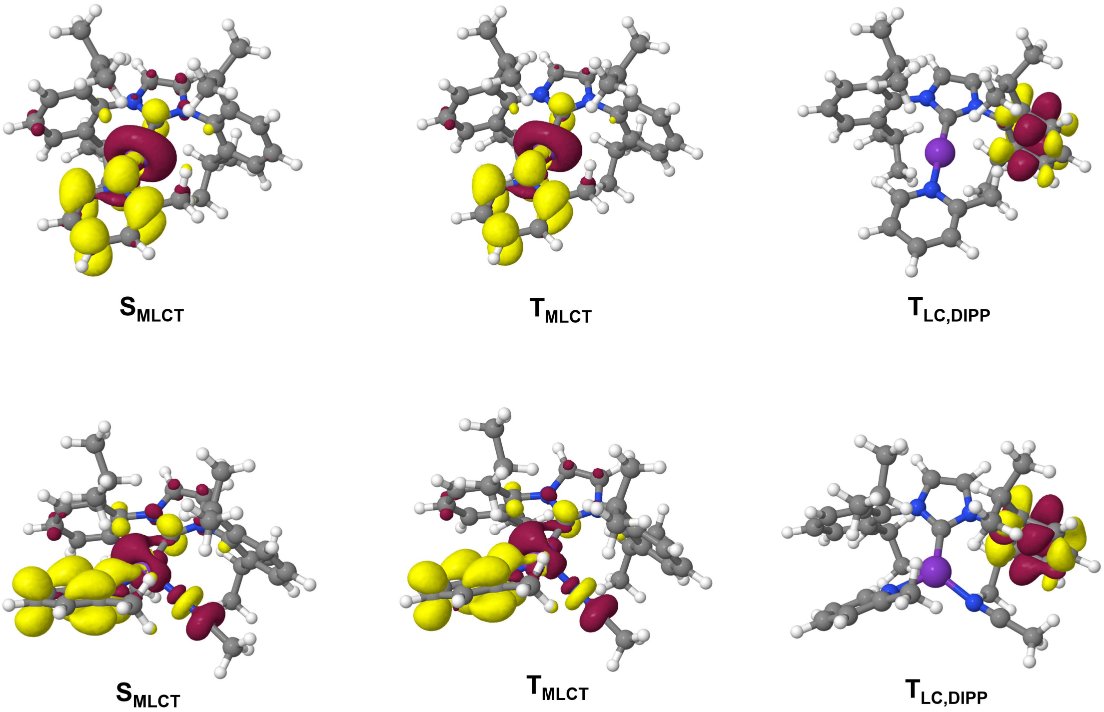

$\mathbf{S_{MLCT}}$ $\mathbf{T_{MLCT}}$ $\mathbf{T_{LC,DIPP}}$

$\mathbf{S_{MLCT}}$ $\mathbf{T_{MLCT}}$ $\mathbf{T_{LC,DIPP}}$

Figure A.7.: Electron difference densities for the S_{MLCT}, T_{MLCT}, and $T_{LC,DIPP}$ states of NHCCuPy (top) and **2b** (bottom). Figure from SI of ref[40].

Table A.1.: Cartesian coordinates (in Å) for the S_0 geometries of compound NHCCuPy in DCM.

C	0.903679	4.401519	-0.447257
C	-0.295125	5.100018	-0.328500
C	-1.406743	4.497918	0.255504
C	-1.341755	3.188559	0.743138
C	-0.113743	2.516360	0.622136
C	1.021153	3.089753	0.024342
N	-0.027964	1.165870	1.091701
C	-0.306534	0.097613	0.312827
N	-0.113554	-0.971301	1.117696
C	0.279046	-0.583047	2.382297
C	0.334253	0.776781	2.365469
C	-0.312563	-2.316762	0.668654
C	0.775369	-2.998182	0.096717
C	0.539252	-4.287845	-0.390422
C	-0.725528	-4.864555	-0.305968
C	-1.782989	-4.163013	0.266708
C	-1.600223	-2.869901	0.768564
C	2.138408	-2.349064	-0.053629
C	3.272890	-3.243895	0.445421
C	-2.769598	-2.092991	1.343652
C	-3.739207	-1.684174	0.231678
C	2.305639	2.308019	-0.174343
C	2.465468	1.930423	-1.650061
C	-2.575801	2.510282	1.306682
C	-3.252433	3.334456	2.402027
C	-3.481388	-2.861162	2.457948
C	-3.548607	2.171250	0.173185
C	3.532526	3.051548	0.353930
C	2.361488	-1.916474	-1.505499
H	0.481930	-1.302338	3.172248
H	0.595545	1.496339	3.137765
H	-2.772109	-4.627092	0.317654
H	1.356675	-4.849256	-0.851391
H	-0.889974	-5.873465	-0.695726
H	-2.346041	5.053764	0.325184
H	1.762164	4.883120	-0.924083
H	-0.366488	6.125173	-0.704000
H	-2.376579	-1.164181	1.789589
H	-2.262844	1.557037	1.764231
H	2.225176	1.367689	0.395861
H	2.150123	-1.435590	0.564010
H	-4.420953	1.617152	0.561800
H	-3.915253	3.088200	-0.321891
H	-2.547542	3.570426	3.217809
H	-4.098694	2.770728	2.831880
H	-3.653368	4.286219	2.011324
H	-2.778035	-3.143495	3.260183
H	-3.956452	-3.783774	2.080807
H	-4.275847	-2.236239	2.901849
H	-3.228141	-1.068616	-0.530293
H	-4.572514	-1.088004	0.642941
H	-4.165882	-2.569408	-0.272845
H	1.576558	-1.210534	-1.831519
H	2.344750	-2.786287	-2.186337
H	3.336780	-1.410724	-1.615970
H	3.381788	-4.152852	-0.171791
H	3.104824	-3.558450	1.489853
H	4.231430	-2.698231	0.400867
H	3.412431	3.313922	1.419250
H	3.721122	3.983197	-0.207800
H	4.431228	2.418016	0.255542
H	2.564120	2.830982	-2.282102
H	1.590299	1.357550	-2.007674
H	3.364219	1.306191	-1.796887
Cu	-0.837437	0.075276	-1.482305
N	-1.364420	0.042411	-3.306895
C	-2.141256	0.079837	-5.964384
C	-1.516101	1.208331	-3.957716
C	-1.589015	-1.125772	-3.947509
C	-1.981807	-1.125616	-5.287139
C	-1.903144	1.274738	-5.287853
H	-1.316393	2.115681	-3.380268
C	-1.399463	-2.390379	-3.171502
H	-2.160743	-2.077704	-5.791661
H	-2.013841	2.245099	-5.776325
H	-2.448904	0.085760	-7.013967
H	-1.611093	-3.275261	-3.790040
H	-2.065090	-2.415256	-2.290790
H	-0.363975	-2.469330	-2.795746

Table A.2.: Cartesian coordinates (in Å) for the S_0 geometries of compound NHCCuPy in MeCN.

C	0.909792	4.408058	-0.433738
C	-0.289266	5.106759	-0.317525
C	-1.403432	4.503313	0.260351
C	-1.341004	3.191983	0.743353
C	-0.113251	2.519163	0.624029
C	1.024577	3.094547	0.033779
N	-0.029706	1.167373	1.089671
C	-0.308889	0.100255	0.309063
N	-0.115819	-0.969494	1.113182
C	0.277511	-0.583051	2.378165
C	0.332636	0.776603	2.363009
C	-0.313428	-2.314443	0.662637
C	0.773138	-2.991538	0.083203
C	0.537750	-4.280355	-0.406938
C	-0.725141	-4.860565	-0.317622
C	-1.781196	-4.163695	0.263676
C	-1.598823	-2.871726	0.768649
C	2.134570	-2.339890	-0.069996
C	3.268693	-3.227955	0.442014
C	-2.766293	-2.098518	1.352325
C	-3.735954	-1.677828	0.244852
C	2.309367	2.312567	-0.161574
C	2.471922	1.933468	-1.636581
C	-2.576779	2.513042	1.302048
C	-3.252293	3.333140	2.401095
C	-3.478729	-2.875397	2.460000
C	-3.549298	2.181382	0.166257
C	3.535497	3.056111	0.368151
C	2.361622	-1.920241	-1.524879
H	0.480643	-1.303218	3.167181
H	0.594151	1.495109	3.136149
H	-2.769031	-4.630161	0.317775
H	1.353913	-4.837637	-0.875298
H	-0.889506	-5.868099	-0.711011
H	-2.342678	5.059584	0.328247
H	1.770312	4.890645	-0.905904
H	-0.358872	6.133008	-0.690453
H	-2.371204	-1.174787	1.806611
H	-2.265995	1.557143	1.755228
H	2.227801	1.373037	0.409628
H	2.142341	-1.420781	0.539041
H	-4.421672	1.625077	0.551722
H	-3.915301	3.101314	-0.323814
H	-2.547483	3.561602	3.219187
H	-4.100763	2.769241	2.826434
H	-3.649491	4.288399	2.014976
H	-2.774915	-3.167061	3.258589
H	-3.957422	-3.792719	2.074459
H	-4.270429	-2.251851	2.910749
H	-3.224292	-1.055677	-0.511231
H	-4.568101	-1.084383	0.662509
H	-4.163481	-2.557913	-0.267959
H	1.575965	-1.219386	-1.859804
H	2.349804	-2.795899	-2.198283
H	3.335837	-1.412454	-1.635594
H	3.377610	-4.145169	-0.163003
H	3.099012	-3.527901	1.490538
H	4.227208	-2.682671	0.391481
H	3.413540	3.319016	1.433172
H	3.725579	3.987082	-0.194352
H	4.433717	2.421519	0.271857
H	2.572599	2.833548	-2.269093
H	1.596916	1.361296	-1.995238
H	3.370490	1.308178	-1.780343
Cu	-0.841635	0.075957	-1.486084
N	-1.368854	0.034222	-3.311197
C	-2.135184	0.057789	-5.972004
C	-1.510174	1.196413	-3.970815
C	-1.599432	-1.136828	-3.944290
C	-1.986776	-1.143881	-5.285484
C	-1.891842	1.255827	-5.302945
H	-1.306558	2.106368	-3.399086
C	-1.422850	-2.396809	-3.158065
H	-2.169942	-2.098369	-5.783908
H	-1.994177	2.223475	-5.798534
H	-2.438553	0.058259	-7.022837
H	-1.639143	-3.284656	-3.770688
H	-2.092541	-2.408951	-2.280235
H	-0.389500	-2.480653	-2.777632

Table A.3.: Cartesian coordinates (in Å) for the S_0 geometries of compound **2a** in DCM.

Cu	0.672682	0.706269	0.102012
N	2.245140	1.031018	-0.996783
C	-0.364579	-0.912686	0.035661
N	-1.576561	-1.159864	0.590492
C	-2.005721	-2.446766	0.332322
C	-1.027669	-3.033586	-0.408911
N	-0.045068	-2.078480	-0.578154
C	-2.286814	-0.189598	1.366578
C	-2.099041	-0.182898	2.759123
C	-2.760685	0.806587	3.493899
C	-3.573286	1.744776	2.860961
C	-3.737321	1.714117	1.478556
C	-3.096712	0.743918	0.699588
C	-1.163595	-1.160667	3.445060
C	0.140358	-0.458090	3.833580
C	-3.242195	0.750443	-0.810094
C	-4.706445	0.723460	-1.250631
C	1.177936	-2.256674	-1.299722
C	1.177061	-2.022674	-2.685584
C	2.398765	-2.133486	-3.357148
C	3.565497	-2.464309	-2.670518
C	3.533237	-2.693141	-1.297666
C	2.335492	-2.595595	-0.580635
C	-0.079074	-1.590328	-3.419056
C	-0.073757	-0.071594	-3.617425
C	2.319071	-2.807433	0.921427
C	2.892691	-4.169079	1.317033
C	-0.278623	-2.327135	-4.742960
C	3.044609	-1.663535	1.634048
C	-2.496108	1.944504	-1.411224
C	-1.813676	-1.852096	4.643418
H	-0.946566	-4.034452	-0.826927
H	-2.956965	-2.828332	0.696468
H	2.444125	-1.949842	-4.434191
H	4.458820	-2.945653	-0.772244
H	4.512101	-2.543573	-3.213569
H	-4.370936	2.463736	0.995505
H	-2.632517	0.852103	4.579308
H	-4.081035	2.512535	3.452601
H	-0.944899	-1.831521	-2.779837
H	-2.766370	-0.164248	-1.201321
H	-0.902864	-1.948395	2.718900
H	1.268561	-2.787346	1.256029
H	-2.552611	1.923338	-2.513681
H	-1.430740	1.928945	-1.120600
H	-2.928100	2.899686	-1.062475
H	-5.236596	-0.145929	-0.824657
H	-4.771058	0.659614	-2.351019
H	-5.243717	1.636513	-0.938880
H	-0.264350	-3.421543	-4.599731
H	0.501426	-2.068426	-5.480424
H	-1.252206	-2.051414	-5.184280
H	0.006406	0.451545	-2.649200
H	-1.003450	0.259522	-4.113416
H	0.780745	0.239618	-4.245468
H	2.592271	-0.689364	1.375918
H	4.111036	-1.628194	1.348077
H	2.986189	-1.789856	2.729297
H	3.963738	-4.250734	1.060522
H	2.357072	-4.991026	0.811115
H	2.799541	-4.318407	2.407129
H	-2.749974	-2.359481	4.352931
H	-2.049365	-1.138261	5.452209
H	-1.128148	-2.610221	5.060749
H	-0.047845	0.356269	4.556685
H	0.628631	-0.020996	2.945732
H	0.843218	-1.172753	4.297409
C	3.116113	1.114176	-1.750921
C	4.194826	1.230006	-2.708416
H	4.880557	0.373493	-2.606303
H	4.750076	2.166250	-2.535351
H	3.780128	1.239996	-3.730043
C	-0.199777	2.985188	1.995501
C	-0.741810	3.943528	2.933557
H	-0.114630	4.849115	2.958335
H	-0.774201	3.494063	3.939652
H	-1.765529	4.214938	2.629148
N	0.221090	2.207424	1.252300

Table A.4.: Cartesian coordinates (in Å) for the S_0 geometries of compound **2b** in DCM.

C	0.855324	4.239279	-0.827039
C	-0.389722	4.834044	-1.009034
C	-1.549680	4.185390	-0.590746
C	-1.491870	2.925474	0.012919
C	-0.221183	2.342741	0.166882
C	0.967956	2.978256	-0.229397
N	-0.129580	1.034199	0.738348
C	-0.031257	-0.095397	-0.005623
N	0.089845	-1.082079	0.917768
C	0.072597	-0.582898	2.206281
C	-0.062333	0.764221	2.092455
C	0.313839	-2.452692	0.571387
C	1.634982	-2.927318	0.576985
C	1.840873	-4.268352	0.231381
C	0.772356	-5.087292	-0.117878
C	-0.526035	-4.579874	-0.141827
C	-0.785541	-3.249435	0.199343
C	2.817540	-2.032783	0.899470
C	3.595655	-2.538502	2.115494
C	-2.193356	-2.682255	0.183748
C	-3.116914	-3.379291	-0.812218
C	2.324989	2.318761	-0.065058
C	2.837892	1.799118	-1.410661
C	-2.751516	2.193530	0.440495
C	-3.816186	3.119202	1.026152
C	-2.805409	-2.693862	1.588735
C	-3.312465	1.370351	-0.722775
C	3.344834	3.241143	0.603377
C	3.723029	-1.862310	-0.322992
H	0.167074	-1.224249	3.079681
H	-0.114748	1.548556	2.843945
H	-1.349116	-5.235184	-0.435535
H	2.856788	-4.674597	0.226598
H	0.951647	-6.133176	-0.385196
H	-2.517454	4.670282	-0.740747
H	1.756156	4.762966	-1.159235
H	-0.458493	5.818372	-1.481683
H	-2.112077	-1.627472	-0.132587
H	-2.468414	1.481288	1.234082
H	2.198582	1.444264	0.594572
H	2.431464	-1.032031	1.151800
H	-4.204727	0.803672	-0.402502
H	-2.560005	0.655215	-1.093748
H	-3.599541	2.024546	-1.565836
H	-3.405879	3.747158	1.835875
H	-4.644628	2.520377	1.442428
H	-4.249270	3.786533	0.260614
H	-2.187174	-2.133207	2.309529
H	-2.906397	-3.729772	1.958815
H	-3.809557	-2.234225	1.574041
H	-2.656085	-3.450502	-1.812447
H	-4.059020	-2.812499	-0.907967
H	-3.381975	-4.399842	-0.484109
H	3.157400	-1.453762	-1.177665
H	4.169800	-2.824297	-0.632381
H	4.548539	-1.165257	-0.094454
H	4.042423	-3.530938	1.926968
H	2.941965	-2.623706	3.000925
H	4.416944	-1.842518	2.360957
H	2.969297	3.618844	1.569994
H	3.591367	4.110887	-0.030481
H	4.284295	2.692353	0.790570
H	2.966852	2.624120	-2.134024
H	2.132109	1.067165	-1.845035
H	3.811395	1.293361	-1.286664
Cu	-0.079491	-0.309757	-1.913016
N	-1.004200	0.848968	-3.284730
C	-2.339925	2.585779	-4.995510
C	-0.604855	2.120093	-3.423461
C	-2.070556	0.411859	-3.983272
C	-2.757472	1.265674	-4.849862
C	-1.237596	3.024860	-4.266188
H	0.252538	2.427927	-2.818074
C	-2.491210	-1.007032	-3.769465
H	-3.620240	0.887644	-5.403839
H	-0.871934	4.051859	-4.334243
H	-2.872685	3.263917	-5.668526
H	-3.330982	-1.285614	-4.423584
H	-2.805064	-1.158216	-2.721226
H	-1.647834	-1.693108	-3.957758
N	0.763845	-1.870694	-2.759992
C	1.249001	-2.873330	-3.067783
C	1.860496	-4.132158	-3.438131
H	1.199406	-4.962061	-3.140208
H	2.824778	-4.242224	-2.915464
H	2.028276	-4.169178	-4.526866

Table A.5.: Cartesian coordinates (in Å) for the S_0 geometries of compound **2b** in MeCN.

C	0.853465	4.236314	-0.832317
C	-0.391673	4.830798	-1.014776
C	-1.551347	4.183358	-0.593425
C	-1.493038	2.924754	0.013083
C	-0.222270	2.342143	0.167421
C	0.966437	2.976717	-0.231556
N	-0.130427	1.034535	0.740579
C	-0.031942	-0.095543	-0.002683
N	0.088723	-1.081594	0.921408
C	0.071253	-0.581592	2.209638
C	-0.063468	0.765496	2.094941
C	0.312150	-2.452083	0.574291
C	1.633329	-2.926690	0.576329
C	1.838974	-4.266512	0.225662
C	0.770077	-5.084444	-0.125004
C	-0.528596	-4.577455	-0.143870
C	-0.787742	-3.248173	0.202216
C	2.816118	-2.032858	0.899737
C	3.595194	-2.542171	2.113612
C	-2.195637	-2.681181	0.190751
C	-3.119693	-3.372861	-0.808449
C	2.323604	2.317600	-0.067119
C	2.837576	1.799474	-1.412903
C	-2.752149	2.192993	0.442384
C	-3.818249	3.119296	1.024293
C	-2.806314	-2.700572	1.596226
C	-3.311308	1.365425	-0.718604
C	3.342324	3.240195	0.602709
C	3.720818	-1.858975	-0.322818
H	0.165605	-1.222021	3.083667
H	-0.115999	1.550152	2.846057
H	-1.351808	-5.231664	-0.439649
H	2.855053	-4.672251	0.215742
H	0.949491	-6.128490	-0.399143
H	-2.519243	4.667758	-0.744433
H	1.753966	4.758440	-1.167925
H	-0.460904	5.813209	-1.491340
H	-2.115022	-1.624757	-0.119728
H	-2.468814	1.483695	1.238391
H	2.197614	1.442652	0.591856
H	2.430339	-1.032898	1.155554
H	-4.200821	0.795572	-0.396323
H	-2.556560	0.652245	-1.088503
H	-3.601562	2.016834	-1.562797
H	-3.409257	3.749219	1.833228
H	-4.646567	2.520542	1.440985
H	-4.250752	3.784454	0.256468
H	-2.186542	-2.144971	2.319678
H	-2.908260	-3.738764	1.959927
H	-3.809837	-2.239410	1.585071
H	-2.659262	-3.437987	-1.809216
H	-4.061803	-2.805414	-0.900311
H	-3.383760	-4.395542	-0.486118
H	3.154135	-1.449927	-1.176502
H	4.168723	-2.819645	-0.634616
H	4.544881	-1.160570	-0.093011
H	4.041074	-3.534344	1.921323
H	2.942096	-2.628941	2.999411
H	4.417021	-1.846994	2.359801
H	2.966447	3.614500	1.570599
H	3.586828	4.111767	-0.029538
H	4.282560	2.692098	0.788193
H	2.965750	2.624964	-2.135847
H	2.132626	1.067039	-1.847745
H	3.811362	1.294377	-1.288398
Cu	-0.078959	-0.311598	-1.909698
N	-1.001125	0.846877	-3.283881
C	-2.330755	2.583039	-5.000048
C	-0.595372	2.115341	-3.428879
C	-2.070843	0.412005	-3.978735
C	-2.754558	1.265581	-4.848289
C	-1.225015	3.019843	-4.274249
H	0.265055	2.421159	-2.826849
C	-2.499231	-1.003270	-3.756948
H	-3.619780	0.889390	-5.399609
H	-0.854362	4.044715	-4.347326
H	-2.861243	3.260963	-5.675056
H	-3.334596	-1.283608	-4.415924
H	-2.823321	-1.143627	-2.710308
H	-1.657220	-1.694689	-3.931376
N	0.767173	-1.869331	-2.759124
C	1.255092	-2.869800	-3.069746
C	1.870750	-4.125267	-3.443617
H	1.195305	-4.956511	-3.184440
H	2.816671	-4.251164	-2.891825
H	2.073843	-4.142066	-4.526766

Table A.6.: Cartesian coordinates (in Å) for the S_{MLCT} geometries of compound NHCCuPy in DCM.

C	0.743789	4.124790	-0.878367
C	-0.490629	4.769594	-0.862493
C	-1.569779	4.221393	-0.173189
C	-1.440057	3.016484	0.523425
C	-0.175993	2.394283	0.496020
C	0.932105	2.916300	-0.201009
N	-0.046964	1.099752	1.104862
C	-0.312622	0.013755	0.364030
N	-0.119851	-1.044007	1.162361
C	0.269683	-0.625185	2.418500
C	0.317043	0.738796	2.383653
C	-0.305289	-2.393244	0.709383
C	0.785613	-3.049638	0.114244
C	0.565879	-4.348775	-0.354763
C	-0.684329	-4.950541	-0.237838
C	-1.746033	-4.266369	0.348299
C	-1.582494	-2.965225	0.834336
C	2.150111	-2.401164	-0.023157
C	3.190368	-3.125202	0.835401
C	-2.748010	-2.224693	1.462277
C	-3.913613	-2.077671	0.481970
C	2.259966	2.187586	-0.268701
C	2.491652	1.620837	-1.672466
C	-2.631314	2.391186	1.222930
C	-3.306903	3.362854	2.192002
C	-3.186975	-2.895986	2.766000
C	-3.628215	1.844217	0.196997
C	3.425218	3.074927	0.173045
C	2.590110	-2.315284	-1.486217
H	0.476997	-1.330059	3.220336
H	0.574005	1.469785	3.146600
H	-2.722821	-4.752193	0.426199
H	1.387024	-4.899070	-0.822776
H	-0.834500	-5.967146	-0.612714
H	-2.534540	4.735520	-0.187404
H	1.573321	4.564685	-1.438408
H	-0.616762	5.710659	-1.405314
H	-2.412107	-1.206218	1.719061
H	-2.271154	1.537061	1.820258
H	2.220751	1.334724	0.429179
H	2.079896	-1.367706	0.354821
H	-4.480358	1.359624	0.703936
H	-3.162266	1.085221	-0.460766
H	-4.020379	2.648574	-0.449307
H	-2.587132	3.754050	2.931020
H	-4.115963	2.847976	2.737961
H	-3.756483	4.221228	1.663514
H	-2.350908	-2.957233	3.484137
H	-3.555167	-3.921265	2.584480
H	-4.004045	-2.321554	3.236414
H	-3.593805	-1.577457	-0.449224
H	-4.718142	-1.472007	0.934027
H	-4.342084	-3.058068	0.209837
H	1.844406	-1.781614	-2.101554
H	2.736614	-3.317400	-1.925747
H	3.547052	-1.770524	-1.564377
H	3.328561	-4.168671	0.501108
H	2.888268	-3.145474	1.896797
H	4.167100	-2.615492	0.764782
H	3.259548	3.474111	1.188163
H	3.571184	3.928614	-0.511292
H	4.361503	2.490918	0.180963
H	2.538965	2.424034	-2.428167
H	1.680960	0.929885	-1.975580
H	3.436715	1.052362	-1.710477
Cu	-0.817426	0.233295	-1.454003
N	-1.264633	0.554715	-3.206870
C	-1.952044	0.943121	-5.906081
C	-1.268094	1.825428	-3.761633
C	-1.604188	-0.534379	-4.007801
C	-1.941582	-0.348165	-5.326212
C	-1.600183	2.034392	-5.074877
H	-0.991182	2.647300	-3.093395
C	-1.561360	-1.856493	-3.314266
H	-2.203112	-1.227100	-5.923285
H	-1.587090	3.056915	-5.463072
H	-2.220226	1.089740	-6.953397
H	-1.855133	-2.682068	-3.980998
H	-2.249848	-1.884109	-2.441522
H	-0.542247	-2.090402	-2.936927

Table A.7.: Cartesian coordinates (in Å) for the S_{MLCT} geometries of compound **2b** in DCM.

C	0.746305	4.310034	-0.768396	H	-3.922989	2.403620	-1.476317
C	-0.539673	4.776312	-1.035468	H	-3.082779	2.973046	2.215271
C	-1.654161	4.020755	-0.686910	H	-4.487390	2.059635	1.591541
C	-1.513479	2.782284	-0.051700	H	-4.045432	3.624366	0.858814
C	-0.203321	2.344626	0.209695	H	-2.119327	-1.946831	2.407597
C	0.946342	3.077472	-0.140491	H	-2.927972	-3.508879	2.100738
N	-0.024176	1.057657	0.817441	H	-3.754189	-1.975007	1.695837
C	0.042157	-0.069701	0.084378	H	-2.730849	-3.313242	-1.681664
N	0.197684	-1.066749	0.975436	H	-4.078166	-2.589022	-0.760510
C	0.233086	-0.565820	2.263005	H	-3.478317	-4.204151	-0.323621
C	0.090466	0.783670	2.163076	H	3.119854	-1.524863	-1.182320
C	0.340755	-2.451628	0.633824	H	4.090402	-2.960817	-0.738338
C	1.635230	-2.992753	0.617167	H	4.580983	-1.339851	-0.174946
C	1.757992	-4.345876	0.279424	H	4.098244	-3.728869	1.806645
C	0.636815	-5.106874	-0.035103	H	3.089525	-2.820509	2.967018
C	-0.632843	-4.530553	-0.034344	H	4.553765	-2.069280	2.268654
C	-0.812846	-3.184499	0.296041	H	2.912620	4.057677	1.542916
C	2.871539	-2.157391	0.895981	H	3.524458	4.365315	-0.107675
C	3.696584	-2.729440	2.049695	H	4.273427	3.099618	0.890740
C	-2.189014	-2.541077	0.292486	H	2.945724	2.635446	-2.009312
C	-3.166726	-3.204691	-0.673837	H	2.232754	1.065218	-1.543640
C	2.342063	2.527434	0.089608	H	3.887710	1.470982	-1.028756
C	2.880504	1.890770	-1.196472	Cu	-0.290279	-0.011630	-1.826282
C	-2.734627	1.958079	0.310047	N	-0.845358	0.753788	-3.463625
C	-3.635759	2.698907	1.300375	C	-2.254815	2.486538	-5.211859
C	-2.776632	-2.488170	1.707175	C	-0.573327	2.115901	-3.523325
C	-3.506059	1.531968	-0.942117	C	-1.825069	0.253958	-4.319577
C	3.311664	3.575922	0.633909	C	-2.509078	1.091936	-5.168937
C	3.710701	-1.989395	-0.374026	C	-1.248388	2.976387	-4.353222
H	0.364578	-1.212592	3.127621	H	0.226333	2.482803	-2.871046
H	0.062620	1.564989	2.918771	C	-2.099870	-1.211528	-4.249110
H	-1.496055	-5.143295	-0.302656	H	-3.269838	0.652171	-5.821392
H	2.748872	-4.808487	0.254034	H	-0.975491	4.035920	-4.339906
H	0.752012	-6.163114	-0.295924	H	-2.803832	3.142986	-5.888902
H	-2.654284	4.396704	-0.919082	H	-2.973349	-1.480371	-4.863021
H	1.608184	4.913403	-1.064261	H	-2.301155	-1.530199	-3.205928
H	-0.673031	5.740389	-1.534648	H	-1.237259	-1.808884	-4.598834
H	-2.065143	-1.498302	-0.051645	N	0.437348	-1.762894	-2.419940
H	-2.392255	1.038109	0.812859	C	0.888418	-2.744763	-2.816376
H	2.272614	1.727914	0.846572	C	1.446979	-3.973907	-3.330675
H	2.547348	-1.148457	1.198208	H	0.761406	-4.807203	-3.108513
H	-4.343493	0.867038	-0.667632	H	2.418546	-4.167640	-2.848643
H	-2.858528	0.992868	-1.657086	H	1.584506	-3.886108	-4.420729

Table A.8.: Cartesian coordinates (in Å) for the T_{MLCT} geometries of compound NHCCuPy in DCM.

C	0.745389	4.127369	-0.878323
C	-0.489205	4.771871	-0.864126
C	-1.568978	4.222317	-0.177104
C	-1.439579	3.016370	0.518356
C	-0.175468	2.394961	0.493394
C	0.932847	2.918158	-0.201620
N	-0.047610	1.099552	1.098972
C	-0.314934	0.012432	0.357796
N	-0.120964	-1.044779	1.158561
C	0.270179	-0.624726	2.414178
C	0.317696	0.738758	2.377812
C	-0.306328	-2.393802	0.707367
C	0.784338	-3.050879	0.112480
C	0.564470	-4.350171	-0.356240
C	-0.685813	-4.951816	-0.238947
C	-1.747397	-4.267289	0.347093
C	-1.583611	-2.965742	0.832112
C	2.149082	-2.402460	-0.023724
C	3.189339	-3.129248	0.832465
C	-2.748356	-2.224591	1.460824
C	-3.916646	-2.079908	0.483469
C	2.261013	2.189669	-0.269387
C	2.496446	1.629125	-1.675085
C	-2.632322	2.390606	1.215138
C	-3.302147	3.358314	2.192124
C	-3.183804	-2.893549	2.766958
C	-3.632908	1.854184	0.187256
C	3.424848	3.074738	0.180406
C	2.588672	-2.311787	-1.486560
H	0.478167	-1.328867	3.216468
H	0.575660	1.470347	3.139842
H	-2.724157	-4.753122	0.425724
H	1.385589	-4.900781	-0.824004
H	-0.836065	-5.968643	-0.613270
H	-2.534140	4.735816	-0.192035
H	1.575926	4.568049	-1.436391
H	-0.614736	5.713584	-1.406058
H	-2.412153	-1.205414	1.714317
H	-2.274258	1.530855	1.805609
H	2.219478	1.333252	0.424024
H	2.079057	-1.370018	0.357037
H	-4.484216	1.366014	0.692290
H	-3.168203	1.101055	-0.478435
H	-4.026343	2.664825	-0.450544
H	-2.579710	3.740393	2.933330
H	-4.113503	2.843821	2.735138
H	-3.747470	4.223041	1.670307
H	-2.345856	-2.953372	3.483026
H	-3.552210	-3.919263	2.588171
H	-3.999774	-2.318499	3.238577
H	-3.599619	-1.579060	-0.448326
H	-4.720917	-1.475232	0.937383
H	-4.344514	-3.060970	0.212625
H	1.845194	-1.770364	-2.097842
H	2.729623	-3.312366	-1.931490
H	3.548270	-1.771359	-1.562684
H	3.327880	-4.171638	0.494922
H	2.886953	-3.152989	1.893726
H	4.166037	-2.619157	0.763831
H	3.256686	3.467927	1.197504
H	3.571974	3.932685	-0.498423
H	4.361563	2.491305	0.187153
H	2.548000	2.435980	-2.426707
H	1.684921	0.940810	-1.982325
H	3.441093	1.059747	-1.712431
Cu	-0.825890	0.225175	-1.458626
N	-1.265051	0.548485	-3.203153
C	-1.950957	0.937778	-5.898099
C	-1.276969	1.818584	-3.751602
C	-1.601003	-0.539689	-4.002664
C	-1.937035	-0.351959	-5.323007
C	-1.607793	2.028546	-5.066183
H	-1.005318	2.640124	-3.080554
C	-1.555098	-1.858517	-3.306157
H	-2.194963	-1.230892	-5.921492
H	-1.599710	3.051839	-5.452091
H	-2.218639	1.085484	-6.945593
H	-1.852262	-2.686631	-3.967900
H	-2.239325	-1.879935	-2.429386
H	-0.534089	-2.088622	-2.931496

Table A.9.: Cartesian coordinates (in Å) for the T_{MLCT} geometries of compound **2b** in DCM.

C	0.792505	4.250075	-0.797804	H	-4.053823	2.654816	-1.409522
C	-0.474126	4.746279	-1.097373	H	-2.940811	2.874683	2.245598
C	-1.615043	4.023073	-0.764671	H	-4.442901	2.124690	1.629709
C	-1.519941	2.786443	-0.117676	H	-3.912276	3.709231	1.000494
C	-0.227990	2.319127	0.179779	H	-2.116743	-2.248173	2.455427
C	0.946585	3.019604	-0.152589	H	-2.837205	-3.826669	2.034003
N	-0.090868	1.029843	0.794820	H	-3.755083	-2.317658	1.750564
C	0.009084	-0.093789	0.059087	H	-2.660524	-3.343341	-1.722719
N	0.153463	-1.092685	0.950316	H	-4.049020	-2.753975	-0.766412
C	0.139091	-0.598467	2.240509	H	-3.368114	-4.361468	-0.434786
C	-0.016578	0.750292	2.141989	H	3.209262	-1.516614	-1.222675
C	0.357834	-2.467572	0.598745	H	4.204779	-2.894504	-0.666935
C	1.675947	-2.949126	0.568821	H	4.607934	-1.234697	-0.151411
C	1.858317	-4.292008	0.218038	H	4.085927	-3.576020	1.893981
C	0.771639	-5.101362	-0.097657	H	3.012362	-2.642564	2.972668
C	-0.523026	-4.584883	-0.080643	H	4.491877	-1.890008	2.309416
C	-0.761691	-3.251768	0.265921	H	2.866719	3.947927	1.610749
C	2.874898	-2.067562	0.866560	H	3.535754	4.268997	-0.014571
C	3.657386	-2.575204	2.079552	H	4.236414	2.980973	0.991002
C	-2.167779	-2.681522	0.303386	H	3.005498	2.560476	-1.954915
C	-3.106980	-3.325767	-0.713775	H	2.256042	0.995535	-1.527486
C	2.324619	2.444088	0.119723	H	3.895501	1.375883	-0.950800
C	2.900666	1.810526	-1.151072	Cu	-0.283518	-0.015172	-1.858022
C	-2.768897	2.005768	0.244304	N	-0.917683	0.816837	-3.408953
C	-3.558587	2.720774	1.343770	C	-2.170095	2.505886	-5.304723
C	-2.749206	-2.771813	1.718828	C	-0.407432	2.076168	-3.711742
C	-3.636504	1.725271	-0.984507	C	-2.018223	0.366142	-4.143345
C	3.289489	3.472722	0.709084	C	-2.638442	1.192282	-5.049430
C	3.772412	-1.923853	-0.365372	C	-1.010693	2.919763	-4.607088
H	0.249193	-1.247563	3.106158	H	0.495659	2.376383	-3.170936
H	-0.077876	1.527230	2.900290	C	-2.493714	-1.013501	-3.832393
H	-1.360263	-5.234422	-0.345487	H	-3.514423	0.807490	-5.581019
H	2.869344	-4.708265	0.184790	H	-0.568735	3.906106	-4.776978
H	0.934014	-6.148509	-0.369808	H	-2.663218	3.152171	-6.032601
H	-2.600151	4.424068	-1.018230	H	-3.416259	-1.253345	-4.383329
H	1.676428	4.827790	-1.080140	H	-2.709023	-1.122256	-2.747875
H	-0.572237	5.708311	-1.608618	H	-1.735907	-1.779746	-4.081000
H	-2.100251	-1.610030	0.044035	N	0.511391	-1.705602	-2.496541
H	-2.455905	1.029220	0.650606	C	0.952048	-2.691169	-2.895230
H	2.216882	1.639604	0.866828	C	1.501772	-3.924969	-3.407431
H	2.508423	-1.058024	1.114352	H	0.794143	-4.746923	-3.213838
H	-4.483484	1.072345	-0.710277	H	2.454452	-4.141295	-2.898223
H	-3.054800	1.227699	-1.779416	H	1.672794	-3.829424	-4.491985

Table A.10.: Cartesian coordinates (in Å) for the $T_{LC,Dipp}$ geometries of compound NHCCuPy in DCM.

C	1.181622	4.490587	0.452897
C	-0.037927	5.103459	0.174670
C	-1.235087	4.438010	0.424822
C	-1.240481	3.147231	0.964504
C	0.005414	2.559649	1.240398
C	1.231112	3.200976	0.991833
N	0.028532	1.223373	1.754751
C	0.031917	0.132205	0.957973
N	0.051924	-0.914006	1.812916
C	0.057592	-0.492474	3.125426
C	0.042863	0.868638	3.089368
C	0.050594	-2.267721	1.348165
C	1.269955	-2.856496	1.039101
C	1.235264	-4.247949	0.468152
C	0.012772	-4.888892	0.243205
C	-1.182510	-4.274621	0.559190
C	-1.198191	-2.882929	1.131608
C	2.595704	-2.168573	1.178059
C	3.549664	-2.951635	2.088983
C	-2.514052	-2.194482	1.331439
C	-3.191846	-1.914037	-0.018770
C	2.557171	2.500901	1.222110
C	3.115943	1.989601	-0.109629
C	-2.544311	2.401607	1.176723
C	-3.551216	3.204978	2.000151
C	-3.441643	-2.985476	2.262776
C	-3.131561	1.971653	-0.170715
C	3.572400	3.375765	1.956672
C	3.224834	-1.913700	-0.198943
H	0.072846	-1.190750	3.958918
H	0.042909	1.610074	3.884920
H	-2.132327	-4.790660	0.405975
H	2.177346	-4.751369	0.244653
H	0.007154	-5.900498	-0.174762
H	-2.183592	4.928858	0.188784
H	2.112161	5.023312	0.238596
H	-0.054885	6.112374	-0.248241
H	-2.325006	-1.218308	1.808995
H	-2.322398	1.482431	1.743828
H	2.369390	1.619131	1.857269
H	2.426795	-1.184634	1.646611
H	-4.046262	1.371205	-0.022743
H	-2.408708	1.356646	-0.737502
H	-3.391348	2.848999	-0.789651
H	-3.124451	3.502662	2.973464
H	-4.453375	2.598301	2.192009
H	-3.873840	4.120967	1.474844
H	-2.963745	-3.164736	3.241103
H	-3.720144	-3.963862	1.833484
H	-4.374785	-2.420399	2.433344
H	-2.563886	-1.249958	-0.638826
H	-4.164752	-1.414750	0.136056
H	-3.373591	-2.845226	-0.584454
H	2.571942	-1.267192	-0.811918
H	3.396253	-2.854383	-0.751735
H	4.197941	-1.404031	-0.086785
H	3.802434	-3.940654	1.668265
H	3.106760	-3.107768	3.087558
H	4.493541	-2.392599	2.214350
H	3.163271	3.749255	2.911225
H	3.879565	4.247081	1.352173
H	4.482768	2.792188	2.178351
H	3.338072	2.828799	-0.792917
H	2.391666	1.322965	-0.612584
H	4.047517	1.419009	0.051785
Cu	0.006772	0.035353	-0.911799
N	-0.017866	-0.074209	-2.809288
C	-0.041876	-0.137016	-5.577658
C	-0.007159	1.067020	-3.518430
C	-0.040492	-1.266431	-3.444581
C	-0.052791	-1.317115	-4.839547
C	-0.018627	1.083403	-4.905313
H	0.011071	1.995899	-2.940890
C	-0.052693	-2.501286	-2.601133
H	-0.070974	-2.288394	-5.339085
H	-0.009287	2.035477	-5.440018
H	-0.051338	-0.170526	-6.670868
H	-0.059631	-3.410272	-3.220582
H	-0.942239	-2.521371	-1.947055
H	0.833184	-2.537278	-1.942687

Table A.11.: Cartesian coordinates (in Å) for the $T_{LC,Dipp}$ geometries of compound **2b** in DCM.

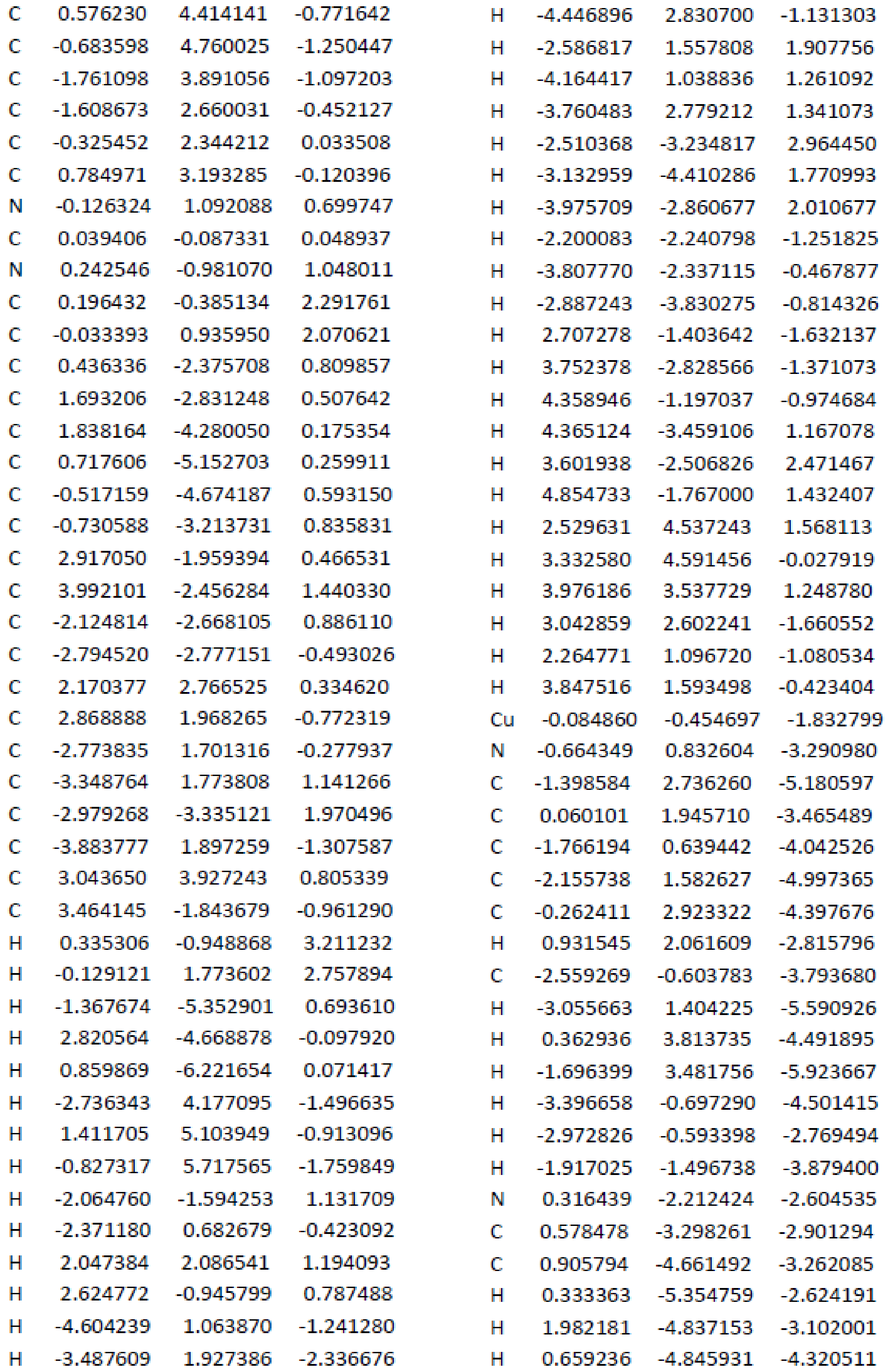

C	0.576230	4.414141	-0.771642
C	-0.683598	4.760025	-1.250447
C	-1.761098	3.891056	-1.097203
C	-1.608673	2.660031	-0.452127
C	-0.325452	2.344212	0.033508
C	0.784971	3.193285	-0.120396
N	-0.126324	1.092088	0.699747
C	0.039406	-0.087331	0.048937
N	0.242546	-0.981070	1.048011
C	0.196432	-0.385134	2.291761
C	-0.033393	0.935950	2.070621
C	0.436336	-2.375708	0.809857
C	1.693206	-2.831248	0.507642
C	1.838164	-4.280050	0.175354
C	0.717606	-5.152703	0.259911
C	-0.517159	-4.674187	0.593150
C	-0.730588	-3.213731	0.835831
C	2.917050	-1.959394	0.466531
C	3.992101	-2.456284	1.440330
C	-2.124814	-2.668105	0.886110
C	-2.794520	-2.777151	-0.493026
C	2.170377	2.766525	0.334620
C	2.868888	1.968265	-0.772319
C	-2.773835	1.701316	-0.277937
C	-3.348764	1.773808	1.141266
C	-2.979268	-3.335121	1.970496
C	-3.883777	1.897259	-1.307587
C	3.043650	3.927243	0.805339
C	3.464145	-1.843679	-0.961290
H	0.335306	-0.948868	3.211232
H	-0.129121	1.773602	2.757894
H	-1.367674	-5.352901	0.693610
H	2.820564	-4.668878	-0.097920
H	0.859869	-6.221654	0.071417
H	-2.736343	4.177095	-1.496635
H	1.411705	5.103949	-0.913096
H	-0.827317	5.717565	-1.759849
H	-2.064760	-1.594253	1.131709
H	-2.371180	0.682679	-0.423092
H	2.047384	2.086541	1.194093
H	2.624772	-0.945799	0.787488
H	-4.604239	1.063870	-1.241280
H	-3.487609	1.927386	-2.336676
H	-4.446896	2.830700	-1.131303
H	-2.586817	1.557808	1.907756
H	-4.164417	1.038836	1.261092
H	-3.760483	2.779212	1.341073
H	-2.510368	-3.234817	2.964450
H	-3.132959	-4.410286	1.770993
H	-3.975709	-2.860677	2.010677
H	-2.200083	-2.240798	-1.251825
H	-3.807770	-2.337115	-0.467877
H	-2.887243	-3.830275	-0.814326
H	2.707278	-1.403642	-1.632137
H	3.752378	-2.828566	-1.371073
H	4.358946	-1.197037	-0.974684
H	4.365124	-3.459106	1.167078
H	3.601938	-2.506826	2.471467
H	4.854733	-1.767000	1.432407
H	2.529631	4.537243	1.568113
H	3.332580	4.591456	-0.027919
H	3.976186	3.537729	1.248780
H	3.042859	2.602241	-1.660552
H	2.264771	1.096720	-1.080534
H	3.847516	1.593498	-0.423404
Cu	-0.084860	-0.454697	-1.832799
N	-0.664349	0.832604	-3.290980
C	-1.398584	2.736260	-5.180597
C	0.060101	1.945710	-3.465489
C	-1.766194	0.639442	-4.042526
C	-2.155738	1.582627	-4.997365
C	-0.262411	2.923322	-4.397676
H	0.931545	2.061609	-2.815796
C	-2.559269	-0.603783	-3.793680
H	-3.055663	1.404225	-5.590926
H	0.362936	3.813735	-4.491895
H	-1.696399	3.481756	-5.923667
H	-3.396658	-0.697290	-4.501415
H	-2.972826	-0.593398	-2.769494
H	-1.917025	-1.496738	-3.879400
N	0.316439	-2.212424	-2.604535
C	0.578478	-3.298261	-2.901294
C	0.905794	-4.661492	-3.262085
H	0.333363	-5.354759	-2.624191
H	1.982181	-4.837153	-3.102001
H	0.659236	-4.845931	-4.320511

Table A.12.: Cartesian coordinates (in Å) for the $T_{LC/MLCT}$ geometries of compound NHCCuPy in DCM.

C	1.173528	4.458840	0.409110
C	-0.046073	5.089398	0.175969
C	-1.243046	4.433286	0.451834
C	-1.247634	3.136218	0.975630
C	-0.000668	2.534084	1.213409
C	1.224102	3.162513	0.932264
N	0.022093	1.196218	1.724200
C	0.018185	0.106618	0.924821
N	0.041204	-0.942662	1.777275
C	0.059363	-0.521732	3.089706
C	0.047242	0.840186	3.055717
C	0.040977	-2.299829	1.319759
C	1.276684	-2.916837	1.061723
C	1.247068	-4.217328	0.547085
C	0.037719	-4.864306	0.306105
C	-1.169966	-4.225470	0.575137
C	-1.196218	-2.925041	1.090233
C	2.594767	-2.195511	1.272788
C	3.572615	-3.010344	2.120019
C	-2.514352	-2.214151	1.333705
C	-3.174649	-1.835895	0.005183
C	2.552571	2.454977	1.119925
C	3.158691	2.101472	-0.241368
C	-2.553797	2.401366	1.209369
C	-3.510548	3.186478	2.106998
C	-3.456446	-3.030917	2.218864
C	-3.202702	2.039150	-0.129758
C	3.526077	3.261131	1.980124
C	3.209440	-1.797174	-0.071749
H	0.079140	-1.220577	3.922704
H	0.054122	1.580012	3.852774
H	-2.110704	-4.745370	0.372816
H	2.186157	-4.730892	0.322469
H	0.036422	-5.879801	-0.100725
H	-2.192648	4.936370	0.247813
H	2.104362	4.981781	0.171434
H	-0.064050	6.103615	-0.233936
H	-2.300778	-1.274155	1.869127
H	-2.326230	1.454966	1.727362
H	2.362700	1.505799	1.647889
H	2.388088	-1.263032	1.823858
H	-4.119176	1.444962	0.031527
H	-2.514491	1.441084	-0.754530
H	-3.476789	2.946056	-0.697719
H	-3.039923	3.429870	3.075164
H	-4.418692	2.591242	2.306313
H	-3.830121	4.132628	1.636046
H	-2.976411	-3.292839	3.177512
H	-3.771071	-3.968385	1.727806
H	-4.368648	-2.449423	2.438837
H	-2.515072	-1.181474	-0.592576
H	-4.118372	-1.290882	0.182536
H	-3.403228	-2.733048	-0.597379
H	2.523600	-1.145895	-0.642599
H	3.429934	-2.686101	-0.689377
H	4.151570	-1.242081	0.081424
H	3.884034	-3.938414	1.609428
H	3.125233	-3.288438	3.089863
H	4.483982	-2.420002	2.318808
H	3.086802	3.498083	2.964518
H	3.810182	4.211880	1.495867
H	4.452207	2.683963	2.147260
H	3.394493	3.011739	-0.821048
H	2.458809	1.489244	-0.838801
H	4.091309	1.524630	-0.112952
Cu	-0.008389	0.047096	-0.951651
N	-0.023512	-0.015075	-2.811028
C	-0.038382	-0.210588	-5.685027
C	-0.038871	1.077638	-3.554091
C	-0.019292	-1.305126	-3.507663
C	-0.024657	-1.348382	-4.929268
C	-0.047641	1.068353	-4.959332
H	-0.042963	2.035367	-3.021776
C	-0.011915	-2.489111	-2.632324
H	-0.018653	-2.335308	-5.401535
H	-0.059843	2.020214	-5.494062
H	-0.043197	-0.229308	-6.775410
H	-0.013584	-3.424717	-3.211852
H	-0.890984	-2.497006	-1.952746
H	0.874657	-2.494516	-1.962482

Table A.13.: Cartesian coordinates (in Å) for the S_0 geometries of MeCN in DCM.

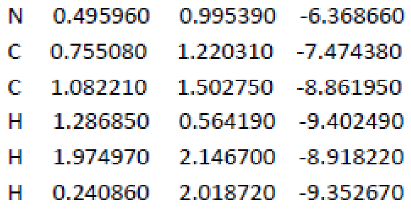

N	0.495960	0.995390	-6.368660
C	0.755080	1.220310	-7.474380
C	1.082210	1.502750	-8.861950
H	1.286850	0.564190	-9.402490
H	1.974970	2.146700	-8.918220
H	0.240860	2.018720	-9.352670

Table A.14.: Cartesian coordinates (in Å) for the S_0 geometries of MeCN in MeCN.

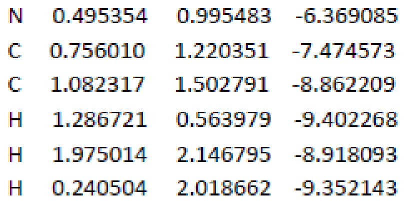

N	0.495354	0.995483	-6.369085
C	0.756010	1.220351	-7.474573
C	1.082317	1.502791	-8.862209
H	1.286721	0.563979	-9.402268
H	1.975014	2.146795	-8.918093
H	0.240504	2.018662	-9.352143

Appendix on the study of NHCCuDBM

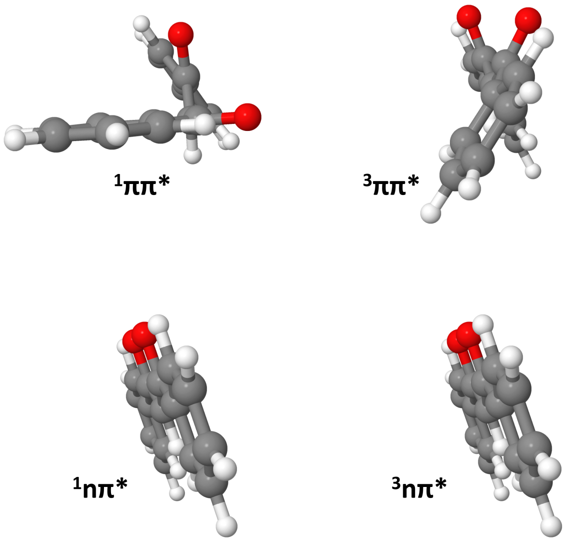

Figure A.8.: Equilibrium geometries of DBM$^-$ in the singlet and triplet $\pi\pi^*$ and $n\pi^*$ states. The geometries are shown from a lateral perspective.

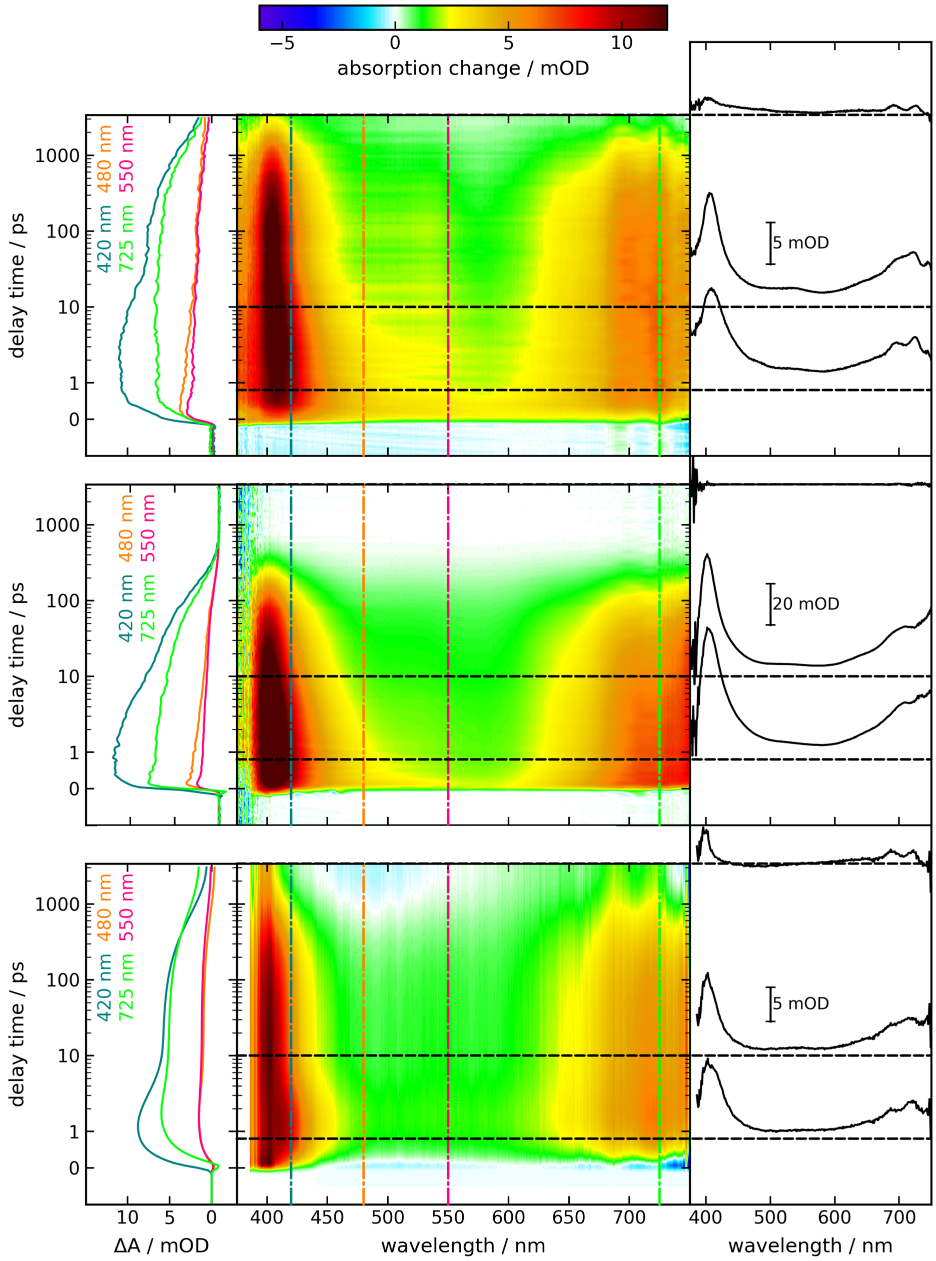

Figure A.9.: Femtosecond time-resolved spectroscopy data acquired for NHCCuDBM in Cx (top) and MeCN (middle), and zeonex as a matrix environment (bottom, fitted data). The excitation was tuned to 400nm. In the contour representation (central), the difference absorption signal is color-coded. Vertical lines mark spectral positions for the time traces plotted on the left while horizontal lines mark certain delay times for the difference spectra plotted on the right.

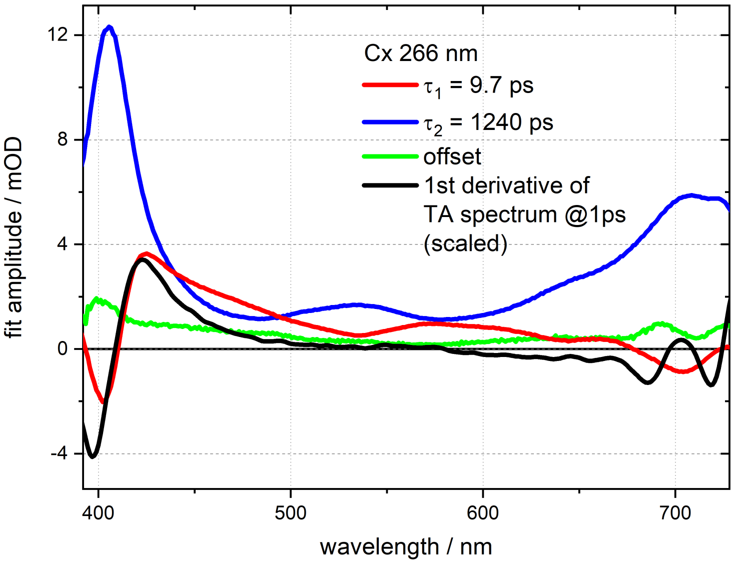

Figure A.10.: Decay-associated difference spectra obtained from the fsTA experiments of NHCCuDBM in Cx for an excitation wavelength of 266 nm. The black line shows the first derivative of the transient spectrum at a delay time of 1 ps. This curve resembles the DADS$_1$, typical for a spectral shift, which occurs with τ_1.

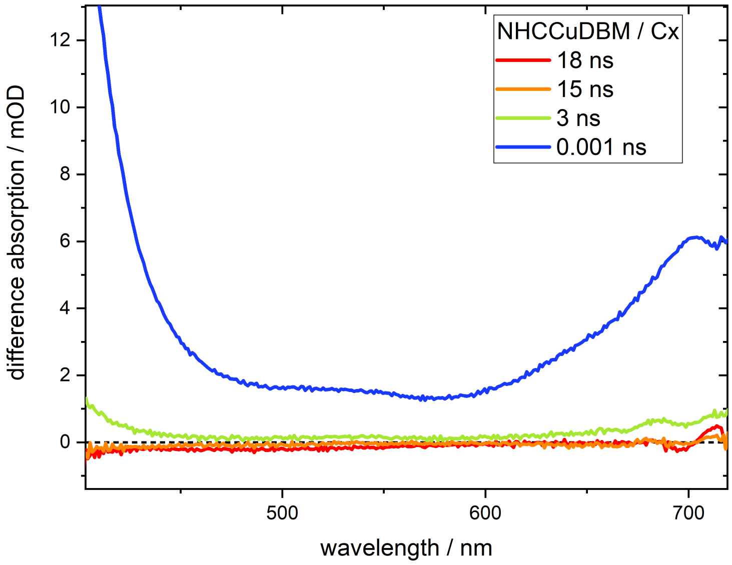

Figure A.11.: fsTA data of NHCCuDBM in Cx at 0.001, 3, 15, and 18 ns. For 0.001 ns the expected TA signature of NHCCuDBM is seen. Some excited state population is still present for 3 ns as seen in a previous experiment (5.34). For 15 and 18 ns this signal has vanished completely.

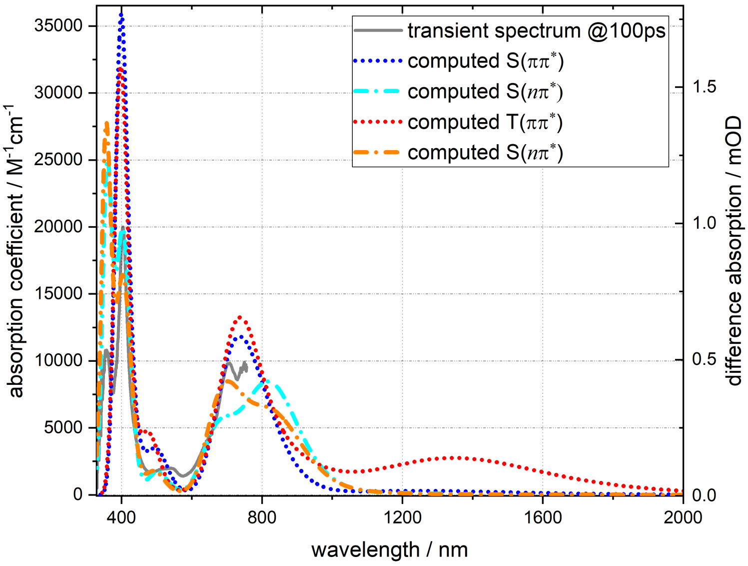

Figure A.12.: Comparison of calculated UV/Vis absorption coefficient spectra (dashed lines, left y-axis) of the singlet (blueish) and triplet (reddish) $n\pi^*$ and $\pi\pi^*$ states of NHCCuDBM in THF, with the experimental transient absorption spectrum for a delay time of 100 ps recorded in Cx (grey solid line, right y-axis). Around 1350 nm another transient absorption band ought to be visible according to calculations in case of a population of the $^3\pi\pi^*$ state.

Table A.15.: Cartesian coordinates (in Å) for the S_0 and $S_{n\pi^*}$ geometries of DBM.

	S_0				**$S_{n\pi^*}$**		
O	0.183332	-1.062175	-2.888136	O	0.636640	-1.047476	-2.717896
C	0.714942	-0.982736	-4.086981	C	0.927035	-1.036533	-3.998172
C	0.957128	0.241784	-4.664909	C	1.047359	0.237648	-4.638420
C	0.625888	1.438315	-3.962555	C	0.848345	1.459973	-3.903619
O	0.129885	1.395159	-2.810845	O	0.563553	1.381648	-2.657485
H	1.444273	0.290280	-5.624226	H	1.290344	0.270753	-5.686465
C	0.883343	2.764589	-4.576903	C	0.965126	2.743097	-4.556129
C	0.907199	3.887813	-3.749447	C	0.744474	3.910629	-3.792409
C	1.142456	5.145048	-4.278418	C	0.843375	5.159044	-4.367145
C	1.343024	5.297765	-5.644932	C	1.164831	5.293161	-5.718800
C	1.308883	4.187758	-6.478199	C	1.386314	4.152315	-6.488303
H	0.744064	3.755513	-2.686945	H	0.494333	3.800526	-2.744900
H	1.168936	6.009866	-3.625504	H	0.669660	6.043614	-3.764396
H	1.523175	6.282616	-6.060814	H	1.241716	6.277083	-6.166890
C	1.085472	2.927151	-5.947626	C	1.289729	2.897800	-5.923856
H	1.046554	2.073671	-6.613185	H	1.469367	2.034209	-6.551242
H	1.454060	4.304367	-7.545898	H	1.636892	4.247979	-7.538714
C	1.651587	-4.732484	-5.871447	C	1.436000	-4.751034	-5.955324
C	1.397788	-4.645498	-4.509352	C	1.128975	-4.698310	-4.591451
C	1.591563	-3.590387	-6.660424	C	1.576854	-3.566408	-6.678694
C	1.086535	-3.423350	-3.936939	C	0.964719	-3.489493	-3.958428
C	1.034959	-2.268810	-4.720385	C	1.103794	-2.273395	-4.676764
C	1.286511	-2.366673	-6.090500	C	1.416192	-2.347114	-6.061289
H	1.442353	-5.533810	-3.890021	H	1.019386	-5.618564	-4.028992
H	1.777282	-3.655205	-7.726151	H	1.814539	-3.603386	-7.735524
H	1.891757	-5.689735	-6.319872	H	1.563720	-5.708063	-6.447690
H	1.223842	-1.488865	-6.721772	H	1.531326	-1.445571	-6.648701
H	0.888580	-3.351733	-2.875078	H	0.726701	-3.447989	-2.903480
H	0.056372	-0.087481	-2.598134	H	0.554440	-0.020434	-2.464702

Table A.16.: Cartesian coordinates (in Å) for the $T_{n\pi^*}$ and $T_{\pi\pi^*}$ geometries of DBM.

		$\mathbf{T_{\pi\pi^*}}$				$\mathbf{T_{n\pi^*}}$	
O	0.996351	-1.108394	-2.650735	O	0.636539	-1.043382	-2.723434
C	1.045448	-1.000203	-4.000192	C	0.927145	-1.040635	-4.004715
C	1.022345	0.230531	-4.627323	C	1.049261	0.236822	-4.651772
C	0.857441	1.461831	-3.958522	C	0.850446	1.464493	-3.913090
O	0.687577	1.530726	-2.665151	O	0.565629	1.375908	-2.660797
H	1.120818	0.279700	-5.710825	H	1.293274	0.270081	-5.709620
C	0.994135	2.770187	-4.573117	C	0.965402	2.755345	-4.557130
C	0.388100	3.903039	-3.947285	C	0.740588	3.924316	-3.782271
C	0.500232	5.162326	-4.518034	C	0.838343	5.183542	-4.351192
C	1.212699	5.338901	-5.708690	C	1.162873	5.328121	-5.708704
C	1.833855	4.228675	-6.322398	C	1.388436	4.186912	-6.489612
H	-0.202595	3.754966	-3.040702	H	0.486770	3.807023	-2.726214
H	0.014729	6.017714	-4.039181	H	0.660567	6.071648	-3.736898
H	1.295603	6.330552	-6.161679	H	1.239192	6.324355	-6.154181
C	1.759003	2.971975	-5.753304	C	1.292900	2.921399	-5.930965
H	2.284107	2.131801	-6.213875	H	1.476510	2.054491	-6.569265
H	2.394373	4.366738	-7.251842	H	1.642444	4.290580	-7.548805
C	1.279311	-4.793237	-5.977366	C	1.435724	-4.789302	-5.949067
C	1.348577	-4.707824	-4.586229	C	1.128769	-4.725993	-4.579209
C	1.125134	-3.622786	-6.726949	C	1.577054	-3.603984	-6.684619
C	1.269363	-3.472124	-3.949554	C	0.965018	-3.504370	-3.952129
C	1.118445	-2.283361	-4.692492	C	1.104388	-2.288412	-4.681980
C	1.042547	-2.386723	-6.097255	C	1.416555	-2.373053	-6.071711
H	1.467123	-5.615590	-3.986630	H	1.018087	-5.649982	-4.003837
H	1.062139	-3.674866	-7.818151	H	1.815729	-3.648177	-7.751256
H	1.341321	-5.764693	-6.476516	H	1.563668	-5.758855	-6.439231
H	0.905260	-1.493220	-6.710844	H	1.532355	-1.467832	-6.671250
H	1.328536	-3.417204	-2.860608	H	0.726073	-3.454388	-2.887565
H	1.019936	-0.216501	-2.250622	H	0.556003	0.009035	-2.475364

Table A.17.: Cartesian coordinates (in Å) for the S_0 and $S_{n\pi^*}$ geometries of DBM$^-$.

	S_0				$S_{n\pi^*}$		
O	3.954913	-1.537522	-4.963589	O	0.783216	-0.927746	-2.844222
C	2.774332	-1.112950	-4.988515	C	1.012231	-0.963443	-4.122865
C	2.457571	0.269307	-5.027734	C	1.106419	0.246428	-4.826862
C	1.196278	0.892502	-4.841374	C	0.931685	1.411102	-4.064186
O	0.103602	0.330160	-4.608188	O	0.691932	1.297163	-2.791920
H	3.327249	0.916663	-5.170359	H	1.302518	0.279446	-5.896276
C	1.171710	2.406019	-4.943298	C	1.005867	2.759300	-4.624674
C	0.008606	3.019364	-5.431292	C	0.796017	3.878170	-3.780420
C	-0.081229	4.405744	-5.542724	C	0.862558	5.177009	-4.274477
C	0.986931	5.211636	-5.141438	C	1.140146	5.415265	-5.624027
C	2.142988	4.616250	-4.634325	C	1.350214	4.318569	-6.473768
H	-0.829636	2.381832	-5.726990	H	0.578441	3.702261	-2.723762
H	-0.992635	4.862956	-5.941856	H	0.695554	6.019860	-3.594812
H	0.915954	6.301304	-5.218958	H	1.193368	6.437207	-6.011286
C	2.236586	3.226526	-4.544310	C	1.285783	3.019425	-5.989222
H	3.144853	2.776220	-4.133901	H	1.458388	2.190765	-6.680606
H	2.980239	5.238997	-4.302693	H	1.569864	4.483952	-7.534049
C	-0.183653	-4.245010	-5.176933	C	1.414521	-4.867365	-5.885077
C	0.765262	-4.231413	-4.153212	C	1.194004	-4.710780	-4.513243
C	-0.190168	-3.220259	-6.127116	C	1.506595	-3.721109	-6.689197
C	1.708417	-3.204380	-4.089052	C	1.067122	-3.443624	-3.953183
C	1.695239	-2.163723	-5.024179	C	1.156700	-2.275602	-4.750952
C	0.734240	-2.180700	-6.041509	C	1.381151	-2.453026	-6.138735
H	0.776476	-5.030393	-3.404610	H	1.119726	-5.593413	-3.868515
H	-0.927250	-3.228923	-6.936781	H	1.678228	-3.822390	-7.766269
H	-0.917062	-5.055675	-5.237115	H	1.513082	-5.864542	-6.324491
H	0.719863	-1.366043	-6.771133	H	1.455387	-1.583685	-6.796935
H	2.467006	-3.200931	-3.300307	H	0.895964	-3.331638	-2.879461

Table A.18.: Cartesian coordinates (in Å) for the $S_{\pi\pi^*}$ and $T_{n\pi^*}$ geometries of DBM$^-$.

	$S_{\pi\pi^*}$		
O	2.936300	-1.132615	-3.051477
C	2.169216	-1.113688	-4.079122
C	2.041699	0.253821	-4.635698
C	1.056444	1.187478	-4.190143
O	0.129690	0.856654	-3.429231
H	2.791943	0.594566	-5.359848
C	1.109367	2.599949	-4.705206
C	-0.091048	3.308470	-4.846921
C	-0.090513	4.621666	-5.311337
C	1.116580	5.251331	-5.625352
C	2.318837	4.559623	-5.474570
H	-1.028479	2.807520	-4.589092
H	-1.036190	5.159885	-5.428271
H	1.119408	6.284708	-5.985824
C	2.314728	3.238737	-5.024636
H	3.264700	2.711482	-4.897236
H	3.268373	5.051684	-5.706351
C	0.272810	-4.504848	-5.866282
C	1.094000	-4.647250	-4.732573
C	0.087646	-3.216193	-6.399847
C	1.712597	-3.554321	-4.149478
C	1.535890	-2.234926	-4.676562
C	0.694401	-2.110273	-5.827630
H	1.249812	-5.643325	-4.301332
H	-0.550384	-3.080461	-7.280854
H	-0.211984	-5.373933	-6.320017
H	0.520806	-1.118438	-6.258833
H	2.350031	-3.679744	-3.269765

	$T_{n\pi^*}$		
O	0.764836	-0.920740	-2.859998
C	1.005234	-0.962100	-4.139688
C	1.105140	0.246741	-4.843001
C	0.924746	1.410028	-4.081162
O	0.674708	1.289734	-2.808170
H	1.310707	0.280119	-5.910956
C	1.002942	2.763034	-4.629002
C	0.789806	3.877057	-3.780748
C	0.860456	5.179038	-4.266357
C	1.145491	5.425441	-5.612714
C	1.358653	4.334360	-6.466585
H	0.566303	3.696655	-2.726113
H	0.690585	6.017590	-3.582121
H	1.201776	6.449686	-5.993479
C	1.290208	3.031683	-5.989727
H	1.465290	2.206657	-6.684897
H	1.584070	4.505341	-7.524801
C	1.420844	-4.877582	-5.875365
C	1.190134	-4.713495	-4.506253
C	1.517860	-3.736346	-6.683570
C	1.058521	-3.443190	-3.954040
C	1.153005	-2.279412	-4.755784
C	1.387438	-2.464785	-6.140242
H	1.111617	-5.592406	-3.856985
H	1.697464	-3.842642	-7.758893
H	1.523384	-5.877058	-6.308669
H	1.465764	-1.598614	-6.802181
H	0.879697	-3.327236	-2.881988

Table A.19.: Cartesian coordinates (in Å) for the $T_{\pi\pi^*}$ geometries of DBM$^-$.

O	1.333765	-1.054508	-2.619763
C	1.150235	-1.032841	-3.874141
C	1.022864	0.237113	-4.556892
C	0.534031	1.462632	-3.963260
O	-0.266323	1.409757	-2.982130
H	1.321426	0.273615	-5.610462
C	0.907268	2.751387	-4.566369
C	0.231092	3.924258	-4.156482
C	0.536415	5.163158	-4.705833
C	1.532003	5.283574	-5.684329
C	2.220034	4.136543	-6.094300
H	-0.546959	3.828482	-3.394446
H	-0.008144	6.052521	-4.370358
H	1.773522	6.260107	-6.115094
C	1.920360	2.893696	-5.543916
H	2.501494	2.024093	-5.863903
H	3.011752	4.214095	-6.847194
C	1.215331	-4.722839	-6.095855
C	1.551347	-4.684942	-4.736006
C	0.838607	-3.535187	-6.732472
C	1.519521	-3.487741	-4.032222
C	1.152886	-2.274249	-4.661117
C	0.801051	-2.333834	-6.030873
H	1.842933	-5.606948	-4.221192
H	0.558095	-3.547899	-7.791213
H	1.238506	-5.666847	-6.648867
H	0.470126	-1.431599	-6.553206
H	1.783444	-3.458037	-2.971592

Table A.20.: Cartesian coordinates (in Å) for the S_0 geometries of NHCCuDBM.

C	1.240583	4.375351	0.079077
C	0.046286	5.084327	-0.010273
C	-1.156030	4.484456	0.356487
C	-1.188214	3.167537	0.825740
C	0.034256	2.479378	0.911318
C	1.260645	3.053777	0.537888
N	0.022856	1.117063	1.348706
C	-0.071139	0.073316	0.485398
N	-0.004265	-1.018545	1.289776
C	0.126584	-0.668754	2.619701
C	0.145812	0.690698	2.657082
C	-0.021757	-2.352662	0.773279
C	1.201586	-2.954745	0.432831
C	1.156646	-4.239202	-0.119162
C	-0.057948	-4.887503	-0.326225
C	-1.254639	-4.262729	0.014579
C	-1.262523	-2.979376	0.570735
C	2.524453	-2.227641	0.582368
C	3.556837	-3.046842	1.357353
C	-2.570720	-2.272471	0.868206
C	-3.229328	-1.821452	-0.438630
C	2.561046	2.273695	0.565945
C	3.054841	2.008055	-0.858693
C	-2.504531	2.484373	1.144059
C	-3.439996	3.349563	1.987483
C	-3.518738	-3.120254	1.716368
C	-3.177149	2.027260	-0.154284
C	3.628039	2.963500	1.417008
C	3.052516	-1.802693	-0.790693
H	0.195044	-1.411141	3.411518
H	0.234593	1.386142	3.488505
H	-2.202019	-4.777568	-0.169297
H	2.087970	-4.735161	-0.407986
H	-0.072735	-5.888785	-0.767473
H	-2.088130	5.048683	0.264124
H	2.175362	4.853362	-0.228618
H	0.050319	6.114392	-0.379717
H	-2.338875	-1.363349	1.447588
H	-2.280191	1.578330	1.731628
H	2.358954	1.293109	1.027586
H	2.341440	-1.305894	1.159189
H	-4.110347	1.477382	0.062710
H	-2.508194	1.360751	-0.726931
H	-3.425145	2.893192	-0.793934
H	-2.946421	3.691436	2.913932
H	-4.337035	2.771195	2.270003
H	-3.786127	4.241427	1.436038
H	-3.038640	-3.438117	2.658323
H	-3.850100	-4.027051	1.180254
H	-4.422528	-2.539209	1.971065
H	-2.543570	-1.177282	-1.017127
H	-4.151088	-1.248811	-0.232911
H	-3.494462	-2.689594	-1.068283
H	2.314211	-1.169910	-1.312645
H	3.255318	-2.681719	-1.428605
H	3.990928	-1.230114	-0.684454
H	3.841260	-3.966097	0.815330
H	3.172583	-3.341948	2.349380
H	4.476473	-2.454380	1.507821
H	3.270498	3.133269	2.447669
H	3.918900	3.940906	0.992738
H	4.537668	2.339331	1.467557
H	3.283073	2.951512	-1.386302
H	2.286737	1.471870	-1.442157
H	3.972350	1.393936	-0.841354
Cu	-0.125103	0.124719	-1.378262
O	0.083105	-1.231485	-2.836022
C	0.599813	-1.036892	-3.970830
C	0.842724	0.232822	-4.540024
C	0.514699	1.453323	-3.909989
O	-0.016875	1.558934	-2.769716
H	1.366137	0.275180	-5.493847
C	0.841429	2.749477	-4.592221
C	0.912392	3.905263	-3.799175
C	1.218973	5.140219	-4.364936
C	1.444940	5.244237	-5.739453
C	1.361452	4.104073	-6.540926
H	0.724074	3.812287	-2.725913
H	1.279716	6.029417	-3.729185
H	1.681111	6.214472	-6.187617
C	1.065370	2.865966	-5.971579
H	0.987223	1.987664	-6.617892
H	1.523889	4.179435	-7.620575
C	1.746576	-4.674428	-5.981149
C	1.474615	-4.658685	-4.611121
C	1.639356	-3.494435	-6.719686
C	1.099766	-3.471362	-3.987642
C	1.003138	-2.275809	-4.716427
C	1.273132	-2.304128	-6.092222
H	1.552769	-5.579864	-4.024742
H	1.838329	-3.500961	-7.795814
H	2.037187	-5.606925	-6.475083
H	1.178223	-1.394890	-6.691625
H	0.873415	-3.445334	-2.918079

Table A.21.: Cartesian coordinates (in Å) for the $S_{n\pi^*}$ geometries of NHCCuDBM.

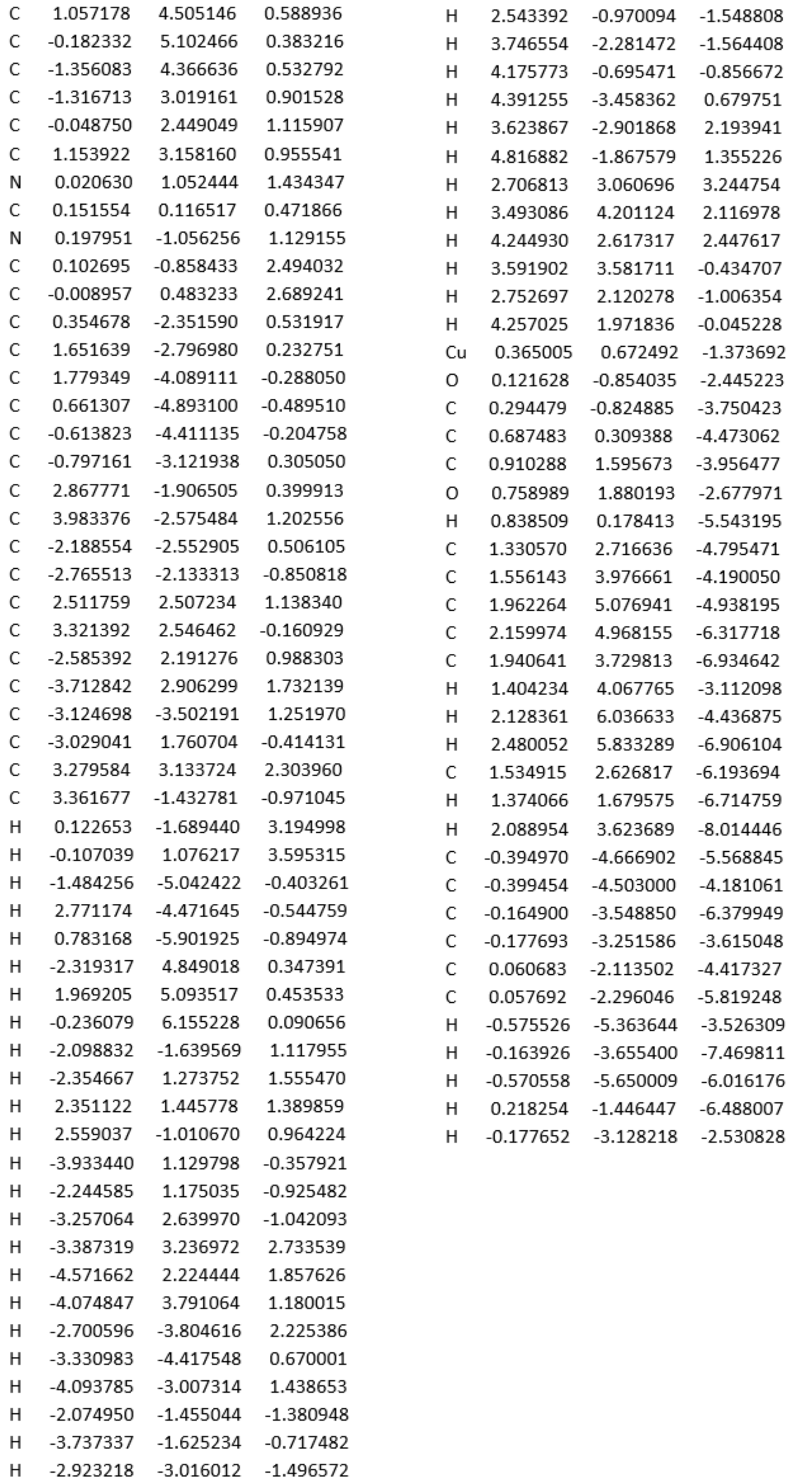

C	1.057178	4.505146	0.588936
C	-0.182332	5.102466	0.383216
C	-1.356083	4.366636	0.532792
C	-1.316713	3.019161	0.901528
C	-0.048750	2.449049	1.115907
C	1.153922	3.158160	0.955541
N	0.020630	1.052444	1.434347
C	0.151554	0.116517	0.471866
N	0.197951	-1.056256	1.129155
C	0.102695	-0.858433	2.494032
C	-0.008957	0.483233	2.689241
C	0.354678	-2.351590	0.531917
C	1.651639	-2.796980	0.232751
C	1.779349	-4.089111	-0.288050
C	0.661307	-4.893100	-0.489510
C	-0.613823	-4.411135	-0.204758
C	-0.797161	-3.121938	0.305050
C	2.867771	-1.906505	0.399913
C	3.983376	-2.575484	1.202556
C	-2.188554	-2.552905	0.506105
C	-2.765513	-2.133313	-0.850818
C	2.511759	2.507234	1.138340
C	3.321392	2.546462	-0.160929
C	-2.585392	2.191276	0.988303
C	-3.712842	2.906299	1.732139
C	-3.124698	-3.502191	1.251970
C	-3.029041	1.760704	-0.414131
C	3.279584	3.133724	2.303960
C	3.361677	-1.432781	-0.971045
H	0.122653	-1.689440	3.194998
H	-0.107039	1.076217	3.595315
H	-1.484256	-5.042422	-0.403261
H	2.771174	-4.471645	-0.544759
H	0.783168	-5.901925	-0.894974
H	-2.319317	4.849018	0.347391
H	1.969205	5.093517	0.453533
H	-0.236079	6.155228	0.090656
H	-2.098832	-1.639569	1.117955
H	-2.354667	1.273752	1.555470
H	2.351122	1.445778	1.389859
H	2.559037	-1.010670	0.964224
H	-3.933440	1.129798	-0.357921
H	-2.244585	1.175035	-0.925482
H	-3.257064	2.639970	-1.042093
H	-3.387319	3.236972	2.733539
H	-4.571662	2.224444	1.857626
H	-4.074847	3.791064	1.180015
H	-2.700596	-3.804616	2.225386
H	-3.330983	-4.417548	0.670001
H	-4.093785	-3.007314	1.438653
H	-2.074950	-1.455044	-1.380948
H	-3.737337	-1.625234	-0.717482
H	-2.923218	-3.016012	-1.496572
H	2.543392	-0.970094	-1.548808
H	3.746554	-2.281472	-1.564408
H	4.175773	-0.695471	-0.856672
H	4.391255	-3.458362	0.679751
H	3.623867	-2.901868	2.193941
H	4.816882	-1.867579	1.355226
H	2.706813	3.060696	3.244754
H	3.493086	4.201124	2.116978
H	4.244930	2.617317	2.447617
H	3.591902	3.581711	-0.434707
H	2.752697	2.120278	-1.006354
H	4.257025	1.971836	-0.045228
Cu	0.365005	0.672492	-1.373692
O	0.121628	-0.854035	-2.445223
C	0.294479	-0.824885	-3.750423
C	0.687483	0.309388	-4.473062
C	0.910288	1.595673	-3.956477
O	0.758989	1.880193	-2.677971
H	0.838509	0.178413	-5.543195
C	1.330570	2.716636	-4.795471
C	1.556143	3.976661	-4.190050
C	1.962264	5.076941	-4.938195
C	2.159974	4.968155	-6.317718
C	1.940641	3.729813	-6.934642
H	1.404234	4.067765	-3.112098
H	2.128361	6.036633	-4.436875
H	2.480052	5.833289	-6.906104
C	1.534915	2.626817	-6.193694
H	1.374066	1.679575	-6.714759
H	2.088954	3.623689	-8.014446
C	-0.394970	-4.666902	-5.568845
C	-0.399454	-4.503000	-4.181061
C	-0.164900	-3.548850	-6.379949
C	-0.177693	-3.251586	-3.615048
C	0.060683	-2.113502	-4.417327
C	0.057692	-2.296046	-5.819248
H	-0.575526	-5.363644	-3.526309
H	-0.163926	-3.655400	-7.469811
H	-0.570558	-5.650009	-6.016176
H	0.218254	-1.446447	-6.488007
H	-0.177652	-3.128218	-2.530828

Table A.22.: Cartesian coordinates (in Å) for the $S_{\pi\pi^*}$ geometries of NHCCuDBM.

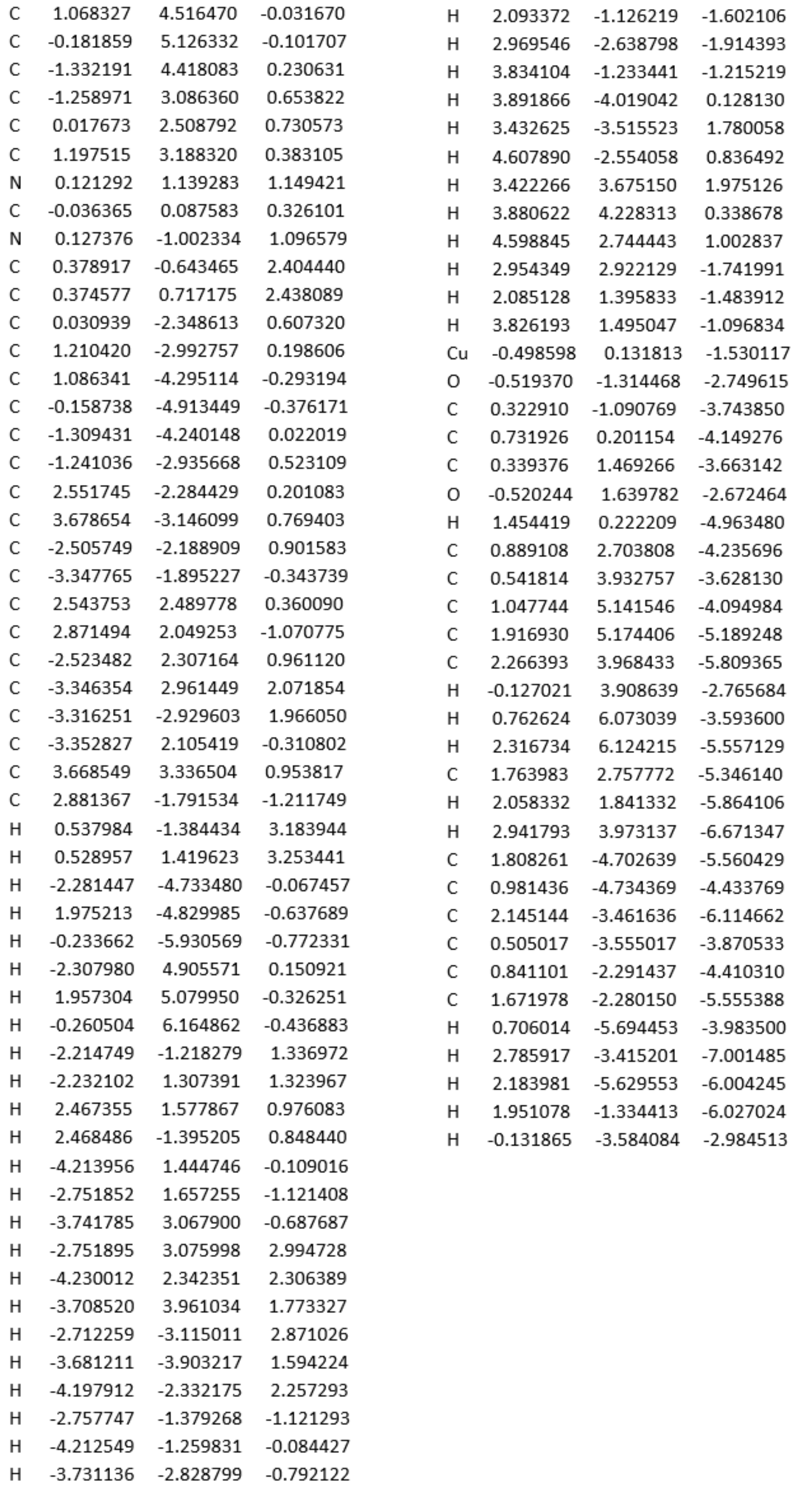

C	1.068327	4.516470	-0.031670
C	-0.181859	5.126332	-0.101707
C	-1.332191	4.418083	0.230631
C	-1.258971	3.086360	0.653822
C	0.017673	2.508792	0.730573
C	1.197515	3.188320	0.383105
N	0.121292	1.139283	1.149421
C	-0.036365	0.087583	0.326101
N	0.127376	-1.002334	1.096579
C	0.378917	-0.643465	2.404440
C	0.374577	0.717175	2.438089
C	0.030939	-2.348613	0.607320
C	1.210420	-2.992757	0.198606
C	1.086341	-4.295114	-0.293194
C	-0.158738	-4.913449	-0.376171
C	-1.309431	-4.240148	0.022019
C	-1.241036	-2.935668	0.523109
C	2.551745	-2.284429	0.201083
C	3.678654	-3.146099	0.769403
C	-2.505749	-2.188909	0.901583
C	-3.347765	-1.895227	-0.343739
C	2.543753	2.489778	0.360090
C	2.871494	2.049253	-1.070775
C	-2.523482	2.307164	0.961120
C	-3.346354	2.961449	2.071854
C	-3.316251	-2.929603	1.966050
C	-3.352827	2.105419	-0.310802
C	3.668549	3.336504	0.953817
C	2.881367	-1.791534	-1.211749
H	0.537984	-1.384434	3.183944
H	0.528957	1.419623	3.253441
H	-2.281447	-4.733480	-0.067457
H	1.975213	-4.829985	-0.637689
H	-0.233662	-5.930569	-0.772331
H	-2.307980	4.905571	0.150921
H	1.957304	5.079950	-0.326251
H	-0.260504	6.164862	-0.436883
H	-2.214749	-1.218279	1.336972
H	-2.232102	1.307391	1.323967
H	2.467355	1.577867	0.976083
H	2.468486	-1.395205	0.848440
H	-4.213956	1.444746	-0.109016
H	-2.751852	1.657255	-1.121408
H	-3.741785	3.067900	-0.687687
H	-2.751895	3.075998	2.994728
H	-4.230012	2.342351	2.306389
H	-3.708520	3.961034	1.773327
H	-2.712259	-3.115011	2.871026
H	-3.681211	-3.903217	1.594224
H	-4.197912	-2.332175	2.257293
H	-2.757747	-1.379268	-1.121293
H	-4.212549	-1.259831	-0.084427
H	-3.731136	-2.828799	-0.792122
H	2.093372	-1.126219	-1.602106
H	2.969546	-2.638798	-1.914393
H	3.834104	-1.233441	-1.215219
H	3.891866	-4.019042	0.128130
H	3.432625	-3.515523	1.780058
H	4.607890	-2.554058	0.836492
H	3.422266	3.675150	1.975126
H	3.880622	4.228313	0.338678
H	4.598845	2.744443	1.002837
H	2.954349	2.922129	-1.741991
H	2.085128	1.395833	-1.483912
H	3.826193	1.495047	-1.096834
Cu	-0.498598	0.131813	-1.530117
O	-0.519370	-1.314468	-2.749615
C	0.322910	-1.090769	-3.743850
C	0.731926	0.201154	-4.149276
C	0.339376	1.469266	-3.663142
O	-0.520244	1.639782	-2.672464
H	1.454419	0.222209	-4.963480
C	0.889108	2.703808	-4.235696
C	0.541814	3.932757	-3.628130
C	1.047744	5.141546	-4.094984
C	1.916930	5.174406	-5.189248
C	2.266393	3.968433	-5.809365
H	-0.127021	3.908639	-2.765684
H	0.762624	6.073039	-3.593600
H	2.316734	6.124215	-5.557129
C	1.763983	2.757772	-5.346140
H	2.058332	1.841332	-5.864106
H	2.941793	3.973137	-6.671347
C	1.808261	-4.702639	-5.560429
C	0.981436	-4.734369	-4.433769
C	2.145144	-3.461636	-6.114662
C	0.505017	-3.555017	-3.870533
C	0.841101	-2.291437	-4.410310
C	1.671978	-2.280150	-5.555388
H	0.706014	-5.694453	-3.983500
H	2.785917	-3.415201	-7.001485
H	2.183981	-5.629553	-6.004245
H	1.951078	-1.334413	-6.027024
H	-0.131865	-3.584084	-2.984513

Table A.23.: Cartesian coordinates (in Å) for the $T_{n\pi^*}$ geometries of NHCCuDBM.

C	1.038337	4.507292	0.600605
C	-0.201385	5.101181	0.386372
C	-1.374041	4.361804	0.526712
C	-1.333512	3.014061	0.894384
C	-0.065449	2.447432	1.117240
C	1.136276	3.160225	0.966608
N	0.005850	1.050574	1.434033
C	0.144870	0.116584	0.470844
N	0.190171	-1.057175	1.126511
C	0.086399	-0.861761	2.491118
C	-0.029854	0.479294	2.687818
C	0.351339	-2.351545	0.528339
C	1.649762	-2.793951	0.231245
C	1.781172	-4.085729	-0.289652
C	0.665344	-4.892228	-0.493135
C	-0.611357	-4.413143	-0.210503
C	-0.798402	-3.124452	0.299182
C	2.863907	-1.901154	0.400557
C	3.977761	-2.566998	1.208285
C	-2.191449	-2.558448	0.497457
C	-2.765377	-2.137739	-0.860416
C	2.494522	2.512797	1.158466
C	3.309934	2.548881	-0.137299
C	-2.600484	2.182629	0.971558
C	-3.734392	2.893367	1.709677
C	-3.127874	-3.510638	1.239208
C	-3.034299	1.753563	-0.434392
C	3.256080	3.145143	2.325010
C	3.361687	-1.429389	-0.969663
H	0.104236	-1.693838	3.190873
H	-0.134832	1.070606	3.594212
H	-1.480029	-5.046360	-0.410599
H	2.774322	-4.465904	-0.544764
H	0.790156	-5.900704	-0.898574
H	-2.337270	4.841696	0.334893
H	1.949641	5.098444	0.472533
H	-0.256082	6.154066	0.094423
H	-2.105291	-1.645885	1.110949
H	-2.370958	1.264592	1.538398
H	2.334848	1.452011	1.413484
H	2.551928	-1.004651	0.961983
H	-3.937571	1.120485	-0.385002
H	-2.245296	1.170523	-0.941734
H	-3.260443	2.633401	-1.062227
H	-3.415875	3.223334	2.713561
H	-4.592104	2.208983	1.828841
H	-4.095434	3.778019	1.156726
H	-2.705848	-3.813961	2.213248
H	-3.331014	-4.425352	0.655135
H	-4.098323	-3.017775	1.424118
H	-2.074673	-1.457056	-1.387236
H	-3.738652	-1.631927	-0.729054
H	2.544559	-0.969327	-1.551148
H	3.750289	-2.278496	-1.559997
H	4.173979	-0.690306	-0.853898
H	4.387772	-3.450981	0.689029
H	3.615649	-2.890999	2.199512
H	4.810250	-1.858003	1.361493
H	2.679337	3.074797	3.263562
H	3.468825	4.212136	2.134957
H	4.221607	2.630857	2.474874
H	3.579378	3.583809	-0.413420
H	2.745984	2.118904	-0.983957
H	4.246185	1.976520	-0.015497
Cu	0.368008	0.674833	-1.372887
O	0.125348	-0.850351	-2.446139
C	0.304519	-0.821133	-3.750498
C	0.704791	0.312122	-4.470672
C	0.929669	1.597406	-3.952371
O	0.773121	1.881949	-2.674491
H	0.860829	0.180911	-5.540070
C	1.358563	2.717070	-4.788740
C	1.585785	3.976086	-4.181791
C	2.000151	5.074923	-4.927543
C	2.204786	4.965664	-6.306028
C	1.983951	3.728329	-6.924413
H	1.428534	4.067631	-3.104629
H	2.167321	6.033868	-4.425147
H	2.531381	5.829677	-6.892481
C	1.569993	2.626777	-6.185882
H	1.408302	1.680273	-6.708026
H	2.137623	3.621854	-8.003435
C	-0.384162	-4.661305	-5.572880
C	-0.391986	-4.498183	-4.185012
C	-0.151140	-3.543012	-6.382812
C	-0.170584	-3.247262	-3.617805
C	0.070855	-2.109002	-4.418880
C	0.071134	-2.290683	-5.820888
H	-0.570339	-5.359032	-3.531143
H	-0.147656	-3.648979	-7.472727
H	-0.559474	-5.644014	-6.021198
H	0.233818	-1.440716	-6.488687
H	-0.172969	-3.124383	-2.533529

Table A.24.: Cartesian coordinates (in Å) for the $T_{\pi\pi^*}$ geometries of NHCCuDBM.

C	1.055982	4.514840	-0.054490
C	-0.194763	5.124191	-0.118799
C	-1.342497	4.414657	0.219612
C	-1.265804	3.083089	0.643136
C	0.010862	2.503946	0.712249
C	1.187764	3.186504	0.359055
N	0.117989	1.135680	1.129975
C	-0.053265	0.083719	0.303483
N	0.122841	-1.004120	1.080364
C	0.393659	-0.644037	2.384413
C	0.389736	0.716272	2.416093
C	0.019483	-2.350024	0.595795
C	1.190068	-2.993350	0.160547
C	1.056962	-4.293359	-0.335712
C	-0.188760	-4.912767	-0.395704
C	-1.330608	-4.243727	0.034655
C	-1.252243	-2.942089	0.541713
C	2.532881	-2.287923	0.144984
C	3.663174	-3.151068	0.704505
C	-2.507583	-2.201001	0.960624
C	-3.366262	-1.866442	-0.262328
C	2.534220	2.488486	0.328297
C	2.839392	2.025521	-1.100294
C	-2.528279	2.305751	0.962917
C	-3.344062	2.966925	2.074909
C	-3.306460	-2.968114	2.015128
C	-3.365544	2.095971	-0.302121
C	3.668348	3.343482	0.891186
C	2.847998	-1.800029	-1.272383
H	0.563745	-1.383152	3.163487
H	0.555738	1.419169	3.228904
H	-2.303586	-4.738677	-0.033478
H	1.939171	-4.825304	-0.701501
H	-0.271443	-5.927548	-0.796472
H	-2.319137	4.901557	0.145966
H	1.943227	5.079089	-0.352743
H	-0.275760	6.162826	-0.453296
H	-2.203840	-1.244922	1.418718
H	-2.233402	1.308382	1.328988
H	2.466033	1.586113	0.959066
H	2.457803	-1.396308	0.789925
H	-4.234488	1.449745	-0.087077
H	-2.772215	1.623923	-1.105126
H	-3.742604	3.057298	-0.693856
H	-2.742496	3.090322	2.992085
H	-4.224169	2.347450	2.321735
H	-3.711599	3.963272	1.771969
H	-2.687963	-3.189626	2.902082
H	-3.690224	-3.925018	1.619587
H	-4.175662	-2.371116	2.342541
H	-2.791386	-1.299308	-1.015368
H	-4.240028	-1.259409	0.032958
H	2.056298	-1.132010	-1.650391
H	2.923854	-2.648588	-1.975001
H	3.802726	-1.245397	-1.288739
H	3.865541	-4.028128	0.065205
H	3.427502	-3.514784	1.719755
H	4.595521	-2.562407	0.758107
H	3.436222	3.702807	1.908799
H	3.875440	4.222466	0.256107
H	4.597711	2.749861	0.939940
H	2.906986	2.887573	-1.787189
H	2.046491	1.362622	-1.485063
H	3.795121	1.473324	-1.134293
Cu	-0.537559	0.137150	-1.537209
O	-0.560908	-1.271894	-2.816394
C	0.318810	-1.079635	-3.777317
C	0.732995	0.212288	-4.183945
C	0.335855	1.480036	-3.693118
O	-0.549901	1.619205	-2.728504
H	1.452573	0.234457	-5.001646
C	0.900234	2.723023	-4.233273
C	0.532154	3.942945	-3.622347
C	1.049945	5.157664	-4.059421
C	1.952968	5.204054	-5.125456
C	2.325465	4.006670	-5.746363
H	-0.161993	3.909308	-2.780218
H	0.747915	6.082652	-3.556122
H	2.362298	6.158668	-5.469574
C	1.811017	2.789400	-5.312122
H	2.127168	1.879349	-5.828619
H	3.029088	4.021756	-6.585249
C	1.873889	-4.718001	-5.476434
C	0.982420	-4.733516	-4.399872
C	2.255490	-3.485601	-6.018104
C	0.485065	-3.545248	-3.875065
C	0.862388	-2.290732	-4.405244
C	1.761105	-2.294698	-5.496261
H	0.673078	-5.687078	-3.958118
H	2.950042	-3.451791	-6.863978
H	2.266904	-5.651808	-5.889709
H	2.082841	-1.355642	-5.954091
H	-0.200379	-3.561337	-3.025602

List of Figures

List of Tables

Bibliography

[1] Lambros Doulos, Dorina Moullou, and Frangiskos Topalis. Artificial Light Sources in Roman, Byzantine, and Post- Byzantine Eras: An Evaluation of their Performance. *Chronos Revue d'Histoire de l'Université de Balamand*, 32:119 –132, 2015.

[2] Sophie A. de Beaune and Randall White. Ice Age Lamps. *Scientific American*, 268(3):108–113, 1993.

[3] Frederick Moore Binder. GAS LIGHT. *Pennsylvania History: A Journal of Mid-Atlantic Studies*, 22(4):359–373, 1955.

[4] Massimo Guarnieri. Switching the Light: From Chemical to Electrical [Historical]. *IEEE Industrial Electronics Magazine*, 9(3):44–47, 2015.

[5] Abhishek P. Kulkarni, Christopher J. Tonzola, Amit Babel, and Samson A. Jenekhe. Electron Transport Materials for Organic Light-Emitting Diodes. *Chemistry of Materials*, 16(23):4556–4573, 2004.

[6] Jayanta Bauri, Ram Bilash Choudhary, and Gobind Mandal. Recent advances in efficient emissive materials-based OLED applications: a review. *Journal of Materials Science*, 56(34):18837–18866, 2021.

[7] Siegfried Hunklinger and Christian Enss. *Solid State Physics*. De Gruyter, Berlin, Boston, 2022.

[8] I. R. Anugrah, A. Mudzakir, and O. Sumarna. Construction of Context-Based Module: How OLED can be used as a Context in High School Chemistry Instruction. *Journal of Physics: Conference Series*, 895(1):012113, 2017.

[9] Takuya Ogawa, Don-Chan Cho, Kazue Kaneko, Tatsuo Mori, and Teruyoshi Mizutani. Numerical analysis of the carrier behavior of organic light-emitting diode: comparing a hopping conduction model with a SCLC model. *Thin Solid Films*, 438-439:171–176, 2003.

[10] Vitor Cristiano Bender, Tiago Bandeira Marchesan, and José Marcos Alonso. Solid-State Lighting: A Concise Review of the State of the Art on LED and OLED Modeling. *IEEE Industrial Electronics Magazine*, 9:6–16, 2015.

[11] Martin Weis, Takako Otsuka, Dai Taguchi, Takaaki Manaka, and Mitsumasa Iwamoto. Charge injection and accumulation in organic light-emitting diode with PEDOT:PSS anode. *Journal of Applied Physics*, 117:155503, 2015.

[12] Boris Minaev, Gleb Baryshnikov, and Hans Agren. Principles of phosphorescent organic light emitting devices. *Phys. Chem. Chem. Phys.*, 16:1719–1758, 2014.

[13] Jwo-Huei Jou, Sudhir Kumar, Abhishek Agrawal, Tsung-Han Li, and Snehashis Sahoo. Approaches for fabricating high efficiency organic light emitting diodes. *J. Mater. Chem. C*, 3:2974–3002, 2015.

[14] Stefan Kappaun, Christian Slugovc, and Emil J. W. List. Phosphorescent Organic Light-Emitting Devices: Working Principle and Iridium Based Emitter Materials. *International Journal of Molecular Sciences*, 9(8):1527–1547, 2008.

[15] A. Kavokin, J. J. Baumberg, G. Malpuech, and F. P. Laussy. *Microcavities*. Oxford University Press, Oxford, 2007.

[16] Stéphane Kéna-Cohen. *Strong exciton-photon coupling in organic semiconductor microcavities*. Princeton University, Princeton, 2010.

[17] Peter Atkins, Julio de Paula, and James Keeler. *Atkins' Physical Chemistry*. Oxford University Press, Oxford, 2018.

[18] Jianpu Wang, Alexei Chepelianskii, Feng Gao, and Neil C. Greenham. Control of exciton spin statistics through spin polarization in organic optoelectronic devices. *Nature Communications*, 3(1):1191, 2012.

[19] Christian Torres Ziegenbein, Sascha Fröbel, Maria Glöß, Roberto S. Nobuyasu, Przemyslaw Data, Andrew Monkman, and Peter Gilch. Triplet Harvesting with a Simple Aromatic Carbonyl. *ChemPhysChem*, 18(17):2314–2317, 2017.

[20] Fernando B. Dias, Konstantinos N. Bourdakos, Vygintas Jankus, Kathryn C. Moss, Kiran T. Kamtekar, Vandana Bhalla, José Santos, Martin R. Bryce, and Andrew P.

Monkman. Triplet Harvesting with 100% Efficiency by Way of Thermally Activated Delayed Fluorescence in Charge Transfer OLED Emitters. *Advanced Materials*, 25(27):3707–3714, 2013.

[21] Daniel Volz, Thomas Baumann, Manuela Wallesch, and Stefan Bräse. Late bloomers: copper complexes in organic LEDs. *SPIE Newsroom*, 2014.

[22] Michael Y. Wong and Eli Zysman-Colman. Purely Organic Thermally Activated Delayed Fluorescence Materials for Organic Light-Emitting Diodes. *Advanced Materials*, 29(22):1605444, 2017.

[23] Hartmut Yersin, Rafal Czerwieniec, Marsel Z. Shafikov, and Alfiya F. Suleymanova. TADF Material Design: Photophysical Background and Case Studies Focusing on Cu(I) and Ag(I) Complexes. *ChemPhysChem*, 18(24):3508–3535, 2017.

[24] Kristoffer A. Thom, Felix Wieser, Kevin Diestelhorst, Anna Reiffers, Constantin Czekelius, Martin Kleinschmidt, Mario Bracker, Christel M. Marian, and Peter Gilch. Acridones: Strongly Emissive HIGHrISC Fluorophores. *The Journal of Physical Chemistry Letters*, 12(24):5703–5709, 2021.

[25] Jayaraman Jayabharathi, Sekar Panimozhi, and Venugopal Thanikachalam. Hot exciton transition for organic light-emitting diodes: tailoring excited-state properties and electroluminescence performances of donor–spacer–acceptor molecules. *RSC Adv.*, 8:37324–37338, 2018.

[26] Christian Torres Ziegenbein. *Effiziente blaue OLED Emitter durch reverse Interkombination in aromatischen Carbonylverbindungen?* PhD thesis, Heinrich-Heine-Universität Düsseldorf, 2018.

[27] J.-K. Lee, D. S. Yoo, E. S. Handy, and M. F. Rubner. Thin film light emitting devices from an electroluminescent ruthenium complex. *Applied Physics Letters*, 69(12):1686–1688, 1996.

[28] Andreas F. Rausch, Herbert H. H. Homeier, and Hartmut Yersin. *Organometallic Pt(II) and Ir(III) Triplet Emitters for OLED Applications and the Role of Spin–Orbit Coupling: A Study Based on High-Resolution Optical Spectroscopy*, pages 193–235. Springer Berlin Heidelberg, Berlin, Heidelberg, 2010.

[29] Haiyang Ma, Di Liu, Jiuyan Li, Yongqiang Mei, Deli Li, Yong Ding, and Wenkui Wei. Sky-blue iridium complexes with pyrimidine ligands for highly efficient phosphorescent organic light-emitting diodes. *New J. Chem.*, 44:8743–8750, 2020.

[30] Armands Ruduss, Valdis Kokars, Natalija Tetervenoka, Aivars Vembris, and Kaspars Traskovskis. Effects of steric encumbrance of iridium(III) complex core on performance of solution-processed organic light emitting diodes. *RSC Adv.*, 10:27552–27559, 2020.

[31] Thomas Hofbeck and Hartmut Yersin. The Triplet State of fac-Ir(ppy)3. *Inorganic Chemistry*, 49(20):9290–9299, 2010.

[32] Christian Hagelüken. Markets for the Catalyst Metals Platinum, Palladium and Rhodium. *Metall*, 60:31–42, 2006.

[33] D. Volz, M. Wallesch, C. Fléchon, M. Danz, A. Verma, J. M. Navarro, D. M. Zink, S. Bräse, and T. Baumann. From iridium and platinum to copper and carbon: new avenues for more sustainability in organic light-emitting diodes. *Green Chem.*, 17:1988–2011, 2015.

[34] Justyna Pawlak, Elżbieta Łodyga Chruścińska, and Jakub Chrustowicz. Fate of platinum metals in the environment. *Journal of Trace Elements in Medicine and Biology*, 28(3):247–254, 2014.

[35] Paul Wagenknecht and Peter Ford. Metal centered ligand field excited states: Their roles in the design and performance of transition metal based photochemical molecular devices. *Coordination Chemistry Reviews*, 255:591–616, 2011.

[36] Thomas Hofbeck, Uwe Monkowius, and Hartmut Yersin. Highly Efficient Luminescence of Cu(I) Compounds: Thermally Activated Delayed Fluorescence Combined with Short-Lived Phosphorescence. *Journal of the American Chemical Society*, 137(1):399–404, 2015.

[37] Caroline Murawski, Karl Leo, and Malte C. Gather. Efficiency Roll-Off in Organic Light-Emitting Diodes. *Advanced Materials*, 25(47):6801–6827, 2013.

[38] Catherine E. Housecroft and Edwin C. Constable. TADF: Enabling luminescent copper(i)

coordination compounds for light-emitting electrochemical cells. *J. Mater. Chem. C*, 10:4456–4482, 2022.

[39] Frédéric Dumur. Recent advances in organic light-emitting devices comprising copper complexes: A realistic approach for low-cost and highly emissive devices? *Organic Electronics*, 21:27–39, 2015.

[40] Oliver Nolden, Jennifer Kremper, Wiebke Haselbach, Mahbobeh Morshedi, Jasper Guhl, Philipp Schmeinck, Christel M. Marian, Christian Ganter, and Peter Gilch. Femtosecond Spectroscopy and Quantum Chemistry of a Linearly Coordinated Copper(I) Carbene Complex. *ChemPhotoChem*, 7(4):e202200231, 2023.

[41] Charlotte L. Linfoot, Markus J. Leitl, Patricia Richardson, Andreas F. Rausch, Oleg Chepelin, Fraser J. White, Hartmut Yersin, and Neil Robertson. Thermally Activated Delayed Fluorescence (TADF) and Enhancing Photoluminescence Quantum Yields of [CuI(diimine)(diphosphine)]$+$ Complexes—Photophysical, Structural, and Computational Studies. *Inorganic Chemistry*, 53(20):10854–10861, 2014.

[42] Masahisa Osawa. Highly efficient blue-green delayed fluorescence from copper(i) thiolate complexes: luminescence color alteration by orientation change of the aryl ring. *Chem. Commun.*, 50:1801–1803, 2014.

[43] Rasha Hamze, Jesse L. Peltier, Daniel Sylvinson, Moonchul Jung, Jose Cardenas, Ralf Haiges, Michele Soleilhavoup, Rodolphe Jazzar, Peter I. Djurovich, Guy Bertrand, and Mark E. Thompson. Eliminating nonradiative decay in Cu(I) emitters: $>$99% quantum efficiency and microsecond lifetime. *Science*, 363(6427):601–606, 2019.

[44] Abdollah Neshat, Reza Babadi Aghakhanpour, Piero Mastrorilli, Stefano Todisco, Farzad Molani, and Andrzej Wojtczak. Dinuclear and tetranuclear copper(I) iodide complexes with P and P$^\wedge$N donor ligands: Structural and photoluminescence studies. *Polyhedron*, 154:217–228, 2018.

[45] J.-B. Dumas. *Memoire sur l'esprit de bois et sur les divers composes etheres qui en proviennent : lu a l'Academie des Sciences les 27 Octobre et 3 novembre 1834*. Imprimerie de E-J Bailly et Co, Paris, 1884.

[46] Matthew N. Hopkinson, Christian Richter, Michael Schedler, and Frank Glorius. An overview of N-heterocyclic carbenes. *Nature*, 510(7506):485–496, 2014.

[47] Alai Igau, Antoine Baceiredo, Georges Trinquier, and Guy Bertrand. [Bis(diisopropylamino)phosphino]trimethylsilylcarbene: A Stable Nucleophilic Carbene. *Angewandte Chemie International Edition in English*, 28(5):621–622, 1989.

[48] Anthony J. III Arduengo, Richard L. Harlow, and Michael Kline. A stable crystalline carbene. *Journal of the American Chemical Society*, 113(1):361–363, 1991.

[49] Claudia Bizzarri, Eduard Spuling, Daniel M. Knoll, Daniel Volz, and Stefan Bräse. Sustainable metal complexes for organic light-emitting diodes (OLEDs). *Coordination Chemistry Reviews*, 373:49–82, 2018.

[50] E. Schikora H.-W. Wanzlick. Ein neuer Zugang zur Carben-Chemie. *Angewandte Chemie*, 72(14):494, 1960.

[51] Tian-yi Li, Daniel Sylvinson Muthiah Ravinson, Ralf Haiges, Peter I. Djurovich, and Mark E. Thompson. Enhancement of the Luminescent Efficiency in Carbene-Au(I)-Aryl Complexes by the Restriction of Renner–Teller Distortion and Bond Rotation. *Journal of the American Chemical Society*, 142(13):6158–6172, 2020.

[52] A. Jablonski. Efficiency of Anti-Stokes Fluorescence in Dyes. *Nature*, 131(3319):839–840, 1933.

[53] William Parson. *Modern Optical Spectroscopy*. Springer Berlin Heidelberg, Berlin, Heidelberg, 2009.

[54] Anna Reiffers. *Zeitaufgelöste Spektroskopie zur Photophysik und Photochemie von Phthalimiden*. PhD thesis, Heinrich-Heine-Universität Düsseldorf, 2020.

[55] Morten Gotthold Vinum, Laura Voigt, Steen H. Hansen, Colby Bell, Kensha Marie Clark, René Wugt Larsen, and Kasper S. Pedersen. Ligand field-actuated redox-activity of acetylacetonate. *Chem. Sci.*, 11:8267–8272, 2020.

[56] Petr Klán and Jakob Wirz. *Photochemistry of Organic Compounds*. John Wiley & Sons Ltd., Chichester, UK., 2009.

[57] Michael Kasha. Characterization of electronic transitions in complex molecules. *Discuss. Faraday Soc.*, 9:14–19, 1950.

[58] Niels Bohr. On the Application of the Quantum Theory to Atomic Structure. *Proceedings of the Cambridge Philosophical Society: Supplement*, pages 28–32, 1924.

[59] M. Born and R. Oppenheimer. Zur Quantentheorie der Molekeln. *Annalen der Physik*, 389(20):457–484, 1927.

[60] Edward Condon. A Theory of Intensity Distribution in Band Systems. *Physical Review*, 28(6):1182–1201, 1926.

[61] J. Franck and E. G. Dymond. Elementary processes of photochemical reactions. *Trans. Faraday Soc.*, 21:536–542, 1926.

[62] Peter W. Atkins and Ronald S. Friedman. *Molecular Quantum Mechanics*. Oxford University Press, Oxford, 2005.

[63] Beer. Bestimmung der Absorption des rothen Lichts in farbigen Flüssigkeiten. *Annalen der Physik*, 162(5):78–88, 1852.

[64] Johann Heinrich Lambert. *I.H. Lambert Photometria, sive, De mensura et gradibus luminis, colorum et umbrae [microform]*. V.E. Klett Augustae Vindelicorum, 1760.

[65] S. J. Strickler and Robert A. Berg. Relationship between Absorption Intensity and Fluorescence Lifetime of Molecules. *The Journal of Chemical Physics*, 37(4):814–822, 1962.

[66] J. B. Birks, D. J. Dyson, and Brian Hilton Flowers. The relations between the fluorescence and absorption properties of organic molecules. *Proceedings of the Royal Society of London. Series A. Mathematical and Physical Sciences*, 275(1360):135–148, 1963.

[67] Christel M. Marian. Understanding and Controlling Intersystem Crossing in Molecules. *Annual Review of Physical Chemistry*, 72(1):617–640, 2021.

[68] A. Maciejewski, A. Safarzadeh-Amiri, R.E. Verrall, and R.P. Steer. Radiationless decay of the second excited singlet states of aromatic thiones: Experimental verification of the energy gap law. *Chemical Physics*, 87(2):295–303, 1984.

[69] Derk J. Stufkens and Antonin Vlček. Ligand-dependent excited state behaviour of Re(I) and Ru(II) carbonyl–diimine complexes. *Coordination Chemistry Reviews*, 177(1):127–179, 1998.

[70] Jonathan V. Caspar, B.Patrick Sullivan, Edward M. Kober, and Thomas J. Meyer. Application of the energy gap law to the decay of charge transfer excited states, solvent effects. *Chemical Physics Letters*, 91(2):91–95, 1982.

[71] Julia Weinstein. *Applied Photochemistry*, pages 105–148. 2013.

[72] Nicholas J.Turro, V.Ramamurthy, and J. C.Scaiano. *Principles of Molecular Photochemistry—An Introduction*. University Science Books, 2009.

[73] Friedrich Kremer. M.D. Fayer (ed): Ultrafast Infrared and Raman Spectroscopy. *Colloid and Polymer Science*, 284(7):822–822, 2006.

[74] J.L. Duncan. The determination of vibrational anharmonicity in molecules from spectroscopic observations. *Spectrochimica Acta Part A: Molecular Spectroscopy*, 47(1):1–27, 1991.

[75] O. Golonzka, M. Khalil, N. Demirdöven, and A. Tokmakoff. Vibrational Anharmonicities Revealed by Coherent Two-Dimensional Infrared Spectroscopy. *Phys. Rev. Lett.*, 86:2154–2157, 2001.

[76] Niels H. Damrauer, Giulio Cerullo, Alvin Yeh, Thomas R. Boussie, Charles V. Shank, and James K. McCusker. Femtosecond Dynamics of Excited-State Evolution in $[\mathrm{Ru(bpy)_3}]^{2+}$. *Science*, 275(5296):54–57, 1997.

[77] Andrea Cannizzo, Frank van Mourik, Wojciech Gawelda, Goran Zgrablic, Christian Bressler, and Majed Chergui. Broadband Femtosecond Fluorescence Spectroscopy of $[\mathrm{Ru(bpy)_3}]^{2+}$. *Angewandte Chemie International Edition*, 45(19):3174–3176, 2006.

[78] Mario N Berberan Santos and Bernard Valeur. *Molecular Fluorescence: Principles and Applications, Second Edition*. 2012.

[79] Tomohisa Takaya, Masato Anan, and Koichi Iwata. Vibrational relaxation dynamics of β-carotene and its derivatives with substituents on terminal rings in electronically excited

states as studied by femtosecond time-resolved stimulated Raman spectroscopy in the near-IR region. *Phys. Chem. Chem. Phys.*, 20:3320–3327, 2018.

[80] Mohammad A. Omary and Howard H. Patterson. Luminescence Theory. In John C. Lindon, editor, *Encyclopedia of Spectroscopy and Spectrometry*, pages 1186–1207. Elsevier, Oxford, 1999.

[81] M. A. El-Sayed. Spin-Orbit Coupling and the Radiationless Processes in Nitrogen Heterocyclics. *The Journal of Chemical Physics*, 38(12):2834–2838, 1963.

[82] Mostafa A. El-Sayed. Triplet state. Its radiative and nonradiative properties. *Accounts of Chemical Research*, 1(1):8–16, 1968.

[83] Elise Li, Tzung-Ying Jiang, Yun Chi, and Pi-Tai Chou. Semi-quantitative assessment of the intersystem crossing rate: An extension of the El-Sayed rule to the emissive transition metal complexes. *Physical chemistry chemical physics*, 16:26184–26192, 2014.

[84] M. Vijayakumar and M.S. Gopinathan. Spin-orbit coupling constants of transition metal atoms and ions in density functional theory. *Journal of Molecular Structure: THEOCHEM*, 361(1):15–19, 1996.

[85] Shiro Koseki, Nikita Matsunaga, Toshio Asada, Michael W. Schmidt, and Mark S. Gordon. Spin–Orbit Coupling Constants in Atoms and Ions of Transition Elements: Comparison of Effective Core Potentials, Model Core Potentials, and All-Electron Methods. *The Journal of Physical Chemistry A*, 123(12):2325–2339, 2019.

[86] Chien-Wei Hsu, Chao-Chen Lin, Min-Wen Chung, Yun Chi, Gene-Hsiang Lee, Pi-Tai Chou, Chih-Hao Chang, and Pin-Yang Chen. Systematic Investigation of the Metal-Structure–Photophysics Relationship of Emissive d10-Complexes of Group 11 Elements: The Prospect of Application in Organic Light Emitting Devices. *Journal of the American Chemical Society*, 133(31):12085–12099, 2011.

[87] J.R. Lakowicz. *Principles of Fluorescence Spectroscopy, Third Edition*. Springer, New York, 2006.

[88] S. F. A. Kettle. *Electronic spectra of transition metal complexes*, pages 156–184. Springer Berlin Heidelberg, Berlin, Heidelberg, 1996.

[89] David W. Thompson, Akitaka Ito, and Thomas J. Meyer. [Ru(bpy)3]$^{2+*}$ and other remarkable metal-to-ligand charge transfer (MLCT) excited states. *Pure and Applied Chemistry*, 85(7):1257–1305, 2013.

[90] Noel S. Hush and Jeffrey R. Reimers. Solvent Effects on the Electronic Spectra of Transition Metal Complexes. *Chemical Reviews*, 100(2):775–786, 2000.

[91] Ariana Rondi, Yuseff Rodriguez, Thomas Feurer, and Andrea Cannizzo. Solvation-Driven Charge Transfer and Localization in Metal Complexes. *Accounts of Chemical Research*, 48(5):1432–1440, 2015.

[92] Anatolio Pigliucci, Guillaume Duvanel, Latévi Max Lawson Daku, and Eric Vauthey. Investigation of the Influence of Solute-Solvent Interactions on the Vibrational Energy Relaxation Dynamics of Large Molecules in Liquids. *The Journal of Physical Chemistry A*, 111(28):6135–6145, 2007.

[93] Biman Bagchi and Biman Jana. Solvation dynamics in dipolar liquids. *Chem. Soc. Rev.*, 39:1936–1954, 2010.

[94] Xiyi Chen and Stephen E. Bradforth. The Ultrafast Dynamics of Photodetachment. *Annual Review of Physical Chemistry*, 59(1):203–231, 2008.

[95] Hans Jakob Wörner, Christopher A. Arrell, Natalie Banerji, Andrea Cannizzo, Majed Chergui, Akshaya K. Das, Peter Hamm, Ursula Keller, Peter M. Kraus, Elisa Liberatore, Pablo Lopez-Tarifa, Matteo Lucchini, Markus Meuwly, Chris Milne, Jacques-E. Moser, Ursula Rothlisberger, Grigory Smolentsev, Joël Teuscher, Jeroen A. van Bokhoven, and Oliver Wenger. Charge migration and charge transfer in molecular systems. *Structural Dynamics*, 4(6):061508, 2017.

[96] Marco Reinhard, Gerald Auböck, Nicholas A. Besley, Ian P. Clark, Gregory M. Greetham, Magnus W. D. Hanson-Heine, Raphael Horvath, Thomas S. Murphy, Thomas J. Penfold, Michael Towrie, Michael W. George, and Majed Chergui. Photoaquation Mechanism of Hexacyanoferrate(II) Ions: Ultrafast 2D UV and Transient Visible and IR Spectroscopies. *Journal of the American Chemical Society*, 139(21):7335–7347, 2017.

[97] K. G. Weil. D. T. Sawyer and J. L. Roberts, Jr.: Experimental Electrochemistry for

Chemists, Verlag John Wiley & Sons Ltd., Baffins Lane 1974. *Berichte der Bunsengesellschaft für physikalische Chemie*, 79(9):842–843, 1975.

[98] J.A. Marinsky and Y. Marcus. *Ion Exchange and Solvent Extraction: A Series of Advances*. CRC Press, Boca Raton, 1997.

[99] V. Gutmann. Coordination chemistry of certain transition-metal ions. The role of the solvent. *Coordination Chemistry Reviews*, 2(2):239–256, 1967.

[100] Jian Li, Peter I. Djurovich, Bert D. Alleyne, Muhammed Yousufuddin, Nam N. Ho, J. Christopher Thomas, Jonas C. Peters, Robert Bau, and Mark E. Thompson. Synthetic Control of Excited-State Properties in Cyclometalated Ir(III) Complexes Using Ancillary Ligands. *Inorganic Chemistry*, 44(6):1713–1727, 2005.

[101] Andreas Rausch. *Der Einfluss von Molekülstruktur und Matrix auf die Emissionseigenschaften phosphoreszierender Übergangsmetallkomplexe für OLED-Anwendungen*. PhD thesis, Universität Regensburg, 2011.

[102] Markus J. Leitl. *Photophysical Characterizations of OLED Relevant Cu(I) Complexes Exhibiting Thermally Activated Delayed Fluorescence (TADF)*. PhD thesis, Universität Regensburg, 2015.

[103] M. Montalti, A. Credi, L. Prodi, and M.T. Gandolfi. *Handbook of Photochemistry*. CRC Press, 2006.

[104] Arnd Vogler and Horst Kunkely. *Luminescent Metal Complexes: Diversity of Excited States*, pages 143–182. Springer Berlin Heidelberg, Berlin, Heidelberg, 2001.

[105] H. Yersin and W. J. Finkenzeller. *Highly Efficient OLEDs with Phosphorescent Materials*. Wiley-VCH, Weinheim, 2008.

[106] Hartmut Yersin, Rafal Czerwieniec, Marsel Z. Shafikov, and Alfiya F. Suleymanova. TADF Material Design: Photophysical Background and Case Studies Focusing on CuI and AgI Complexes. *ChemPhysChem*, 18(24):3508–3535, 2017.

[107] Tony Owen. *Fundamentals of modern UV-visible spectroscopy : primer*. Agilent Technologies, Waldbronn, 2000.

[108] Bernard Valeur and Mário Nuno Berberan-Santos. *Molecular Fluorescence: Principles and Applications*. Wiley-VCH, Oxford, 2012.

[109] Adolfas K Gaigalas and Lili Wang. Measurement of the Fluorescence Quantum Yield Using a Spectrometer With an Integrating Sphere Detector. *Journal of research of the National Institute of Standards and Technology*, 113(1):17–28, 2008.

[110] D.O. Faulkner, J.J. McDowell, Alastair Price, D. Perovic, N.P. Kherani, and Geof Ozin. Measurement of absolute photoluminescence quantum yields using integrating spheres – Which way to go? *Laser & Photonics Reviews*, 6, 2012.

[111] Joseph Kimball, Jose Chavez, Luca Ceresa, Emma Kitchner, Zhangatay Nurekeyev, Hung Doan, Mariusz Szabelski, Julian Borejdo, Ignacy Gryczynski, and Zygmunt Gryczynski. On the origin and correction for inner filter effects in fluorescence Part I: primary inner filter effect-the proper approach for sample absorbance correction. *Methods and Applications in Fluorescence*, 8(3):033002, 2020.

[112] Luca Ceresa, Joseph Kimball, Jose Chavez, Emma Kitchner, Zhangatay Nurekeyev, Hung Doan, Julian Borejdo, Ignacy Gryczynski, and Zygmunt Gryczynski. On the origin and correction for inner filter effects in fluorescence. Part II: secondary inner filter effect -the proper use of front-face configuration for highly absorbing and scattering samples. *Methods and Applications in Fluorescence*, 9(3):035005, 2021.

[113] Torben T. Villnow. *Schnelle Interkombination aromatischer Carbonylverbindungen am Beispiel von Thioxanthon und Anthrachinon*. PhD thesis, Heinrich-Heine-Universität Düsseldorf, 2015.

[114] T. Q. Ye, C. J. Arnold, D. I. Pattison, C. L. Anderton, D. Dukic, R. N. Perutz, R. E. Hester, and John N. Moore. Development of an ultrafast laser apparatus for time-resolved UV-visible and infrared spectroscopy. *APPLIED SPECTROSCOPY*, 50(5):597–607, 1996.

[115] Sae Jeoung, Satoshi Takeuchi, Tahei Tahara, and Dongho Kim. Ultrafast decay dynamics of photoexcited Cu(II)(TMpy-P4) in water solvent. *Chemical Physics Letters - CHEM PHYS LETT*, 309:369–376, 1999.

[116] Claude Rullière. *Femtosecond Laser Pulses*. Springer New York, New York, 2004.

[117] Giulio Cerullo and Sandro De Silvestri. Ultrafast optical parametric amplifiers. *Review of Scientific Instruments*, 74(1):1–18, 2003.

[118] Philip J. M. Johnson, Valentyn I. Prokhorenko, and R. J. Dwayne Miller. Stable UV to IR supercontinuum generation in calcium fluoride with conserved circular polarization states. *Opt. Express*, 17(24):21488–21496, 2009.

[119] M. Bradler and E. Riedle. Temporal and spectral correlations in bulk continua and improved use in transient spectroscopy. *J. Opt. Soc. Am. B*, 31(7):1465–1475, 2014.

[120] Johanna Brazard, Laurie A. Bizimana, and Daniel B. Turner. Accurate convergence of transient-absorption spectra using pulsed lasers. *Review of Scientific Instruments*, 86(5), 2015.

[121] B. Schmidt, S. Laimgruber, W. Zinth, and P. Gilch. A broadband Kerr shutter for femtosecond fluorescence spectroscopy. *Applied Physics B*, 76(8):809–814, 2003.

[122] Ramona Mundt. *Femtosekunden-Fluoreszenzspektroskopie an kurzlebigen UV-Chromophoren*. PhD thesis, Heinrich-Heine-Universitat Dusseldorf, 2016.

[123] Anna Reiffers, Christian Torres Ziegenbein, Luiz Schubert, Janina Diekmann, Kristoffer A. Thom, Ralf Kühnemuth, Axel Griesbeck, Oliver Weingart, and Peter Gilch. On the large apparent Stokes shift of phthalimides. *Phys. Chem. Chem. Phys.*, 21:4839–4853, 2019.

[124] Matthias Wollenhaupt, Andreas Assion, and Thomas Baumert. *Femtosecond Laser Pulses: Linear Properties, Manipulation, Generation and Measurement*, pages 937–983. Springer New York, New York, 2007.

[125] H. Satzger and W. Zinth. Visualization of transient absorption dynamics – towards a qualitative view of complex reaction kinetics. *Chemical Physics*, 295(3):287–295, 2003.

[126] M. Gruebele and A. H. Zewail. Femtosecond wave packet spectroscopy: Coherences, the potential, and structural determination. *The Journal of Chemical Physics*, 98(2):883–902, 1993.

[127] Henning Marciniak and Stefan Lochbrunner. On the interpretation of decay associated spectra in the presence of time dependent spectral shifts. *Chemical Physics Letters*, 609:184–188, 2014.

[128] Ron Simkovitch, Rinat Gepshtein, and Dan Huppert. Fast Photoinduced Reactions in the Condensed Phase Are Nonexponential. *The Journal of Physical Chemistry A*, 119(10):1797–1812, 2015.

[129] Marcin Ziolek, Maciej Lorenc, and Ryszard Naskrecki. Determination of the temporal response function in femtosecond pump-probe systems. *Applied Physics B: Lasers and Optics*, 72:843–847, 2001.

[130] Jorge J. Moré. The Levenberg-Marquardt algorithm: Implementation and theory. In G. A. Watson, editor, *Numerical Analysis*, pages 105–116, Berlin, Heidelberg, 1978. Springer Berlin Heidelberg.

[131] D. Onidas, D. Markovitsi, S. Marguet, A. Sharonov, and T. Gustavsson. Fluorescence Properties of DNA Nucleosides and Nucleotides: A Refined Steady-State and Femtosecond Investigation. *The Journal of Physical Chemistry B*, 106(43):11367–11374, 2002.

[132] Kengo Suzuki, Atsushi Kobayashi, Shigeo Kaneko, Kazuyuki Takehira, Toshitada Yoshihara, Hitoshi Ishida, Yoshimi Shiina, Shigero Oishi, and Seiji Tobita. Reevaluation of absolute luminescence quantum yields of standard solutions using a spectrometer with an integrating sphere and a back-thinned CCD detector. *Physical Chemistry Chemical Physics*, 11(42):9850–9860, 2009.

[133] Knut Rurack and Monika Spieles. Fluorescence Quantum Yields of a Series of Red and Near-Infrared Dyes Emitting at 600 - 1000 nm. *Analytical Chemistry*, 83(4):1232–1242, 2011.

[134] Mikael Kubista, Robert Sjöback, Svante Eriksson, and Bo Albinsson. Experimental correction for the inner-filter effect in fluorescence spectra. *Analyst*, 119:417–419, 1994.

[135] Wiebke Haselbach, Jeremy Kaminski, Laura Kloeters, Thomas Müller, Oliver Weingart, Christel Marian, Peter Gilch, and Barbara Faria. Investigating a TADF Emitter by Time Resolved Near Infrared Spectroscopy. *Chemistry (Weinheim an der Bergstrasse, Germany)*, 29, 2022.

[136] Kristoffer A. Thom. *Direkte und sensibilisierte Untersuchung von aromatischen Carbonylen als neuartige OLED-Emitter*. PhD thesis, Heinrich-Heine-Universität Düsseldorf, 2021.

[137] M. Lorenc, M. Ziolek, R. Naskrecki, J. Karolczak, J. Kubicki, and A. Maciejewski. Artifacts in femtosecond transient absorption spectroscopy. *Applied Physics B*, 74(1):19–27, 2002.

[138] Carlo Adamo and Vincenzo Barone. Toward reliable density functional methods without adjustable parameters: The PBE0 model. *The Journal of Chemical Physics*, 110(13):6158–6170, 1999.

[139] M. J. Frisch, G. W. Trucks, H. B. Schlegel, G. E. Scuseria, M. A. Robb, J. R. Cheeseman, G. Scalmani, V. Barone, G. A. Petersson, H. Nakatsuji, X. Li, M. Caricato, A. V. Marenich, J. Bloino, B. G. Janesko, R. Gomperts, B. Mennucci, H. P. Hratchian, J. V. Ortiz, A. F. Izmaylov, J. L. Sonnenberg, D. Williams-Young, F. Ding, F. Lipparini, F. Egidi, J. Goings, B. Peng, A. Petrone, T. Henderson, D. Ranasinghe, V. G. Zakrzewski, J. Gao, N. Rega, G. Zheng, W. Liang, M. Hada, M. Ehara, K. Toyota, R. Fukuda, J. Hasegawa, M. Ishida, T. Nakajima, Y. Honda, O. Kitao, H. Nakai, T. Vreven, K. Throssell, J. A. Montgomery, Jr., J. E. Peralta, F. Ogliaro, M. J. Bearpark, J. J. Heyd, E. N. Brothers, K. N. Kudin, V. N. Staroverov, T. A. Keith, R. Kobayashi, J. Normand, K. Raghavachari, A. P. Rendell, J. C. Burant, S. S. Iyengar, J. Tomasi, M. Cossi, J. M. Millam, M. Klene, C. Adamo, R. Cammi, J. W. Ochterski, R. L. Martin, K. Morokuma, O. Farkas, J. B. Foresman, and D. J. Fox. Gaussian 16 Revision C.01, 2016. Gaussian Inc. Wallingford CT.

[140] Stefan Grimme, Jens Antony, Stephan Ehrlich, and Helge Krieg. A consistent and accurate ab initio parametrization of density functional dispersion correction (DFT-D) for the 94 elements H-Pu. *The Journal of Chemical Physics*, 132(15):154104, 2010.

[141] Ansgar Schäfer, Hans Horn, and Reinhart Ahlrichs. Fully optimized contracted Gaussian basis sets for atoms Li to Kr. *The Journal of Chemical Physics*, 97(4):2571–2577, 1992.

[142] Detlev Figgen, Guntram Rauhut, Michael Dolg, and Hermann Stoll. Energy-consistent pseudopotentials for group 11 and 12 atoms: Adjustment to multi-configuration Dirac-Hartree-Fock data. *Chemical Physics*, 311:227–244, 2005.

[143] Kirk A. Peterson and Cristina Puzzarini. Systematically convergent basis sets for transition metals. II. Pseudopotential-based correlation consistent basis sets for the group 11 (Cu, Ag, Au) and 12 (Zn, Cd, Hg) elements. *Theoretical Chemistry Accounts*, 114(4):283–296, 2005.

[144] Jacopo Tomasi, Benedetta Mennucci, and Roberto Cammi. Quantum Mechanical Continuum Solvation Models. *Chemical Reviews*, 105(8):2999–3094, 2005.

[145] TURBOMOLE V6.3 2010, a development of University of Karlsruhe and Forschungszentrum Karlsruhe GmbH, 1989-2007, TURBOMOLE GmbH, since 2007.

[146] Reinhart Ahlrichs, Michael Bär, Marco Häser, Hans Horn, and Christoph Kölmel. Electronic structure calculations on workstation computers: The program system turbomole. *Chemical Physics Letters*, 162(3):165–169, 1989.

[147] Adrian Heil, Martin Kleinschmidt, and Christel M. Marian. Erratum: "On the performance of DFT/MRCI Hamiltonians for electronic excitations in transition metal complexes: The role of the damping function" [J. Chem. Phys. 149, 164106 (2018)]. *The Journal of Chemical Physics*, 150(21):219903, 2019.

[148] Axel D. Becke. A new mixing of Hartree–Fock and local density-functional theories. *The Journal of Chemical Physics*, 98(2):1372–1377, 1993.

[149] Stefan Grimme and Mirko Waletzke. A combination of Kohn–Sham density functional theory and multi-reference configuration interaction methods. *The Journal of Chemical Physics*, 111(13):5645–5655, 1999.

[150] Martin Kleinschmidt, Jörg Tatchen, and Christel M. Marian. SPOCK.CI: A multireference spin-orbit configuration interaction method for large molecules. *The Journal of Chemical Physics*, 124(12):124101, 2006.

[151] Mihajlo Etinski, Jörg Tatchen, and Christel M. Marian. Time-dependent approaches for the calculation of intersystem crossing rates. *The Journal of Chemical Physics*, 134(15):154105, 2011.

[152] Annika Liske, Lars Wallbaum, Torsten Hölzel, Jelena Föller, Markus Gernert, Benjamin Hupp, Christian Ganter, Christel M. Marian, and Andreas Steffen. Cu–F Interactions

between Cationic Linear N-Heterocyclic Carbene Copper(I) Pyridine Complexes and Their Counterions Greatly Enhance Blue Luminescence Efficiency. *Inorganic Chemistry*, 58(9):5433–5445, 2019.

[153] L. Hintermann. Expedient syntheses of the N-heterocyclic carbene precursor imidazolium salts IPr-HCl, IMes-HCl and IXy-HCl. *Beilstein J. Org. Chem.*, 3:22, 207.

[154] Jelena Föller, Christian Ganter, Andreas Steffen, and Christel M. Marian. Computer-Aided Design of Luminescent Linear N-Heterocyclic Carbene Copper(I) Pyridine Complexes. *Inorganic Chemistry*, 58(9):5446–5456, 2019.

[155] Nora Lüdtke, Jelena Föller, and Christel M. Marian. Understanding the luminescence properties of Cu(i) complexes: a quantum chemical perusal. *Phys. Chem. Chem. Phys.*, 22:23530–23544, 2020.

[156] Franco Cataldo. A revision of the Gutmann donor numbers of a series of phosphoramides including TEPA. *European Chemical Bulletin*, 2015:92–97, 2015.

[157] Ivo H.M. van Stokkum, Delmar S. Larsen, and Rienk van Grondelle. Global and target analysis of time-resolved spectra. *Biochimica et Biophysica Acta (BBA) - Bioenergetics*, 1657(2):82–104, 2004.

[158] Abraham Nitzan. *Chemical Dynamics in Condensed Phases: Relaxation, Transfer and Reactions in Condensed Molecular Systems*. Oxford University Press, 2006.

[159] Benjamin Hupp, Carl Schiller, Carsten Lenczyk, Marco Stanoppi, Katharina Edkins, Andreas Lorbach, and Andreas Steffen. Synthesis, Structures, and Photophysical Properties of a Series of Rare Near-IR Emitting Copper(I) Complexes. *Inorganic Chemistry*, 56(15):8996–9008, 2017.

[160] P. Gacoin. Studies of the Triplet State of Carbonyl Compounds. I. Phosphorescence of β-Diketones. *The Journal of Chemical Physics*, 57(4):1418–1425, 1972.

[161] D. Veierov, T. Bercovici, E. Fischer, Y. Mazur, and A. Yogev. Photoisomerization of the enol form of 1,3-dicarbonyl compounds. *Journal of the American Chemical Society*, 99(8):2723–2729, 1977.

[162] Alejandro J. Vila, Claudia M. Lagier, and Alejandro C. Olivieri. Proton transfer in solid 1-phenylbutane-1,3-dione and related 1,3-diones as studied by carbon-13 CPMAS NMR spectroscopy and AM1 calculations. *The Journal of Physical Chemistry*, 95(13):5069–5073, 1991.

[163] P. Yankov, S. Saltiel, and I. Petkov. Photoketonization and excited state relaxation of dibenzoylmethane in non-polar solvents. *Journal of Photochemistry and Photobiology A: Chemistry*, 41(2):205–214, 1988.

[164] Seiji Tobita, Jin Ohba, Kenji Nakagawa, and Haruo Shizuka. Recovery mechanism of the reaction intermediate produced by photoinduced cleavage of the intramolecular hydrogen bond of dibenzoylmethane. *Journal of Photochemistry and Photobiology A: Chemistry*, 92(1):61–67, 1995.

[165] Francis P. Gasparro, Mark Mitchnick, and J. Frank Nash. A Review of Sunscreen Safety and Efficacy. *Photochemistry and Photobiology*, 68(3):243–256, 1998.

[166] Alexis Aspée, Carolina Aliaga, and J.C. Scaiano. Transient Enol Isomers of Dibenzoylmethane and Avobenzone as Efficient Hydrogen Donors toward a Nitroxide Pre-fluorescent Probe†. *Photochemistry and Photobiology*, 83(3):481–485, 2007.

[167] Nadim A. Shaath. Ultraviolet filters. *Photochem. Photobiol. Sci.*, 9:464–469, 2010.

[168] Atsushi Kobayashi, Minoru Yamaji, Satoru Nakajima, Kimio Akiyama, Shozo Tero-Kubota, Shin ichiro Kato, and Yosuke Nakamura. Photochemical behaviors of a tethered 1,3-diketone derivative studied by transient absorption and time-resolved EPR measurements. *Chemical Physics Letters*, 555:101–105, 2013.

[169] Pramod Kumar Verma, Federico Koch, Andreas Steinbacher, Patrick Nuernberger, and Tobias Brixner. Ultrafast UV-Induced Photoisomerization of Intramolecularly H-Bonded Symmetric β-Diketones. *Journal of the American Chemical Society*, 136(42):14981–14989, 2014.

[170] Pramod Kumar Verma, Andreas Steinbacher, Federico Koch, Patrick Nuernberger, and Tobias Brixner. Monitoring ultrafast intramolecular proton transfer processes in an unsymmetric β-diketone. *Phys. Chem. Chem. Phys.*, 17:8459–8466, 2015.

[171] Xianqi Kong, Andreas Brinkmann, Victor Terskikh, Roderick E. Wasylishen, Guy M. Bernard, Zhuang Duan, Qichao Wu, and Gang Wu. Proton Probability Distribution in the O···H···O Low-Barrier Hydrogen Bond: A Combined Solid-State NMR and Quantum Chemical Computational Study of Dibenzoylmethane and Curcumin. *The Journal of Physical Chemistry B*, 120(45):11692–11704, 2016.

[172] J. Paul, K. Schlögl, and W. Silhan. Die Anwendung von Tris(dipivalomethanato)europium in der NMR-Spektroskopie von Metallocenen. *Monatshefte für Chemie / Chemical Monthly*, 103(1):243–254, 1972.

[173] R.G. Charles and E.P. Riedel. Properties of some europium laser chelates derived from benzoyltrifluoroacetone. *Journal of Inorganic and Nuclear Chemistry*, 28(12):3005–3018, 1966.

[174] Jian Liu and Jing-Sheng Miao. Blue electroluminescence of a novel Zn2+–β-diketone complex with a carbazole moiety. *Chinese Chemical Letters*, 25(1):69–72, 2014.

[175] Maximilian N. Kopylovich, Tatiana C.O. Mac Leod, Matti Haukka, Gunel I. Amanullayeva, Kamran T. Mahmudov, and Armando J.L. Pombeiro. Aquasoluble iron(III)-arylhydrazone-β-diketone complexes: Structure and catalytic activity for the peroxidative oxidation of C5–C8 cycloalkanes. *Journal of Inorganic Biochemistry*, 115:72–77, 2012. Special Issue in Memory of Hans Freeman.

[176] Koen Binnemans. Chapter 225 - Rare-earth β-diketonates. volume 35 of *Handbook on the Physics and Chemistry of Rare Earths*, pages 107–272. Elsevier, 2005.

[177] Bronislaw Marciniak and Gonzalo E. Buono-Core. Photochemical properties of 1,3-diketonate transition metal chelates. *Journal of Photochemistry and Photobiology A: Chemistry*, 52(1):1–25, 1990.

[178] Teng Fei, Xin Gu, Ming Zhang, Chunlei Wang, Muddasir Hanif, Houyu Zhang, and Yuguang Ma. Optical and electronic properties of phosphorescent iridium(III) complexes with phenylpyrazole and ancillary ligands. *Synthetic Metals*, 159(1):113–118, 2009.

[179] Ann Cantrell and David J McGarvey. Photochemical studies of 4-tert-butyl-4'-methoxydibenzoylmethane (BM-DBM). *Journal of Photochemistry and Photobiology B: Biology*, 64(2):117–122, 2001.

[180] Stanislav S. Stanimirov, Anton A. Trifonov, and Ivan C. Buchvarov. Discovering of the L ligand impact on luminescence enhancement of Eu(Dibenzoylmethane)3.Lx complexes employing transient absorption spectroscopy. *Spectrochimica Acta Part A: Molecular and Biomolecular Spectroscopy*, 258:119832, 2021.

[181] André M. T. Muthig, Marcel Krumrein, Justin Wieland, Markus Gernert, Florian Kerner, Jens Pflaum, and Andreas Steffen. Trigonal Copper(I) Complexes with Cyclic (Alkyl)(amino)carbene Ligands for Single-Photon Near-IR Triplet Emission. *Inorganic Chemistry*, 61(37):14833–14844, 2022.

[182] Markus Gernert, Lukas Balles-Wolf, Florian Kerner, Ulrich Müller, Alexander Schmiedel, Marco Holzapfel, Christel M. Marian, Jens Pflaum, Christoph Lambert, and Andreas Steffen. Cyclic (Amino)(aryl)carbenes Enter the Field of Chromophore Ligands: Expanded π System Leads to Unusually Deep Red Emitting CuI Compounds. *Journal of the American Chemical Society*, 142(19):8897–8909, 2020.

[183] Zheng Gao, Yongcao Hao, and Mei-Ling Zheng. A fluorescent dye with large Stokes shift and high stability: synthesis and application to live cell imaging. *RSC Adv.*, 7:7604–7609, 2017.

[184] T.V. Healy. Synergism in the solvent extraction of metal ions by dibenzoylmethane. *Journal of Inorganic and Nuclear Chemistry*, 31(2):499–511, 1969.

[185] Witt, Katarzyna and Radzyminska-Lenarcik, Elzbieta. Studies of the aromatic etones as extractant of copper ions. *E3S Web Conf.*, 18:01016, 2017.

[186] Fabio Novelli, Kaixuan Chen, Adrian Buchmann, Thorsten Ockelmann, Claudius Hoberg, Teresa Head-Gordon, and Martina Havenith. The birth and evolution of solvated electrons in the water. *Proceedings of the National Academy of Sciences*, 120(8):e2216480120, 2023.

[187] F. Gobert, S. Pommeret, G. Vigneron, S. Buguet, R. Haidar, J.-C. Mialocq, I. Lampre, and M. Mostafavi. Nanosecond kinetics of hydrated electrons upon water photolysis by high intensity femtosecond UV pulses. *Research on Chemical Intermediates*, 27(7):901–910, 2001.

[188] Shalini Nigam and Sarah Rutan. Principles and Applications of Solvatochromism. *Applied Spectroscopy*, 55(11):362A–370A, 2001.

[189] Laurel A. Goj, Elizabeth D. Blue, Colleen Munro-Leighton, T. Brent Gunnoe, and Jeffrey L. Petersen. Cleavage of X-H Bonds (X = N, O, or C) by Copper(I) Alkyl Complexes To Form Monomeric Two-Coordinate Copper(I) Systems. *Inorganic Chemistry*, 44(24):8647–8649, 2005.

[190] Laurel A. Goj, Elizabeth D. Blue, Samuel A. Delp, T. Brent Gunnoe, Thomas R. Cundari, Aaron W. Pierpont, Jeffrey L. Petersen, and Paul D. Boyle. Chemistry Surrounding Monomeric Copper(I) Methyl, Phenyl, Anilido, Ethoxide, and Phenoxide Complexes Supported by N-Heterocyclic Carbene Ligands: Reactivity Consistent with Both Early and Late Transition Metal Systems. *Inorganic Chemistry*, 45(22):9032–9045, 2006.

[191] Ivo H. M. van Stokkum, Miroslav Kloz, Dario Polli, Daniele Viola, Jörn Weißenborn, Ebo Peerbooms, Giulio Cerullo, and John T. M. Kennis. Vibronic dynamics resolved by global and target analysis of ultrafast transient absorption spectra. *The Journal of Chemical Physics*, 155(11):114113, 2021.

[192] Ivan A Shuklov, Natalia V Dubrovina, and Armin Börner. Fluorinated Alcohols as Solvents, Cosolvents and Additives in Homogeneous Catalysis. *Synthesis*, 2007(19):2925–2943, 2007.

[193] Bowen Li, Xiang'an Song, Xi Jiang, Zhiyi Li, Fengyun Guo, Ying Wang, Liancheng Zhao, and Yong Zhang. Stable deep blue organic light emitting diodes with CIE of $y < 0.10$ based on quinazoline and carbazole units. *Chinese Chemical Letters*, 31(5):1188–1192, 2020.

Respective Contributions

Parts of this work have already been published. This concerns chapter 5.1, i.e. the photophysical characterization of the complex NHCCuPy (see ref.[40]). I am the first author of this publication. The planning and coordination of the experiments, as well as the evaluation and interpretation of the results, were my responsibility. All illustrations, if not otherwise indicated, were composed by me. The manuscript was written by me, corrected by Peter Gilch, and proofread by the other authors. In the quantum chemical part, supplementary texts were added by Jasper Guhl and Christel Marian. The quantum chemical calculations, planned and coordinated by me, were conducted by Jasper Guhl. The respective Figure 5.15 was drawn by Jasper Guhl. He also provided the difference density molecular structures shown in Figure A.7, Figure 5.38, and Figure 5.41. The nsTA measurements were conducted by Wiebke Haselbach, and parts of the steady-state measurements (absorption and emission) were performed by Jennifer Kremper as part of her bachelor thesis and a consecutive research internship under my guidance and supervision. The measurements on the Kerr setup were conducted by Mahbobeh Morshedi. The synthesis of the complex NHCCuPy, as well as the verification by ^{1}H-NMR, ^{13}C{^{1}H}-NMR, ESI mass spectrometry and elemental analysis, were performed by Philipp Schmeinck (Institute of Organometallic Chemistry, Prof. C. Ganter).

Concerning the photophysical characterization of the complex NHCCuDBM (chapter 5.2), all text was written by me and corrected by Peter Gilch. All illustrations were composed by me. The planning and coordination of the experiments, as well as the evaluation and interpretation of the results, were my responsibility. Parts of the steady-state measurements (absorption and emission) were performed by Oliver Röth as part of his master's thesis under my guidance and supervision. The measurements on the Kerr setup were performed by Mahbobeh Morshedi. The quantum chemical calculations, planned and coordinated by me, were conducted by Jasper Guhl. The key experiments of femtosecond transient absorption spectroscopy were conducted by me as part of both projects.

Declaration

I declare under oath that I have produced my thesis independently and without any undue assistance by third parties under consideration of the 'Principles for the Safeguarding of Good Scientific Practice at Heinrich Heine University' Düsseldorf. The dissertation has not been submitted to any other faculty. I have not made any previous attempts to obtain a doctorate.

Place, Date

Oliver Nolden